CONTROLLING THE CONFORMATION OF Π-CONJUGATED ORGANIC MOLECULES

USING HYDROGEN BOND INTERACTIONS

A Dissertation

by

ANTHONY UEI MU

Submitted to the Graduate and Professional School of
Texas A&M University
in partial fulfillment of the requirements for the degree of

DOCTOR OF PHILOSOPHY

Chair of Committee,	Lei Fang
Committee Members,	Daniel A. Singleton
	Donald J. Darensbourg
	Shiren Wang
Head of Department,	Simon North

December 2022

Major Subject: Chemistry

ABSTRACT

Intramolecular hydrogen bonding as a means of conformational control represents a promising strategy for manipulating a wide range of properties of organic π-conjugated molecules. The past few decades saw significant advances and developments in the field of organic π-conjugated materials, but there still remains significant knowledge gaps in the design principles associated with conformation. This dissertation focuses on the control of molecular conformation of π-conjugated molecules and macromolecules using hydrogen bonds.

This work begins with a brief introduction of π-conjugated materials involving hydrogen-bond conformational locks in Chapter I. It also outlines the importance of theoretical simulations in this field. Specific challenges in this field are identified in order to discuss the breakthroughs in employing hydrogen-bonds to achieve high-performing electronic materials.

Chapter II demonstrates the use of density functional theory computational method as a means of screening molecular designs, corroborating experimental data, and mechanistically investigating unprecedented results. Particularly important methods include the investigations into the thermodynamics of torsional rotation for strategic structural comparisons, and also the correlation of simulated electrostatic potential maps to experimental investigations in intermolecular interactions.

Reaching beyond the theoretical realm, Chapter III discusses the experimental integration of pre-organized hydrogen bond strategy upon diazaisoindigo building blocks, involving synthesis and characterization. As a result of the robust intramolecular hydrogen bonds, thermally unyielding molecular conformations were achieved, elucidated not only by theoretical resources, but through thermal analysis and variable temperature toughness experiments. Facile syntheses of

these materials allowed for the systematic study from fundamental optical and electronic experiments to applications in organic electronics.

In this context, Chapter IV describes several molecular engineering and process engineering approaches to optimize solubility, thin-film processibility, solid state packing, and ultimately electronic device performances of π-conjugated model compounds. The robust hydrogen-bonds aided in thin-film processing and, consequently, led to the fabrication of organic field-effect transistor devices that show hole transport mobility up to $0.27 \text{ cm}^2\text{V}^{-1}\text{s}^{-1}$. Furthermore, the measured organic field-effect transistor performances established clear correlations between rudimentary chemical properties and bulk organic electronic material engineering principles.

Last but not least, attempts at extending these hydrogen-bond-bridged π-conjugated structures into macromolecular backbone is detailed in Chapter V. Synthetic challenges illuminated the importance of frontier molecular orbital energy tuning for palladium-catalyzed cross-coupling reactions and the necessity of adequate polymer solubility. To overcome these hurdles, new polymer building blocks were developed to ameliorate these concerns for the future development of H-bond-bridged π-conjugated materials.

In summary, this dissertation describes a series of approaches to elucidate the structure-property relationships of hydrogen-bond-centered conformational control towards the performance of π-conjugated materials through (i) density functional theory exploration of π-conjugated molecules, (ii) installation of hydrogen bond conformational locks on these materials through pre-organized bridging moieties, (iii) and effective molecular and process engineering for use in the fabrication of functioning organic electronic devices.

DEDICATION

To my friends and family

ACKNOWLEDGEMENTS

It is a genuine pleasure to express my gratitude to my advisor, Professor Lei Fang, for the continued guidance and advice through all the stages of my academic journey. I am immensely thankful that he allowed me many opportunities to travel to perform various unconventional experiments in other cities and even other countries. The experiences that he opened up for me transcended academic affairs and allowed me to experience my graduate career to the fullest.

I would also like to express thanks to Professors Daniel A. Singleton, Donald J. Darensbourg. and Shiren Wang for their continued support as part of my committee. I especially thank Prof. Singleton for familiarizing me with the idea that embarrassment is when we know that we are learning. I would also like to thank Prof. Darensbourg for expanding my enthusiasm for chemistry in CHEM 483 - Green Chemistry, and also, for the Earth Day T-shirt that I continue to wear. All of these things made my academic path better.

I would like to acknowledge the group members I have had the pleasure of crossing paths with through my undergraduate and graduate career, many of which I hope to be lifelong friends with: Dr. Congzhi Zhu, Dr. Jongbok Lee, Dr. Tianyu Yuan, Dr. Yang Zou, Dr. Zi-Hao Guo, Dr. Sai Che, Dr. Bailey Phillips, Dr. Alex Kalin, Dr. Yirui Cao, Dr. Chenxu Wang, Dr. Xiaozhou Ji, Dr. Yun-Hyuk Choi, Dr. Yen-Hao Lin, Dr. Vikki Shindi, Bo-Ji Peng, Che-Hsuan Chang, Octavio Miranda, Mingwan Leng, Abani, Steven Hodge, Shao-Jiun Yang and Guanghua Yu. Thank all group members for being the best group I could ever imagine in graduate school. I would like to specially thank my longtime mentor, Dr. Congzhi Zhu, who was integral for convincing me to pursue my Ph.D. when I was an undergraduate student, leading me to where I am today.

CONTRIBUTORS AND FUNDING SOURCES

Contributors

This work was supervised by a dissertation committee consisting of Professors Lei Fang (principal investigator), Daniel A. Singleton (committee member) and Donald J. Darensbourg (committee member) of the Department of Chemistry and Professor Shiren Wang (committee member) of the Department of Industrial & Systems Engineering. Part of this work was also supervised by Professor Mohammed Al-Hashimi (internship supervisor) of the Texas A&M University at Qatar Department of Science during Summer 2019.

Dr. Yirui Cao performed the synthesis of **Th-IDCZ-BTh**, **Th-IDCZ-Cl-BTh**, **Ph-IDCZ-BTh**, and **Ph-IDCZ-Cl-BTh** and provided this material in Chapter IV. Dr. Maciej Barłóg provided the **IDTZ** material in Chapter V. Mariela Vazquez performed AFM, TGA, and DSC for several compounds in Chapter III. Dr. Joseph Strzalka at the Advanced Photon Source of Argonne National Laboratory provided beamline support for GIXS measurements in Chapter IV. Dr. Alex Kalin and Dr. Bailey Phillips aided with various GIXS measurements. Dr. Yi Liu and Teresa Chen and at the Molecular Foundry of Lawrence Berkeley National Laboratory aided in device fabrication of organic field effect transistors in 4.2.1. Dr. Jie Xu and Dr. Yeonju Kim at the Center for Nanoscale Materials of Argonne National Laboratory aided in the device fabrication of organic field effect transistors in 4.2.3. Synthesis of some molecules for GIXS measurements and DFT calculations were performed by Dr. Marc Comí in the group of Dr. Mohammed Al-Hashimi. The Laboratory for Molecular Simulation at Texas A&M University provided the Gaussian 16 software for DFT calculations.

Funding Sources

NOMENCLATURE

AFM	Atomic Force Microscopy
BBI	Benzobisimidazole
Boc	t-Butyloxycarbonyl
BTH	Benzo[d]thiazole
CV	Cyclic Voltammetry
DAIID	Diazaisoindigo
DCM	Dichloromethane
DFT	Density Functional Theory
DMAP	4-Dimethylaminopyridine
DMF	N,N-Dimethylformamide
DMSO	Dimethyl Sulfoxide
DSC	Differential Scanning Calorimetry
EPR	Electron Paramagnetic Resonance
ESI	Electron Spray Ionization
Fc	Ferrocene
Fc^+	Ferrocenium
FET	Field-Effect Transistor
FT-IR	Fourier-Transform Infrared Spectroscopy
GIWAXS	Grazing Incidence Wide Angle X-ray Scattering
HOMO	Highest Occupied Molecular Orbital
IDCZ	Indolo[3,2-b]carbazole

IDTZ	*s*-indaceno[2,1-*d*:6,5-*d′*]bisthiazole
IID	Isoindigo
LUMO	Lowest Unoccupied Molecular Orbital
MS	Mass Spectroscopy
NBO	Natural Bond Orbital
NIR	Near-Infrared
NMR	Nuclear Magnetic Resonance
P3HT	Poly(3-hexyl)thiophene
PCE	Power Conversion Efficiency
Ph	Phenyl
OSC	Organic Solar Cell
OLED	Organic Light Emitting Diode
OFET	Organic Field Effect Transistor
TBAF	Tetrabutylammonium Fluoride
TBAPF$_6$	Tetrabutylammonium Hexafluorophosphate
TD-DFT	Time-Dependent Density Functional Theory
TGA	Thermogravimetric Analysis
THF	Tetrahydrofuran
XRD	X-Ray Diffraction

TABLE OF CONTENTS

LIST OF FIGURES

xv

LIST OF SCHEMES

LIST OF TABLES

CHAPTER I

INTRODUCTION

1.1 Conformation Control of π-Conjugated Molecules and Macromolecules

1.1.1 Overview of π-Conjugated Materials

The chemistry of π-conjugated materials has attracted ongoing attention over the past decade. Spawning from an academic research setting half a century ago,[1] organic electronic materials are now in the homes of people all over the world. Driven by the success of organic semiconductors, the fields of organic solar cells (OSC),[2] organic light emitting diodes (OLED),[3, 4] and organic thin-film transistors (OTFT),[5] *etc*. continue to grow.[6, 7] As electronic devices have already revolutionized our modern lives by increasing the convenience of everyday tasks, it is expected that next-generation organic electronics, such as wearable devices and sensors, [8, 9] will further assist in our way of life. Although organic semiconductors are desired for wide-ranging chemical tunability, synthesis from nonprecious elements, and mechanical adaptability, to date, inorganic materials continue to dominate the field of semiconductors due to their superior charge-transfer mobilities.[10] Despite this intrinsic drawback, recent advancements in this field have demonstrated promise for next-generation materials, *e.g.* increasing the early organic semiconductor mobilities[11] from less than 10^{-5} cm^2 V^{-1} s^{-1} to around 40 cm^2 V^{-1} s^{-1}. [12, 13] While organic semiconductor of past decades have demonstrated that donor-acceptor coupling,[14, 15] electrochemical doping,[16] and extending effective conjugation length[17] are crucial, clear fundamental structure-property relationships have yet to be drawn to achieve performances on the level of inorganic materials.

In the context of semiconducting performance, molecular conformations of π-systems play a pivotal role in governing a wide range of their properties, including solubility, solid-state

characteristics, as well as optical and electronic functions.[18] In general, coplanar π-conjugated molecules are expected to possess more extended coherent conjugation,[19] giving rise to faster intramolecular charge transport[20] and lower band gaps.[21] To further illustrate the impacts of conformational control, in order for electron transfer processes to occur at a fast rate, the reorganizational energy must be minimized according to Marcus theory.[22] Since rotational freedom increases this reorganization energy, limiting torsional motion leads to higher charge-carrier mobilities, which is important to many of the aforementioned applications. Achieving these rigid structures proves difficult, due to commonly being done by covalent bond linkages, such as in ladder-type structures (**Figure 1.1b**).
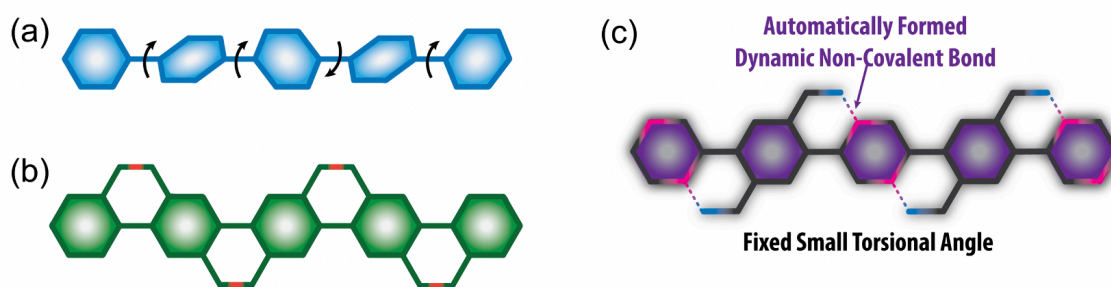
Figure 1.1 Graphic representations of (a) a traditional π-conjugated polymer, (b) a ladder-type π-conjugated polymer and (c) a π-conjugated polymer coplanarized by dynamic noncovalent bonds. Adapted from *Macromol. Rapid Commun.* 2018, 39, 1700241 with permission from John Wiley and Sons.

In this regard, active and rational conformational control strategies are highly desired for organic electronics, not only decreases the reorganization energy for charge transport processes, but also allows for improved intermolecular packing in the solid state.[23] Coplanar conformations of extended π-systems are often accomplished by covalently fusing aromatic rings in a bottom up manner.[20, 24-26] However, extensive employment of this strategy has been limited due to challenges with precise synthesis and solution processability.[27] The use of intramolecular non-covalent bonding interactions emerged as a promising strategy to confine the backbone conformation of

conjugated polymers. Various types of dynamic bonding interactions have been investigated for this purpose. Among these dynamic interactions, weak intrachain interactions of heteroatoms (such as S—O, S—S, S—N, S—F, S—Cl, and P—O) are currently the most widely employed for electronically active polymers.[18, 28-34] While the installation of these heteroatoms in π-conjugated polymers often led to high performing charge-transport and photovoltaics, these interactions are typically limited to <1.0 kcal/mol and can easily be disrupted by thermal energy. In the past few years, intramolecular hydrogen bonds (H-bonds) have been found to offer greater bonding strengths (2~15 kcal/mol for electrically neutral H-bonds) for conjugated polymers.[35-52]

1.1.2 Intramolecular Hydrogen Bonds for Conformational Control of Conjugated Molecules

As ubiquitous as the term "hydrogen bond" is in the current day scientific literature and even all levels of school curriculum, the definition of the expression has been contested as recently as 2010. While many scientists credit Linus Pauling's initial work[53] in valence bond theory for first coining such profound hydrogen attractions as acting as a "bond," the use of this word has faced objection due to the unscrupulous terminology of those times. The term "hydrogen bond" has experienced common use in describing the interactions in banal chemical systems, such as water,[54] DNA,[55] and proteins.[56] Despite this, when newer accounts of hydrogen interactions arose (*i.e.* O–H$\cdots\pi$, N–H$\cdots\pi$, and C–H$\cdots\pi$) an area of contention emerged as chemists debated on the meticulousness of calling these "hydrogen bonds."[57] Although strong hydrogen bonds, as alluded to earlier, have remained noncontroversial, problems arise as the hydrogen interactions become weaker and multifaceted. The term was revisited numerous times due to this dispute regardless of the trivial nature of this matter.[58-60] Two attempts to address this nomenclature issue were made by The International Union of Pure and Applied Chemistry (IUPAC), which first led to extremely

stringent parameters. Following this, an assigned task force worked tireless from 2005 until a consensus was finally reached in 2011, which remains our current guidelines for "hydrogen bonding" in present day.[61] Regardless, the initial IUPAC definition remains ubiquitous, specifically explaining hydrogen bonding as electrostatic interactions or dipole-dipole interactions that are modulated or strengthened by increasing acidity or basicity. Furthermore, charge-transfer models were also used to describe these interactions. The importance of this dispute, only roughly a decade ago, becomes blatant as research into hydrogen bonding (H-bonding) expands. In fact, many of the older definitions for H-bonding are still prevalent in scientist's understanding of these interactions.
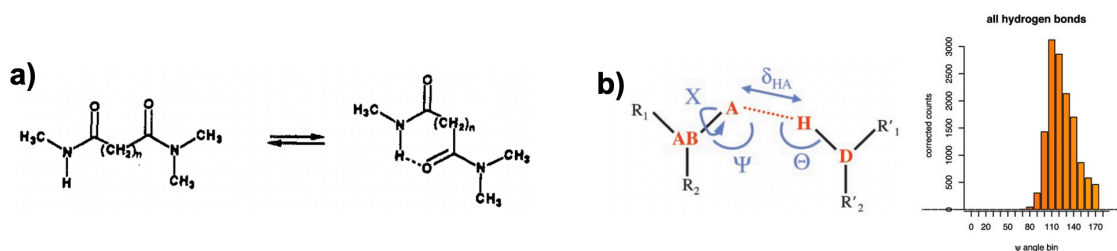
Figure 1.2. Representative literature demonstrating the ubiquity of non-linear hydrogen bonding. Adapted from *J. Am. Chem. Soc.* 1991, 113, 4, 1164–1173 and *PNAS,* 2004, *101*, 6946-6951 with permissions from American Chemical Society and The Proceedings of the National Academy of Sciences.

As IUPAC first defined in 1997, the electrostatic model implied a high degree of directionality for hydrogen bonds, due to the 180° geometries of dipole-dipole interactions. Similarly, in the charge transfer model of the hydrogen bond, the lone-pair to σ* orbital alignments also infer high directionality.[62, 63] Despite this, a high degree of strong hydrogen bonds in nature extend at less than 180° angles (**Figure 1.2**).[64-66] These H-bonds are indicative that other intermolecular forces play a nontrivial role in the interaction. For example, London dispersion forces and other van der Waals forces do not limit directionality as in electrostatic and charge-

transfer interactions. In these instances, increased polarizability could strengthen H-bonds, as evidenced in cases of many C–H···S interactions (e.g. streptavidin-biotin noncovalent interactions).[67, 68] Besides this, the intramolecular hydrogen bonds of many proteins demonstrate shorter bond lengths than intermolecular hydrogen bonds of the same ΔpK_a. Interestingly, the O–H···O angles of these intramolecular hydrogen bonds mostly adopt less than 180° angles, presumably due to the unfavorable process of relaxing the H-bond groups to linear conformations by rearranging the covalent scaffold.[69]
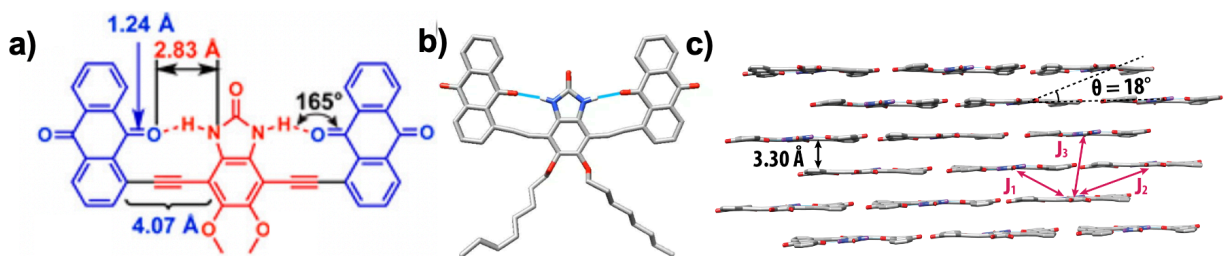
Figure 1.3. Previous work of structure with (a) <180° hydrogen-bonding angle, (b) front view and (c) packing mode of single-crystal structure. Adapted from *Org. Lett.* 2016, 18, 24, 6332–6335 with permission from American Chemical Society.

In the context of introducing H-bonds to conformationally control π-conjugated molecules, previous work in our group has demonstrated robust bent intramolecular H-bond angles (**Figure 1.3**). The resulting scaffold resulted in conformationally favorable nonlinear H-bonds, forming 165° angles about the H-bond-accepting groups. The nonlinear angle about the hydrogens allowed for geometrically favorable interaction with the carbonyl oxygen lone-pairs. The resulting robust H-bonding enforced a highly coplanar backbone, as seen in the single-crystal structure, leading to short-range π-π stacking distances of 3.30 Å. There are numerous benefits to the observed conformation locking that will be discussed as a main subject of this dissertation. Nevertheless, improving on the molecular design structure shown in **Figure 1.3** involves geometric favorability to intramolecular hydrogen bonding. As documented many times before, the formation of

intramolecular hydrogen bonds in planar conjugated six-membered rings enhances the propensity for resonance-assisted hydrogen bonding and forms the shortest contacts in comparison to, not only smaller or larger ring scaffolds, but also intermolecular hydrogen bonding.[70-72] Therefore, These geometric factors must be considered when choosing building blocks for π-conjugated materials.
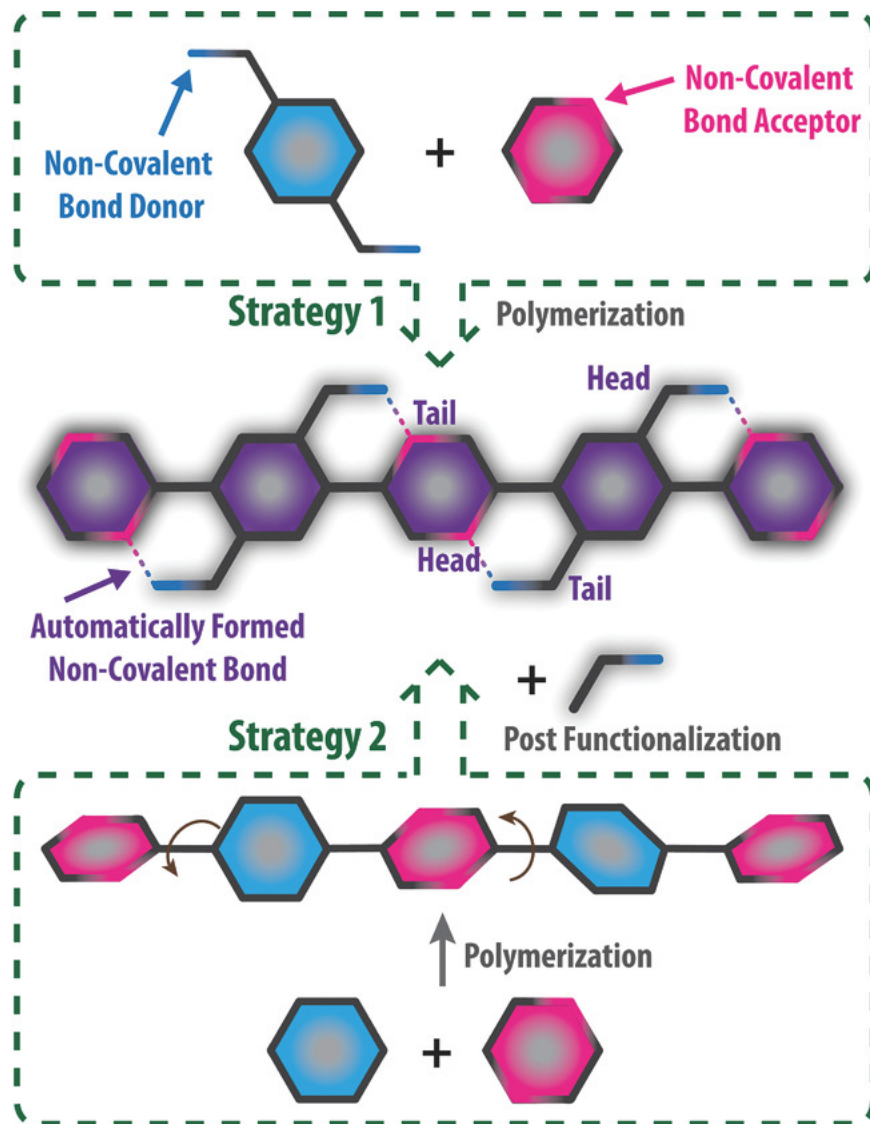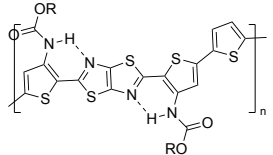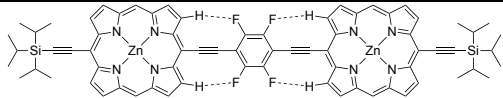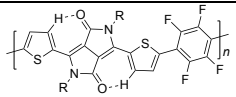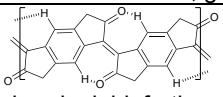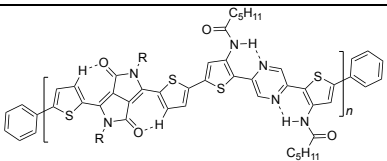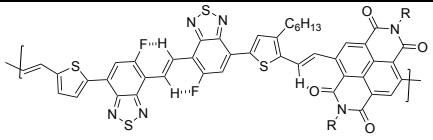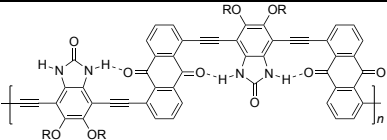
Figure 1.4 Graphic representations of two different synthetic strategies to construct a π-conjugated polymer coplanarized by dynamic noncovalent bonds. Adapted from *Macromol. Rapid Commun.* 2018, 39, 1700241 with permission from John Wiley and Sons.

In order to ensure geometric favorability for these conformational locks, two general synthetic strategies can be used to incorporate dynamic noncovalent bonds, such as H-bonds, into these π-conjugated systems (**Figure 1.4**). In the first regime, hydrogen bond functionalities can be pre-installed on the monomeric building blocks, such that, after coupling, the pre-organized conformational locks form spontaneously.

In the past few years, the concept of intramolecular hydrogen bonds in conjugated polymers has grown, showing that bonding strengths could be achieved from 2-15 kcal/mol.[35-52] Representative examples of the advantages of these H-bonds are shown in **Table 1.1**. These H-bonds were effective in confining π-conjugated backbones into coplanar conformations, stabilizing these conformations from 4-15 kcal/mol compared to their non-H-bond analogues. As hypothesized, conformational control consistently demonstrated the increase of semiconducting performance, as noted by charge mobilities greater than 7 cm^2 V^{-1} s^{-1}, even just in the presence of weak hydrogen bonds. Although there continues to be growing literature in this field, there are still many gaps in knowledge and synthetic challenges before clear structure-property relationships can be drawn. For example, many H-bond bridged polymeric structures in the literature do not consist of fully fused ladder-type structures as a result of their included conformational locks. Thus, although sections of chain lengths are rigidified, there is still high rotational disorder that other conventional conjugated polymers suffer from. Although there are various reports of improved electronic device performance using this method,[35-49] a systematic compilation of theoretical data and experimental data must be developed to fully elucidate the mechanistic effects at play.

Table 1.1. Representative recent examples of conjugated π-systems featuring conformation locking H-bonds

Structure and Comment	Torsional Barrier (kcal/mol)	Conformation Stabilization (kcal/mol)[a]	Charge Mobility (cm^{2}V^{-1}s^{-1})[b]	Ref
Partially confined backbone, high hole mobility	NA	NA	1.98 (h)	45
Weak C—H---F H-bonds	7.05	−4.25 (free energy)	NA	46
Backbone partially confined by H-bond and partially bridged by weak S—F interactions, good hole mobility	9.2	−4.7 (free energy)	0.44 (h)	49
The backbone is already rigid, further enforced by weak C—H…O H-bonds, high performance and good stability of electronic and thermoelectric functions	NA	NA	0.16 (e)	39
Free rotating bonds remain, good hole mobility	10.0	−5.5 (free energy)	0.162 (h)	47
Partially confined backbone, two type of H-bond incorporated, excellent electron mobility	NA	NA	7.16 (e)	41
Entire backbone confined by H-bonds. Demonstrated control on solubility and processability by masking/unmasking H-bonds	13.9	NA	NA	51, 52

[a] Stabilization of the coplanar conformation compared to non-H bond control, defined as $E_{\text{H-bonded}} - E_{\text{control}}$, E is either Gibbs free energy or enthalpy. [b] (h) hole mobility, (e) electron mobility.

1.2. Density Functional Theory Analysis of Molecular Conformation of π-Conjugated Structures

As the collection of experimental data grows for π-conjugated molecules and macromolecules and interest in these materials for use in next-generation materials increases,[6] theoretical investigations have emerged as an important method in the rationalization of investigational data. Discussed in the previous chapter, the desired properties for these organic functional materials consist of favorable frontier molecular orbital energies, such as low band gaps, and controlled conformations, and many other undiscovered structure-property relationships. Due to the surge in progress of computer technology in the recent decades, computer hardware has evolved to allow for higher level calculations. In this context, Density Functional Theory (DFT) has become an invaluable tool for studying a variety of structural, optical, and electronic properties of organic electronic materials. DFT has demonstrated better performance than other computational methods, because it accounts for electron correlation effects.[73] For example, the Møller−Plesset (MP2) method,[74] which has garnered great interest in the past decade,[75, 76] overestimates frequency values significantly.[77] Also, Hartree-Fock (HF) calculations are also known to estimate frequencies by >10%.[78] In further comparison between these methodology, computational results correlated with well-studied properties of common organic conjugated materials, such as furan and thiophene, at a much greater accuracy for DFT than MP2 and HF methods (**Table 1.2**).[78] In fact, DFT-based calculations have demonstrated consistently better results than those from other methods during investigations into many pertinent properties, such as heats of formation,[79, 80] crystal-structure prediction,[81] excited-states,[82] *etc.*

				6-31G**					
sym	no.	exptl[b]	HF	MP2 full	MP2 fc	DFT BLYP	DFT B3LYP	DFT LDA	DFT BVWN
A_1	1	3126	3427	3346	3341	3189	3271	3207	3226
	2	3098	3390	3312	3308	3144	3229	3168	3181
	3	1409	1597	1488	1483	1416	1470	1477	1419
	4	1360	1530	1436	1433	1360	1407	1374	1373
	5	1083	1207	1132	1131	1082	1112	1062	1099
	6	1036	1106	1094	1092	1030	1059	1054	1034
	7	839	890	867	883	803	832	856	802
	8	608	658	630	628	591	610	609	592
A_2	9	898	1053	867	855	877	920	883	888
	10	683	804	673	667	647	683	654	655
	11	565	618	550	542	555	575	570	556
B_1	12	3125	3425	3343	3338	3187	3269	3205	3224
	13	3098	3376	3299	3294	3131	3215	3155	3167
	14	1507	1740	1571	1568	1515	1578	1549	1524
B_1	15	1256	1407	1314	1311	1240	1282	1226	1259
	16	1085	1210	1134	1133	1084	1115	1068	1099
	17	872	951	912	910	846	876	866	853
	18	751	808	781	778	713	742	754	711
B_2	19	867	1029	857	847	833	880	833	845
	20	712	813	732	726	701	728	700	710
	21	452	484	457	453	437	453	458	438
error[c]	CH		293	213	209	48	130	67	88
	in-plane[d]		118	50	49	14	28	22	17
	out-of-plane		104	15	20	21	10	17	14
	mid-IR[e]		113	38	39	16	22	20	16
	total		147	71	71	23	43	30	30
SF[f]			0.819	0.888	0.894	0.980	0.925	0.962	0.964
error[c]			29	24	26	23	16	21	26

In addition to the superiority of DFT over other theories, a large number of density functionals also remain in competition with one another. As the field of DFT methodologies continues to expand to match our current rate of technological advancements, many past density functionals have been eclipsed by the Becke's three-parameter functional using the gradient-corrected Lee-Yang-Parr functional (B3LYP).[83, 84] Although the initial intention of this hybrid functional was to study the vibrational absorption and circular dichroism of molecules, it has emerged as a standard method for gas-phase investigations of a considerable set of organic molecules.[79, 85] The initial benefits of the B3LYP functional were first demonstrated decades ago in comparison to BLYP, LDA, and BVWN methods (**Table 1.2**).[78] The advantages that this method possesses in comparison to others are due to the favorable balance between low computational cost and accuracy of results. In the case of wide molecular coverage, it has even been demonstrated that the accuracies in calculated heats of formation, ionization potentials, electron affinities, vibrational frequencies, reaction barriers, and most importantly, conformational and hydrogen bonding energies ranked consistently low for B3LYP in comparison to a variety of other common DFT methods.[86] Despite other methods having an edge over B3LYP for certain individual categories, B3LYP still exhibited the best broad-property precision, demonstrating its importance on testing extensive, diverse sets of data.
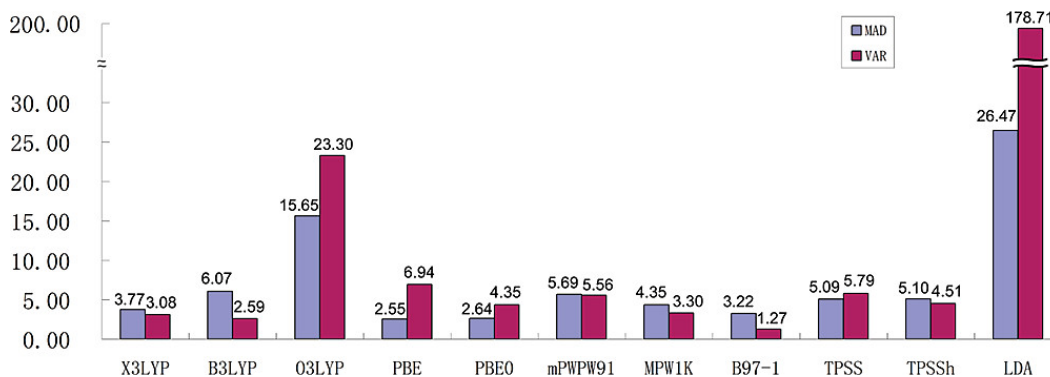
Figure 1.5. MAD (mean absolute deviation) in kJ/mol and VAR (variance) in kJ^2/mol^2 of DFT methods on binding energy calculations of fourteen intermolecularly hydrogen-bonded complexes. Adapted from *J. Chem. Theory Comput.* 2009, 5, 1, 86–96 with permission from American Chemical Society.[87]

On this front, the popularity of DFT methods must be considered. Although many other functionals have demonstrated comparatively increased accuracies, such as X3LYP[88] and K2-BVWN,[89] an important aspect that must not be overlooked is the relatively widespread use of B3LYP for organic electronic materials for cross-comparison. To allow for future systematic investigations between the vast range of B3LYP calculated organic material data, the selection of the hybrid functional B3LYP continues to be the favored choice among researchers.

As stated before, one of the challenges in computational methods for the current field of organic electronics lies in the system size of many notable organic molecules. In the context of electronically active π-conjugated materials, recent studies have shown the B3LYP functional at the DFT level is polythiophenes,[90] oligothiophenes,[78] and other key derivatives.[91, 92] Furthermore, B3LYP has recently demonstrated accurate results for the position of electron levels and exciton effects.[93] Specifically to the DFT investigations in Chapter II, H-bonding dynamics must be accurately predicted to model the desired properties for π-conjugated materials. While other functionals may show high promise in the prediction of H-bond strengths, such as the aforementioned X3LYP, B3LYP still demonstrated one of the lowest errors of other common functionals (**Figure 1.5**). In addition to intermolecular H-bond investigations, modelling

intramolecular H-bond interactions in amino acids has further demonstrated the accuracy of the method.[87] In the pioneering work by Dr. Congzhi Zhu (**Figure 1.3**) we have evaluated the effects of controlling the conformation of conjugated molecules several times. Much of the insight of these projects were gained through theoretical calculations. For example, common or basic geometric optimizations and frequency calculations can allow us to predict or compare relative frontier molecular orbital values, as shown here. In these respects, DFT is an important choice for (i) selecting conjugated building units with favorable electronic properties, (ii) determining the thermodynamics of rigidification of planar structures, (ii) use these results to tune molecular packing for the desired applications.

1.3 Challenges and Outlook

As mentioned earlier in this chapter, the incorporation of intramolecular H-bonds serves as a promising strategy to control the conformation of π-conjugated systems. As these π-conjugated molecules and macromolecules adopt coplanar conformations promoted by H-bonding, desirable properties are greatly enhanced for materials applications. On this front, important recent developments have been summarized in previous sections. Examples listed demonstrate the current knowledge of the structure-property relationships of rotational control for these π-conjugated systems. Although it is well established that controlling the conformation of π-the conjugated backbone through a variety of noncovalent bonds represents a promising strategy to achieve high-performing semiconductor performances and other materials applications, there still exist many challenges in molecular design, synthesis, characterization, and processing.

To achieve these goals, a fundamental understanding must be established between the tuning of intramolecular H-bond strength and the bulk material properties, such as intermolecular packing order and thin-film processibility. In terms of non-covalent bond locking, robust H-bonds

can be used to stabilize the desired coplanar conformations even during thermal treatments required for Boc-cleavage or for thin-film annealing. In contrast, weak H-bonds can be manipulated by external stimuli, allowing for active dynamic control over molecular conformation. Although previously demonstrated H-bond conformationally locked molecules and polymers have not achieved notable performance in electronic devices, this issue can be resolved by certain molecular design elements. For instance, developing novel building blocks can be accomplished by installing H-bond moieties onto π-conjugated molecules that already exhibit notable materials performances. The additional rigidity and coplanarity imparted by the resulting H-bond conformational lock is expected to enhance the already proven high performances of such molecules and macromolecules.

Despite the vast expansion of the field in recent years, there are still numerous unexplained facets to the development of effective organic electronic materials. In addition to the experimental characterization of backbone conformation and materials performance, theoretical studies are increasingly important to corroborate investigational data, predict a wide-range of desirable properties, and elucidate previously indecipherable mechanisms that determine certain observed structure-property relationships. Further, previously overlooked properties, such as electrostatic interactions and molecular quadrupoles are much more accessible through computational methods. Therefore, correlations between such molecular-scale properties and bulk interactions can be probed to determine previously disregarded intermolecular interactions. Therefore, DFT calculations carried out with the hybrid functional B3LYP is a preferred strategy for the theoretical investigation of π-conjugated organic molecules.

CHAPTER II

DENSITY FUNCTIONAL THEORY CONFORMATIONAL INVESTIGATIONS OF

POLYCYCLIC AROMATIC MOLECULES AND MACROMOLECULES

2.1 Introduction

In our pioneering work described in the previous chapter, we evaluated the effects of conformational control on π-conjugated molecules. Previously demonstrated, many insights were gained through DFT calculations to corroborate experimental results. For example, common or basic geometric optimizations and frequency calculations can allow us to predict or compare relative frontier molecular orbital values (Figure 2.1).
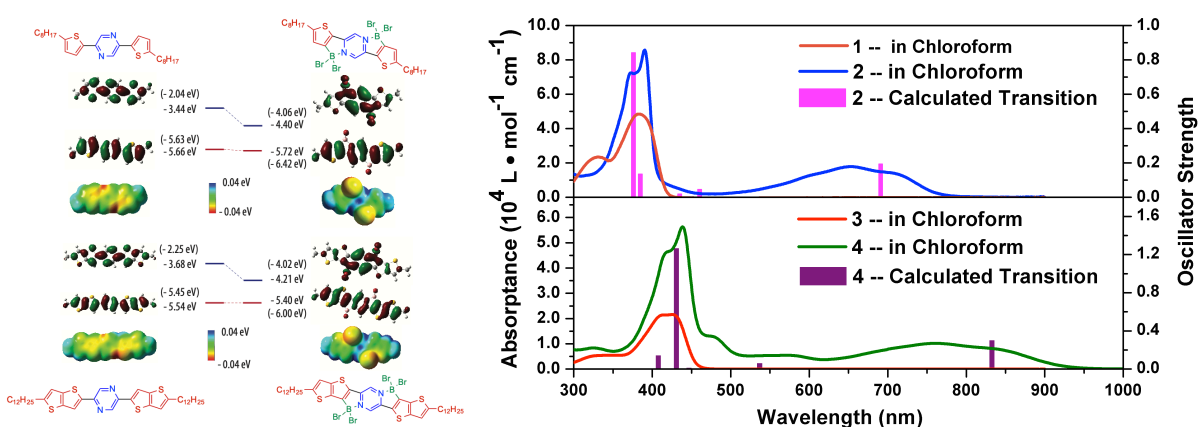
Figure 2.1. Previous examples of DFT corroboration of experimental data. Adapted from *J. Org. Chem. 2016, 81, 10, 4347–4352* with permission from American Chemical Society.[94]

In CV and absorbance spectroscopy experiments, this low computational cost calculation can be used to screen, corroborate, or even predict relative bandgaps of organic electronic materials (**Figure 2.1**). This method also represents a useful tool in determining how conformation affects optoelectronic properties of conjugated materials. More complex calculations using DFT can give evidence of transition states or energy surfaces. For example, in polycyclic systems where several

rigid rings are present, the rotational barriers between these units is important for determining not only the optoelectronic properties, but the bulk intermolecular interactions.
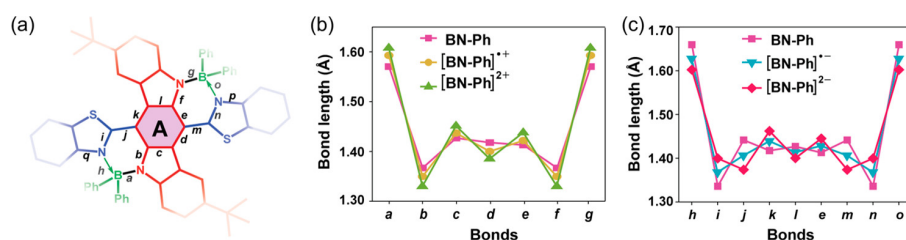
Figure 2.2. (a) DFT calculated lengths of the bonds a~g in BN-Ph before and after oxidation; (b) DFT calculated lengths of the bonds e and h~o in BN-Ph before and after reduction (B3LYP/TZVP with D3 version of Grimme's dispersion correction). Adapted from *J. Am. Chem. Soc.* 2018, 140, 51, 18173–18182 with permission from American Chemical Society.[94]

As we've seen in previous work, DFT facilitated geometry optimizations allows the analysis of bond length alternations without necessitating single-crystal x-ray crystallography.[95, 96] By analyzing bond length alternations, many crucial properties can be elucidated, such as optical excitation energies and charge transfer processes.[97] Namely, this was done in the past by Dr. Congzhi Zhu to elucidate the benzenoid to quininoid transitions facilitated by the single and double electron redox activity of this compound, providing crucial insights in determining the stabilization mechanisms behind these molecules.
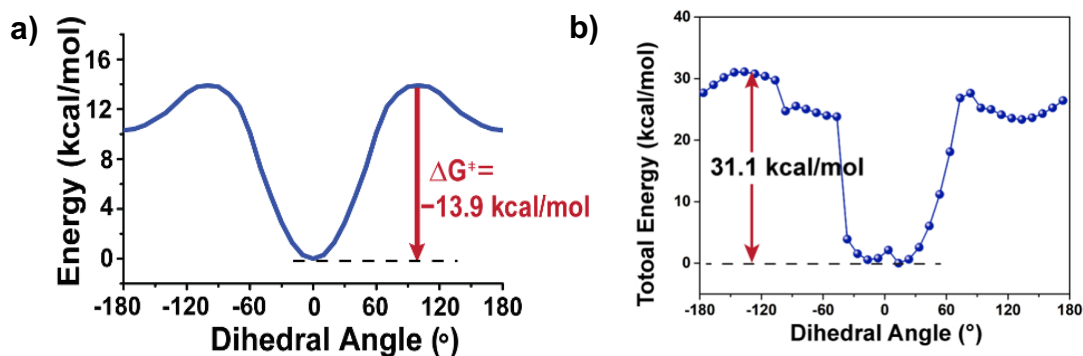
Figure 2.3 Previous examples of computational screening of torsional energies. Adapted from (a) *Org. Lett.* 2016, 18, 24, 6332–6335 and (b) *J. Org. Chem.* 2021, 86, 3, 2100–2106 with permission from American Chemical Society.[94]

15

Moreover, the strength to coplanarization induced by intramolecular noncovalent bonding could be elucidated by DFT (**Figure 2.3**), further leading to a better understanding of the influence of this rigidity on self-assembly properties. In this method, the dihedral angles (φ) between the monomeric planes were varied from 0° to ±180° in increments to obtain the rotational energy profiles. In this way, the rotational energy barriers could provide necessary information into the robustness of hydrogen bonds. Though these methods were heavily reliant on using free energy or enthalpic barriers as a quantifying factor for molecular planarity,[51] the factor is less intuitive in the case of variable temperatures and in bulk material. Perepichka, *et. al.* has proposed a more impactful strategy for quantifying coplanarity, which provides a more statistical and quantitative analysis of backbone planarity.[98] In this method, geometry-restricted DFT optimization of different torsional conformers and dihedral angle scans performed at the bridging bond between adjacent units still remains important to obtain the energy profile $E(\phi)$, as done previously. Contrastingly, the probability function $P(\phi)$ should also calculated as a Boltzmann distribution to provide a more precise factor for bulk material coplanarity, as shown in **Equation 1**.

$$P(\varphi) = Ae^{\frac{E(\varphi)}{RT}} \qquad (1)$$

By employing these factors, a more meaningful coplanarity index $\langle\cos^2\varphi\rangle$ can be used, as demonstrated in later in this chapter (**2.2.2.2**). For these studies, the [B3LYP/6-31G(d)] level of theory was chosen due to its reasonable accuracy, low computational cost, and widespread use in the field, which facilitates cross examination, as discussed in Chapter I. Based on these theoretical methods, the DFT facilitated conformational analysis of polymers and rotational thermodynamics will be investigated in this chapter.

2.2 Results and Discussion

2.2.1 Conformational Investigation of Fused and Nonfused Diselenophene Pyrrole-2,5-dione[*]

In a collaborative effort with Dr. Marc Comi in the Al-Hashimi Group at TAMUQ, the synthesis of homopolymers **MC-1** and **MC-2** and their corresponding copolymers **MC-3** and **MC-4** was reported.[99] **MC-2** and **MC-4** were synthesized with nonfused diselenophene–pyrrole-2,5-dione units while **MC-1** and **MC-3** were synthesized with fused diselenophene–phthalimide units (**Figure 2.4**). The resulting **MC-1** and **MC-3** possessed much more rigid backbones due the covalent bond locks, as compared to **MC-2** and **MC-4**. Unexpectedly, the fused-ring rigidified polymers **MC-2** and **MC-3** exhibited larger HOMO-LUMO bandgaps than the photocyclized **MC-1** and **MC-3** in contrast to common rigidified conjugated polymers (**Figure 2.4b,c**).[25] The polymers with the fused units all exhibited higher bandgaps and unfavorable molecular orbital energies. In addition, the thin-film morphology comparisons of **MC-1** to **MC-2** and **MC-3** to **MC-4** suffered as a result of the fused diselenophene–phthalimide rings, contrary to the numerous results of increased packing order by limiting rotational motion.[20] Moreover, OFET devices of each of the four polymers were fabricated. Orders of magnitude decreases in hole mobilities were demonstrated by fused **MC-1** and **MC-3** in comparison to nonfused **MC-2** and **MC-4**.
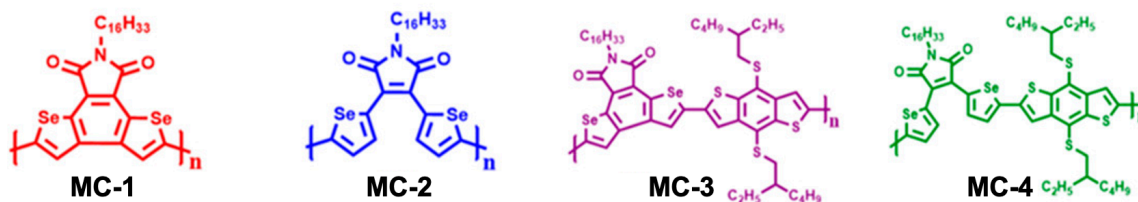
Figure 2.4. Polymer structures of fused MC-1 and MC-3 and nonfused MC-2 and MC-4.

Elucidating these results through the other characterization methods remains challenging, especially for polymeric materials, in which even NMR spectra are ill-defined. Therefore, DFT methods were used to gain insight into the experimental observations, as shown in **Figure 2.5**, and by optimizing the geometries and calculating the frequencies of oligomeric sections of the four polymers, first calculating with 4 repeating units and confirming with 8 repeating unit structures. In these results, the experimental CV determined FMO energy levels were corroborated by theoretical calculations, which also substantiated the accuracy of the DFT results (**Figure 2.5**). Specifically, the bandgap values of **MC-1** < **MC-2** and **MC-3** < **MC-4** were supported by the calculations, also demonstrating that **MC-1** had the smallest bandgap and **MC-2** had the largest.
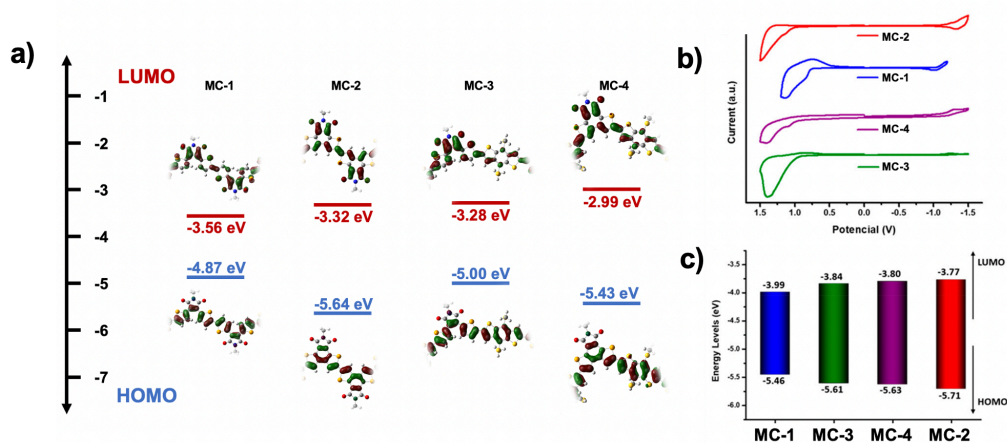
Figure 2.5. Frontier molecular energy levels from (a) DFT optimized ground-state structure obtained at the [B3LYP/6-311G(d,p)] level of theory and (b,c) cyclic voltammetry.

Optimizations between each of the polymers revealed that the calculated dihedral angles between repeating monomers in **MC-1** was smaller (~6°) than the fused **MC-2** (~11°) monomer (**Figure 2.6a**). As depicted in **Figure 2.6**, the bond lengths in the fused heterocyclic system appear to be partially distorted in comparison to the non-fused systems, confirming that the aromaticity was lost on the selenophene rings of the fused polymer structure **MC-2**, thus resulting in a decrease of the coplanarity in the polymer backbone. This was also observed for the other polymers, where

the dihedral angle in **MC-3** and the fused polymer **MC-4** was calculated to be ~20° and ~30°, respectively. This structural distortion in the fused system affected the morphology in **MC-2** and **MC-4**, leading to a decrease in the packing order between the polymer chains. In fact, distortion of the bond-length-alternation is also consistent with the disruption in π-conjugation across the backbone, leading to increased molecular orbital bandgaps and decreased semiconducting properties after fusing the diselenophene units. As a result, DFT calculations were crucial in elucidating the unexpected behavior of the fused-ring structures through analysis of optimized conformations.
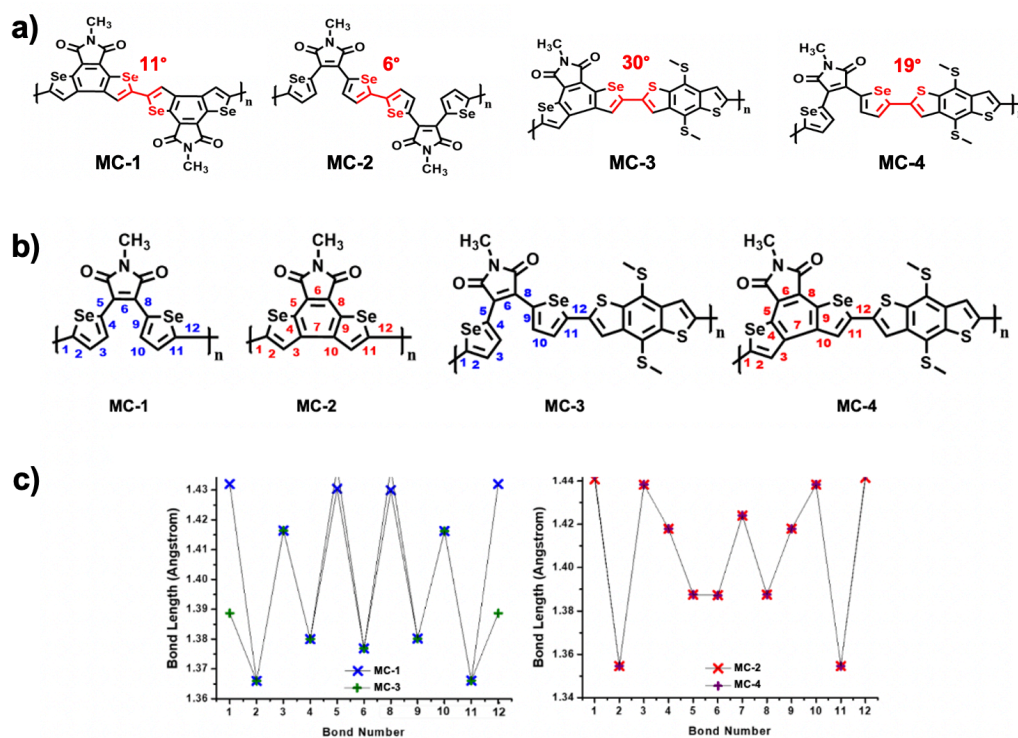
Figure 2.6. Structural conformations of MC-1, MC-2, MC-3, and MC-4: (a) dihedral angles about the single bond between monomeric units and (b,c) bond length alternation of MC-1, MC-2, MC-3, and MC-4 optimized at the [B3LYP/6-311G(d,p)] level of theory.

Inspired by the previous DFT results, Dr. Salahuddin Attar from the Al-Hashimi group preserved interested in developing further coplanarized polymers for OFET applications. In order

to avoid the effects outlined before, a screening process of numerous polymers containing the Al-Hashimi group's extensive database of conjugated building blocks yielded polymers **IID-Tz-Th** and **IID-Tz-Se**, shown in **Figure 2.7**. While the resulting polymers are undergoing investigation, DFT conformational studies has demonstrated itself as an effective strategy for, not only understanding the mechanisms behind experimental data, but also predicting properties for further molecular design.
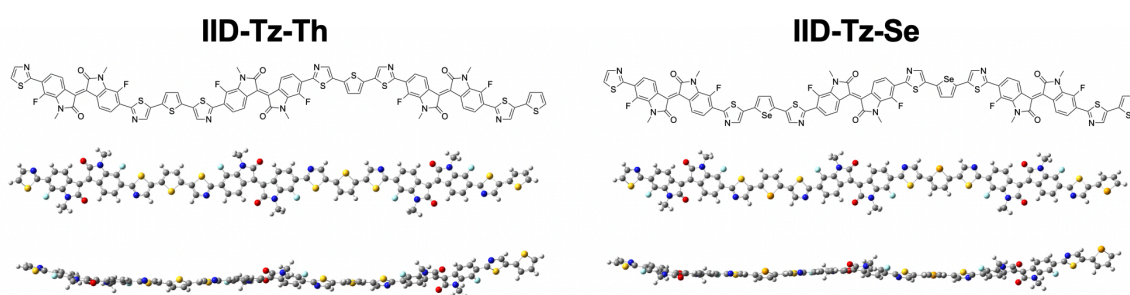
Figure 2.7. Optimized structures of thiazole-flanked IID-Tz-Th and IID-Tz-Se.

2.2.2 Rotational Thermodynamics Simulations of Polycyclic Compounds

2.2.2.1 Desymmetrized Leaning Pillar[6]arene[*]

Rapid development of supramolecular chemistry has been heavily dependent on the design and synthesis of precisely defined macrocyclic compounds with specifically tailored host-guest properties. In the past five decades, pillararenes have provided a wide range of functions as high-performance supramolecular hosts.[100-103] The synthetic accessibility, preorganized structures, facile functionalization methods, and predictable noncovalent interactions enable their applications in host-guest binding, supramolecular self-assembly, molecular machinery, stimuli-

---

responsive materials, and many others.[104] Despite these significant advancements, however, it is still challenging to achieve adaptability of the binding cavity, desired control over substituent groups, and diversification in the modification of the cavity backbone into most of the aforementioned macrocyclic systems. For example, in the class of pillararene derivatives, all the repeating units must be either hydroxy or alkoxy functionalized, limiting their structural versatility and performance. We envisioned that one way to address this issue was to selectively remove the hydroxy/alkoxy functionalities on pillararenes to enhance the cavity adaptability and synthetic versatility. However, no examples of selectively de-functionalized pillararenes have been reported yet. Herein, investigations into the first synthesis of such examples, namely, leaning pillar[6]arene (**LP6**; **Figure 2.8**) are performed through DFT conformational analysis.
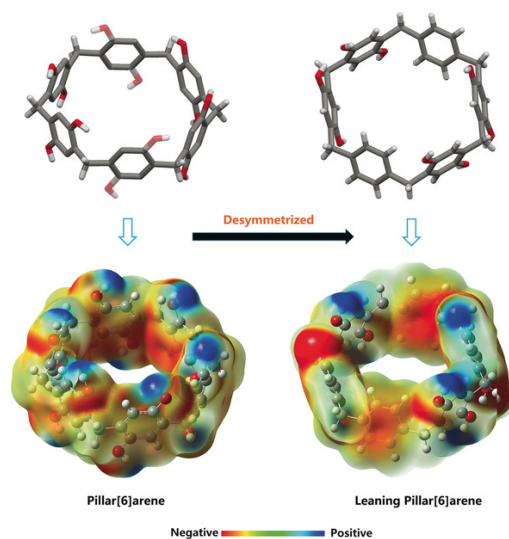
Figure 2.8. The structure and calculated electrostatic potential maps of traditional pillar[6]arene and the newly designed leaning pillar[6]arene (LP6).

Conformational free-energies of **OHLP6** were first calculated using density-functional theory (DFT) by rotating the dihedral angle of a single unsubstituted phenylene ring every 20°

with respect to the plane of its six methylene bridges. The result was compared to equivalent DFT calculations on a single phenylene ring of **OHP6** (**Figure 2.9**).
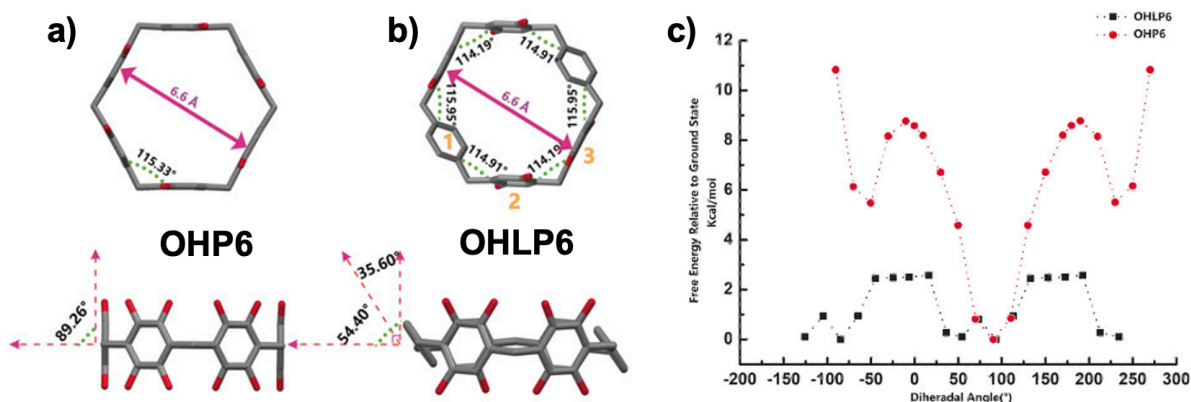
Figure 2.9. Crystal structures of (a) OHP6 and (b) OHLP6 and DFT-calculated rotational free-energy comparison of OHP6 and OHLP6.

The rotational barrier of **OHLP6** was over $6\,\text{kcal}\,\text{mol}^{-1}$ less than that of **OHP6** and the energy well of **OHLP6** was considerably wider than that of **OHP6** (**Figure 2.9b**). In addition to the low-energy state at 90° exhibited by both compounds, another energy minimum was also exhibited by **OHLP6** at around 50°. In comparison with **OHP6**, these results indicated a substantially increased flexible rotation of **OHLP6** allowing the phenylene rings to adopt a favorable leaning conformation and potentially tune guest-binding affinities within the cavity. Crystallographic analysis corroborated a leaning conformation of **OHLP6**, previously shown by DFT calculations (**Figure 2.9b**) in which the dihedral angles between the phenylene rings and the plane of methylene bridges were decreased to 54.4° and 77° for ring 1 and ring 2, respectively.
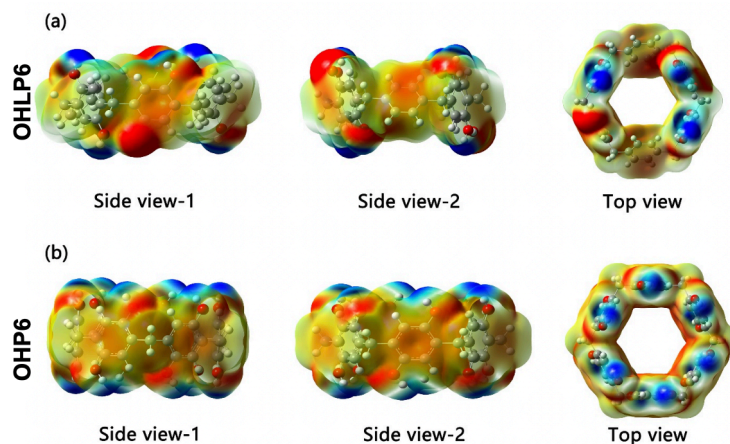
Figure 2.10. Electrostatic potential maps of (b) leaning pillar[6]arene and (b) traditional pillar[6]arene.

In addition to the structural analyses, electrostatic potential (ESP) maps of **OHP6** and **OHLP6** in their ground states were also calculated by DFT (**Figure 2.10**) to observe the effects of conformation on electron density. The ESP map of **OHP6** exhibited a high electron density around the inner π faces of the phenyl rings, whereas, the ESP map of **OHLP6** demonstrated an uneven electron density centered at the leaning phenyl rings. Furthermore, the hydrogen-bond-induced orientation of the hydroxy groups on **OHLP6** generated a polarization effect along the edge, corroborating the crystallographically observed binding of acetone to the rim rather than inside the cavity.

2.2.2.2 Hydrogen-Bond-Promoted Planar Conformation of Diazaisindigo Derivatives[*]

Compounds *N,N'*-bis(2-octyldodecyl)-6,6'-di(1*H*-indol-7-yl)-7,7'-diazaisoindigo (*o*-**AID**) and *N,N'*-bis(2-octyldodecyl)-6,6'-di(1*H*-indol-7-yl)-5,5'-diazaisoindigo (*p*-**AID**) were designed

---

[*]Adapted with permission from "Hydrogen-Bond-Promoted Planar Conformation, Crystallinity, and Charge Transport in Semiconducting Diazaisoindigo Derivatives" by Anthony U. Mu, Yeon-Ju Kim, Octavio Miranda, Mariela Vazquez, Joseph Strzalka, Jie Xu, and Lei Fang, *ACS Materials Lett.* **2022**, 4, *7*, *1270–1278*. Copyright © 2022 American Chemical Society.

as the models for this work. In these molecules, we employed a design[105] of H-bond "donor-acceptor-donor" systems, with indole as the flanking H-bond donor units and nitrogen containing diazaisoindigo units as the H-bond acceptor in the center.[106, 107] The central moieties in **o-AID** and **p-AID** (7,7′-diazaisoindigo[108] and 5,5′-diazaisoindigo,[109] respectively) were selected because of (i) their promising optoelectronic properties; and (ii) their strain-free, favorable six-membered ring H-bonds[110, 111] with indole. We also designed a non-H-bonded control compound *N,N′*-bis(2-octyldodecyl)-6,6'-di(1*H*-indol-7-yl)-isoindigo (**ID-C**), which had a very similar constitution compared to **o-AID** and **p-AID,** except for its non-nitrogen containing center unit. **ID-C** did not possess a H-bond accepting unit so that it lacked any intramolecular conformational locking effect.

Figure 2.11. Structures of isoindigo- and diazaisoindigo-based compounds ID-C, *o*-AID, and *p*-AID.

DFT calculations were employed to evaluate the strength of the intramolecular H-bonds and their effects on molecular coplanarity of **o-AID** and **p-AID** (**Figure 2.11**). Geometry optimizations [at the B3LYP/6-311G(d,p) level of theory][37, 112, 113] demonstrated that both molecules exhibited coplanar ground-state conformations (**Figure 2.11**), while the control compound **ID-C** exhibited a 44° dihedral angle between the indole and isoindigo planes in its most stable conformation. The H-bond H···N distances for **o-AID** and **p-AID** were 2.11 Å and 2.07 Å,

respectively, which are significantly shorter than the sum of van der Waals radii of N and H (2.75 Å).[114] In addition, the six-membered ring orientation allowed a ∠N–H⋯N angle of 120° that was favorable for the formation of H-bonds.[64, 65]

To further quantify the conformational energy diagram of each compound and evaluate the strength of H-bonding, geometry-restricted DFT calculations were conducted at B3LYP/6-31G(d). In this study, the (diaza)isoindigo core of **ID-C**, ***o*-AID**, ***p*-AID** were restricted, while the dihedral angles φ between the isoindigo plane and the indole plane were varied from 0° to 180° in 15° intervals. The enthalpic energy profile $\Delta H(\varphi)$ was obtained at each dihedral angle (**Figure 2.12**).
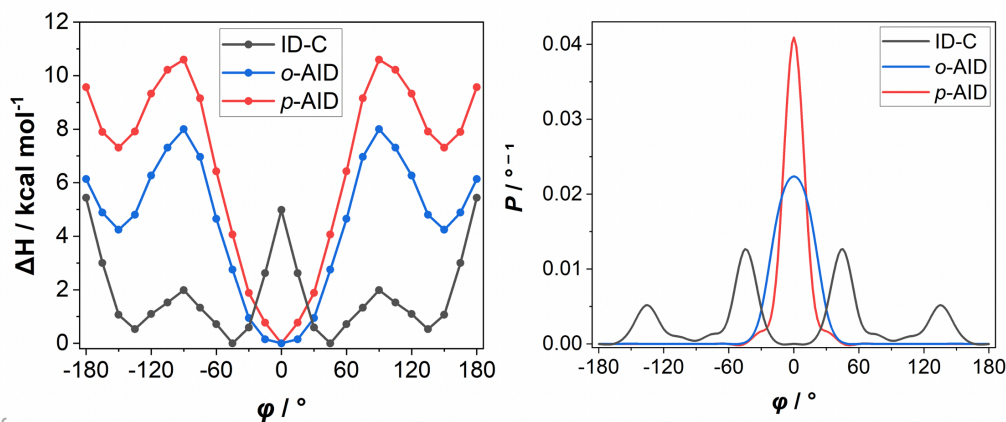
Figure 2.12. The rotational energies of ID-C, o-AID, and p-AID: (a) ΔH(φ) and (b) P(φ) for the three compounds as functions of the dihedral angle φ. Calculated at [B3LYP/6-31G(d)].

For **ID-C**, $\varphi = 0°$ was defined at the coplanar conformation closer to its ground state orientation. For ***o*-AID** and ***p*-AID**, $\varphi = 0°$ was defined at their H-bonded coplanar conformations (**Figure 2.11**). As anticipated, the rotational barriers for ***o*-AID** (8.00 kcal/mol) and ***p*-AID** (10.60 kcal/mol) were significantly higher than that of the non-H-bond **ID-C** control (4.98 kcal/mol from 45°) due to the unfavorable transition state during torsional motion, in which the intramolecular H-bonds must be broken. The increased stabilization energy for ***p*-AID** compared to ***o*-AID** also implied the stronger basicity of the *para*-nitrogen H-bond acceptor in ***p*-AID**. Probability functions

25

$P(\varphi)$ (**Figure 2.12**) were calculated for each molecule based on the Boltzmann distribution of each conformation from the aforementioned data, to give the planarity index $\langle\cos^2\varphi\rangle$ as an empirical parameter according to **Equation 2**.[98]

$$\langle cos^2\varphi\rangle = \int_0^{2\pi} P(\varphi)cos^2\varphi d\varphi / \int_0^{2\pi} P(\varphi)d\varphi \qquad (2)$$

The planarity index $\langle\cos^2\varphi\rangle$ [ranges between 0 (perpendicular) and 1 (coplanar)] represented an effective quantification method for planarization. A higher planarity index was seen on **p-AID** (0.964) as compared to **o-AID** (0.927) although both molecules were considered to have a planar ground state conformation, quantifying the more rigid nature and strong intramolecular H-bonds in **p-AID**. These values were much higher than $\langle\cos^2\varphi\rangle = 0.474$ for **ID-C**, as expected from its non-planar ground state.

Entropic changes of the H-bonds in **o-AID** and **p-AID** were not expected to contribute significantly, as evidenced by the relatively small yet favorable calculated entropy of formation (ΔS) values of +9.12 cal•mol^{-1}•K^{-1} and +2.02 cal•mol^{-1}•K^{-1}, respectively. These positive ΔS values suggested that the intramolecular H-bonds would not dissociate at high temperatures driven by entropy. The temperature-insensitivity of the H-bonds observed in **o-AID** and **p-AID** was similar to those of independently reported examples of small molecules and proteins.[115, 116] Such high temperature robustness is critical to the thermal stability of these compounds and corresponding materials, and allows for high temperature treatments, such as solid-state thermal annealing, of these samples without disrupting the molecular conformation.
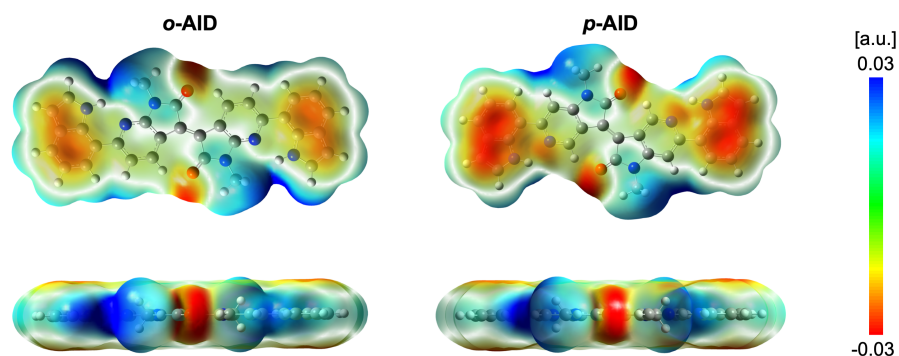
Figure 2.13. DFT calculated electrostatic potential maps of *o*-AID (left) and *p*-AID (right).

Electrostatic potential maps calculated from the DFT optimizations were used to provide insight into potential intermolecular interactions in the solid state. ***p*-AID** demonstrated an enhanced quadrupole moment in comparison to ***o*-AID** (**Figure 2.13**), attributed to the polarizing positions of the heteroatoms of ***p*-AID**. In contrast, the effects of the pyridinic nitrogen atoms of ***o*-AID** are mitigated by their close proximity to the solubilizing chains. The electron rich π-faces of ***p*-AID** were expected to lead to stronger solid-state C–H···π interactions, which were expected to promote edge-to-face stacking instead of π-π stacking.[117]

2.2.3 Mechanistic Investigations

Besides conformational studies of molecules and polymers, DFT also demonstrates considerable efficacy for determining the fundamental mechanistic properties of many processes. In an above-mentioned process (Chapter I**)**, a strategy was used to mask the H-bond donating groups with labile Boc groups to ensure solubility during polymer coupling. These H-bond masking groups could be thermally cleaved, leading to global H-bond reinstation.[52]
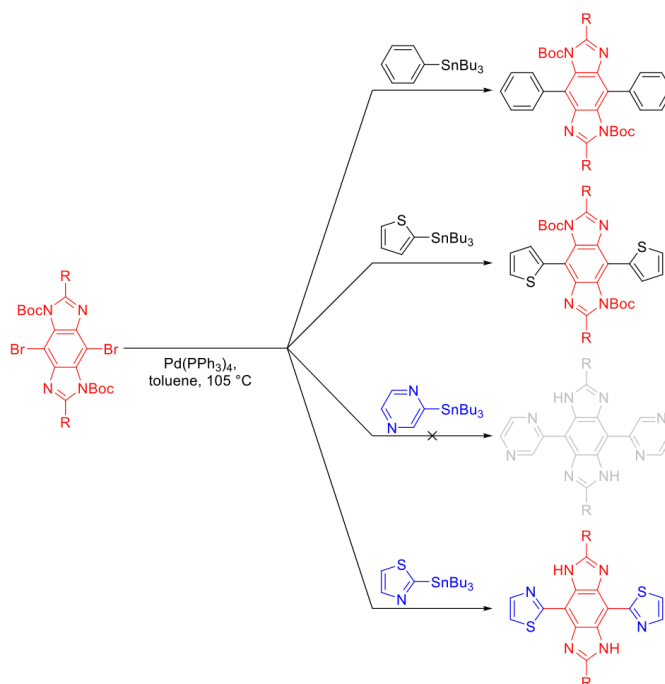
Scheme 2.1. Thermal Boc-deprotection as a synthetic hurdle for cross-coupling reactions.

We and others have used the t-butylcarbamate (Boc) group extensively to mask and unmask H-bonds,[118-121] because Boc groups can endure basic conditions, be installed in high efficiency, and be thermally cleaved into gas byproducts at around 180 °C. The thermal lability of Boc groups has led to deprotection during palladium-catalyzed coupling reactions at modest temperatures (~130 °C) (**Scheme 2.1**). Regarding this process, coupling the Boc H-bond masked moieties to aza-building blocks (thiazole and pyrazole) led to Boc-deprotection, specifically in the case of geometrically favorable H-bond formations. In contrast, this synthetic hurdle was nonexistent for benzene and thiophene. We hypothesized that the more labile nature of Boc group is attributed to the presence of the neighboring H-bond acceptor. Thus, the thermal cleavage temperatures become too low to withstand standard palladium-catalyzed coupling reactions.

$E_a = 26.25$ kcal/mol $\qquad\qquad$ $E_a = 31.42$ kcal/mol
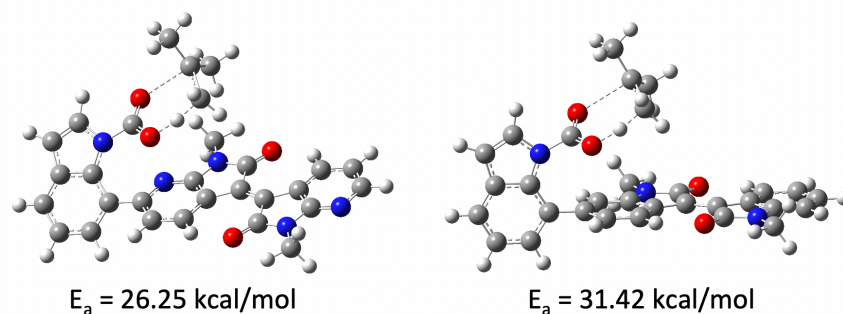
Figure 2.14. Transition state calculation using the QST2 algorithm performed at the [B3LYP/6-31G*] level of theory.

To mechanistically investigate this phenomenon, the QST2 algorithm of DFT transition state calculations were employed to determine effects of adjacent H-bond acceptors to the thermal Boc cleavage activation energies (**Figure 2.14**). In this study, we find that with the intramolecular H-bond acceptor Boc deprotection exhibited a lower transition state activation energy than without the H-bond acceptor. This transition state shows us that the rate determining step is during this 6-membered ring conformation in the formation of isobutylene.
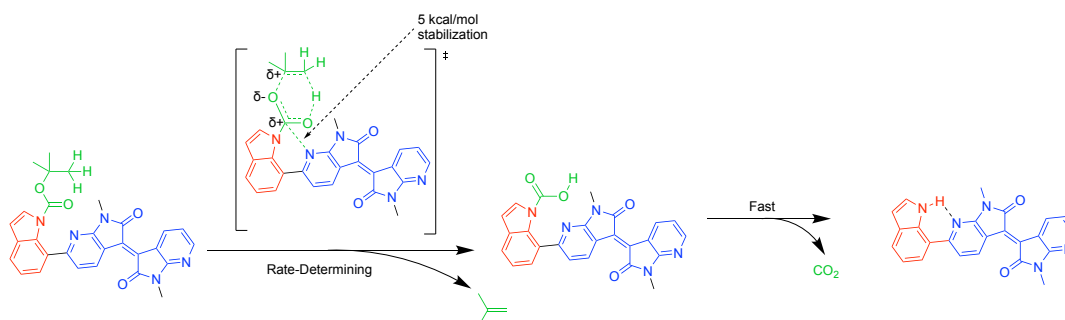
Figure 2.15. Proposed mechanism of low temperature Boc-cleave assisted by neighboring H-bond acceptor, in which the transition state is stabilized for ~5 kcal/mol.

In particular, insight from DFT calculation leads to the proposed mechanism to Boc cleavage, detailed in **Figure 2.15**, in which the transition state is stabilized by 5 kcal/mol through

electrostatic interactions. After isobutylene is cleaved, the CO_2 cleavage is then a fast reaction step, thus, including adjacent H-bond accepting unit impacts the rate of the rate-limiting step. This insight is important for the development of H-bond masked polymers and could not be easily elucidated without the aid of computational DFT calculations.

2.3 Conclusions

The importance of DFT in the prediction, characterization, and even furthering our understanding of structure-property relationships for future development of organic electronics. These results were obtained through geometric optimization and frequency calculations to study molecular orbital energy levels and vibrational modes, as well as simulated rotational thermodynamics to investigate the effects of free energy, enthalpy, and entropy on molecular properties. Furthermore, electrostatics and bond length alternation studies could be used to corroborate experimental data or support future hypotheses.

In previous literature, conformational rigidity and coplanarity consistently led to lower bandgaps,[20, 64] but in our investigations, we show that these effects could negatively lead to poor electronic properties. In the case of fused and nonfused Diselenophene Pyrrole-2,5-dione disrupting surrounding conformation, Intermolecular interactions, such as host-guest binding and crystalline organization was also shown to be a product of conformational control. Lastly, the thermodynamic robustness of intramolecular H-bonds could be relatively quantified to explain temperature independence.

The leaning pillar[6]arene work done with Dr. Jia-Rui Wu from the Yang Group at Jilin University represented the first-time that defunctionalized pillararenes were synthesized, leading to a desymmetrized, leaning column packing structure. Specifically, pillararenes were generally synthesized in which each phenylene ring was the same, usually with two hydroxy groups para- to

each other, whereas this leaning pillararene had two rings without hydroxy functionalization, leading to much different polarization of electron density and leaning or torsional behavior of the unsubstituted phenylene rings, and consequently different host-guest properties. DFT optimizations correlated with the crystallography data. Because the hydrogens between unsubstituted units did not interact with each other, uniform repeating orientation was not observed as in traditional pillararene. Instead, the substituted benzylic groups pair up and H-bond with one another. Thus, from the DFT calculated electrostatic potential map, a polarization of electron density could be observed. Along with the rotational free energy barrier data, the experimental observation in which the traditional pillararene binds within the cavity and the leaning pillararene binds outside the cavity could be explained.

In advancing this rotational scan method, **ID-C**, *o*-**AID**, and *p*-**AID** investigated systematically through DFT calculations to contrast the effects of intramolecular H-bonding vs non-H-bonding. **ID-C** did not consist of any intramolecular H-bonding, while *o*-**AID** and *p*-**AID** did. In the initial geometry optimizations, we saw that the frontier molecular orbitals were lower for the H-bonding molecules. This was consistent with previous work demonstrating that coplanarity leads to enhanced coherent conjugation, lowering the orbital bandgaps. Further, the H-bonding molecules were coplanar while the control exhibited twisted conformations. As we have seen before with the pillararene research, a single molecule's favorable ground-state conformation does not give adequate information in regard to bulk intermolecular interactions, thus, the thermodynamic energy levels were calculated through rotational scan, demonstrating the high preference to bulk coplanarity for H-bonded structures. Electrostatic potential maps calculated from the DFT optimizations were used to provide insight into potential intermolecular interactions

in the solid state, demonstrating key differences in the quadrupole moments of **o-AID and p-AID**, which is expected to lead to profound differences in intermolecular interactions.

In conclusion, the development of these DFT strategies has significantly enhanced the quest to utilize conformation locking strategies for favorable bulk properties in organic electronic applications. With these methods, screening of building blocks, conformational investigations, as well as determining reaction mechanisms becomes more crucial in the current field of π-conjugated electronic materials.

2.4 Experimental Section

2.4.1 Density Functional Theory Calculations

Density functional theory (DFT) based calculations were performed on the monomers **5Se** and **6Se** and polymers **MC-1**, **MC-2**, **MC-3**, **MC-4, IID-Tz-Th, and IID-Tz-Se** were calculated at the [B3LYP/6-311G(d,p)] level using the Gaussian 09 package.[122] To decrease computation time, four repeating units were chosen as simplified models and hexyldecyl imide-side chains were replaced with a methyl group.

The structures of **ID-C**, **o-AID**, and **p-AID** were optimized with density functional theory (DFT) at the level of B3LYP/6-311g(d,p). Octyldodecyl chains were replaced with methyl groups for the sake of simplicity. Calculations of torsional energies and probabilities were carried out at B3LYP/6-31g(d).[98] All DFT calculations were performed with the Gaussian16 package.[122]
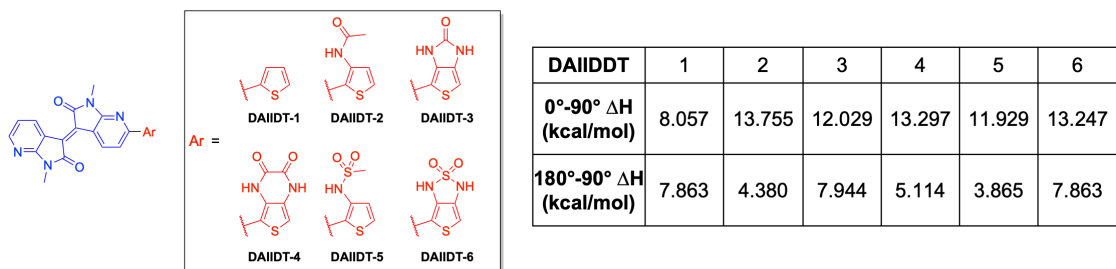
Figure 2.16. Preliminary testing of theoretical rotational transition-state determination.

DAIIDDT	1	2	3	4	5	6
0°-90° ΔH (kcal/mol)	8.057	13.755	12.029	13.297	11.929	13.247
180°-90° ΔH (kcal/mol)	7.863	4.380	7.944	5.114	3.865	7.863
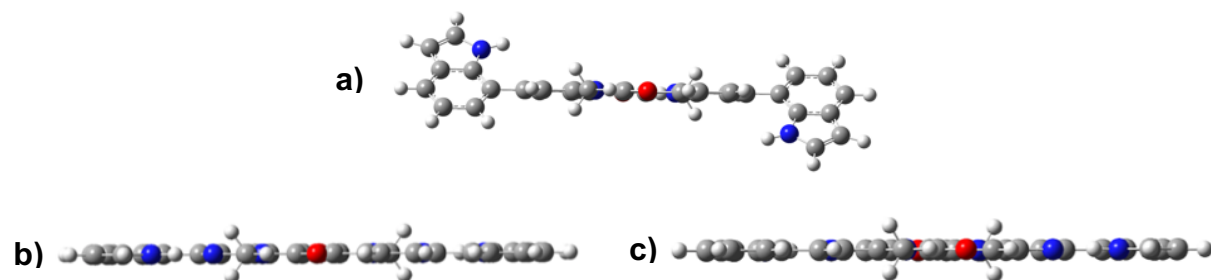
Figure 2.17. Side view of DFT calculated optimized geometries of compound (a) ID-C, (b) *o*-AID, and (c) *p*-AID. ID-C exhibited a 44° torsional angle while *o*-AID and *p*-AID exhibited 0° torsional angles.

Table 2.1. DFT Computed frontier molecular orbital levels of ID-C, *o*-AID, and *p*-AID.

Compound	LUMO^{DFT} (eV)	HOMO^{DFT} (eV)	E$_g^{DFT}$
ID-C	-3.08	-5.56	2.48 eV
o-AID	-3.40	-5.54	2.14 eV
p-AID	-3.41	-5.56	2.15 eV

CHAPTER III

SYNTHESIS AND PROPERTIES OF INTRAMOLECULAR HYDROGEN-BOND BRIDGED

DIAZAISOINDIGO DERIVATIVES[*]

3.1 Introduction

Molecular conformation of conjugated π-systems plays a pivotal role in governing a wide range of their properties, including solubility, solid-state characteristics, as well as optical and electronic functions. Generally, coplanar π-conjugated molecules are expected to possess more extended coherent conjugation,[19] giving rise to faster intramolecular charge transport[20] and lower band gaps.[21] A rigid coplanar conformation also favors low reorganizational energy of charge transport and close intermolecular packing in the solid state,[23] which are anticipated to result in strong intermolecular electronic coupling and long exciton diffusion lengths.[123] Coplanar conformations of extended π-systems are often accomplished by covalently fusing aromatic rings in a bottom up manner.[20, 24-26] However, extensive employment of this strategy has been limited due to challenges with precise synthesis and solution processability.[27]

In contrast to covalent fusing, the use of dynamic noncovalent bonds can also confine the backbone conformation of conjugated molecules,[124, 125] while potentially mitigating the aforementioned issues in synthesis and solubility. Various types of noncovalent interactions have been investigated for this purpose. For example, the installation of intrachain heteroatom interactions (*e.g.,* S—O, S—S, S—N, S—F, S—Cl, and P—O interactions)[18, 28-34] often leads to higher performances in solid-state charge transport and photovoltaics of conjugated systems.

However, these interactions are typically very weak (usually < 1.0 kcal/mol) so that the locked coplanar conformation can easily be disrupted by thermal energy. Stronger intramolecular hydrogen bonds (H-bonds) have also been used to lock the conformation of π-conjugated molecular systems. For the typical C—H···F,[41, 46] C—H···O,[39, 126] N—H···O,[51, 52] and N—H···N[45] interactions, the H-bond-induced stabilizations of coplanar conformations are in the range of 7~14 kcal/mol. A number of literature reported examples exhibited intriguing properties induced by the coplanar conformation, such as anisotropic molecular aggregation,[51] solvent resistance,[52] and increased charge carrier mobility.[41, 45, 49, 126] Despite the potential of the H-bond approach, efficient synthetic strategies to incorporate robust intramolecular H-bonds into conjugated π-systems are still relatively limited. Moreover, the thermodynamic nature of intramolecular H-bonds in these π-systems and the mechanism on how they impact the solid-state properties are still unclear. Herein, we report a new strategy to incorporate intramolecular H-bonds into conjugated π-systems by utilizing diazaisoindigo acceptors; and demonstrate the crucial role of noncovalent conformational control on enhanced coplanar molecular conformation, solid-state packing, and charge-transport abilities of semiconducting organic materials.

3.2 Results and Discussion

Compounds *N,N'*-bis(2-octyldodecyl)-6,6'-di(1*H*-indol-7-yl)-7,7'-diazaisoindigo (***o*-AID**) and *N,N'*-bis(2-octyldodecyl)-6,6'-di(1*H*-indol-7-yl)-5,5'-diazaisoindigo (***p*-AID**) were designed as the models for this work. In these molecules**,** we employed a design[105] of H-bond "donor-acceptor-donor" systems, with indole as the flanking H-bond donor units and nitrogen containing diazaisoindigo units as the H-bond acceptor in the center.[106, 107] The central moieties in ***o*-AID** and ***p*-AID** (7,7'-diazaisoindigo[108] and 5,5'-diazaisoindigo,[109] respectively) were selected because of

(i) their promising optoelectronic properties; and (ii) their strain-free, favorable six-membered ring H-bonds[110, 111] with indole. We also designed a non-H-bonded control compound *N,N'*-bis(2-octyldodecyl)-6,6'-di(1*H*-indol-7-yl)-isoindigo (**ID-C**), which had a very similar constitution compared to *o*-**AID** and *p*-**AID,** except for its non-nitrogen containing center unit. **ID-C** did not possess a H-bond accepting unit so that it lacked any intramolecular conformational locking effect. On all of these molecules, branched alkyl chains were installed on the *N*-positions of the diazaisoindigo or isoindigo units to promote solubility and solution processability.
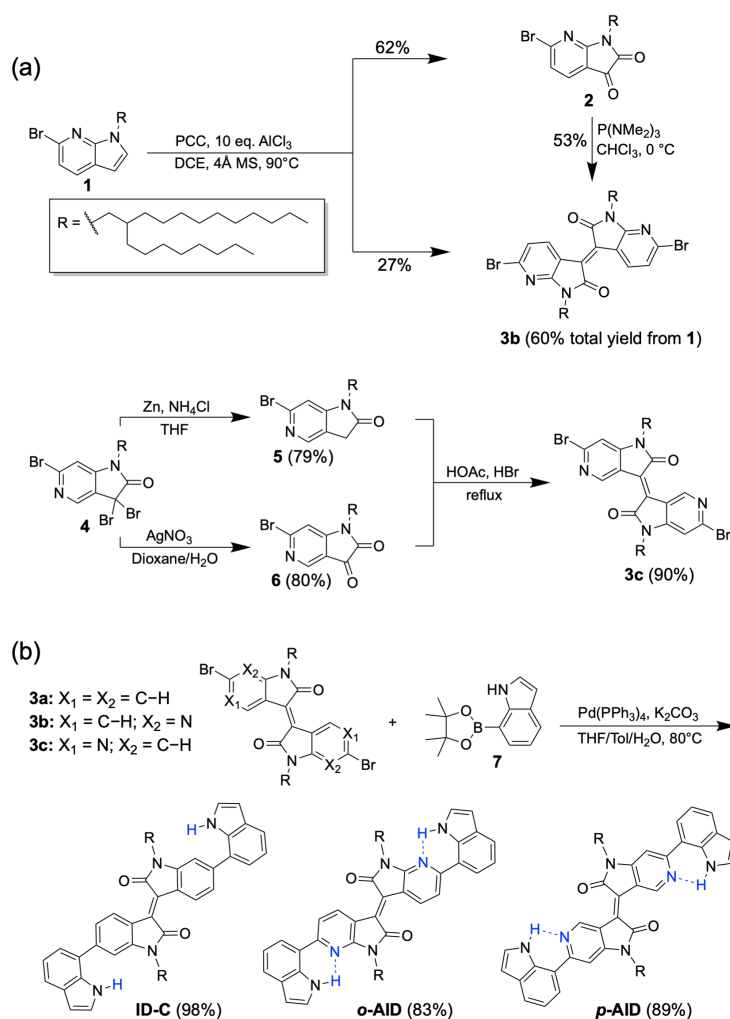
Scheme 3.1 Synthetic scheme of (a) diazaisoindigo starting materials and (b) the final products ID-C, o-AID, and p-AID.

The key synthetic steps to **ID-C**, *o*-**AID**, and *p*-**AID** are shown in **Scheme 3.1**. The non-nitrogen isoindigo core **3a** (**Scheme 3.1b**) was synthesized according to the previously reported method.[127] For the synthesis of diazaisoindigo intermediates **3b** and **3c**, modified synthetic procedures were developed based on literature reported conditions,[37] with significantly improved efficiencies (**Scheme 3.1b**). First, azaindole derived starting materials **1** and **4** were synthesized in 10-gram scales (detailed in **3.4.2**). To synthesize the 7,7'-diazaisoindigo intermediate **3b**, compound **1** was oxidized into 6-bromo-7-azaisatin (**2**) by pyridinium chlorochromate with excess $AlCl_3$ in 62% yield. Interestingly, a small amount of **3b** was already formed in this step in 27% yield as a result of acid-promoted condensation between **1** and **2**. Subsequently, in a separate batch, **2** and **1** were paired up to undergo condensation in the presence of $P(NMe_2)_3$ to afford **3b**. A significantly improved 53% yield in this step was achieved compared to the literature reported 23% yield,[108] by slowly adding a solution of **2** into $P(NMe_2)_3$. The increased yield was attributed to the need of 2 equivalents of $P(NMe_2)_3$ with high local concentration to drive **2** through a Kukhtin-Ramirez facilitated carbene in order to form an ylide. Subsequently, additional equivalents of **2** undergo a Wittig reaction with the ylide to form **3b** (**Scheme 3.11**).[128, 129] As a result, the total yield of **3b** from **1** was doubled from the literature reports of ~30%[108, 109] to 60% here. Similarly, the 5,5'-diazaisoindigo core **3c** was synthesized by modifying a reported method.[109] First, both intermediates **5** and **6** were synthesized from dibromo-functionalized starting material **4** in parallel by treating **4** with zinc or silver nitrate, respectively (details in 3.4.2). Purified sample **5** was then immediately condensed with **6** in an acidic condition to afford **3c** in 90% yield. The yield was optimized by proceeding directly after the purification of **5** and **6** and degassing the reaction mixture to prevent the compounds from undergoing decomposition. Our modified synthesis of both **3b** and **3c** provide a more cost-effective approach to these diazaisoindigo-derived

intermediates. Finally, Suzuki coupling between **3a**, **3b**, or **3c** and boronic ester-functionalized

indole **7** afforded the desired products **ID-C, *o*-AID,** and ***p*-AID** in 50-98% yields, respectively

(**Scheme 3.1b**). In corroboration with the DFT calculations of **Figure 3.1**, the exceptionally

downfield-shifted N—H proton signals of over 11 ppm in ^{1}H NMR (**Figure 3.6** and **Figure 3.10**)

indicate the presence of strong H-bonding interactions.[130, 131]
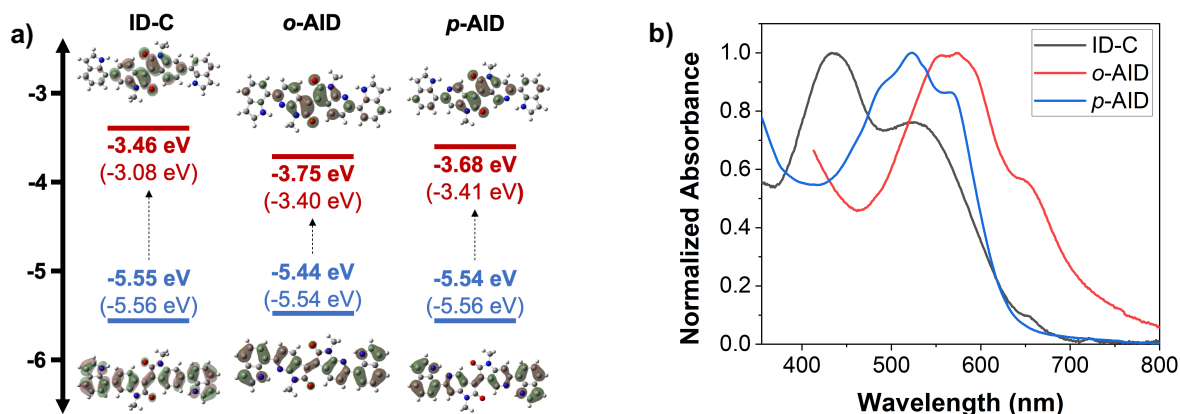
Figure 3.1. The optoelectronic properties of ID-C, *o*-AID, and *p*-AID: (a) DFT calculated frontier molecular orbital distributions of the three compounds, labeled by the corresponding energy levels obtained from CV experiments and from DFT calculation (in parenthesis) and (b) UV-Vis spectroscopy of thin films (drop-casted on quartz glass).

In order to investigate the electronic structures and energy levels of **ID-C**, ***o*-AID**, and ***p*-AID**, UV-Vis absorption (**Figure 3.1**; **Figure 3.11**; **Figure 3.12**) spectra and cyclic voltammetry

(CV) measurements were performed (**Figure 3.14**). The observed optical bandgaps and

electrochemical bandgaps were in good agreements (**Figure 3.1a)**. According to the reduction

potentials, the lowest occupied molecular orbital (LUMO) level of ***o*-AID** and ***p*-AID** (−3.75 eV

and −3.68 eV) were significantly lower than that of **ID-C** (−3.46 eV). However, the oxidation

potentials were not as significantly impacted and all showed highest occupied molecular orbital

(HOMO) levels in the range of –5.55 eV ~ –5.44 eV for typical *p*-type organic semiconductors.[132,]

[133] According to these values, ***o*-AID** and ***p*-AID** were expected to give a *p*-type semiconducting

behavior while the *n*-type property was anticipated to be unstable because the LUMO was not low enough.[134] The overall bandgaps of *o*-**AID** and *p*-**AID** were also smaller compared to that of **ID-C**. Indeed, their UV-vis absorption spectra (**Figure 3.1b**) were redshifted accordingly,[109, 135] to give E_g^{opt} = 1.74 eV, and 1.91 eV for *o*-**AID**, and *p*-**AID**, respectively, compared to 2.02 eV for **ID-C**. The decreased optical and electronic bandgaps of *o*-**AID**, and *p*-**AID** were likely originated from H-bond-promoted coplanarity and the introduction of nitrogen heteroatoms. Furthermore, the solid-state absorption spectra of *o*-**AID** and *p*-**AID** demonstrated clear vibrational peaks in contrast to the smooth bands of **ID-C**, indicating their higher backbone rigidity induced by the conformational locking intramolecular H-bonds. Thermal gravimetric analysis was performed for **ID-C**, *o*-**AID**, and *p*-**AID** to investigate their thermal stabilities (**Figure 3.15a**). While **ID-C** showed thermal decomposition (T_d) with 5% weight loss at a temperatures of 226 °C, *o*-**AID** and *p*-**AID** demonstrated higher thermal stabilities of 257 °C and 316 °C, respectively. The relatively low T_d of **ID-C** was attributed to the thermal instability of indole,[109, 135, 136] while the higher decomposition temperatures of *o*-**AID** and *p*-**AID** implied a stabilization effect on the labile indole units after the formation of H-bonds. Their thermal properties were investigated by differential scanning calorimetry measurements (**Figure 3.15b-d**). While **ID-C** did not exhibit any characteristic peaks, *o*-**AID** and *p*-**AID** demonstrated clear melting temperatures (T_m) of 182 °C and 111 °C, respectively and crystallization temperatures (T_c) of 163 °C and 65 °C, respectively. To further confirm the existence and validate the intramolecular nature of these H-bonds, thereby estimating their thermodynamic robustness, variable temperature UV-Vis experiments of *o*-**AID** and *p*-**AID** in toluene were recorded in a range from 0 °C to 110 °C. Indeed, no change was observed on these spectra even at 110 °C (**Figure 3.13**). Similarly, high temperature ^{1}H NMR in toluene-d_8 performed at 100 °C demonstrated no significant changes compared to that at room

temperature. The lack of response of observed in both the UV-vis spectra and ^{1}H NMR in these variable conditions ruled out the possibility of intermolecular nature of these H-bonds (either with the solvent or between molecules), validating that they are intramolecular in correlation with the DFT calculations (**Figure 2.11**).

3.3 Conclusions

We investigated mechanistically the impact of intramolecular H-bonds on the molecular conformation, of conjugated organic compounds. Conformation-locking intramolecular H-bonds were incorporated into diazaisoindigo-derived molecules. Facile syntheses of the key starting materials 5,5'-diazaisoindigo (**5DAIID**) and 7,7'-diazaisinidigo (**7DAIID**) were achieved after optimizing the condensation reactions. Combined computational and experimental investigations suggested that the stabilization energy of the H-bonds promoted a high-temperature-tolerating, rigid conformation of *o*-**AID** and *p*-**AID**, in contrast to the disordered non-H-bonded control **ID-C**. The entropic favorability for H-bond formation shows promise for thermal annealing during thin-film processing. The rigid conformation and influence of molecular design on the molecular quadrupole moment is expected to result in significantly enhanced orientation of solid-state molecular packing, and subsequently, increase the semiconducting transistor performances of the thin films. Overall, this work demonstrates the effective strategy of using intramolecular H-bonds to tailor the molecular conformation, solid-state packing, and electronic properties of conjugated organic compounds.

3.4 Experimental Section

3.4.1 General Methods and Materials

Starting materials and reagents were purchased from Sigma Aldrich, Acros Organics, Alfa Aesar, Oakwood, or Combi-Blocks and used as received. Anhydrous dichloromethane (CH_2Cl_2) was purchased from EMD Millipore and used without further purification. THF was dried and distilled under nitrogen from sodium using benzophenone as the indicator. Toluene and acetonitrile were dried using an Innovative Technology pure solvent system (PureSolv-MD-5) and degassed by three cycles of freeze-pump-thaw before use. 9-(bromomethyl)nonadecane was synthesized according to a reported literature procedure.[137] Compounds 6-bromo-1*H*-pyrrolo[2,3-*b*]pyridine (**S1**), 6-bromo-1-(2-octyldodecyl)-1H-pyrrolo[3,2-c]pyridine (**S3**) and 7-(4,4,5,5-tetramethyl-1,3,2-dioxaborolan-2-yl)-1*H*-indole (**7**) were purchased from Combi-Blocks. Preparative gel permeation chromatography (GPC) was performed in chloroform solution at room temperature using Japan Analytical Industry recycling preparative HPLC (LC-92XXII NEXT SERIES). ^{1}H and ^{13}C NMR spectra were recorded on a Varian Inova 500 MHz spectrometer and variable temperature ^{1}H NMR spectra were recorded on a Varian VnmrS 500 MHz spectrometer. The NMR chemical shifts were reported in ppm relative to the signals corresponding to the residual non-deuterated solvents ($CDCl_3$: [1]H 7.26 ppm, [13]C 77.16 ppm; CD_3CN: [1]H 1.94 ppm) or the internal standard (tetramethylsilane: [1]H 0.00 ppm). Abbreviations for reported signal multiplicities are as follows: s, singlet; d, doublet; t, triplet; q, quartet; m, multiplet; br, broad. High resolution mass spectra were obtained via electrospray ionization (ESI) on an Applied Biosystems PE SCIEX QSTAR or matrix-assisted laser desorption/ionization (MALDI) on a Bruker microflex with a time-of-flight (TOF) analyzer. Column chromatography was carried out using Biotage® IsoleraTM Prime instrument with various size of SiO_2 Biotage ZIP® cartridge. UV-vis absorption

spectra were recorded on a Shimadzu UV-2600 Spectrophotometer. Differential scanning calorimetry (DSC) was carried out on a Mettler-Toledo DSC3/700/1190 (Mettler-Toledo, Inc., Columbus, OH) under N_2 atmosphere with a heating rate of 10 °C/min. Thermogravimetric analysis (TGA) was performed under an N_2 atmosphere using a Mettler-Toledo TGA2/1100/464 (Mettler-Toledo, Inc.) TGA/DSC 1, with a heating rate of 10 °C/min, from 25 to 500 °C. Data were acquired and analyzed with STAR^e V. 1500a software (Mettler-Toledo, Inc., Columbus, OH).

3.4.2 Synthesis

Compounds 1,[108] 2,[37] S4, 4, 5, 6[109] and 3a[127] were synthesized according to literature reports.
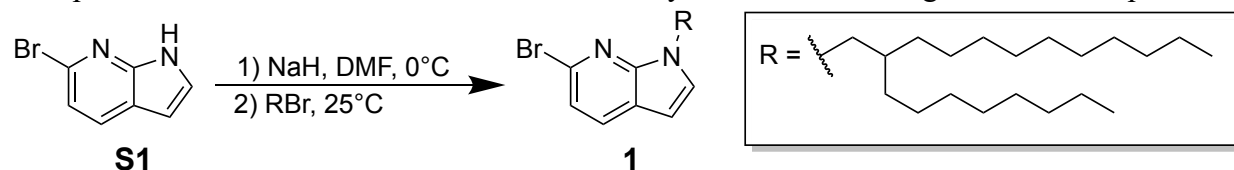
Scheme 3.2 Synthesis of 1 by installing an octyldodecyl chain onto S1.

6-bromo-1-(2-octyldodecyl)-1H-pyrrolo[2,3-b]pyridine (1). To a suspension of NaH (60% in paraffin oil, 2.50 g, 60.8 mmol) in dimethylformamide (100 mL) was added **S1** (10.0 g, 50.8 mmol) portion-wise at 0 °C. After the suspension was stirred at room temperature for 30 min, excess 9-(bromomethyl)nonadecane was added and stirring of the reaction mixture continued for 8 h. The reaction mixture was then quenched by addition of water and extracted with CH_2Cl_2 (100 mL × 3). The organic layers were concentrated and purified by column chromatography (SiO$_2$; hexanes) to give **1** as a colorless oil (20.1 g, 83%). ^{1}H NMR (500 MHz, CDCl$_3$): δ 7.71 (s, 1H), 7.17 (d, J = 8.2 Hz, 1H), 7.14 (d, J = 3.5 Hz, 1H), 6.43 (d, J = 3.5 Hz, 1H), 4.14 (d, J = 7.2 Hz, 2H), 1.95 (p, J = 6.9 Hz, 1H), 1.39 – 1.15 (m, 39H), 0.91 – 0.85 (m, 7H). ^{13}C NMR (125 MHz, CDCl$_3$): δ 147.61, 134.67, 130.75, 128.47, 119.20, 119.06, 99.79, 48.47, 38.95, 32.07, 32.04, 31.53, 30.06, 29.77, 29.70, 29.66, 29.49, 29.44, 26.42, 22.84, 22.81, 14.26. HRMS (ESI-TOF): [M − H]$^-$, *m/z* Calc'd for C$_{27}$H$_{45}$BrN$_2$ 476.2766; Found 476.2784.
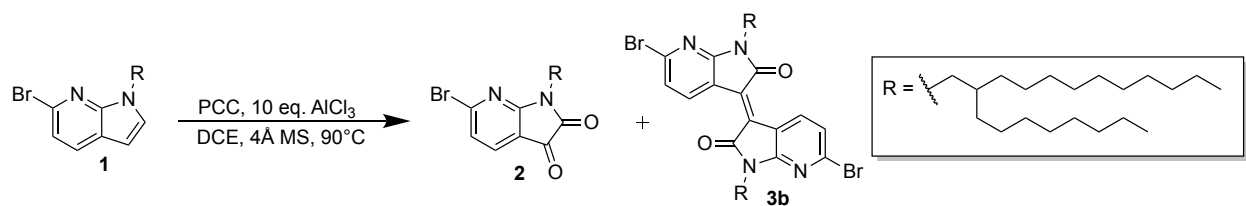
Scheme 3.3. Synthesis of 2 and 3b from 1 by PCC oxidation.

6-bromo-1-(2-octyldodecyll)-1H-pyrrolo[2,3-b]pyridine-2,3-dione (2). To a suspension of pyridinium chlorochromate (17.2 g, 80.0 mmol) and 4 Å molecular sieves in anhydrous 1,2-dichloroethane (100 mL) was added a solution of **1** (10.0 g, 20.9 mmol) in 1,2-dichloroethane (40 mL) at room temperature. After adding excess AlCl$_3$, the mixture was heated to 80 °C for 3 h. After evaporating the organic solvents, the residue was purified by column chromatography (SiO$_2$; hexanes/CH$_2$Cl$_2$ 5:1 to 1:1) to give **3b** (2.78 g, 27%) as a red powder and **2** as orange crystals (6.59 g, 62%). ^{1}H NMR (500 MHz, CDCl$_3$): δ 7.62 (d, J = 7.7 Hz, 1H), 7.26 (d, J = 7.8 Hz, 1H), 3.71 (d, J = 7.2 Hz, 2H), 2.14 – 1.83 (m, 1H), 1.47 – 1.09 (m, 32H), 0.93 – 0.78 (m, 6H). ^{13}C NMR (125 MHz, CDCl$_3$): δ 181.05, 164.70, 158.58, 150.30, 134.02, 123.35, 110.33, 43.88, 36.21, 32.06, 32.04, 31.56, 30.06, 29.81, 29.78, 29.76, 29.71, 29.49, 29.46, 26.28, 22.84, 22.82, 14.26. HRMS (ESI-TOF): [M − H]$^-$ m/z Calc'd for C$_{27}$H$_{45}$BrN$_2$O$_2$ 506.2508; Found 506.2511.
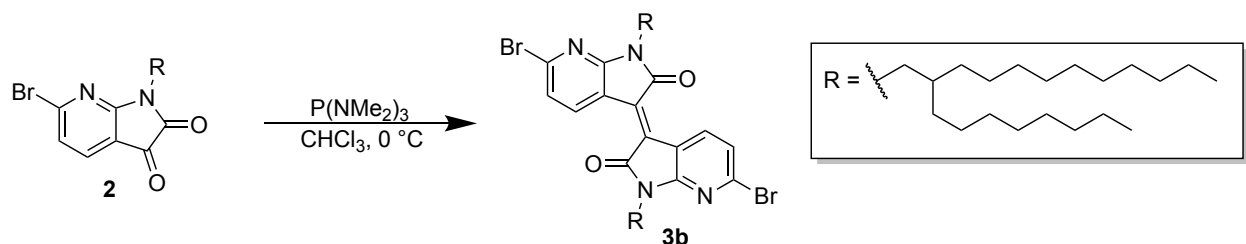
Scheme 3.4. Synthesis of 3b from 2 through a Wittig reaction involving P(NMe$_2$)$_3$.

N,N'-Bis(2-octyldodecyl)-6,6'-dibromo-7,7'-diazaisoindigo (3b). To a solution of tris(dimethylamino)phosphine (175 mg, 10.5 mmol) in CHCl$_3$ (4 mL) was added a solution of **2** (3.00 g, 5.91 mmol) in CHCl$_3$ (50 mL) dropwise at −60 °C. After returning to room temperature, the reaction mixture was heated to 40 °C for 3 h. The mixture was quenched by the addition of water and extracted with CH$_2$Cl$_2$ (100 mL × 3). The combined organic layer was concentrated and

purified by column chromatography (SiO$_2$; hexanes/CH$_2$Cl$_2$ 4:1 to 2:1) to afford **3b** as a red solid (yield: 1.54 g, 53%). The total yield of **3b** combining the product from last step was 60% from **1**. ^{1}H NMR (500 MHz, CDCl$_3$): δ 9.31 (d, J = 8.3 Hz, 2H), 7.20 (d, J = 8.3 Hz, 2H), 3.90 – 3.87 (m, 4H), 1.75 (s, 2H), 1.31 (d, J = 51.4 Hz, 64H), 0.88 (t, J = 7.0 Hz, 12H). ^{13}C NMR (125 MHz, CDCl$_3$): δ 147.61, 134.67, 130.75, 128.47, 119.20, 119.07, 99.79, 48.47, 38.95, 32.07, 32.04, 31.53, 31.43, 30.06, 30.01, 29.78, 29.70, 29.66, 29.49, 29.44, 26.43, 26.39, 26.29, 22.84, 22.82, 14.27. HRMS (ESI-TOF): [M − H]$^-$ m/z Calc'd for C$_{54}$H$_{86}$Br$_2$N$_4$O$_2$ 980.5118; Found 980.5127.
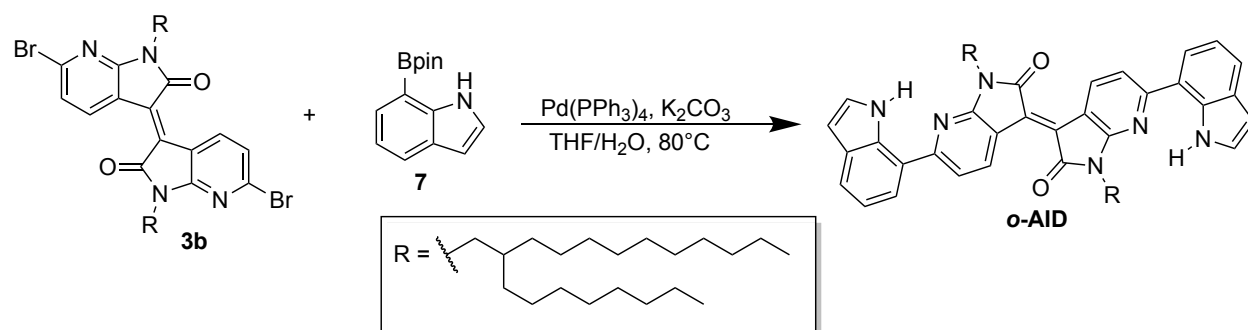
Scheme 3.5. Synthesis of o-AID through Suzuki coupling between 3b and 7.

N,N'-bis(2-octyldodecyl)-6,6'-di(1H-indol-7-yl)-7,7'-diazaisoindigo (o-AID). A suspension of **3b** (450 mg, 0.458 mmol) and K$_2$CO$_3$ (532 mg, 4.00 mmol) in toluene (8 mL) and water (8 mL) was degassed by three cycles of freeze-pump-thaw. Pd(PPh$_3$)$_4$ (5 mol%) and **7** (390 mg, 1.62 mmol) were added under nitrogen and the subsequent reaction mixture was stirred at 80 °C for 24 h. The reaction mixture was then quenched by the addition of water and extracted with CH$_2$Cl$_2$ (50 mL × 3). The combined organic layer washed with water (100 mL × 2), brine (100 mL) and dried with MgSO$_4$. After removing organic solvents, the residue was purified by preparative GPC using CHCl$_3$ as the eluent (retention time: 30 min, flow rate: 14 mL/min) to afford **o-AID** as a violet solid (179 mg, 83%). ^{1}H NMR (500 MHz, CDCl$_3$): δ 11.01 (s, 2H), 9.50 (d, J = 8.8 Hz, 2H), 7.84 (d, J = 7.5 Hz, 2H), 7.73 (dd, J = 14.7, 8.1 Hz, 4H), 7.35 – 7.28 (m, 2H), 7.22 (t, J = 8.1 Hz, 2H), 6.64 – 6.55 (m, 2H), 4.01 (t, J = 7.7 Hz, 4H), 2.08 – 1.63 (m, 2H), 1.63 – 1.02 (m, 64H), 1.02 –

0.65 (m, 12H). ^{13}C NMR (125 MHz, CDCl$_3$): δ 168.41, 158.12, 157.48, 137.59, 134.66, 130.02, 129.79, 124.60, 123.80, 120.78, 120.37, 119.89, 114.13, 113.83, 102.51, 36.96, 32.06, 32.00, 31.84, 30.31, 29.83, 29.76, 29.69, 29.50, 29.45, 26.58, 22.82, 14.25, 1.19. HRMS (ESI-TOF): [M − H]$^-$ m/z Calc'd for C$_{70}$H$_{98}$N$_6$O$_2$ 1054.7751; Found 1054.7744.
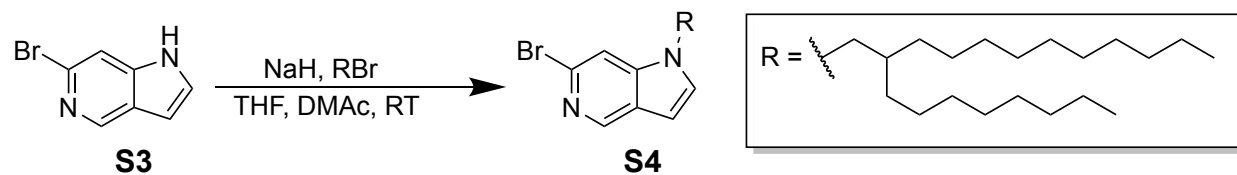
Scheme 3.6. Synthesis of S4 by installing an octyldodecyl chain onto S3.

6-bromo-1-(2-octyldodecyl)-1H-pyrrolo[3,2-c]pyridine (S4). To a solution of **S3** (10.0 g, 50.5 mmol) in tetrahydrofuran and dimethylacetamide was added excess 9-(bromomethyl)nonadecane and NaH (60% in paraffin oil, 2.00 g, 48.7 mmol), at room temperature. After stirring for 8 h, the reaction was quenched by addition of water and extracted with CH$_2$Cl$_2$ (100 mL × 3). The combined organic layer washed with water (100 mL × 2), brine (100 mL) and dried with MgSO$_4$. After removing organic solvents, the residue was purified by column chromatography (SiO$_2$; hexanes/CH$_2$Cl$_2$ 4:1) to give 6-bromo-1-(2-octyldodecyl)-1*H*-pyrrolo[3,2-*c*]pyridine (**S4**) as a colorless oil (yield: 21.7 g; 90%). ^{1}H NMR (500 MHz, CDCl$_3$): δ 8.50 (s, 1H), 7.26 (s, 1H), 6.94 (d, J = 3.2 Hz, 1H), 6.42 (d, J = 3.2 Hz, 1H), 3.79 (d, J = 7.3 Hz, 2H), 1.87 – 1.66 (m, 1H), 1.41 – 0.95 (m, 32H), 0.96 – 0.73 (m, 6H). ^{13}C NMR (125 MHz, CDCl$_3$): δ 143.37, 142.06, 132.51, 130.58, 125.37, 108.30, 101.15, 50.80, 38.91, 32.03, 31.97, 31.56, 29.99, 29.72, 29.66, 29.64, 29.59, 29.44, 29.37, 26.43, 22.81, 22.77, 14.24, 14.22. HRMS (ESI-TOF): [M – H]$^-$ m/z Calc'd for C$_{27}$H$_{45}$BrN$_2$ 476.2766; Found 476.2788.
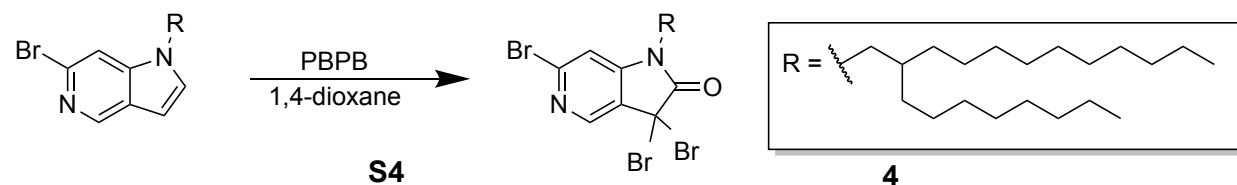
Scheme 3.7. Synthesis of 4 from S4 by through PBPB oxidation.

3,3,6-tribromo-1-(2-octyldodecyl)-1,3-dihydro-2H-pyrrolo[3,2-c]pyridin-2-one (4). To a solution

of 6-bromo-1-(2-octyldodecyl)-1H-pyrrolo[3,2-c]pyridine (10.0 g, 20.9 mmol) in 1,4-dioxane (3.5

mL) was added pyridinium bromide perbromide (33.0 g, 100 mmol). The reaction mixture was

stirred at room temperature for 12 h. After completion of the reaction, the mixture was extracted

with CH_2Cl_2 (100 mL × 3) and purified by column chromatography (SiO_2; hexanes/CH_2Cl_2 9:1)

to yield **4** as a clear oil (yield: 13.0 g; 95%). ^{1}H NMR (500 MHz, $CDCl_3$): δ 8.46 (s, 1H), 6.93 (s,

1H), 3.58 (d, *J* = 7.5 Hz, 4H), 1.95 – 1.80 (m, 1H), 1.51 – 1.15 (m, 32H), 0.93 – 0.82 (m, 12H).

^{13}C NMR (125 MHz, $CDCl_3$): δ 169.62, 148.62, 146.44, 144.23, 127.41, 108.94, 45.69, 39.97,

36.06, 32.04, 31.99, 31.43, 30.01, 29.74, 29.63, 29.58, 29.45, 29.39, 26.34, 22.81, 22.78, 14.25,

14.23. HRMS (ESI-TOF) [M − H]⁻ *m/z* Calc'd for $C_{27}H_{43}Br_3N_2O$ 648.0926; Found 648.0948.
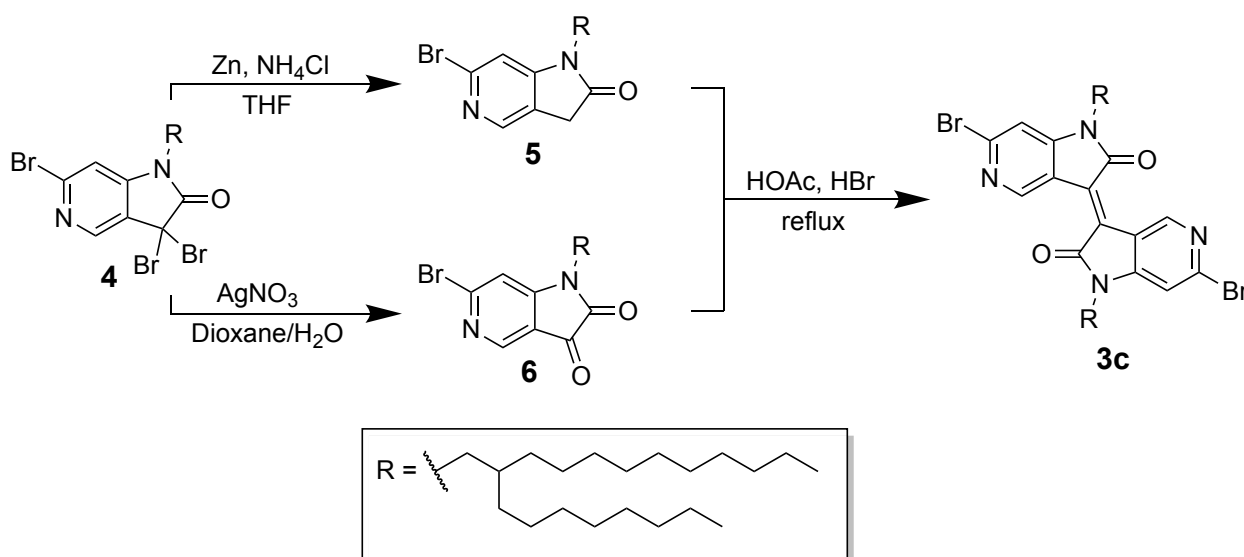
**Scheme 3.8. Synthesis of 3c by oxidation of 4 to form compounds 5 and 6 and then coupling
through aldol condensation.**

N,N'-bis(2-octyldodecyl)-6,6'-dibromo-5,5'-diazaisoindigo (3c). To a solution of **4** (3.00 g, 4.60

mmol) in THF (20 mL) was added a saturated aqueous solution of NH_4Cl (20 mL) and excess zinc

powder. After stirring for 1 hour, the mixture was concentrated under vacuum and purified by flash

column chromatography (SiO_2; hexanes/CH_2Cl_2 3:2) to yield **5** as a clear oil (yield: 1.80 g, 79%).

In tandem, a solution of **4** (3.00 g, 4.60 mmol) in a 10:1 mixture of 1,4-dioxane and water (17 mL) was degassed. AgNO$_3$ was added and the reaction was stirred under nitrogen at room temperature for 12 h. The reaction mixture was then concentrated under vacuum, extracted with CH$_2$Cl$_2$ (30 mL × 3) and subject to column chromatography (SiO$_2$; hexanes/CH$_2$Cl$_2$ 1:4 to 1:9) to yield **6** as a yellow oil (yield: 1.87 g, 80%). To a solution of **5** (1.48 g, 3.00 mmol) and **6** (1.52 g, 3.00 mmol) dissolved in acetic acid (10 mL), a catalytic amount of concentrated HBr (1 mL) was added under nitrogen in a pressure tube. The mixture was heated under reflux conditions for 12 h. After removing the solvent, the residue was subjected to silica gel flash column chromatography (SiO$_2$; hexanes/CH$_2$Cl$_2$ 1:1) to afford **3c** (yield: 2.65 g, 90%) as an orange solid. ^{1}H NMR (500 MHz, CDCl$_3$): δ 9.96 (s, 2H), 6.94 (s, 2H), 3.64 (d, J = 7.5 Hz, 4H), 1.92 – 1.78 (m, 2H), 1.42 – 1.10 (m, 64H), 0.94 – 0.80 (m, 12H). ^{13}C NMR (125 MHz, CDCl$_3$): δ 167.64, 152.83, 150.31, 145.21, 130.23, 117.60, 107.80, 45.07, 36.40, 32.05, 32.00, 31.57, 30.07, 29.76, 29.72, 29.66, 29.48, 29.42, 26.42, 22.83, 22.80, 14.27, 14.25. HRMS (MALDI-TOF): [M − H]$^-$ *m/z* Calc'd for C$_{54}$H$_{86}$Br$_2$N$_4$O$_2$ 980.5118; Found 980.5110.
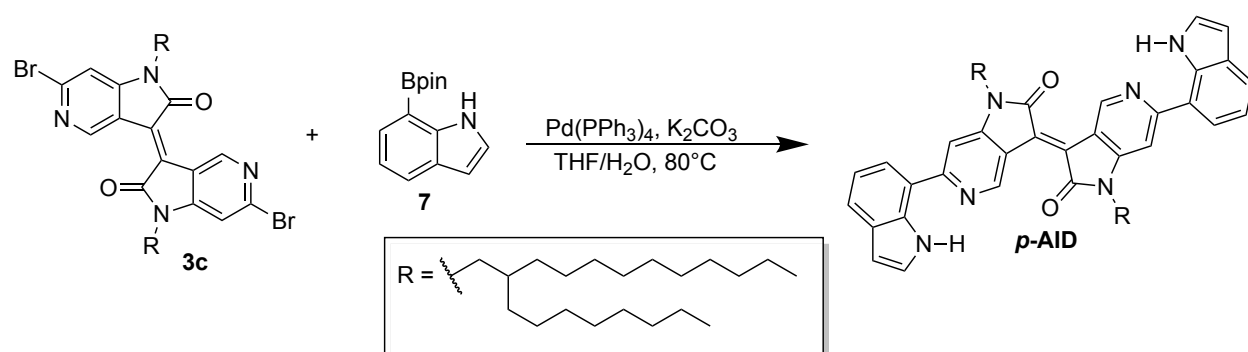
Scheme 3.9. Synthesis of *p*-AID through Suzuki coupling between 3c and 7.

N,N'-bis(2-octyldodecyl)-6,6'-di(1H-indol-7-yl)-5,5'-diazaisoindigo (p-AID). To a Schlenk tube were added **3c** (200 mg, 0.203 mmol), **7** (125 mg, 0.50 mmol), a catalytic amount of Pd(PPh$_3$)$_4$, K$_2$CO$_3$ (175 mg, 1.25 mmol), and a 1:1 mixture of THF and water (5 mL). The tube was charged with nitrogen through three cycles of freeze–pump–thaw. The mixture was stirred for 36 h at 80

°C under nitrogen atmosphere and then extracted with CH_2Cl_2 (30 mL × 3). After removing the solvent, the residue was subjected to flash column chromatography (SiO_2; hexanes/CH_2Cl_2 4:1) and further purified by preparative GPC using $CHCl_3$ as the eluent (retention time: 30 min, flow rate: 14 mL/min) to yield **p-AID** (191 mg, 89%) as a pink solid. ^{1}H NMR (500 MHz, $CDCl_3$): δ 11.72 (s, 2H), 10.37 (s, 2H), 7.82 (d, J = 7.7 Hz, 2H), 7.67 (d, J = 7.5 Hz, 2H), 7.42 (t, J = 2.4 Hz, 2H), 7.20 (t, J = 7.6 Hz, 2H), 6.65 (t, J = 2.7 Hz, 2H), 3.62 (d, J = 7.4 Hz, 4H), 1.93 – 1.80 (m, 2H), 1.42 – 1.13 (m, 64H), 0.95 – 0.77 (m, 12H). ^{13}C NMR (125 MHz, $CDCl_3$): δ 160.15, 151.36, 135.18, 129.92, 129.25, 125.21, 124.05, 120.55, 119.97, 119.49, 116.41, 102.20, 99.00, 44.68, 36.67, 32.04, 31.88, 30.13, 29.79, 29.48, 29.44, 26.73, 22.82, 14.24. HRMS (ESI-TOF) m/z [M − H]⁻ Calc'd for $C_{70}H_{98}N_6O_2$ 1054.7751; Found 1054.7726.
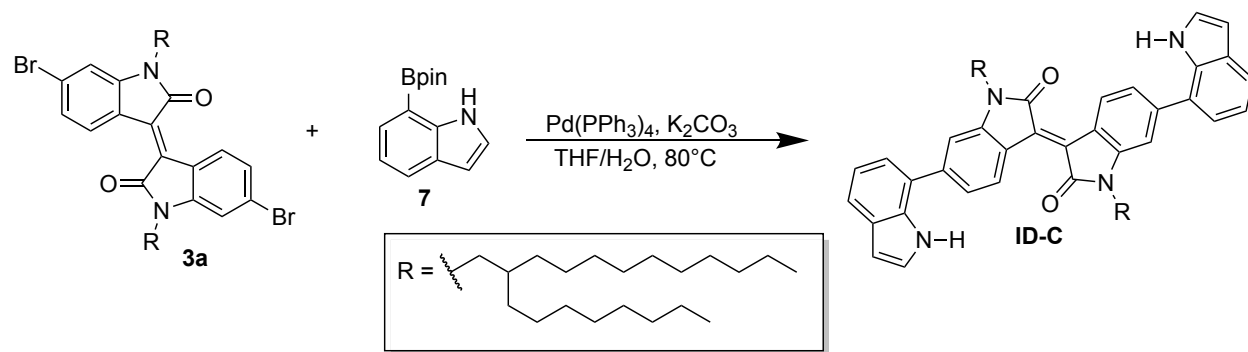
Scheme 3.10. Synthesis of Synthesis of ID-C through Suzuki coupling between 3a and 7.

N,N'-bis(2-octyldodecyl)-6,6'-di(1H-indol-7-yl)-isoindigo (ID-C). To a Schlenk tube were added **3a** (1.00 g, 1.02 mmol), **7** (600 mg, 2.5 mmol), a catalytic amount of Pd(PPh₃)₄, K_2CO_3 (900 mg, 6.25 mmol), and a 1:1 mixture of THF and water (20 mL). The tube was charged with nitrogen through three cycles of freeze–pump–thaw. The mixture was stirred for 36 h at 80 °C under nitrogen atmosphere and then extracted with CH_2Cl_2 (50 mL × 3). After removing the solvent, the residue was subjected to flash column chromatography (SiO_2; hexanes/CH_2Cl_2 9:1) to yield **ID-C** as a red solid (1.05 g, 98%). ^{1}H NMR (500 MHz, $(CD_3)_2CO$): δ 10.44 (s, 2H), 9.43 (d, J = 9.6 Hz, 2H), 7.66 (d, J = 6.8 Hz, 2H), 7.44 – 7.38 (m, 4H), 7.34 – 7.27 (m, 4H), 7.18 (t, J = 7.7 Hz, 2H),

6.63 – 6.59 (m, 2H), 3.87 (d, J = 7.6 Hz, 4H), 1.34 (d, J = 259.0 Hz, 66H), 0.83 (q, J = 6.9 Hz, 12H). ^{13}C NMR (125 MHz, CDCl$_3$): δ 168.77, 146.29, 143.64, 133.63, 132.71, 130.46, 128.74, 125.29, 124.81, 124.75, 121.71, 121.13, 120.97, 120.51, 108.25, 103.39, 44.91, 36.56, 32.05, 32.00, 31.84, 30.20, 29.78, 29.71, 29.48, 29.43, 26.68, 22.82, 22.79, 14.24. HRMS (ESI-TOF) [M − H]$^-$ m/z Calc'd for C$_{72}$H$_{100}$N$_4$O$_2$ 1052.7846; Found 1052.7850.

3.4.3 Reaction Mechanisms
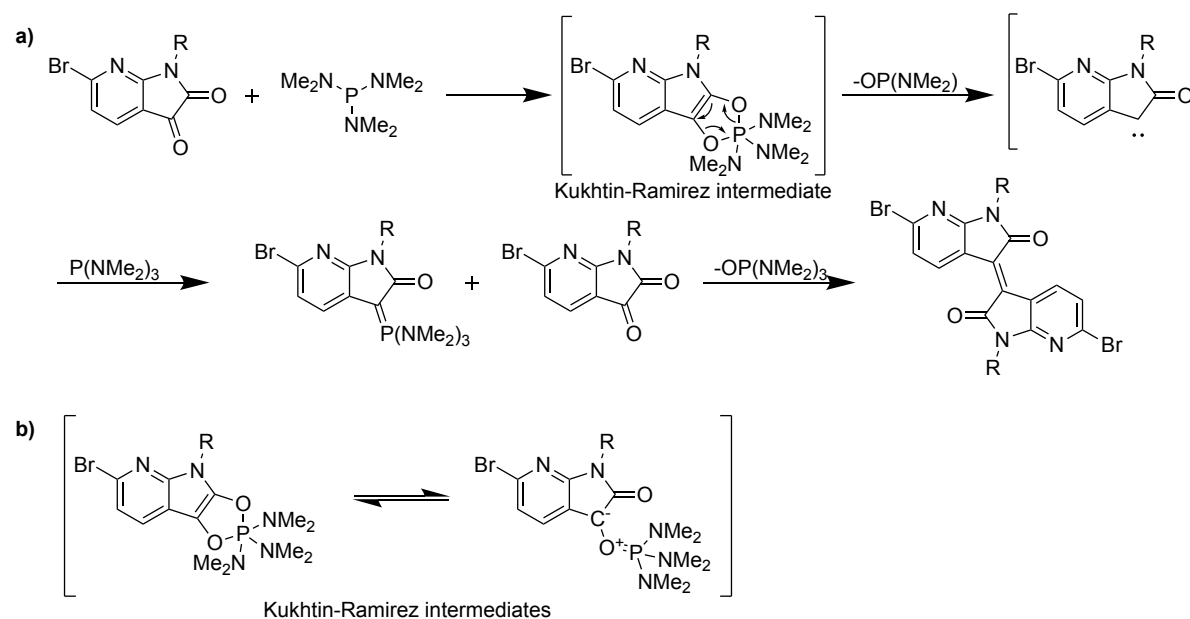
Scheme 3.11. Proposed pathway of (a) condensation mechanism of 6-bromo-7-azaisatin to 6,6'-bromo-7,7'-diazaisindigo by ylide formation with P(NMe$_2$)$_3$ proceeding through (b) a Kukhtin-Ramirez intermediate.[128, 129]

3.4.4 NMR Spectra
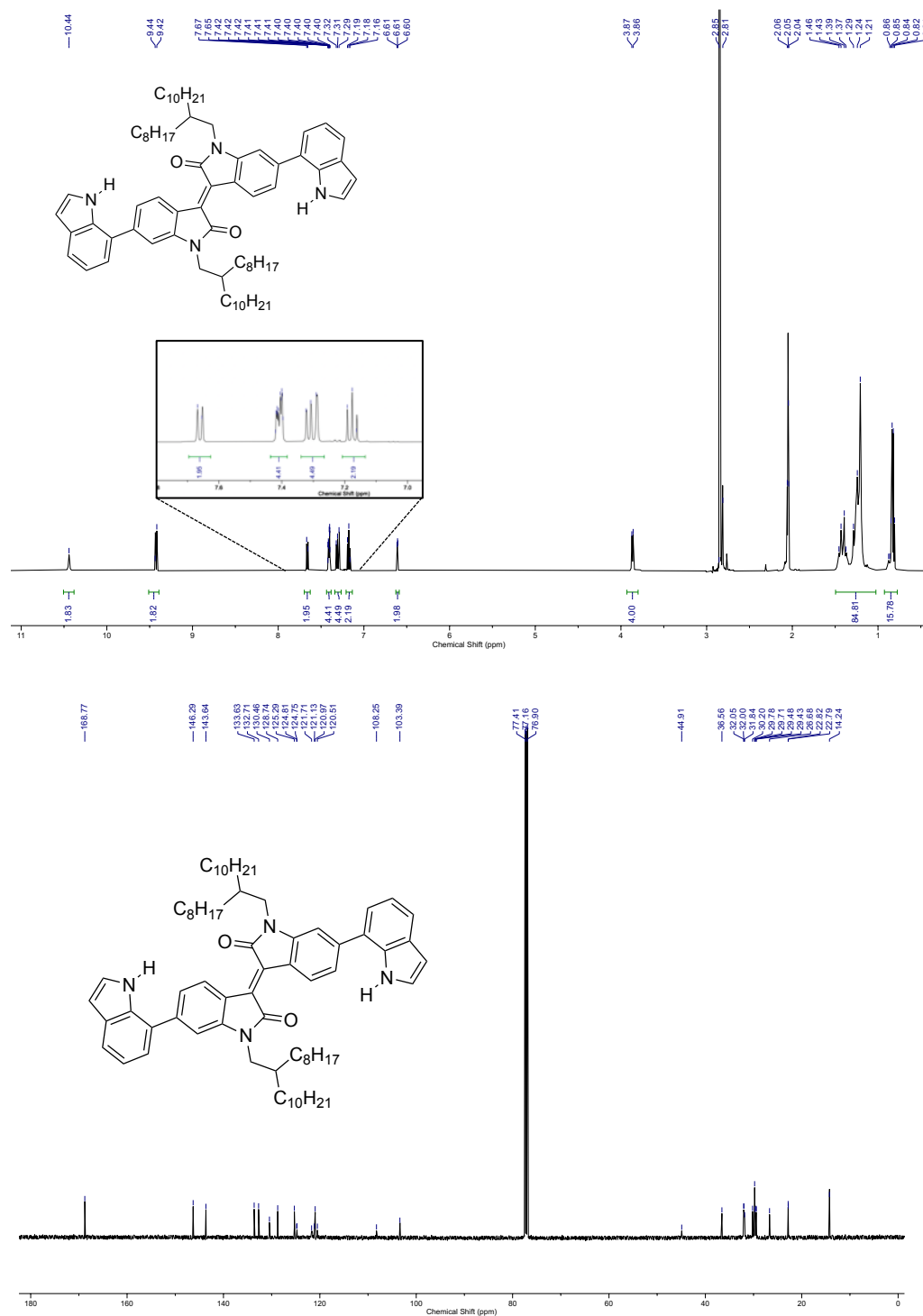
Figure 3.2. ^{1}H (500 MHz) and ^{13}C{^{1}H} (125 MHz) NMR of ID-C at 25 °C in (CD$_3$)$_2$CO and CDCl$_3$, respectively.
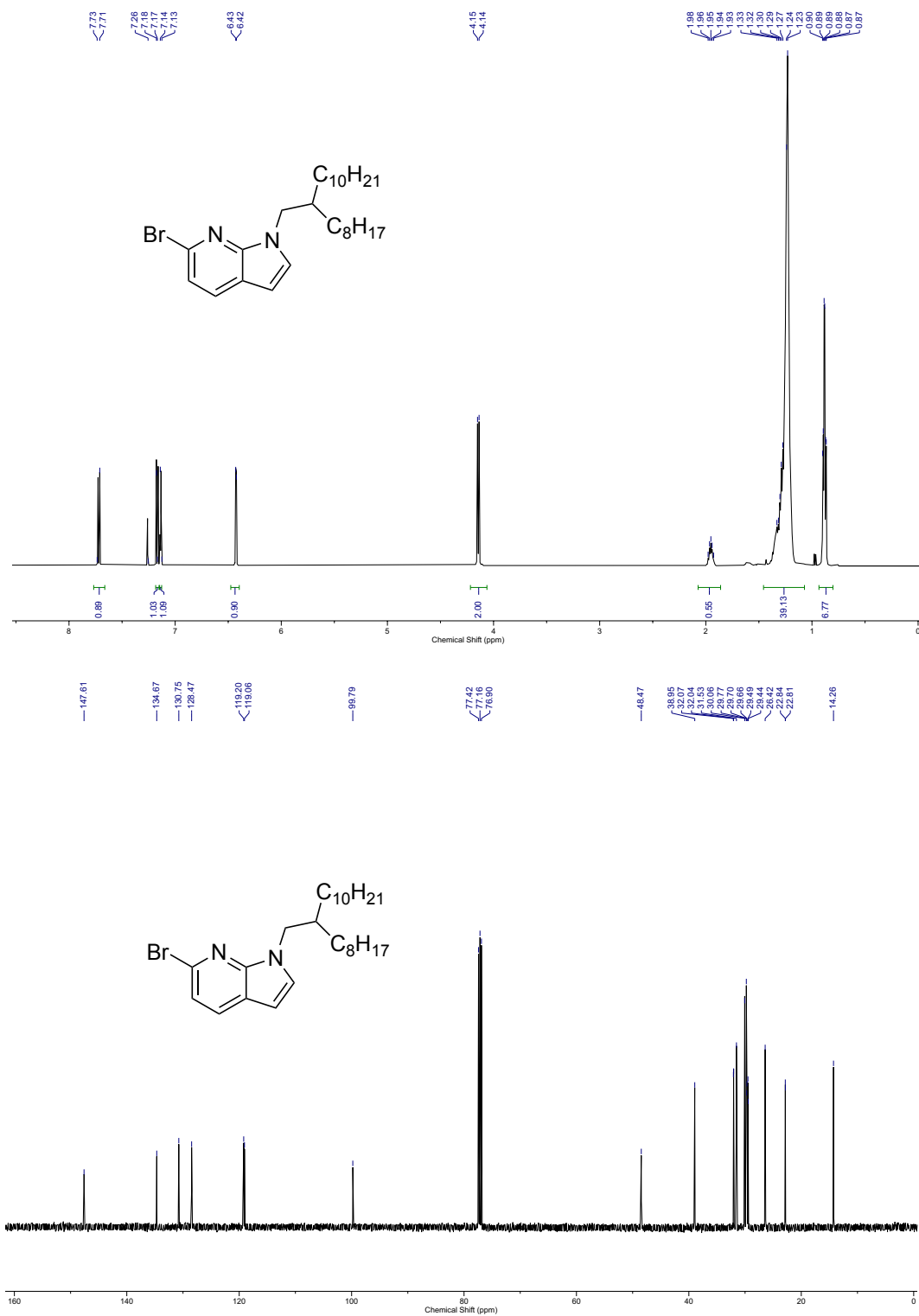
Figure 3.3. ^{1}H (500 MHz) and ^{13}C{^{1}H} (125 MHz) NMR of **1** in CDCl$_3$ at 25 °C.
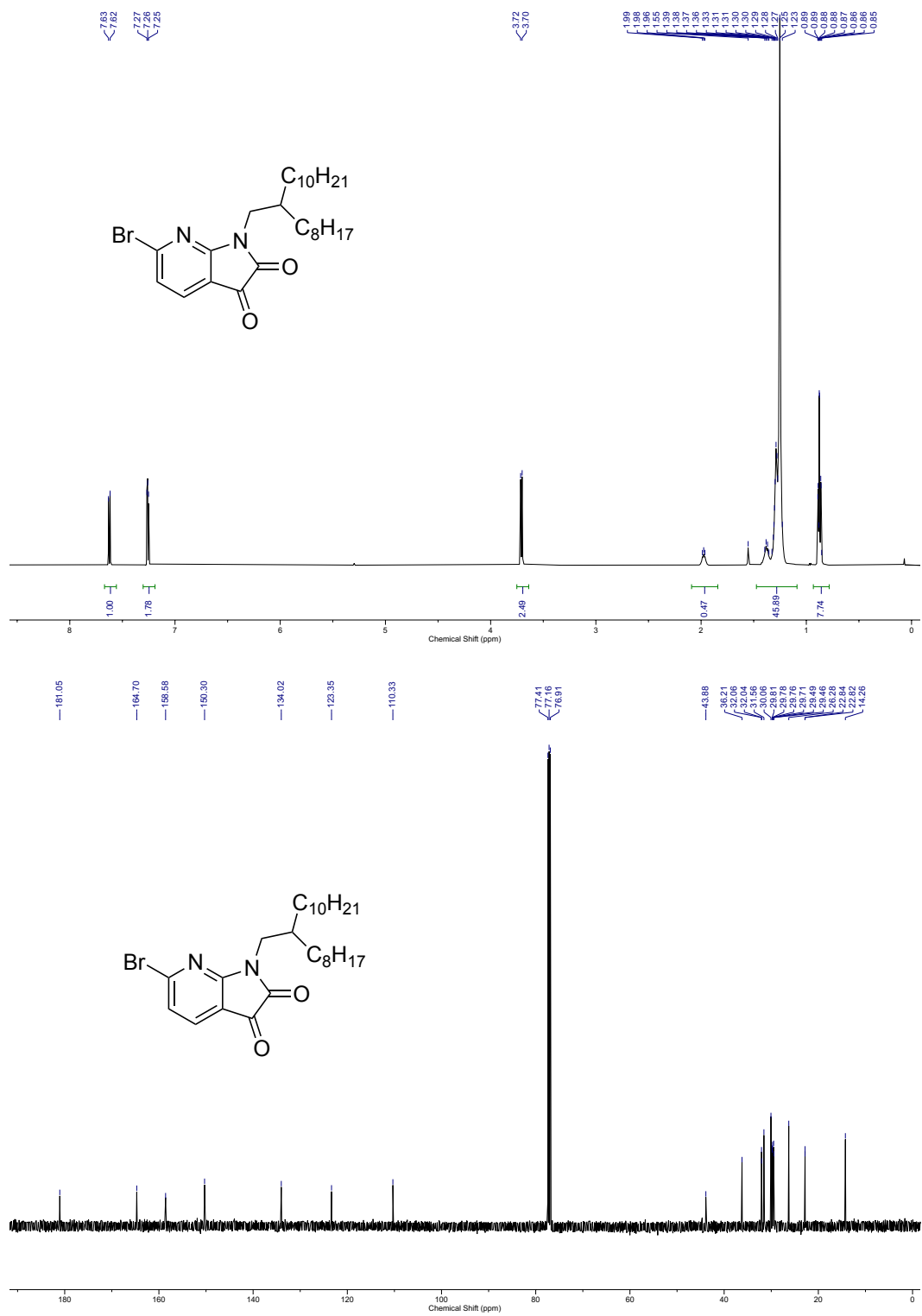
Figure 3.4. ^{1}H (500 MHz) and ^{13}C{^{1}H} (125 MHz) NMR of **2** in CDCl$_3$ at 25 °C.
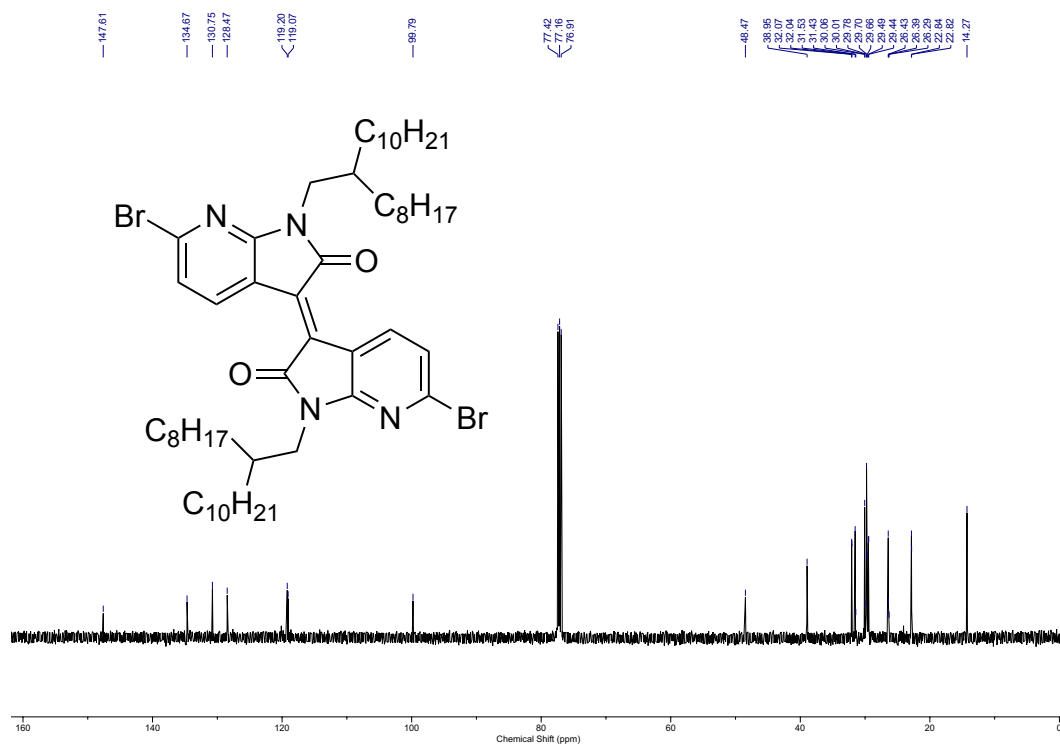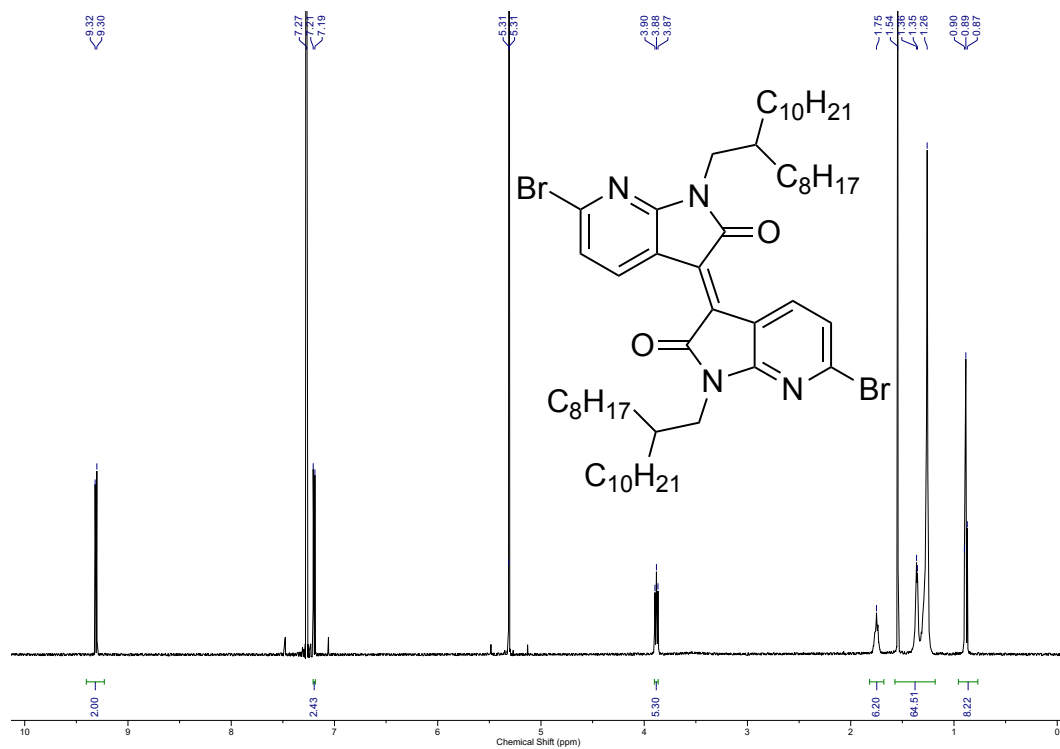
Figure 3.5. ^{1}H (500 MHz) and ^{13}C{^{1}H} (125 MHz) NMR of 3b in CDCl$_3$ at 25 °C.
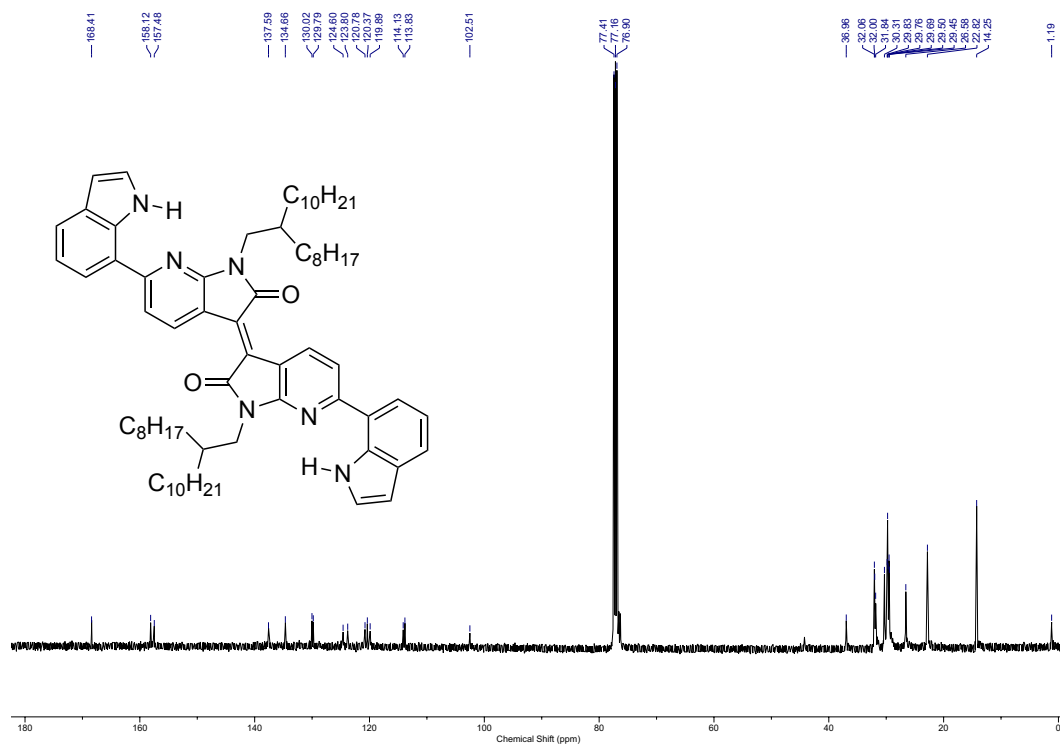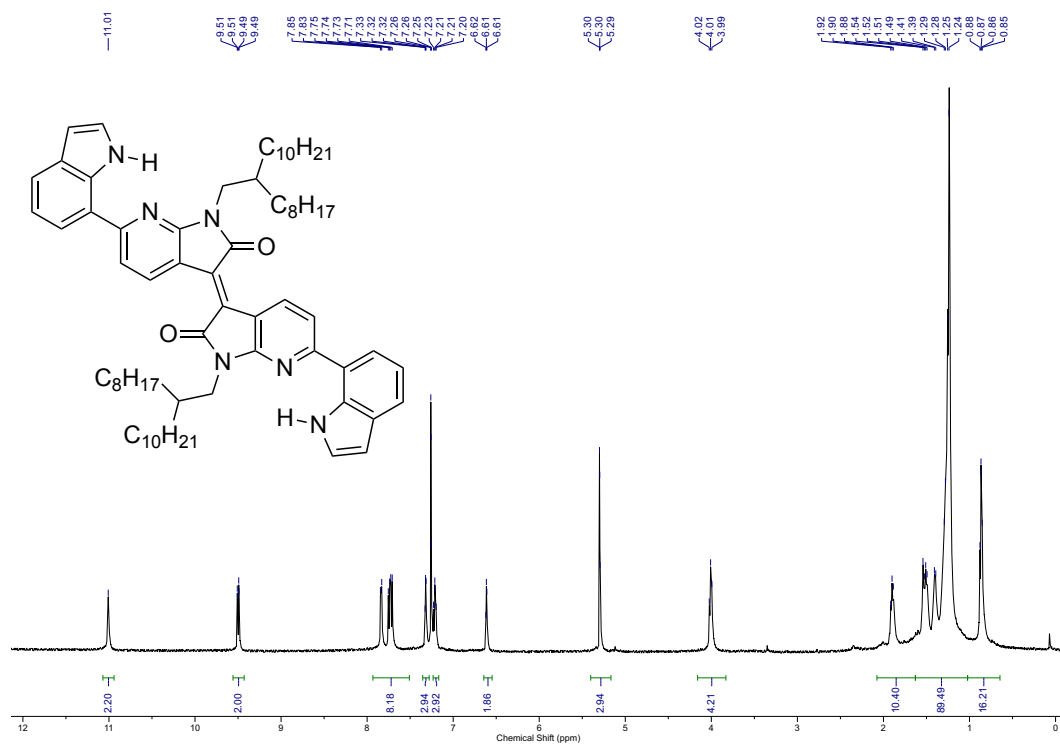
Figure 3.6. ^{1}H (500 MHz) and ^{13}C{^{1}H} (125 MHz) NMR of *o*-AID in CDCl$_3$ at 25 °C.
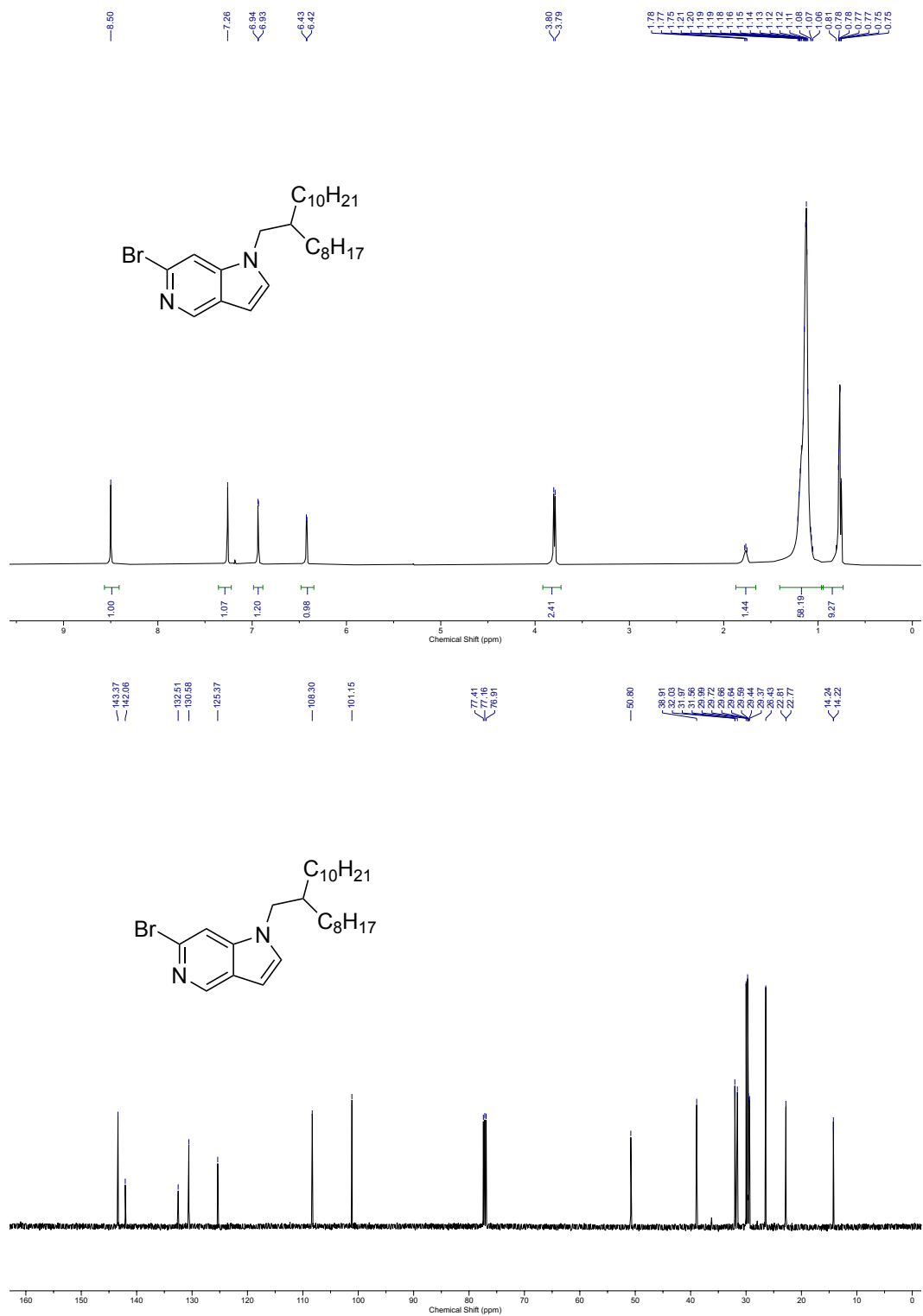
Figure 3.7. ^{1}H (500 MHz) and ^{13}C{^{1}H} (125 MHz) NMR of S4 in CDCl$_3$ at 25 °C.
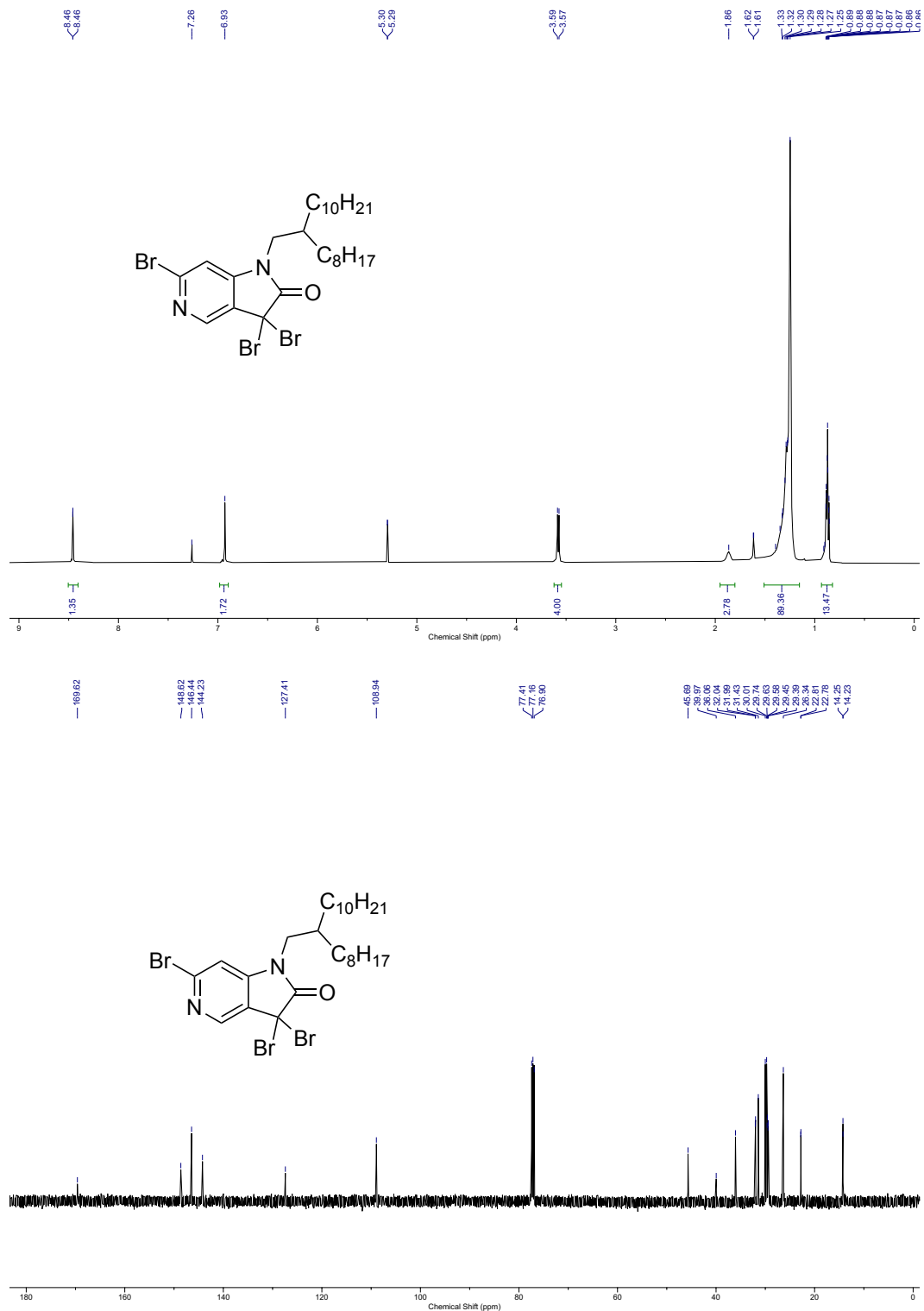
Figure 3.8. ^{1}H (500 MHz) and ^{13}C{^{1}H} (125 MHz) NMR of 4 in CDCl$_3$ at 25 °C
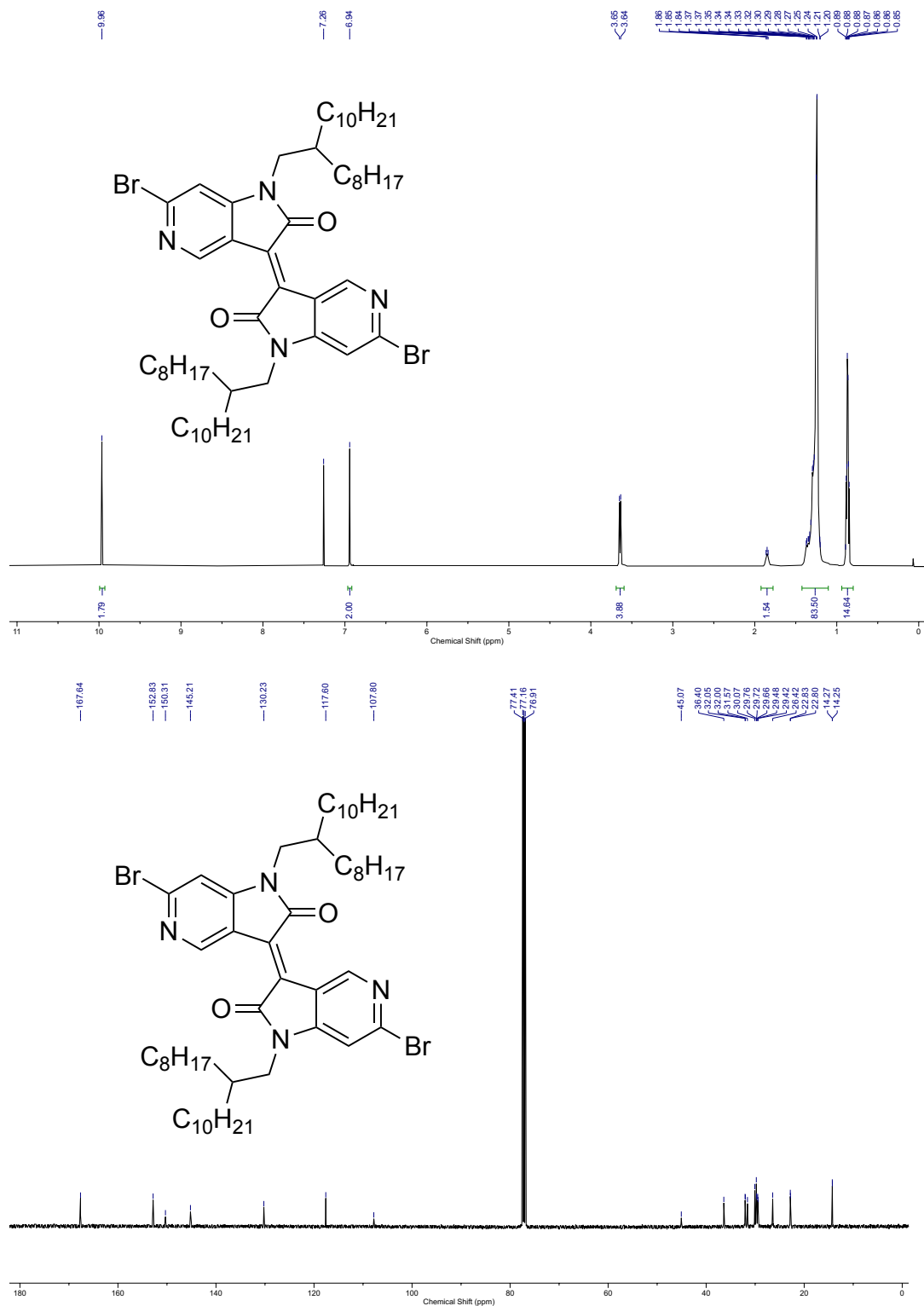
Figure 3.9. ¹H (500 MHz) and ¹³C{¹H} (125 MHz) NMR of 3c in CDCl₃ at 25 °C.
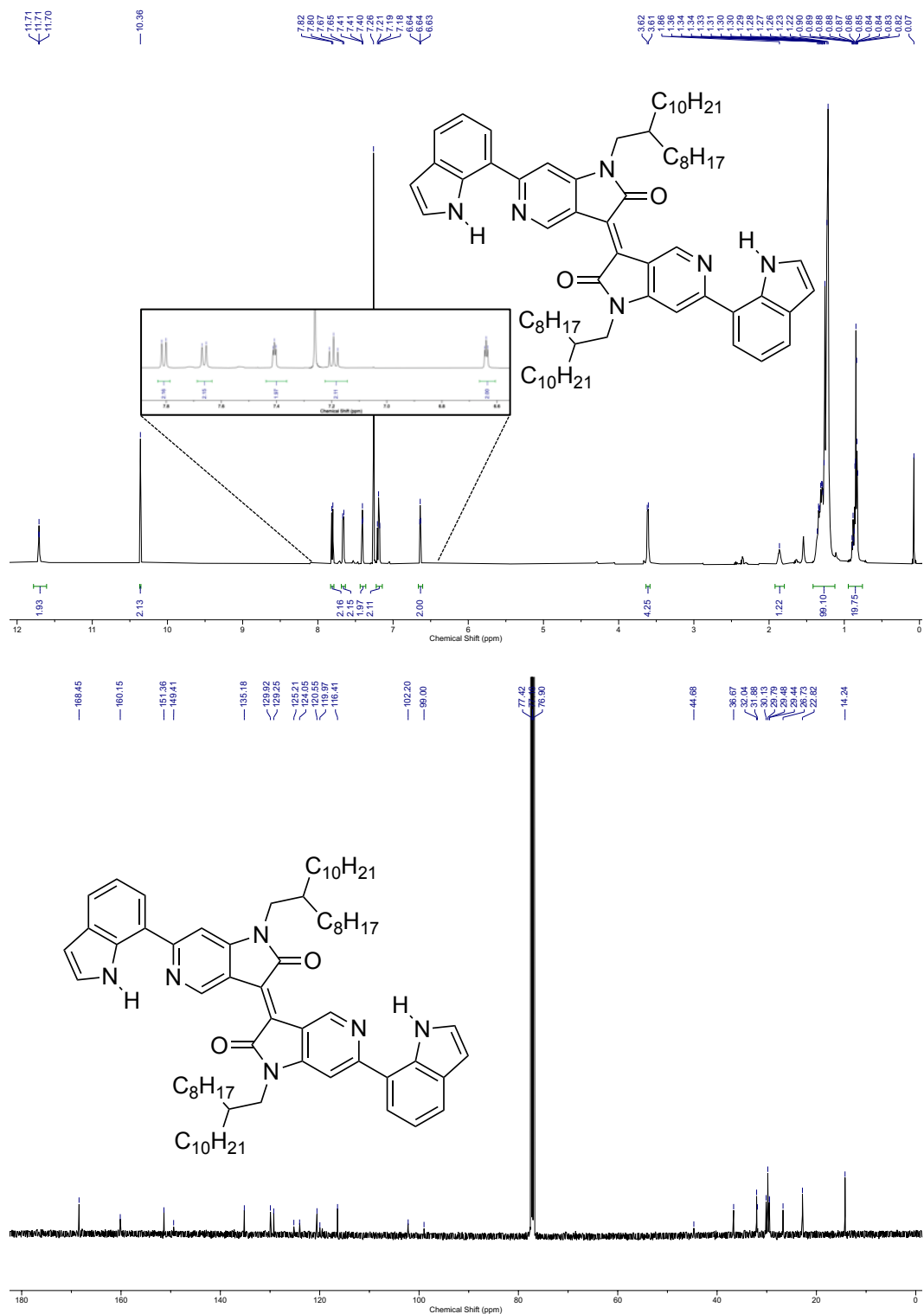
Figure 3.10. ^1H (500 MHz) and $^{13}C\{^1H\}$ (125 MHz) NMR of *p*-AID in CDCl$_3$ at 25 °C.
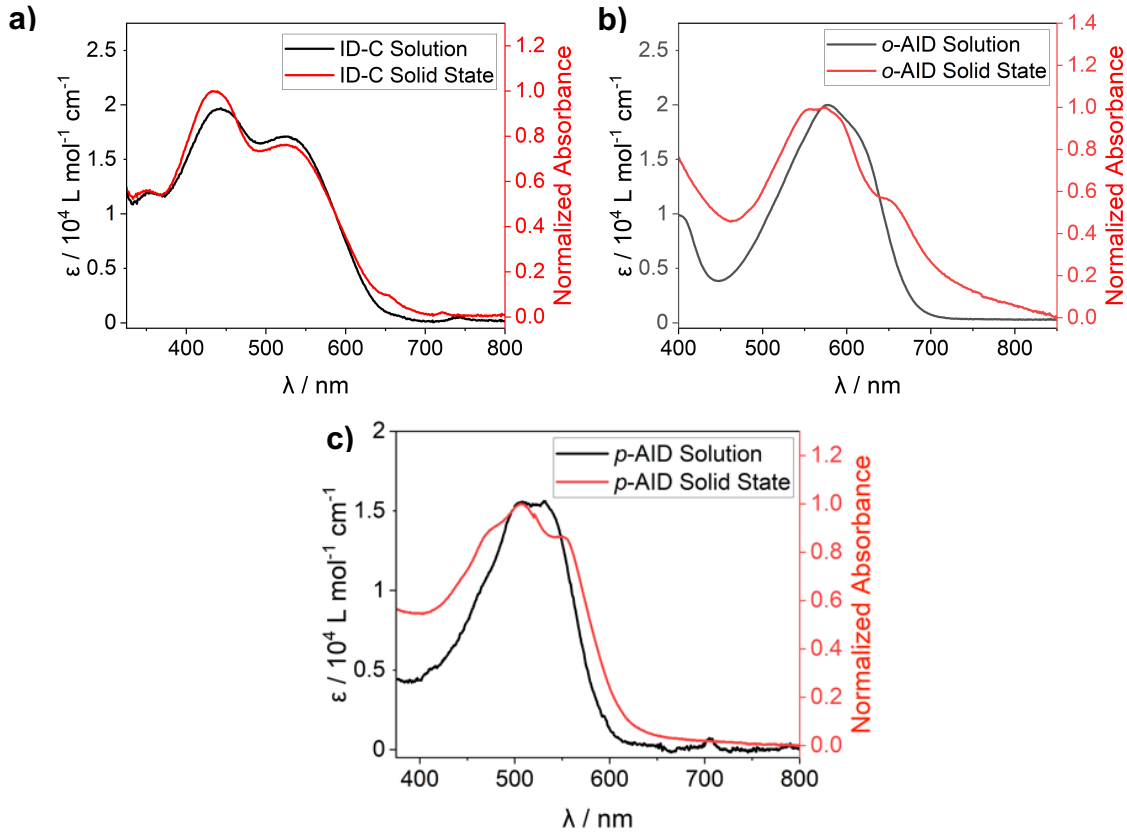
Figure 3.11. UV-Vis absorption spectra of (a) ID-C (b) o-AID (c) p-AID in solution (black) and solid state (red). Solutions were prepared at a concentration of $1x10^{-5}$ M in CH_2Cl_2. Solid-phase thin films were formed by drop-casting CH_2Cl_2 solutions ($1x10^{-3}$ M) of ID-C, o-AID, p-AID onto quartz glass slides.
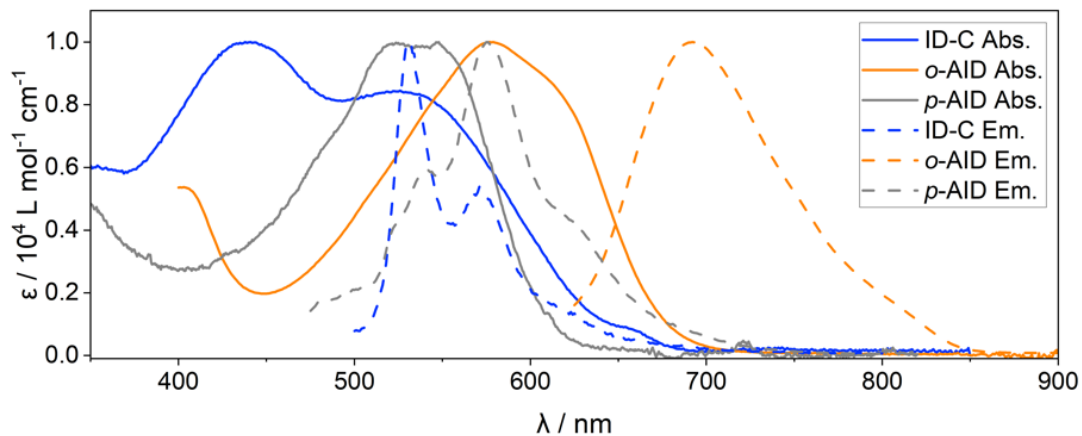
Figure 3.12. Normalized UV-Vis absorption spectra and emission spectra of ID-C, o-AID and p-AID with excitation wavelengths of 455 nm, 450 nm, and 550 nm, respectively. Solutions were all prepared at a concentration of $1x10^{-5}$ M in CH_2Cl_2 for absorbance spectroscopy and $1x10^{-6}$ M in CH_2Cl_2 for emission spectroscopy.
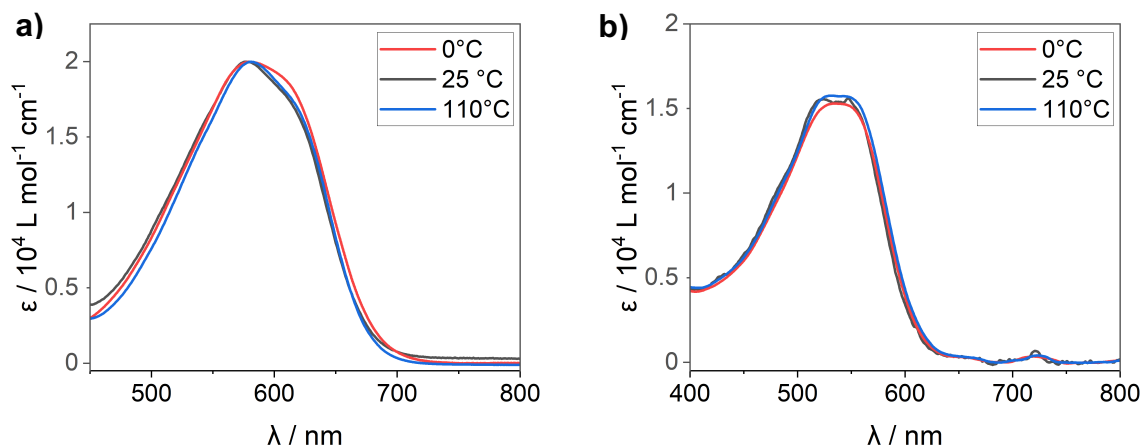
Figure 3.13. Variable temperature UV-Vis spectra of (a) o-AID and (b) p-AID. Solutions were prepared at a concentration of 1×10^{-5} M in toluene and subsequently heated to 110 °C and cooled to 0 °C. No significant change was observed at either high temperature or low temperature.

3.5.5 Cyclic Voltammetry

Cyclic voltammetry (CV) experiments were carried out in nitrogen-purged CH_2Cl_2 at room temperature with a CHI voltametric analyzer. Tetra-*n*-butylammonium hexafluorophosphate (0.1 mol/L) was used as the supporting electrolyte. The conventional three-electrode configuration consisted of a platinum working electrode, a platinum wire auxiliary electrode, and an Ag/AgCl electrode with ferrocenium/ferrocene as the standard. Cyclic voltammograms were obtained at a scan rate of 100 mV/s.

The energy levels were calculated using ferrocene/ferrocenium (Fc/Fc^+) as the standard reference.

Fc/Fc^+ vs Ag/AgCl = 0.45 V.

$E_{HOMO/LUMO} = -4.80 + (E_{1/2})$ eV

$E_{1/2}$ represented the half-wave potential of a redox process on cyclic voltammogram.
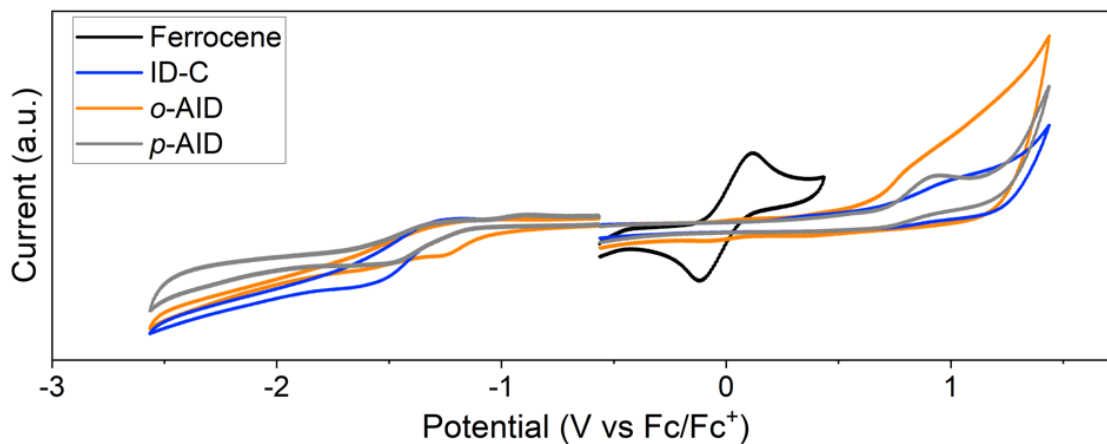
Figure 3.14. Cyclic voltammograms of ID-C, o-AID and p-AID measured in 0.1 M TBAPF₆ acetonitrile solutions.

Table 3.1. Energy levels of frontier molecular orbitals derived from CV.

Compound	LUMO^{CV} (eV)	HOMO^{CV} (eV)	E_g^{CV}
ID-C	-3.46	-5.55	2.09 eV
o-AID	-3.75	-5.44	1.69 eV
p-AID	-3.68	-5.54	1.84 eV
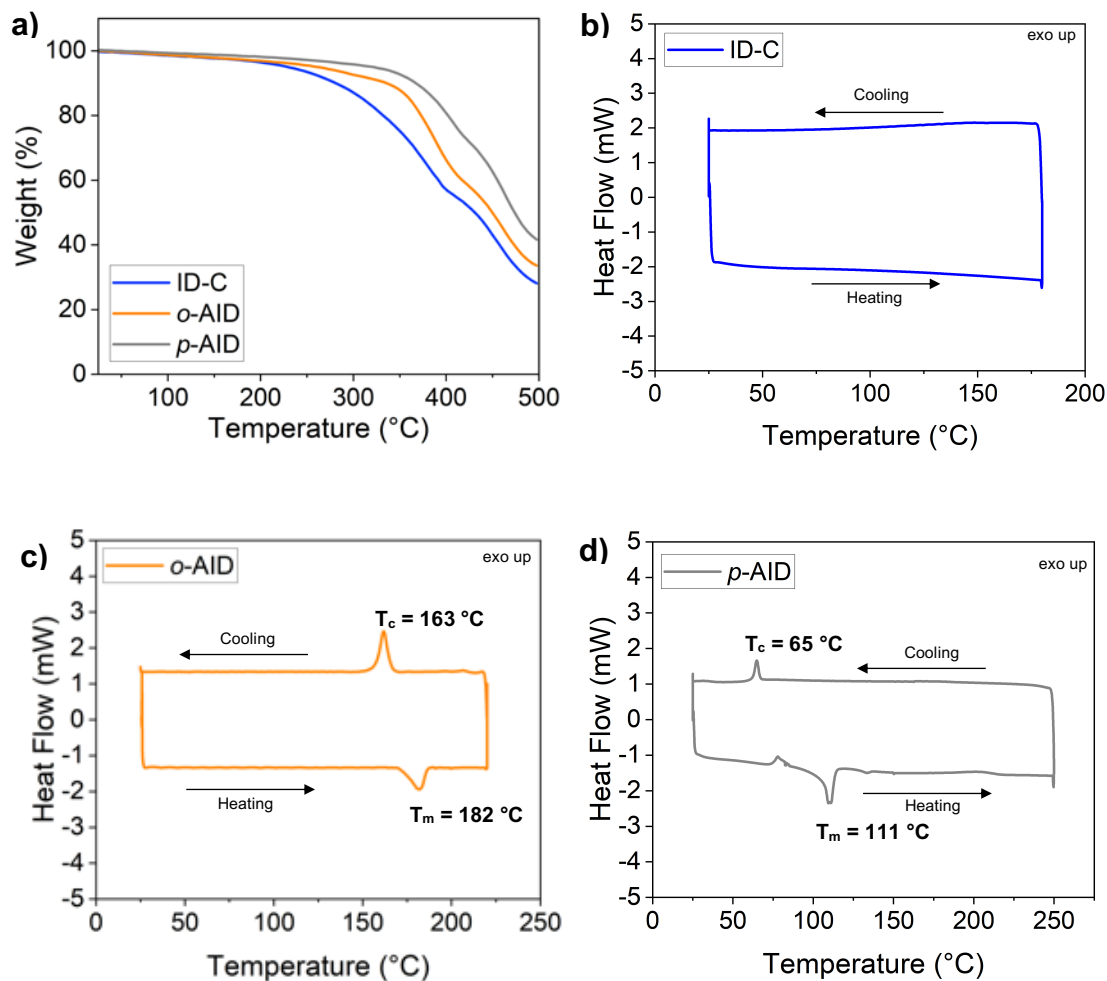
Figure 3.15. Thermal analysis of ID-C, o-AID, and p-AID: (a) TGA thermograms of ID-C, o-AID, and p-AID under nitrogen flow at 10 °C min⁻¹ of heating rate from 25 °C to 500 °C. Decompositions temperatures were defined at 5% weight loss of 226 °C, 257 °C, and 316 °C, respectively. DSC thermograms (2nd cycles) of (b) ID-C, (c) o-AID and (d) p-AID from 25 °C to 180 °C, 250 °C, and 220 °C, respectively. Heating and cooling scans were at a ramp rate of 10 °C min⁻¹ under nitrogen.

CHAPTER IV

ENGINEERING OF LADDER-TYPE MOLECULES FOR THIN-FILM PROCESSING AND

APPLICATIONS IN ORGANIC FIELD-EFFECT TRANSISTORS

4.1 Introduction

As the global population continues to grow and modern technology advances, the demand

for next generation electronics has increased. In this context, there has been remarkable progress

in the investigations in organic electronics, such as organic solar cells (OSC), organic light

emitting diodes (OLED), and organic thin-film transistors (OTFT), *etc*.[6] As electronic devices have

already revolutionized our modern lives by increasing the convenience of everyday tasks, it is

expected that next-generation organic electronics, such as wearable devices and sensors, [8, 9] will

further assist in our way of life. Although organic semiconductors are desired for wide-ranging

chemical tunability, synthesis from nonprecious elements, and mechanical adaptability, to date,

inorganic materials continue to dominate the field of semiconductors due to their higher charge-

transfer mobilities.[10] Despite this intrinsic drawback, recent advancements in this field have

demonstrated promise for next-generation materials, *e.g.* increasing the early organic

semiconductor mobilities[11] from less than 10^{-5} cm^2 V^{-1} s^{-1} to around 40 cm^2 V^{-1} s^{-1}. [12, 13] While

organic semiconductor of past decades have demonstrated that donor-acceptor coupling,[14, 15]

electrochemical doping,[16] and extending effective conjugation length[17] are crucial, clear

fundamental structure-property relationships have yet to be drawn to achieve performances on the

level of inorganic materials.

Figure 4.1. Conformationally locked intramolecular H-bond small molecule (top) and polymer (bottom) of previous works.[51, 52]

Previously, our group has incorporated non-covalent bonding approaches in order to conformationally lock the coplanar and rigid molecular structures over extended conjugation backbones to facilitate charge transport.[124, 138] These non-covalent bonds consisted of B←N coordination bonds[21, 94, 139] and hydrogen bonding.[51, 52] Because the fully coplanarized structures extended the effective conjugation across the backbones, frontier molecular orbital energy levels were manipulated and decreased HOMO-LUMO bandgaps were achieved. For the H-bond-bridged small molecules, the coplanar conformation produced strong aggregation behavior, leading to the controllable molecular self-assembly of one-dimensional nano-microfibers (**Figure 4.1**). Further elongation of this model yielded low molecular weight oligomers due to the insolubility of the polymer possessing a fully rigidified backbone. Despite this, Boc groups were installed to mask H-bonding and promote high molecular weight **BocP1**. The solubility was then switched off by thermal cleavage of Boc-groups, which reinstated global H-bonding forming

insoluble **P1** and demonstrating a practical strategy for multilayer solution casting method for conjugated polymer materials.
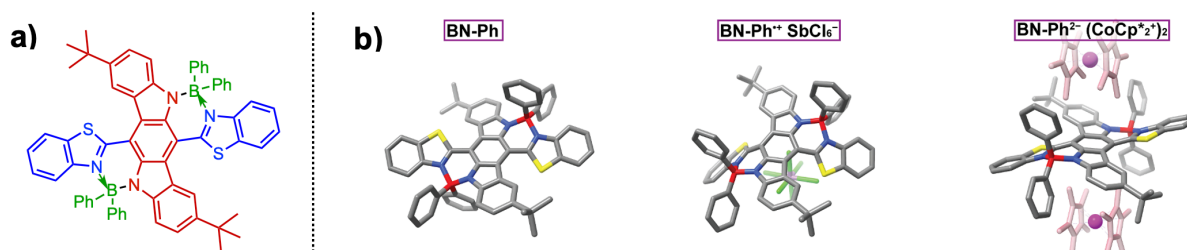
Figure 4.2. Previous B←N coordination work: (a) Structure of BN-Ph and (b) single-crystal structures of key redox states of BN-Ph featuring two distinct pathways from benzenoid to quinonoid constitutions.[94]

Apart from these H-bonding compounds, our group also demonstrated the effects of B←N coordination conformation locking towards the enhancement of chemical stability, even in one to two electron redox processes (**Figure 4.2**). Through BLA measurements from DFT optimized structures, BLA measurements from single-crystal structures of the different redox states, and NBO analyses, a unique hyperconjugation mechanism involving boron ligands enhanced the stability of the redox species.[94] As chemical stability is challenging when subjecting molecules to varying voltages,[140-142] the B←N bridge method provides an effective method in producing electronically stable conjugated structures.
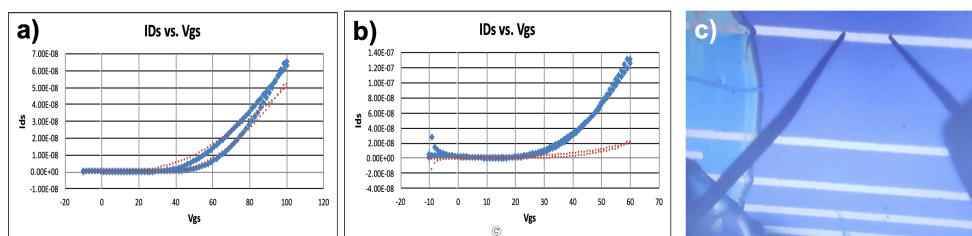
Figure 4.3. OFET device fabrication challenges: (a) high gate-leakage current of IDCZ where charge-transfer curve (blue) is indistinguishable from gate-current (red), (b) low gate-

leakage current where charge-transfer curve (blue) is much lower than gate-current (red). (c) high defect contact electrodes caused by rough *o*-AID film.

As a consequence of the promisingly low bandgap (~1.6 eV) and chemical stability of these IDCZ-based small molecules, this project was initiated by fabricating OFET devices with **BN-Ph** thin-films as the active layer (performed at the Molecular Foundry of Lawrence Berkeley National Laboratory). These devices led to unfavorably large gate currents which dominated over the thin-film's charge-transfer currents (**Figure 4.3a**) Ideally, gate-current must remain low (**Figure 4.3b**) for effective transistor performance. For most solution-processed organic semiconductors, subtle changes to surface morphology, chemical impurities, and physicochemical interactions between the dielectric layer and active layer strongly influence the amount of gate-leakage current.[143, 144] Moreover, these variables can also lead to nano-fracturing of deposited electrodes during device assembly (**Figure 4.3c**) which is likely to increase contact resistance or entirely interrupt conductivity. Combined, the aforementioned H-bonding studies (**Figure 4.1**) and preliminary **BN-Ph** results highlight that, although installing non-covalent conformational locks represents an effective method for achieving desired HOMO-LUMO bandgaps and controlling aggregation behavior of conjugated materials, this strategy may lead to undesirably poor processibility. Thus, a careful balance between aggregation-induced self-organization and solution processibility must be achieved to realize micro-to-meso-scale processing of organic semiconductors

Through the work of another Fang group member, Dr. Yirui Cao, **BN-Ph** analogues **Th-IDCZ-BTh**, **Th-IDCZ-Cl-BTh**, **Ph-IDCZ-BTh**, and **Ph-IDCZ-Cl-BTh** were synthesized with the goal of increasing film-forming ability (**Figure 4.4**).[145] In this design strategy, tert-butyl groups solubilizing-chains were replaced with considerably longer alkyl chains connected by different aryl groups (benzene and thiophene) *via* coupling reactions. Also, extra chlorine atoms were

installed on the benzothiazole acceptor as a previously successful method[25, 146] to tune the optical and electronic properties and enhance semiconducting performances.
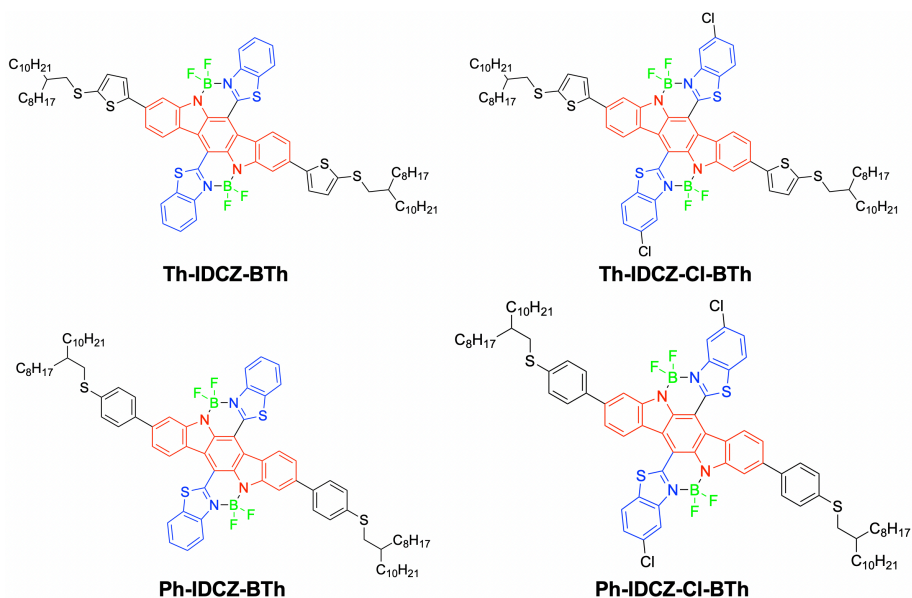
Figure 4.4. IDCZ-based molecules derived from BN-Ph.

Lastly, a nontrivial aspect to OFET active layer performance are the intermolecular electrostatics between organic molecules in respect to constructing charge-transfer channels for electrons or holes to traverse between electrodes. While the effects of molecular charge-distribution on packing orientation can potentially lead to enhanced active layer performance,[147, 148] this concept still represents an overlooked area of study in present day.[149] In this regard, investigation of thin-film nanostructurs proves to be important. Although AFM remains a crucial characterization technique in determining surface morphologies and roughness of thin-films, grazing-incidence X-ray scattering (GIXS) has emerged as a powerful tool probe sub-surface structures, giving necessary information complementary to other microscopy measurements.[150-153] By altering the angle of scattering from the sample, the length scales of observable features can be

determined. These angles are dependent on sample-detector distance and can be divided into wide-angle (GIWAXS) and small-angle (GISAXS) geometries. Specific to our interest, GIWAXS can detect large q values of molecular distance, corresponding to the atomic or molecular distances on the scale of Å lengths. This method can be used to identify unit cell packing of small molecules as well as interchain distances of π-conjugated polymers. In addition, the packing direction with respect to the substrate can also be elucidated (**Figure 4.5**).[154] GIWAXS is often a preferential method for investigating the thin-films of organic materials because the intermolecular distances and packing direction are of great importance for semiconducting performance. Therefore, GIWAXS will herein be a focal characterization method.
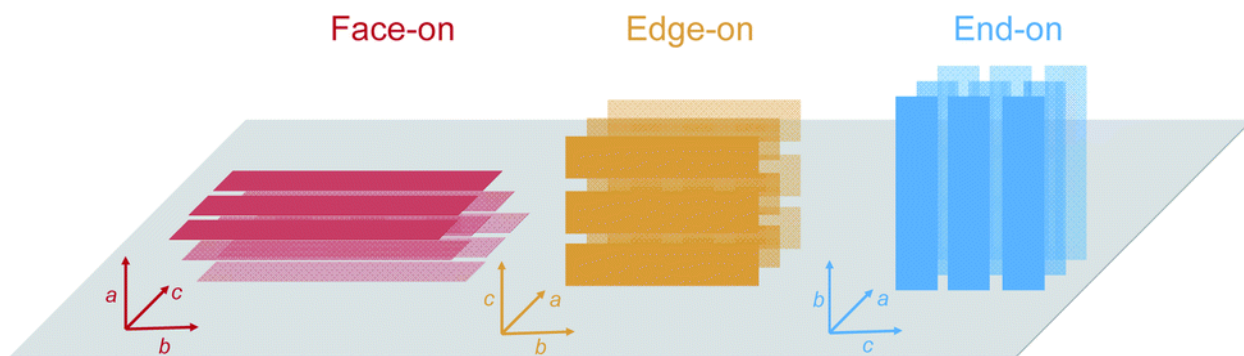
Figure 4.5 Schematic of the face-on, edge-on, and end-on orientationally ordered π-conjugated polymers on substrate surface. Adapted from *J. Mater. Chem. A*, 2020, 8, 6268-6275 with permission from Royal Society of Chemistry.

In this chapter, I first discuss the morphologies and OFET performances of thin-films based on **Ph-IDCZ-BTh, Ph-IDCZ-Cl-BTh, Th-IDCZ-BTh, and Th-IDCZ-Cl-BTh**. We will then discuss the important design principles gained through that study and applied to the H-bond-bridged molecules of the previous chapter, isoindigo-derived molecules **ID-C**, *o*-**AID**, and *p*-**AID**, as well as further side-chain optimization of *o*-**AID** to systematically investigate the following

areas of contention: (i) selecting conjugated building units with appropriate electronic properties to tune charge transport, (ii) thermodynamically enhancing rigidification of planar structures to promote intra- and inter-molecular electron-hole transfer and to allow for high-temperature annealing, (iii) harmonizing molecular solubilizing-chains with substrate treatments to enhance processibility and semiconducting performance while mitigating gate-leakage and device defects, and (iv) tuning of molecular-scale packing orientation by manipulation of intermolecular forces.

4.2 Results and Discussion

4.2.1 Optimization of Indolo[3,2-b]carbazole-based Materials

Following Dr. Yirui Cao's synthesis of **Ph-IDCZ-BTh, Ph-IDCZ-Cl-BTh, Th-IDCZ-BTh,** and **Th-IDCZ-Cl-BTh**,[145] the solution processibilities and morphologies of the four materials were studied through GIWAXS (**Figure 4.6**), an extensively used method to determine relative crystallinity, crystal orientation, and even crystal lattice spacing.[155] Similar to their parent molecule **BN-Ph**, the four molecules were also expected to possess coplanar backbones and display similar chemical stabilities. The as-cast films of **Ph-IDCZ-BTh** and **Th-IDCZ-BTh** exhibited distinct lamellar stacking peaks in the out-of-plane direction with no clear short-range π-π stacking distances (>1.5 Å^{-1} in reciprocal space). In contrast, the chlorine-containing compounds **Ph-IDCZ-Cl-BTh** and **Th-IDCZ-Cl-BTh** exhibited predominantly isotropic scattering, indicating disordered crystallinity with no orientation. The significantly decreased molecular ordering was attributed to the steric hindrance of large chlorine atoms, which has a larger van der Waals radius (1.80 Å) compared to hydrogen (1.20 Å).[25] Nevertheless, all four samples demonstrated an increase in crystallinity after annealing at 110 °C for 1 hour. In fact, a reversed trend was observed, in which **Ph-IDCZ-Cl-BTh** and **Th-IDCZ-Cl-BTh** exhibited

stronger in-plane π-π stacking peaks (~4 Å) than their non-chlorine-containing counterparts. Furthermore, **Ph-IDCZ-Cl-BTh** demonstrated the strongest π-π stacking peak (~3.6 Å) in the 30° direction, indicating tilting of the molecular backbones.
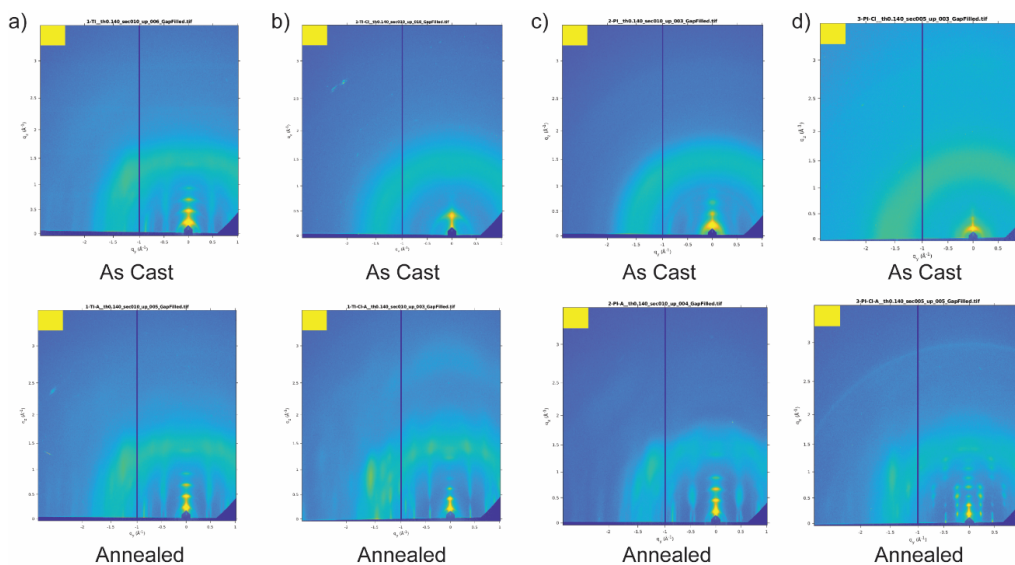
Figure 4.6. GIWAXS of thin films of the four small molecules as-cast (top) and after thermal annealing (bottom) at 110 °C: (a) Ph-IDCZ-BTh, (b) Ph-IDCZ-Cl-BTh, (c) Th-IDCZ-BTh, (d) Th-IDCZ-Cl-BTh.

As a result of the promising morphology, **Ph-IDCZ-BTh**, **Ph-IDCZ-Cl-BTh**, **Th-IDCZ-BTh**, and **Th-IDCZ-Cl-BTh** were employed as the semiconducting active layers of OFET devices to determine their charge-transport properties. First, heavily doped n-type Si wafers with 300 nm SiO2 were used as substrates. After cleaning the substrates and subjecting them to oxidation under ozone treatment, the four materials were deposited by spin-coating and gold electrodes were installed by physical vapor deposition in a bottom-gate top-contact architecture (detailed in **4.4.4**).

Following the GIWAXS results, thermal annealing was performed at 110 °C for 1 h to increase molecular ordering. As shown in **Scheme 4.1**

To solve this issue, OTS treatment of the substrates was employed (detailed in **4.4.4**), which has been previously utilized extensively as an effective method of improving wettability during thin-film processing.[157, 158] As-cast and annealed OFET devices of **Ph-IDCZ-BTh**, **Ph-IDCZ-Cl-BTh**, **Th-IDCZ-BTh**, and **Th-IDCZ-Cl-BTh** were once again fabricated, leading to visually thicker and more uniform films. Through this method, all four compounds exhibited measurable charge-transfer mobilities. Specifically, as-cast **Ph-IDCZ-BTh** and **Th-IDCZ-BTh** both demonstrated ambipolar mobilities in the range of 10-5 cm2 V-1 s-1 to 10-4 cm2 V-1 s-1. The hindered performance of the annealed devices was hypothesized to be due to the crystallinity-induced grain boundaries in the thin films, leading to more defined boundaries between crystalline domains and, consequently, barriers to charge-hopping.

Table 4.1, these devices demonstrated virtually no charge-transport. These results were expected to be due to the inadequate solvent (CBz) wettability on the bare substrates, leading to insufficient film thicknesses. Although charge-transport occurs in the nanometer scale of active layers, increased thickness is crucial for increasing the number of charge-transfer pathways within the material.[156]

To solve this issue, OTS treatment of the substrates was employed (detailed in **4.4.4**), which has been previously utilized extensively as an effective method of improving wettability during thin-film processing.[157, 158] As-cast and annealed OFET devices of **Ph-IDCZ-BTh**, **Ph-IDCZ-Cl-BTh**, **Th-IDCZ-BTh**, and **Th-IDCZ-Cl-BTh** were once again fabricated, leading to visually thicker and more uniform films. Through this method, all four compounds exhibited

measurable charge-transfer mobilities. Specifically, as-cast **Ph-IDCZ-BTh** and **Th-IDCZ-BTh** both demonstrated ambipolar mobilities in the range of 10^{-5} cm^2 V^{-1} s^{-1} to 10^{-4} cm^2 V^{-1} s^{-1}. The hindered performance of the annealed devices was hypothesized to be due to the crystallinity-induced grain boundaries in the thin films, leading to more defined boundaries between crystalline domains and, consequently, barriers to charge-hopping.

Table 4.1. Summary of semiconducting performances of OFET devices fabricated with Ph-IDCZ-BTh, Ph-IDCZ-Cl-BTh, Th-IDCZ-BTh, and Th-IDCZ-Cl-BTh.

Compound	Surface Treatment	Annealing	Avg μ_e (cm^2/Vs)	Highest μ_e (cm^2/Vs)	Avg μ_h (cm^2/Vs)	Highest μ_h (cm^2/Vs)
Ph-IDCZ-BTh	None	None	-	-	-	-
	None	110°C	-	-	-	-
	OTS	None	9.34×10^{-5}	1.01×10^{-4}	5.34×10^{-5}	1.32×10^{-4}
	OTS	110°C	-	-	2.08×10^{-5}	3.90×10^{-5}
Ph-IDCZ-Cl-BTh	None	None	-	-	-	-
	None	110°C	-	-	-	-
	OTS	None	5.65×10^{-4}	7.49×10^{-4}	-	-
	OTS	110°C	8.06×10^{-5}	2.28×10^{-4}	-	-
Th-IDCZ-BTh	None	None	-	-	-	-
	None	110°C	-	-	-	-
	OTS	None	1.56×10^{-5}	2.51×10^{-5}	6.51×10^{-5}	1.15×10^{-4}
	OTS	110°C	-	1.72×10^{-6}	1.33×10^{-5}	1.33×10^{-5}
Th-IDCZ-Cl-BTh	None	None	-	-	-	-
	None	110°C	-	-	-	-
	OTS	None	-	-	-	-
	OTS	110°C	-	7.61×10^{-9}	-	1.43×10^{-8}

Furthermore, **Ph-IDCZ-Cl-BTh** demonstrated the highest electron mobilities of 7.49×10^{-4} cm^2 V^{-1} s^{-1}. Corroborated by the GIWAXS data, **Ph-IDCZ-Cl-BTh** exhibited the strongest π-π stacking peak (~3.6 Å) in the ~30° direction, which indicated tilting of the molecular backbones. In contrast to orthogonally-directed edge-on packing, which leads to charge-transfer trapping

between divergent crystalline domains, the higher predominance of off-set packing of **Ph-IDCZ-Cl-BTh** led to diminished grain-boundaries and increased charge-transfer mobility in comparison to the other three analogues.[159-161] In agreeance with these results, the diagonal peak of **Th-IDCZ-BTh** exhibited the weakest intensity and the shortest π-π stacking distance (~4.2 Å), which led to low device performances (<1.43×10^{-8} cm^2 V^{-1} s^{-1}). As a last important note, the ambipolar to n-type performance that these compounds exhibited were unprecedented in respect to their experimental LUMO energy levels (~-3.5 eV), which were not lower than the theoretical -4 eV requirement for stable n-type performance.[134] This observation was attributed to the aforementioned enhanced stability that these **BN-Ph** derivatives possess.

4.2.2 Side-chain Engineering of Diazaisoinigo-based Materials

While it took multiple iterations of devices to achieve the optimized conditions for **Ph-IDCZ-BTh**, **Ph-IDCZ-Cl-BTh**, **Th-IDCZ-BTh**, and **Th-IDCZ-Cl-BTh**, the highest charge-transfer mobility of 7.49×10^{-4} cm^2 V^{-1} s^{-1} was not competitive with the current state-of-the-art. We hypothesize that the FMO energy levels and intrinsic semiconducting ability of indolo[3,2-b]carbazole-based donor-acceptor-donor materials were unfit for semiconducting applications. In this regard, lactam-based acceptors were considered for these molecules due their well-studied broad applications,[162] favorable FMO energy levels,[163] and the wide variety of nitrogen functionalization to tune material processability.[164] In specific, since its first use in electronic materials,[127] isoindigo and its derivatives have demonstrated extraordinary semiconducting capabilities. For example, isoindigo-derived polymers have realized high hole mobilities[165] of 14.4 cm^2 V^{-1} s^{-1}, electron mobilities of up to 9.70 cm^2 V^{-1} s^{-1}, and ambipolar charge-transport mobilities

of over 6 cm^2 V^{-1} s^{-1}.[106, 166] On this front, successfully synthesized **ID-C**, **o-AID**, and **p-AID** (Chapter III) were employed as isoindigo-derived donor-acceptor-donor materials.
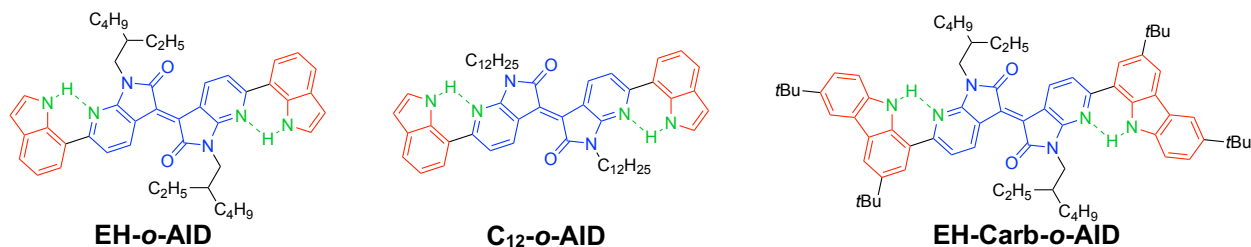
Figure 4.7. Molecular structures of o-AID-based compounds: EH-o-AID, C$_{12}$-o-AID and EH-Carb-o-AID.

To systematically probe the ramifications of side-chain length and bulkiness, **o-AID** was equipped with varying solubilizing alkyl chains. In comparison to the octyldodecyl side-chains of **o-AID**, the 7,7'-diazaindigo core was equipped with ethylhexyl side-chains (**EH-o-AID**) to investigate the effects of branched chain length on, and also, dodecyl chains (**C$_{12}$-o-AID**) to investigated the effects of less bulky linear side-chains (**Figure 4.7**). Although the solubility of **EH-o-AID** was decreased in the same solvents used to dissolve **o-AID** (CH$_2$Cl$_2$, toluene, CBz, *etc.*), the compound still retained adequate solubility for thin-film processing (>10 mg/mL in CBz). Following these results, the ethylhexyl-equipped 7,7'-diazaisoindigo core was coupled with 3,6-di-*tert*-butylcarbazole in-place of indole as the H-bond-donating electron rich moiety to form (**Figure 4.7**). The resulting compound **EH-Carb-o-AID** was expected to provide more insight into the appropriate balance of solubilizing-group efficacy to the aggregation-inducing extended pi-face to determine fundamental structure-property relationships. **EH-Carb-o-AID** maintained adequate solubility for thin-film processing (>5 mg/mL in CBz). Following the synthesis of these three compounds, it was initially hypothesized that **C$_{12}$-o-AID** was a good candidate for single-

crystal growth due to its linear alkyl chain, but the process presented many challenges and resulted in no single crystals suitable for X-ray analysis. For example, **C$_{12}$-o-AID** exhibited extremely poor solubility (<5 mg/mL in CBz) and could not even be spin-coated as a means of thin-film processing. As a result, GIWAXS was only performed on **EH-o-AID** and **EH-Carb-o-AID** as shown in **Figure 4.8**.
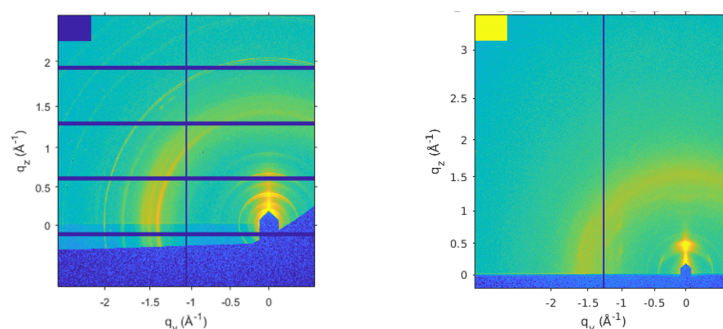
Figure 4.8. GIWAXS of thin films of EH-o-AID (left) and EH-Carb-o-AID (right) after annealing at 110 °C for 1 hour.

The GIWAXS measurements of **EH-o-AID** and **EH-Carb-o-AID** both demonstrated isotropic scattering (**Figure 4.8**). For **EH-o-AID**, although generally isotropic, the ~4.2 Å (q_y = -1.5 Å^{-1}) short-range π-π stacking peak was more intense in the in-plane direction. Furthermore, long-range lamellar stacking peaks were visible in the out-of-plane direction, consistent with edge-on packing with respect to the substrate. **EH-Carb-o-AID** demonstrated distinct crystalline peaks, but they were exceptionally weak, demonstrating a predominance of disorder. Despite this, an intense long-range packing denoting a distance of >12 Å (q_y = -0.5 Å^{-1}) is visible in the out-of-plane direction, which is consistent with the lamellar stacking of **EH-o-AID**. These results give initial evidence that these **o-AID**-based compounds have a preference for edge-on packing, which

is favorable since it aligns the direction of the π-faces in the direction of expected charge-transport in OFETs (parallel to the substrate).[25]
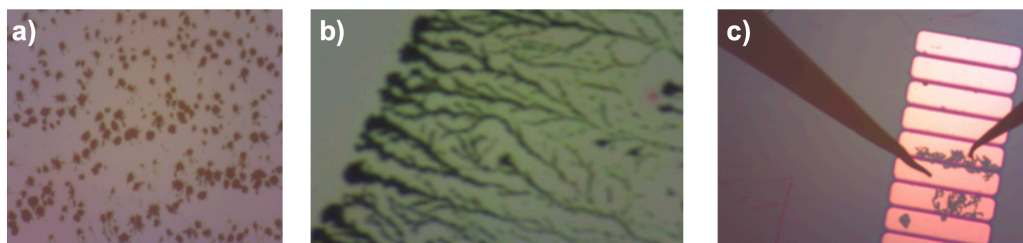
Figure 4.9. Optical microscopy of devices for o-AID-based compounds: (a) spin-coated morphology of EH-o-AID, (b) droplet-pinned morphology of C$_{12}$-o-AID, and representative example of device short-circuit issue for rough devices.

With this molecular orientation in mind, OFET devices were fabricated based on these three ***o*-AID**-based molecules. Initially, solutions (5 mg/mL in CBz) of each compound were spin-coated on OTS-treated Si wafers (detailed in **4.4.4**), but owing to the lower solubility in comparison to ***o*-AID**, the film-forming ability during spin-coating yielded large aggregates and non-uniform films (**Figure 4.9a**). In order to circumvent the poor film-forming ability, droplet-pinning was used to deposit the active layers.[167] In this method, an improvement was made on the traditional drop-casting process by placing a small Si wafer "pinner" in the center of the droplet to secure the droplet in one place and direct crystal growth. As expected, the aggregated crystallites demonstrated higher ordering on the substrate, forming a long tree-like morphology (**C12-*o*-AID** as an example in **Figure 4.9b**). Despite the ordered dendrite-like structures, further installation of 40 nm gold electrodes proved to be difficult due to the roughness of the features, disrupting electrodes as described before in **Figure 4.3c**. Even when uniform electrodes were deposited, the electrodes would break as soon as voltage was applied, presumably due to short-circuiting (**Figure**

4.9c). As a result of the crystallite roughness, each device demonstrated very low hole and electron mobilities.

Despite the low mobilities from these results, important design principles were drawn in terms of choosing functional groups for these non-covalent-bond-bridged rigid molecules. Firstly, the inadequacy of linear and short-branched alkyl chains must be a major focus when designing these compounds for OFET applications. In this respect, highly rigid π-conjugated molecules must have much larger alkyl-chains due to the increased strength of their intermolecular interactions. Furthermore, solubilities of over 10 mg/mL in a solvent system may not be adequate for highly aggregating compounds such as these. For example, while it is logical that **C₁₂-o-AID** was not able to be processed using the spin-coating method (low <5 mg/mL in CBz), **EH-o-AID** and **EH-Carb-o-AID** both exhibited solubilities of >10 mg/mL, and >5 mg/mL, respectively, and exhibited a high propensity to form aggregated islands as opposed to a uniform film.
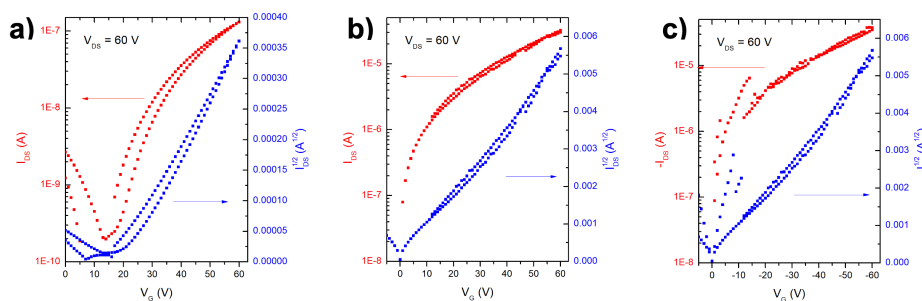
Figure 4.10. Preliminary OFET results: charge-transfer curves for the electron mobility of (a) BN-Ph and ambipolar mobility of (b,c) o-AID.

To contextualize these results, preliminary OFET devices fabricated with **o-AID** active layers at the Molecular Foundry of Lawrence Berkeley National Lab demonstrated ambipolar maximum electron mobilities and hole mobilities of 7.65×10^{-2} cm² V⁻¹ s⁻¹ ($\mu_{e,ave} = 5.67 \times 10^{-2}$ cm²

V^{-1} s^{-1}) and 5.28 x 10^{-2} cm^2 V^{-1} s^{-1} ($\mu_{h,ave}$ = 4.92 $\times$ 10^{-2} cm^2 V^{-1} s^{-1}), respectively, adding to the success of the aforementioned **BN-Ph** device (**Figure 4.10**). While aggregates were prevalent during thin-film processing for the other *o*-**AID** derivatives, *o*-**AID** itself demonstrated uniform thin-films by spin-coating a 5 mg/mL solution in CBz at standard conditions (1000 RPM for 1 minute).

With the preceding challenges in mind, this project will move forward in the next section detailing a systematic study between **ID-C**, *o*-**AID**, and *p*-**AID**, which are all equipped with octyldodecyl chains, with respect to design strategies learned from the preceding *o*-**AID**-based compounds in this chapter. In this work, clear structure-property relationships are drawn by, first, drawing correlations between thermodynamically enhanced rigidification of molecular coplanarity for *o*-**AID** and *p*-**AID** (DFT optimizations and DSC measurements from Chapter II and Chapter III). High-temperature stability of conformation-locking H-bonds demonstrates its importance for high-temperature annealing, in contrast to the **BN-Ph**-based compounds. Furthermore, robust H-bonding is proven to be an effective way of promoting intra- and inter-molecular electron-hole transfer, leading to a clear correlation between H-bonding vigor and OFET performance.

4.2.3 Hydrogen-bond-promoted Planarity, Crystallinity and Charge Transport of Diazaisoindigo-based Derivatives[*]

In order to investigate the intermolecular interactions and crystallinity with regard to solid-state charge transport properties, grazing incidence wide angle X-ray scattering (GIWAXS) was conducted on spin-casted thin films of **ID-C**, *o*-**AID**, and *p*-**AID**, with or without thermal annealing

---

(**Figure 4.11**). While single-crystal growth was unsuccessful, likely due to the bulky octyldodecyl chains necessary for solubility, GIWAXS was employed to represent the molecular packing in thin-film applications. Without thermal annealing, the spin-casted **p-AID** thin film showed clear isotropic diffraction patterns while **ID-C** and **o-AID** were significantly less crystalline. Nevertheless, all these thin films exhibited poor orientation in the as-cast state. Based on the differential scanning calorimetry results, these samples were then thermally treated at 100 °C for **ID-C** and **p-AID** and 170 °C for **o-AID**. After this thermal annealing, multiple distinct diffraction peaks were observed on the GIWAXS results of **o-AID** and **p-AID**, demonstrating high order and orientation in these samples, while **ID-C** retained its amorphous character. For **o-AID** (**Figure 4.11b**), the diffraction pattern suggested edge-on packing (**Figure 4.13**) with two types of π-π distances of 3.51 Å and 3.85 Å. Similarly, for **p-AID** (**Figure 4.11**; **Figure 4.14**), the distinct π-π distance peaks at ~3.95 Å indicated tilting of the molecular backbones to 131°/49° and 121°/59°, corresponding to π-π packing oriented along the (220) and (210) planes, respectively. This diagonal packing was in good correlation with the DFT calculated electrostatic potential maps, in which **p-AID** demonstrated a higher propensity to form edge-to-face packing as compared to **o-AID**.[117] In addition, these diagonal peaks are consistent with other well-known small molecules, such as DNTT[147] and tetrabenzoporphyrin,[148] that exhibit off-set packing with respect to the substrate, which potentially leads to higher charge-transfer mobilities due to diminished grain-boundary effects in thin films.[159, 160, 168]
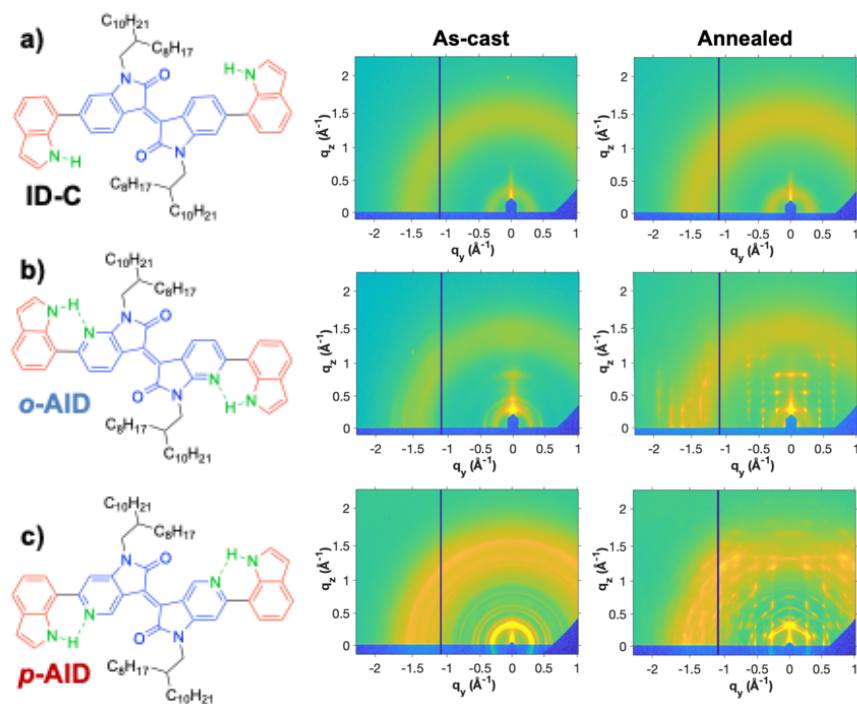
Figure 4.11. GIWAXS diffraction patterns for as-cast and thermally annealed thin films of (a) ID-C, (b) o-AID, and (c) p-AID.

The significant differences observed here on **o-AID** and **p-AID** *vs* **ID-C** can be attributed to the thermally-robust and coplanar conformation of **o-AID** and **p-AID**, which are promoted by intramolecular H-bonds. Because the H-bonds were not disrupted at higher temperatures, the rigid structures could be maintained to facilitate strong intermolecular interactions and firm molecular conformations for the formation of highly crystalline thin films with thermal annealing. In contrast, the non-crystalline property of **ID-C** is likely a result of the low barrier molecular torsional motion, which leads to conformational disorder and weak intermolecular interactions that hinder ordered molecular packing in the solid state.
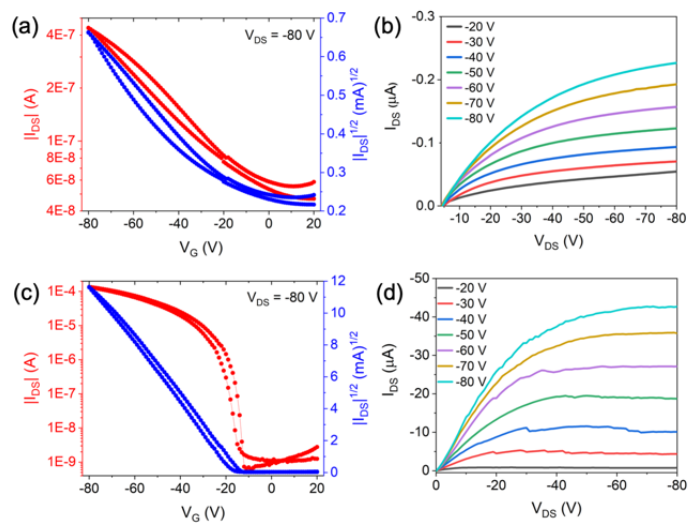
Figure 4.12. Transfer characteristics in the saturation regime at $V_{DS} = -80$ V (red) with the square root of drain current (blue) and output curves for gate voltage $V_g = -20$ V to -80 V in 10 V increments of (a,b) o-AID and (c,d) p-AID.

To probe the correlation of intramolecular H-bonds and thin-film crystallinity to charge transport properties, **ID-C**, ***o*-AID**, and ***p*-AID** were tested in the setting of organic thin-film transistors with bottom-gate/top-contact architectures. These organic materials were spin-coated onto bare or *n*-octadecyltrichlorosilane (OTS)-treated SiO_2/Si substrates using Au source and drain electrodes as detailed in the Supporting Information (SI). As-cast films of **ID-C**, ***o*-AID**, and ***p*-AID** showed no current modulation with the application of gate voltage, suggesting that the lack of ordered and oriented molecular packing (as indicated by GIWAXS data) is detrimental for the charge transport. Upon thermal annealing, as anticipated, the more crystalline and oriented thin films of ***o*-AID** and ***p*-AID** exhibited significantly enhanced *p*-type transistor performances (**Figure 4.12**). It is noteworthy that ***o*-AID** and ***p*-AID** exhibited optimized performances on different substrates, likely due to the difference in their packing modes. On the more hydrophobic OTS-modified SiO_2/Si substrate, ***o*-AID** exhibited significantly increased grain boundaries with its brick-like stacking and could not form a uniform film on OTS-modified substrate. In contrast, the edge-to-face packing

81

mode of **p-AID** rendered it less likely to have grain boundaries and maintained good thin film forming ability on OTS substrates. After optimizing **o-AID** on bare SiO_2/Si and **p-AID** on OTS-modified SiO_2/Si, their maximum hole mobilities reached 5.37×10^{-4} $cm^2\,V^{-1}\,s^{-1}$ and 0.270 $cm^2\,V^{-1}\,s^{-1}$, respectively, while corresponding average hole mobilities were 4.25×10^{-4} $cm^2\,V^{-1}\,s^{-1}$ and 0.187 $cm^2\,V^{-1}\,s^{-1}$ over 12 devices each. The charge transport mobilities of **p-AID** are higher than most of that of other small molecular isoindigo-derived π-systems,[169, 170] and are comparable to the charge transport mobilities of extended fused-ring isoindigo[171, 172] and hemi-isoindigo derivatives.[173-175] The increased mobility of **p-AID** was in accordance with the favorable diagonal π-π packing observed by GIWAXS. In sharp contrast, the control experiment with **ID-C** did not exhibit any significant field-effect transport (**Figure 4.16**) even after thermal annealing, due to its lack of order in the absence of the intramolecular H-bonds.

4.3 Conclusions

In conclusion, we investigated mechanistically the impact of intramolecular H-bonds on the molecular conformation, solid-state packing, and thin-film charge transport of conjugated organic compounds. Conformation-locking intramolecular H-bonds were incorporated into diazaisoindigo-derived molecules. Facile syntheses of the key starting materials 5,5'-diazaisoindigo and 7,7'-diazaisinidigo were achieved after optimizing the condensation reactions. Combined computational and experimental investigations suggested that the stabilization energy of the H-bonds promoted a high-temperature-tolerating, rigid conformation of **o-AID** and **p-AID,** in contrast to the disordered non-H-bonded control **ID-C**. The rigid conformation and influence of molecular design on the molecular quadrupole moment resulted in significantly enhanced orientation of solid-state molecular packing, which was clearly correlated to the semiconducting transistor performances of the thin films. Overall, this work demonstrates the effective strategy of

using intramolecular H-bonds to tailor the molecular conformation, solid-state packing, and electronic properties of conjugated organic compounds.

4.4 Experimental Section

4.4.1 General Materials and Methods

Starting materials and reagents were purchased from Sigma Aldrich, Acros Organics, Alfa Aesar, Oakwood, or Combi-Blocks and used as received. Anhydrous dichloromethane (CH_2Cl_2) was purchased from EMD Millipore and used without further purification. THF was dried and distilled under nitrogen from sodium using benzophenone as the indicator. Toluene and acetonitrile were dried using an Innovative Technology pure solvent system (PureSolv-MD-5) and degassed by three cycles of freeze-pump-thaw before use. 9-(bromomethyl)nonadecane was synthesized according to a reported literature procedure.[137] Preparative gel permeation chromatography (GPC) was performed in chloroform solution at room temperature using Japan Analytical Industry recycling preparative HPLC (LC-92XXII NEXT SERIES). ^{1}H and ^{13}C NMR spectra were recorded on a Varian Inova 500 MHz spectrometer and variable temperature ^{1}H NMR spectra were recorded on a Varian VnmrS 500 MHz spectrometer. The NMR chemical shifts were reported in ppm relative to the signals corresponding to the residual non-deuterated solvents (CDCl$_3$: ^{1}H 7.26 ppm, ^{13}C 77.16 ppm; CD$_3$CN: ^{1}H 1.94 ppm) or the internal standard (tetramethylsilane: ^{1}H 0.00 ppm). Abbreviations for reported signal multiplicities are as follows: s, singlet; d, doublet; t, triplet; q, quartet; m, multiplet; br, broad. High resolution mass spectra were obtained via electrospray ionization (ESI) on an Applied Biosystems PE SCIEX QSTAR or matrix-assisted laser desorption/ionization (MALDI) on a Bruker microflex with a time-of-flight (TOF) analyzer.

Column chromatography was carried out using Biotage® IsoleraTM Prime instrument with various size of SiO_2 Biotage ZIP® cartridge.

4.4.2 Synthesis
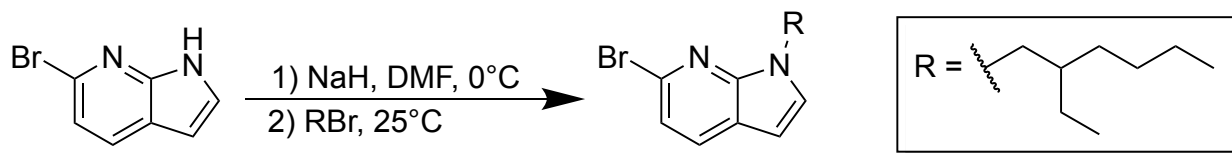
Scheme 4.1. Synthesis of 6-bromo-1-(2-ethylhexyl)-1H-pyrrolo[2,3-b]pyridine.

6-bromo-1-(2-ethylhexyl)-1H-pyrrolo[2,3-b]pyridine. To a suspension of NaH (60% in paraffin oil, 200 mg, 4.87 mmol) in dimethylformamide (8 mL) was added 6-bromo-1*H*-pyrrolo[2,3-*b*]pyridine (800 mg, 4.06 mmol) portion-wise at 0 °C. After the suspension was stirred at room temperature for 30 min, 2-ethylhexyl bromide (784 mg, 4.06 mmol) was added and stirring of the reaction mixture continued overnight. The reaction mixture was then quenched by addition of water and the contents were extracted with CH_2Cl_2. The organic layers were concentrated and purified by column chromatography with hexanes as the eluent to give 6-bromo-1-(2-ethylhexyl)-1*H*-pyrrolo[2,3-*b*]pyridine as a colorless oil (yield: 1.043 g, 83%). ^{1}H NMR (300 MHz, $CDCl_3$): δ 7.73 (d, J = 8.1 Hz, 1H), 7.18 (d, *J* = 8.1 Hz, 1H), 7.15 (d, *J* = 3.5 Hz, 1H), 6.44 (d, *J* = 3.5 Hz, 1H), 4.16 (d, *J* = 7.1 Hz, 2H), 2.14 – 1.74 (m, 1H), 1.42 – 1.12 (m, 8H), 0.91 (t, *J* = 7.5 Hz, 3H), 0.88 (t, *J* = 7.5 Hz, 3H). ^{13}C NMR (75 MHz, $CDCl_3$): δ 147.77, 134.83, 130.94, 128.63, 119.37, 119.25, 99.99, 48.29, 40.50, 30.76, 28.79, 24.18, 23.29, 14.34, 10.93.
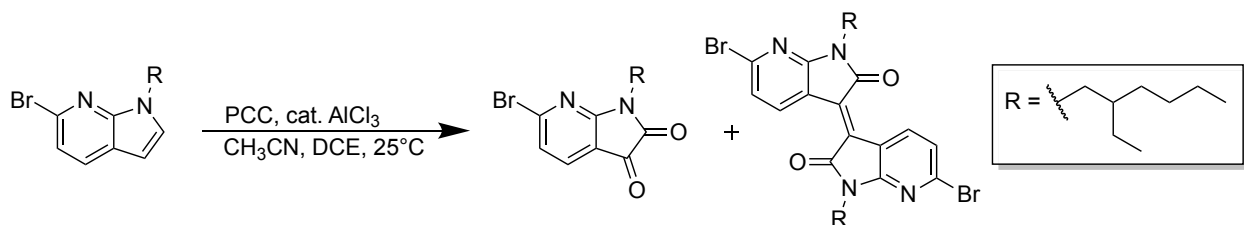
Scheme 4.2. Synthesis of 6-bromo-1-(2-ethylhexyl)-1H-pyrrolo[2,3-b]pyridine-2,3-dione.

6-bromo-1-(2-ethylhexyl)-1H-pyrrolo[2,3-b]pyridine-2,3-dione. To a suspension of pyridinium chlorochromate (860 mg, 4.00 mmol) and silica gel (860 mg) in anhydrous 1,2-dichloroethane (5 mL) was added a solution of 6-bromo-1-(2-ethylhexyl)-1H-pyrrolo[2,3-b]pyridine (502 mg, 1.62 mmol) in 1,2-dichloroethane (2 mL) at room temperature. A catalytic amount of AlCl$_3$ was added and the mixture was heated to 80 °C for 3 h. Then, the solvent was evaporated and the residue was purified by column chromatography to give N,N'-Bis(2-ethylhexyl)-6,6'-dibromo-7,7'-diazaisoindigo (DAIID-EtH) (yield: 88 mg, 9%) as a red powder and (6-bromo-1-(2-ethylhexyl)-1H-pyrrolo[2,3-b]pyridine-2,3-dione as orange crystals (yield: 330 mg, 60%). ^{1}H NMR (300 MHz, CDCl$_3$): δ 7.62 (d, $J = 7.7$ Hz, 1H), 7.26 (d, $J = 7.7$ Hz, 1H), 3.73 (d, $J = 0.5$ Hz, 1H), 1.93 (m, 1H), 1.48 – 1.07 (m, 8H), 0.97 – 0.85 (m, 6H).
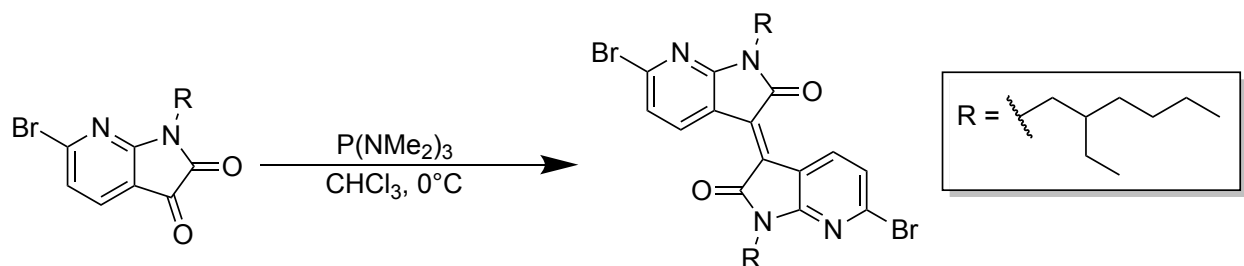
Scheme 4.3 Synthesis of N,N'-Bis(2-ethylhexyl)-6,6'-dibromo-7,7'-diazaisoindigo.

N,N'-Bis(2-ethylhexyl)-6,6'-dibromo-7,7'-diazaisoindigo. To a solution of tris(dimethylamino)phosphine (34 mg, 0.21 mmol) in CHCl$_3$ (4 mL) was added a solution of 6-bromo-1-(2-ethylhexyl)-1H-pyrrolo[2,3-b]pyridine-2,3-dione (70 mg, 0.21 mmol) in CHCl$_3$ (1 mL) dropwise at -60 °C. After returning to room temperature, the reaction mixture was heated to

40 °C for 3 h. The contents were quenched by the addition of water and extracted with CH_2Cl_2. The organic layers were concentrated and purified by column chromatography to afford N,N'-Bis(2-ethylhexyl)-6,6'-dibromo-7,7'-diazaisoindigo as a red solid (yield: 36 g, 53%). ^{1}H NMR (300 MHz, CDCl$_3$): δ 9.29 (d, J = 8.3 Hz, 2H) 7.18 (d, J = 8.3 Hz, 2H), 3.77 (d, J = 7.2 Hz, 4H), 2.28 – 1.81 (m, 2H), 1.38 – 1.18 (m, 16H), 0.91 (m, 12H).
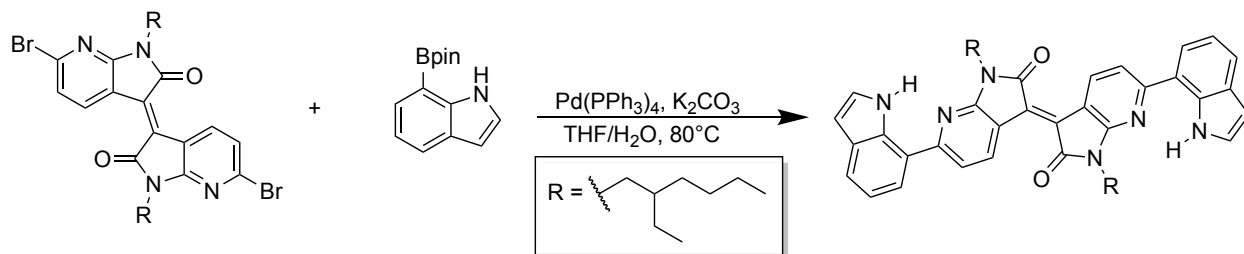
Scheme 4.4. Synthesis of EH-*o*-AID.

N,N'-1,1'-bis(2-ethylhexyl)-6,6'-di(1H-indol-7-yl)-7,7'-diazaisoindigo **(EH-*o*-AID)**. A suspension of N,N'-Bis(2-ethylhexyl)-6,6'-dibromo-7,7'-diazaisoindigo (100 mg, 0.15 mmol) and K_2CO_3 (133 mg, 0.94 mmol) in THF (1.7 mL) and water (0.9 mL) was degassed by freeze-pump-thaw. Pd(PPh$_3$)$_4$ (5 mol%) and 7-(4,4,5,5-tetramethyl-1,3,2-dioxaborolan-2-yl)-1*H*-indole (94 mg, 0.39 mmol) were added under nitrogen and the subsequent reaction mixture was stirred at 80 °C for 24 h. The reaction mixture was then quenched by the addition of water and extracted with CH_2Cl_2. The organic layers were concentrated and purified by preparatory GPC to afford N,N'-1,1'-bis(2-ethylhexyl)-6,6'-di(1H-indol-7-yl)-7,7'-diazaisoindigo as a violet powder (yield: 55 mg, 51%). ^{1}H NMR (300 MHz, CDCl$_3$): δ 11.02 (s, 2H), 9.53 (dd, J = 8.5, 1.1 Hz, 2H), 7.88 (dd, J = 7.8, 1.0 Hz, 2H), 7.83 – 7.69 (m, 4H), 7.34 (dd, J = 3.2, 2.2 Hz, 2H), 7.23 (t, J = 7.7 Hz, 2H), 6.62 (dd, J = 3.2, 2.2 Hz, 2H), 5.34 (dt, J = 3.4, 1.0 Hz, 4H), 3.90 (d, J = 7.6 Hz, 2H), 2.12 (d, J = 7.0 Hz, 2H), 2.12 (d, J = 7.0 Hz, 16H), 0.99 (t, J = 7.4 Hz, 3H), 0.90 (t, J = 7.0 Hz, 3H). ^{13}C NMR (75 MHz, CDCl$_3$): δ 168.41, 157.97, 157.67, 137.33, 134.43, 129.59, 124.55, 123.40, 120.59, 120.36,

119.64, 113.99, 113.96, 102.18. LRMS (ESI-TOF) m/z [M − H]⁻ Calc'd for $C_{46}H_{50}N_6O_2$ 1054.7751; Found 1054.7755.
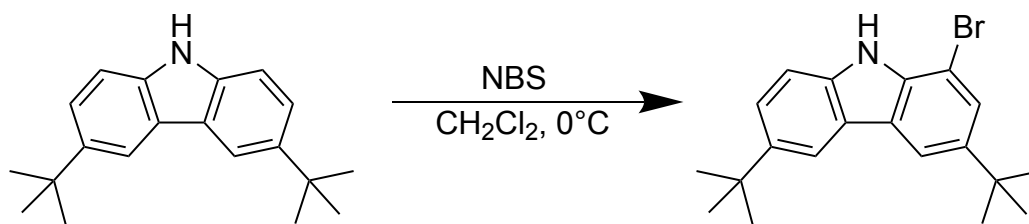
Scheme 4.5. Synthesis of 1-bromo-3,6-di-tert-butyl-9H-carbazole.

1-bromo-3,6-di-tert-butyl-9H-carbazole. To a stirred solution of 3,6-*di*-tert-butyl-9H-carbazole (800 mg, 3.58 mmol) in CH_2Cl_2 (30 mL) was added a mixture of NBS (509 mg, 2.86 mmol) in CH_2Cl_2 (40 mL) dropwise at 0 °C. The reaction mixture was stirred in the absence of light for 4 h at room temperature. After completion, the reaction mixture was concentrated and purified by column chromatography to yield 1-bromo-3,6-di-tert-butyl-9H-carbazole as a colorless oil (yield: 964 mg, 2.57 mmol). ¹H NMR (500 MHz, CDCl₃): 8.21 – 8.04 (m, 3H), 7.71 (s, 1H), 7.63 – 7.56 (m, 1H), 7.49 – 7.39 (m, 1H), 5.37 – 5.28 (m, 1H), 1.55 (dd, J = 6.0, 2.2 Hz, 18H).
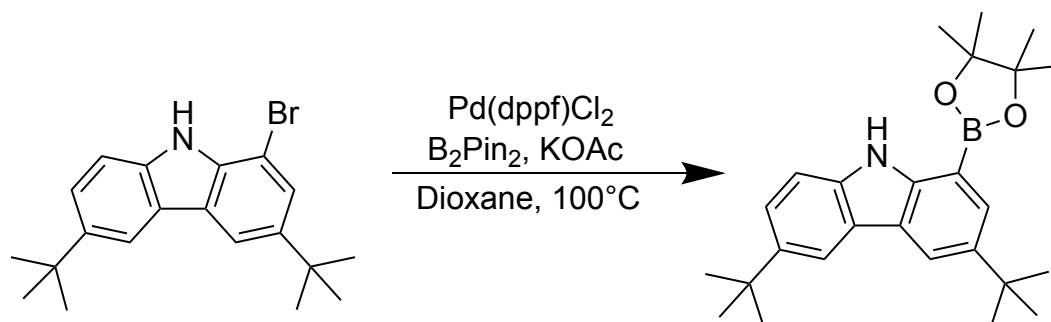
Scheme 4.6. Synthesis of 3,6-di-tert-butyl-1-(4,4,5,5-tetramethyl-1,3,2-dioxaborolan-2-yl)-9H-carbazole.

3,6-di-tert-butyl-1-(4,4,5,5-tetramethyl-1,3,2-dioxaborolan-2-yl)-9H-carbazole. To a solution of 1-bromo-3,6-di-tert-butyl-9H-carbazole (739 mg, 2.06 mmol) and bis(pinacolato)diboron (786 mg, 3.09 mmol) in degassed dioxane (10 mL) was added KOAc (404 mg, 4.12 mmol) and Pd(dppf)Cl₂ (75 mg) under nitrogen. The reaction mixture was stirred at reflux

for 12 hours. After completion of the reaction, the mixture was extracted with CH_2Cl_2 and purified by column chromatography to yield 3,6-di-tert-butyl-1-(4,4,5,5-tetramethyl-1,3,2-dioxaborolan-2-yl)-9H-carbazole as a white solid (yield: 530 mg, 62%). ^{1}H NMR (500 MHz, CDCl$_3$): δ 8.99 (s, 1H), 8.24 (dd, J = 2.0, 0.6 Hz, 1H), 8.11 (dd, J = 1.9, 0.7 Hz, 1H), 7.92 (dd, J = 2.0, 0.6 Hz, 1H), 7.50 (dd, J = 8.5, 1.9 Hz, 1H), 7.43 (dd, J = 8.4, 0.7 Hz, 1H), 1.53 – 1.42 (m, 30H).
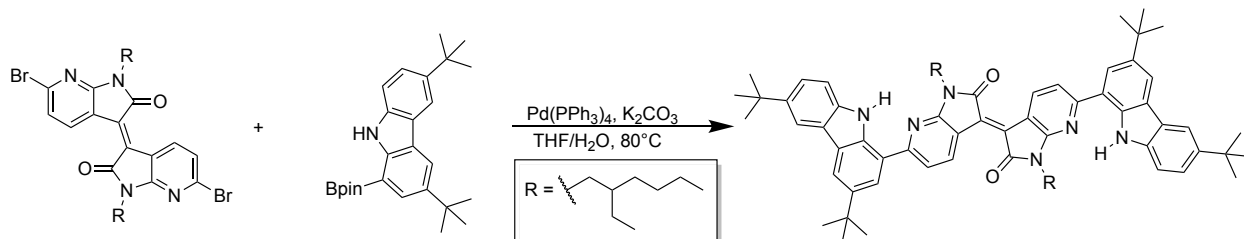
Scheme 4.7. Synthesis of EH-Carb-*o*-AID.

N,N'-6,6'-bis(3,6-di-tert-butyl-9H-carbazol-1-yl)-1,1'-bis(2-ethylhexyl)-7,7'-

*diazaisoindigo (***EH-Carb-*o*-AID***)*. The procedure was similar to that described above. ^{1}H NMR (500 MHz, CDCl$_3$): δ 12.72 (s, 2H), 11.57 (d, J = 8.5 Hz, 2H), 10.23 (d, J = 1.7 Hz, 2H), 10.11 (d, J = 19.1 Hz, 4H), 9.80 (d, J = 8.7 Hz, 2H), 9.51 (dd, J = 8.5, 2.0 Hz, 2H), 9.41 (d, J = 8.5 Hz, 2H), 6.02 (d, J = 7.7 Hz, 4H), 3.63 – 2.65 (m, 30H).
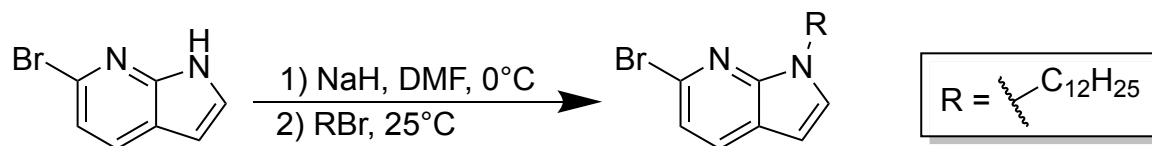
Scheme 4.8. Synthesis of 6-bromo-1-dodecyl-1H-pyrrolo[2,3-b]pyridine.

6-bromo-1-dodecyl-1H-pyrrolo[2,3-b]pyridine. The procedure was similar to that described above. ^{1}H NMR (500 MHz, CDCl$_3$): δ 7.73 (d, J = 8.1 Hz, 1H), 7.18 (d, J = 8.1 Hz, 1H), 7.15 (d, J = 3.5 Hz, 1H), 6.44 (d, J = 3.5 Hz, 1H), 4.24 (d, J = 7.2 Hz, 2H), 1.84 (p, J = 7.2 Hz, 2H), 1.39 – 1.18 (m, 18H), 0.90 (t, J = 6.9 Hz, 3H). ^{13}C NMR (125 MHz, CDCl$_3$): δ 147.31, 134.80,

130.97, 128.24, 119.44, 119.38, 99.96, 44.88, 32.23, 32.22, 30.57, 29.93, 29.86, 29.81, 29.65, 29.50, 27.07, 23.00, 14.43.
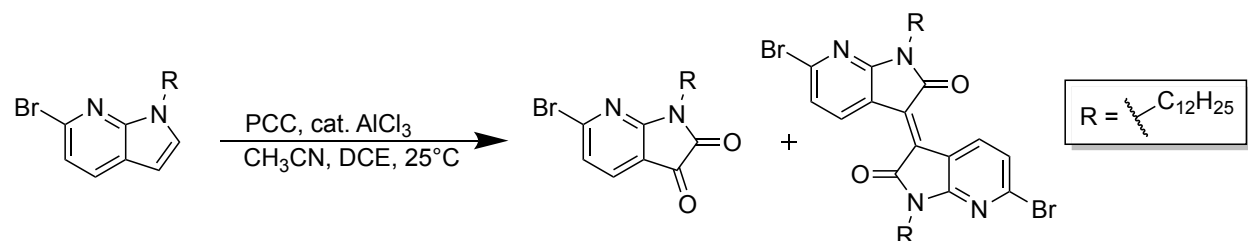
Scheme 4.9. Synthesis of 6-bromo-1-dodecyl-1H-pyrrolo[2,3-b]pyridine-2,3-dione.

6-bromo-1-dodecyl-1H-pyrrolo[2,3-b]pyridine-2,3-dione. The procedure was similar to that described above. ^{1}H NMR (500 MHz, CDCl$_3$): δ 7.64 (d, J = 7.7 Hz, 1H), 7.28 (d, J = 7.4 Hz, 1H), 3.83 (t, J = 3.5 Hz 2H), 1.75 (m, 2H), 1.41 – 1.19 (m, 18H), 0.89 (t, J = 6.9 Hz, 3H).
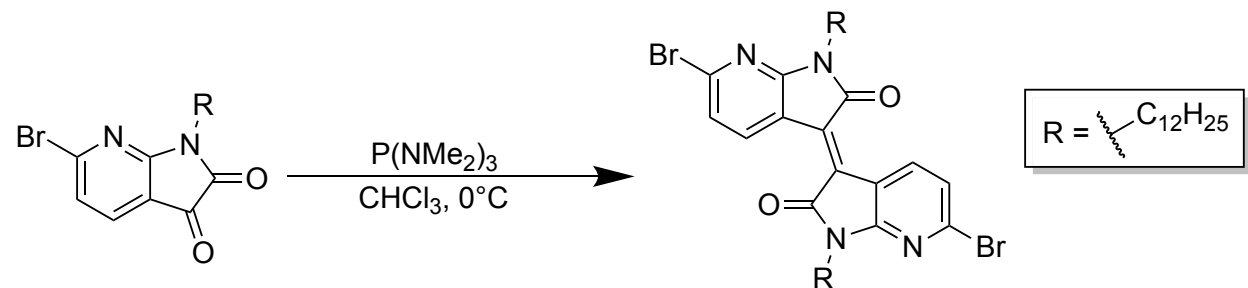
Scheme 4.10. Synthesis of N,N'-Bis(dodecyl)-6,6'-dibromo-7,7'-diazaisoindigo.

N,N'-Bis(dodecyl)-6,6'-dibromo-7,7'-diazaisoindigo (DAIID-C12). The procedure is similar to that described above. ^{1}H NMR (500 MHz, CDCl$_3$): δ 9.31 (d, J = 8.2 Hz, 2H), 7.20 (d, J = 8.3 Hz, 2H), 3.88 (dd, J = 8.0, 6.7 Hz, 4H), 1.82 – 1.69 (m, 4H), 1.31 (d, J = 51.1 Hz, 36H), 0.94 – 0.84 (m, 6H).
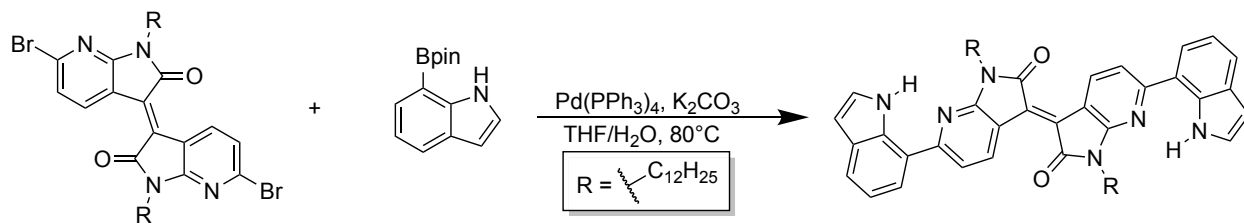
Scheme 4.11. Synthesis of C$_{12}$-o-AID.

     N,N'-1,1'-bis(dodecyl)-6,6'-di(1H-indol-7-yl)-7,7'-diazaisoindigo **(C$_{12}$-o-AID)**. The procedure was similar to that described above. ^{1}H NMR (500 MHz, CD$_2$Cl$_2$): δ 11.02 (s, 2H), 9.51 (d, J = 7.9 Hz, 2H), 7.85 (d, J = 7.6 Hz, 2H), 7.74 (dd, J = 14.7, 8.0 Hz, 4H), 7.33 (q, J = 6.4, 4.6 Hz, 2H), 7.23 (t, J = 7.7 Hz, 2H), 6.63 (t, J = 2.9 Hz, 2H), 4.02 (t, J = 7.6 Hz, 4H), 1.94 – 1.74 (m, 4H), 1.63 – 1.35 (m, 36H), 0.88 (t, J = 6.7 Hz, 6H). ^{13}C NMR (125 MHz, CDCl$_3$): δ 168.13, 158.15, 157.15, 137.58, 134.59, 130.34, 129.56, 124.41, 123.65, 120.71, 120.37, 119.76, 114.16, 113.82, 102.45, 53.41, 39.77, 31.89, 29.64, 29.61, 29.59, 29.57, 29.40, 29.32, 28.17, 27.43, 22.67, 14.10.

4.4.3 GIWAXS Sample Preparation and Morphology Measurements

     Grazing-incidence wide-angle X-ray scattering (GIWAXS) measurements were carried out in Sector 8-ID-E at the Advanced Photon Source, Argonne National Laboratory.[176] Beamline 8-ID-E operates at an energy of 10.92 keV and the images were collected from a Pilatus 1MF camera (Dectris), with two exposures for different vertical positions of the detector. After flat field correction for detector nonuniformity, the images are combined to fill in the gaps for rows at the borders between modules, leaving dark only the columns of inactive pixels at the center. Using the GIXSGUI package[177] for MATLAB (Mathworks), data are corrected for X-ray polarization, detector sensitivity and geometrical solid-angle. The beam size was 0.2 mm × 0.02 mm for **ID-C** and **o-AID** samples and 0.2 mm × 0.01 mm for **p-AID** samples. The incident angle was 0.14°, the resolution (ΔE/E) was 1×10^{-4}, and the sample detector distance was 217 mm. Solid-state samples

were prepared by spin-casting (5 mg/mL in chlorobenzene) thin films of **ID-C**, **o-AID**, and **p-AID** on UV-Ozone cleaned bare n-type Si wafers with 300 nm SiO_2 at 1000 RPM for 1 minute. The as-cast samples were measured directly and the annealed samples were thermally treated (100 °C for **ID-C** and **p-AID**; 170 °C for **o-AID**) before the measurements.
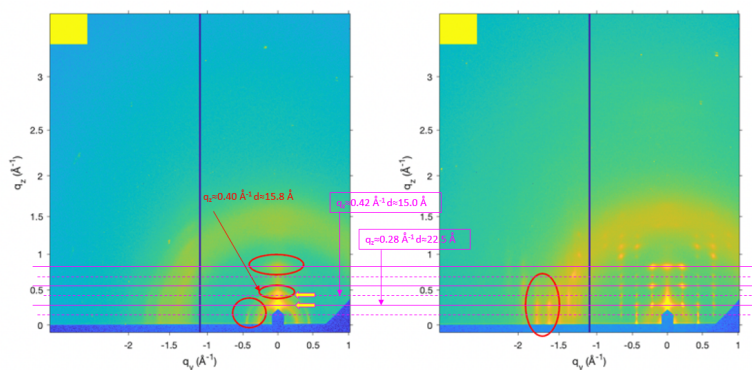
Figure 4.13. Comparison of as-cast and annealed o-AID with discussed peaks marked.
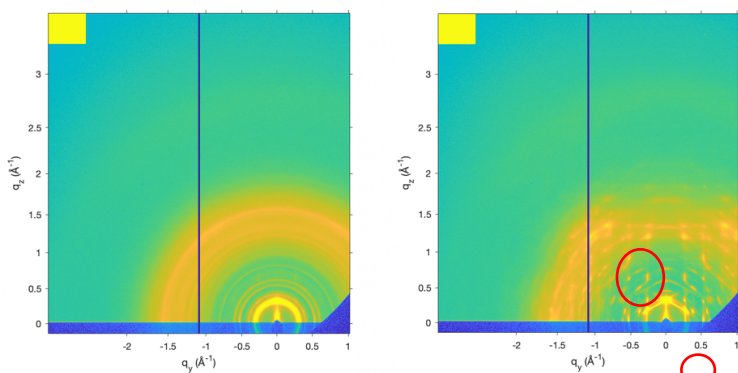
Figure 4.14. Comparison of as-cast and annealed p-AID with discussed peaks marked

For **o-AID** without annealing, narrower textured lamellar stacking primarily in the out-of-plane direction was shown at two different q values corresponding to d-spacings of about 22.5 and 15.0 Å that match closely with q-values of reflections in the crystalline phase apparent with annealing (**Figure 4.13**). In addition, the distinct in-plane peaks with annealing denoted π-π distances of 3.51Å – 3.85 Å and in-plane lamellar packing peaks suggest edge-on packing. For **p-AID**, distinct lamellar peaks at corresponding to a d-spacing of 18.9 Å indicate packing oriented in the (210), corresponding to the pi-pi stacking peak (**Figure 4.14**). The diffraction pattern of **o-**

AID is characteristic of brick-like stacking while for **p-AID,** the less predominant out-of-plane lamellar stacking and diagonal peaks suggest herringbone stacking.

Atomic Force Microscopy (AFM) was performed on a Multimode 8 system (Bruker, Santa Barbara, CA) in PeakForce Tapping® Mode with ScanAsyst® image optimization software and a ScanAsyst® -Air probe (silicon tip on nitride cantilever, cantilever tip = 650 nm, length = 115 μm, width = 25 μm, frequency = 70 kHz, (spring constant) k = 0.4 N/m, Bruker) at a rate of 0.99 kHz/min. with 512 scans per image. AFM images were analyzed using the Nanoscope Analysis software (Bruker) to obtain the height of the nanostructures, and the average heights and lengths were measured by averaging 5-10 bottlebrush polymers. Dilute polymer solution and nanoparticle solutions (stock solution 700 μg/mL, pipetted 20 μL of stock solution onto substrate for a final concentration of ~14 μg of bottlebrush polymers) were drop-casted onto freshly cleaved mica and HOPG substrates and allowed to dry overnight under ambient conditions prior to imaging.
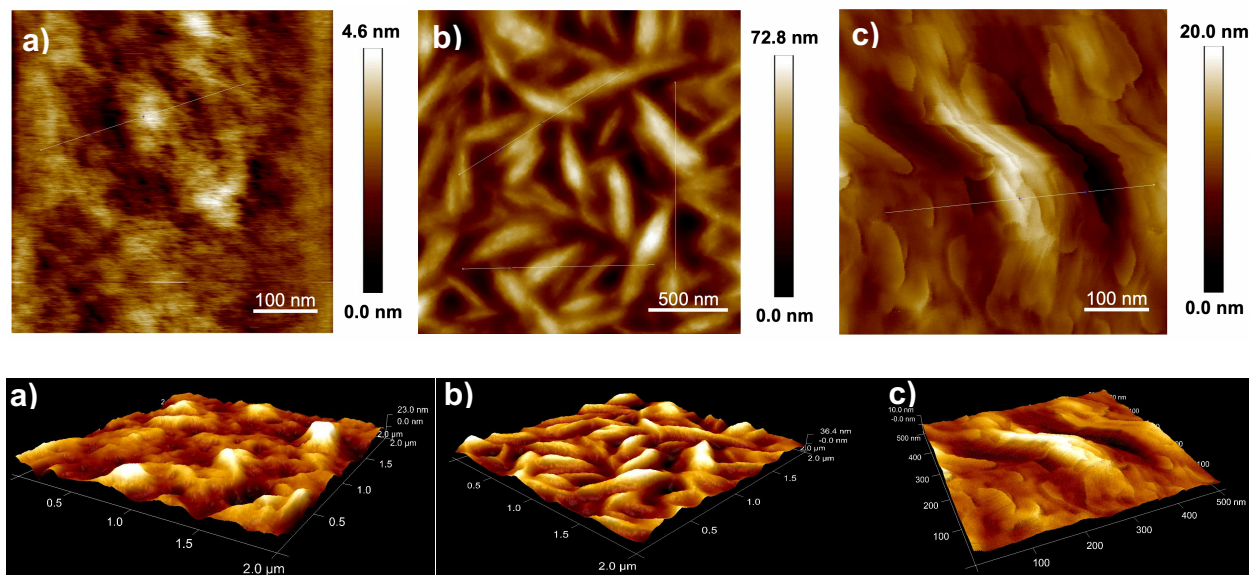
Figure 4.15. Atomic force microscopy images of (a) ID-C (b) *o*-AID on SiO₂/Si substrates and (c) *p*-AID on OTS treated SiO₂/Si substrate. The thin-films of ID-C and *o*-AID were prepared by spincoating on SiO₂/Si substrates and the thin-film of *p*-AID was prepared by spincoating on an OTS-treated SiO₂/Si substrate at 1000 RPM for 60 seconds.

4.4.4 Organic Field Effect Transistors

Treatment of Substrates. Heavily doped *n*-type Si wafers with 300 nm SiO$_2$ were used as substrates for thin-film organic field effect transistors (OFET). The wafers were cleaned with piranha solution (H$_2$SO$_4$:H$_2$O$_2$=7:3), deionized water, isopropanol and blow-dried by nitrogen. After oxidation under ozone treatment, the silicon was either left bare or spin-coated with a solution of *n*-octadecyltrichlorosilane (OTS) in toluene. Finally, the substrates were washed with hexane, toluene, and isopropanol and blow-dried by nitrogen.

Fabrication and Measurement of Organic Field Effect Transistors. Organic field effect transistors were fabricated by spin-coating the organic materials ***o*-AID** and **ID-C** on bare SiO$_2$/Si and ***p*-AID** OTS-modified SiO$_2$/Si with a bottom-gate/top-contact architecture. Spin-coating was done at 1000 RPM for 60 seconds. Then 50 nm Au as source and drain electrodes were deposited on the film by physical vapor deposition and templated by shadow masks with defined channel lengths of 50 µm and widths of 10 mm. The OFET characteristics were recorded using Agilent B1500A in ambient conditions. The mobility was calculated by the formula: $I_D = W/2L\mu C_i(V_G - V_T)^2$ where I_{DS} is the drain-source current, W and L are the channel width and length, C_i is the dielectric capacitance, V_G is the gate voltage, and V_T is the threshold voltage.
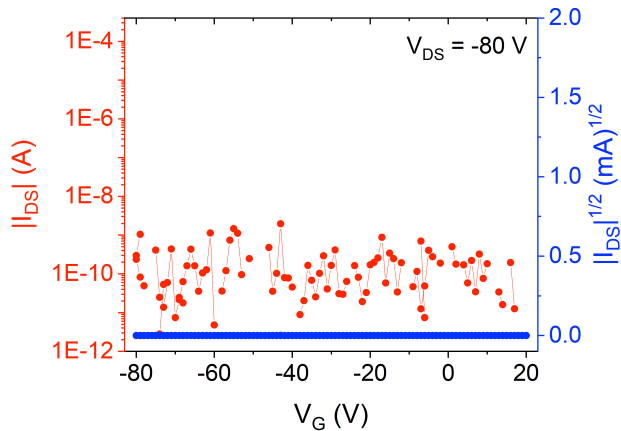
Figure 4.16. Transfer characteristics for ID-C at $V_{DS} = -80$ V (red) and the square root of drain current (blue).

Table 4.2. Performance for bottom-gate/top-contact p-Channel OFETs based on o-AID and p-AID. $\mu_{h,aver}$ taken over 12 devices, respectively.

Compound	$\mu_{h,aver}$, cm^2 V^{-1} s^{-1}	$\mu_{h,max}$, cm^2 V^{-1} s^{-1}	$I_{on/off}$	V_T, V
o-AID	$4.25 \times 10^{-4} \pm 1.64 \times 10^{-4}$	5.37×10^{-4}	$\sim 10^1$	-9.64 ± 5.68
p-AID	0.187 ± 0.0833	0.270	$\sim 10^5$	-12.5 ± 4.32

4.4.5 NMR Spectra
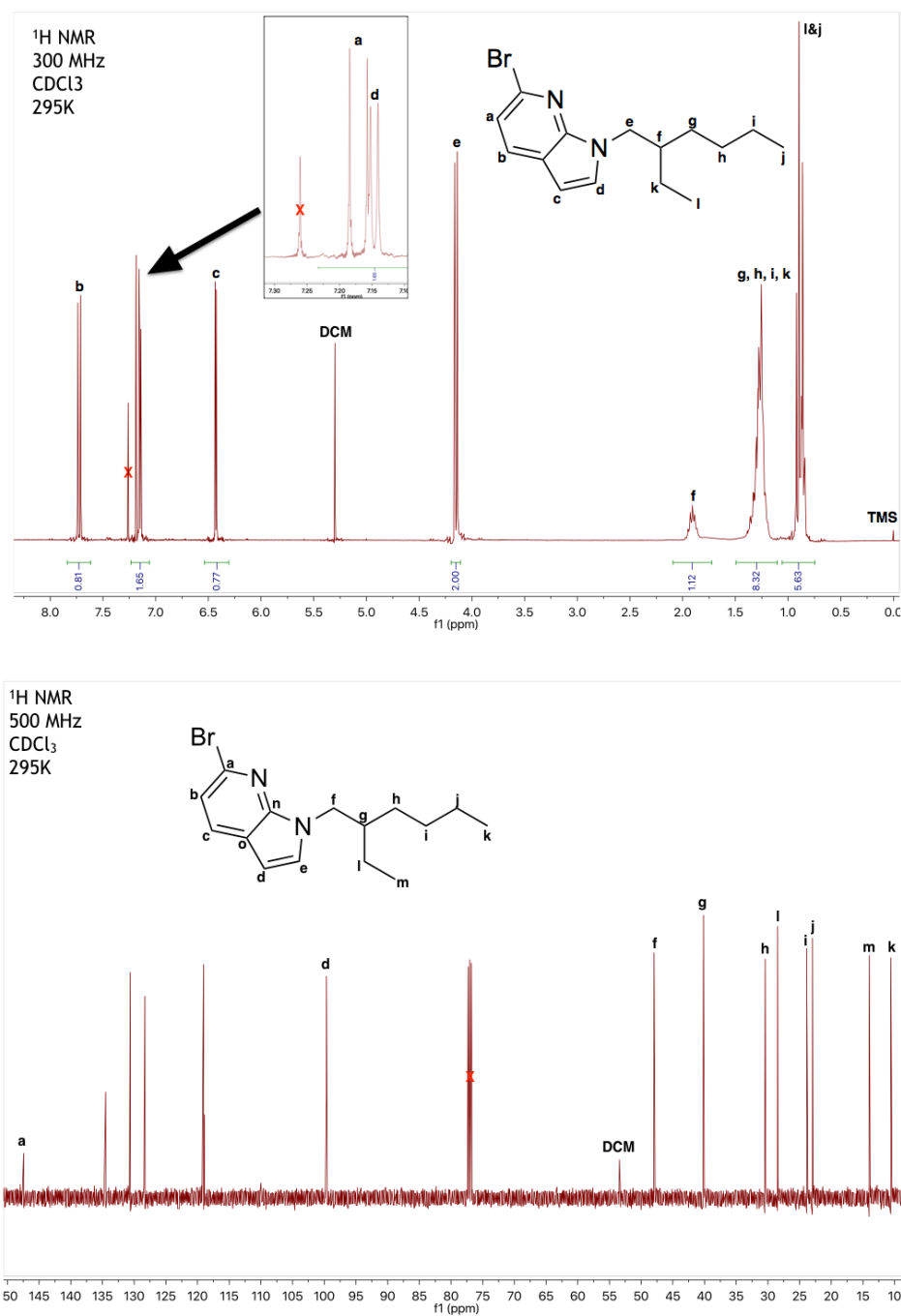
Figure 4.17. ¹H (300 MHz) and ¹³C{¹H} (125 MHz) NMR of 6-bromo-1-(2-ethylhexyl)-1H-pyrrolo[2,3-*b*]pyridine in CDCl₃ at room temperature.
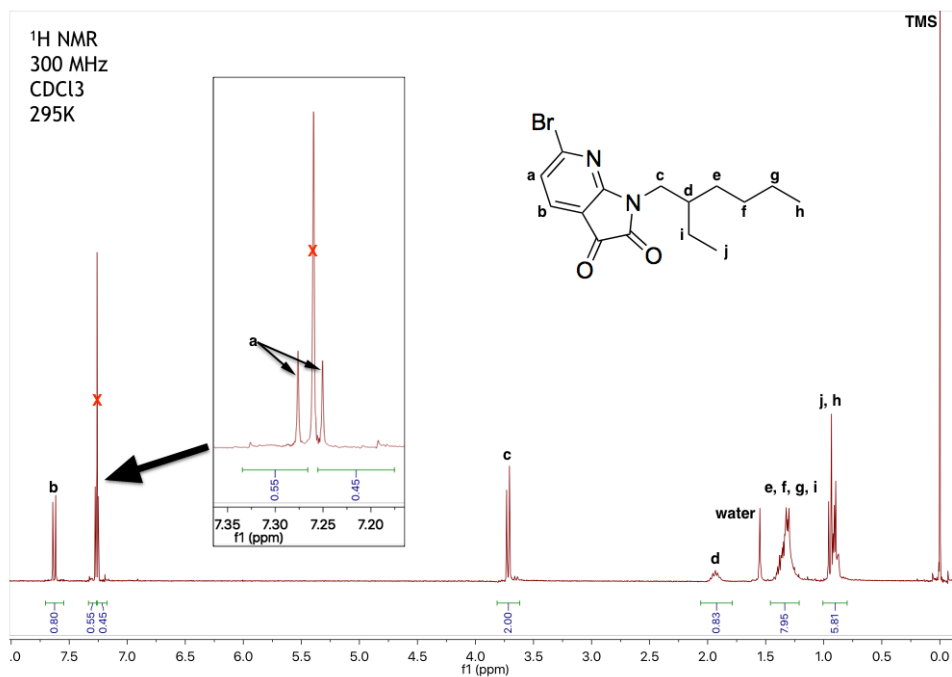
Figure 4.18. ^{1}H (300 MHz) NMR of 6-bromo-1-(2-ethylhexyl)-1H-pyrrolo[2,3-*b*]pyridine-2,3-dione in CDCl$_3$ at room temperature.
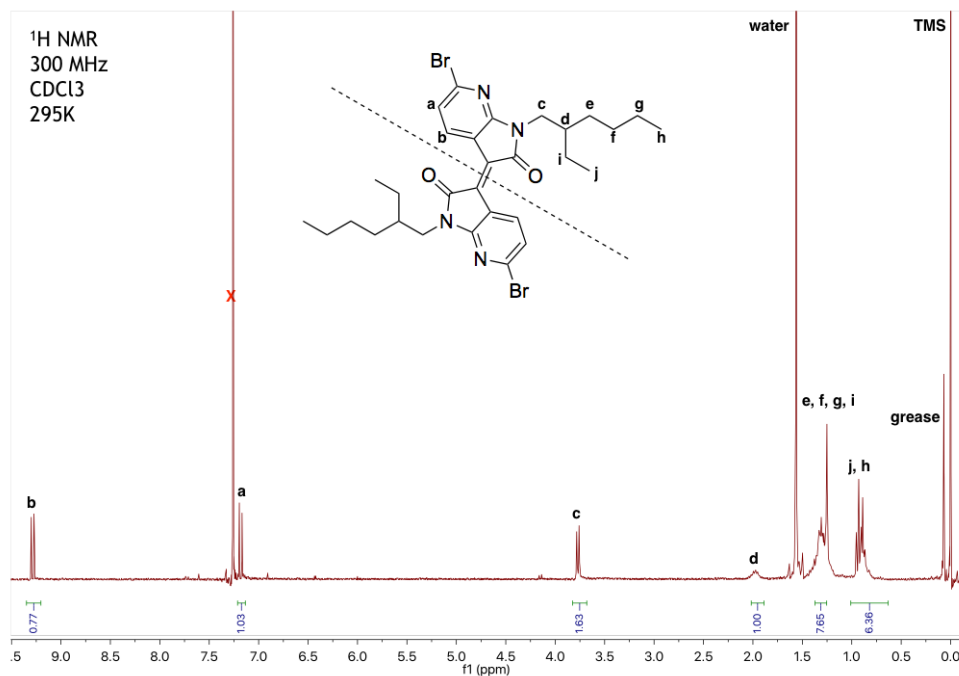
Figure 4.19. ^{1}H (300 MHz) NMR of N,N'-Bis(2-ethylhexyl)-6,6'-dibromo-7,7'-diazaisoindigo in CDCl$_3$ at room temperature.
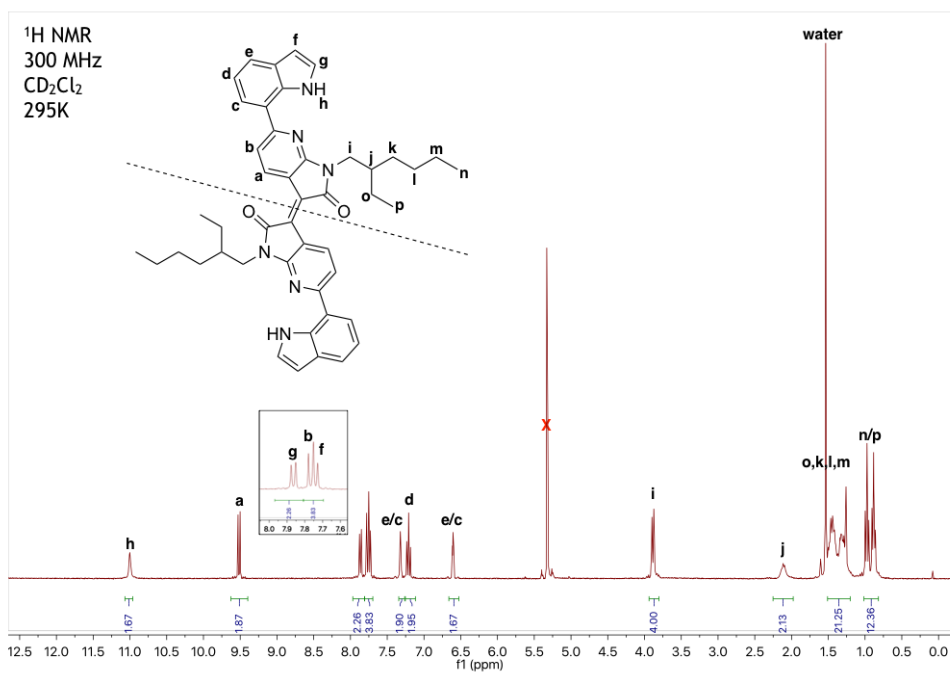
Figure 4.20. ^{1}H (300 MHz) NMR of EH-*o*-AID in CD$_2$Cl$_2$ at room temperature.
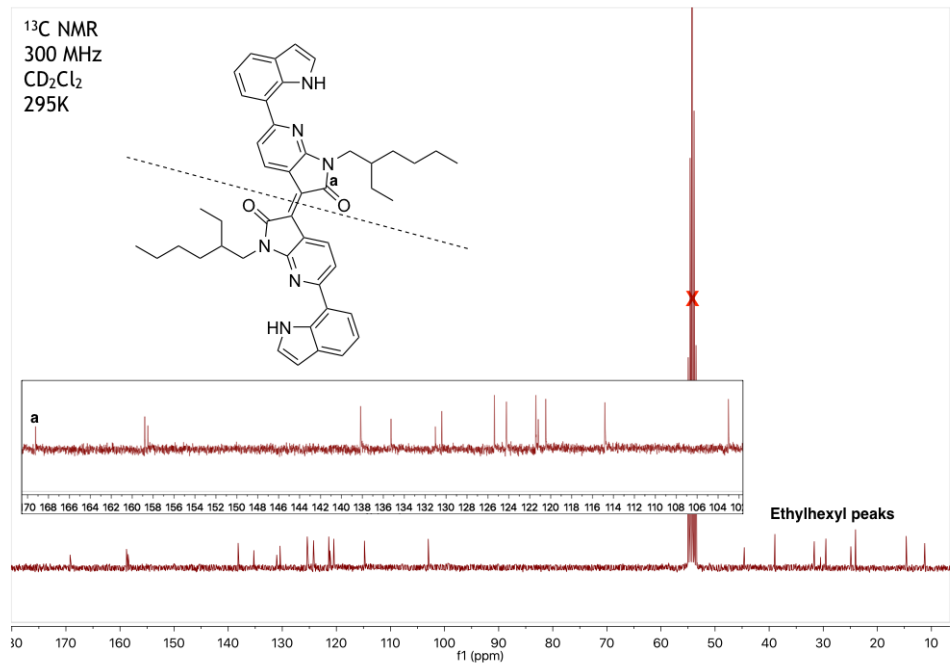
Figure 4.21. ^{13}C{^{1}H} (75 MHz) NMR of EH-*o*-AID in CD$_2$Cl$_2$ at room temperature.
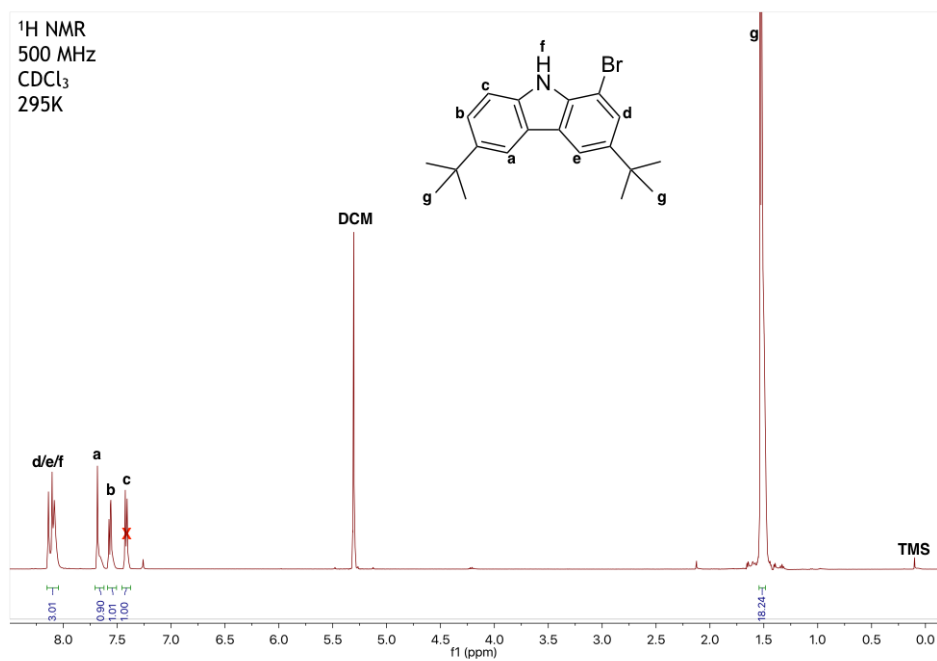
Figure 4.22 ¹H (500 MHz) NMR of 1-bromo-3,6-di-tert-butyl-9H-carbazole in CDCl₃ at room temperature.
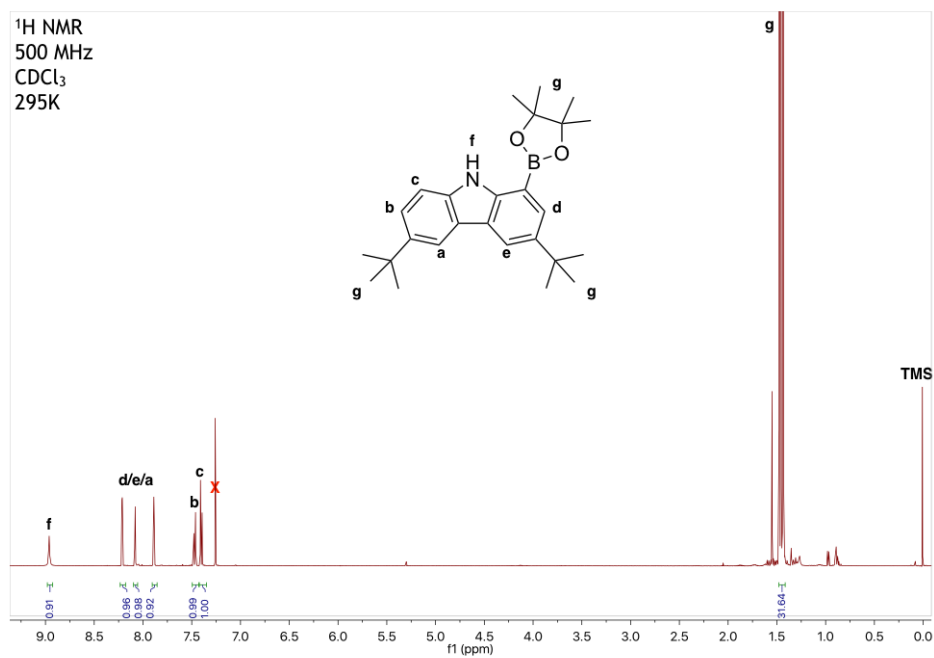
Figure 4.23. ¹H (500 MHz) NMR of 1-bromo-3,6-di-tert-butyl-9H-carbazole in CDCl₃ at room temperature.
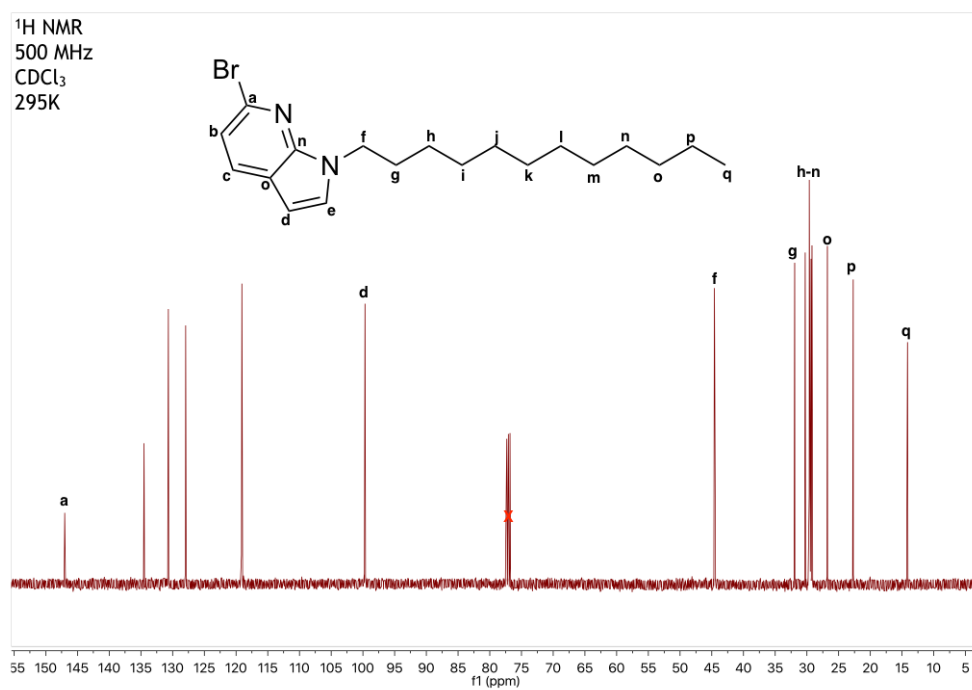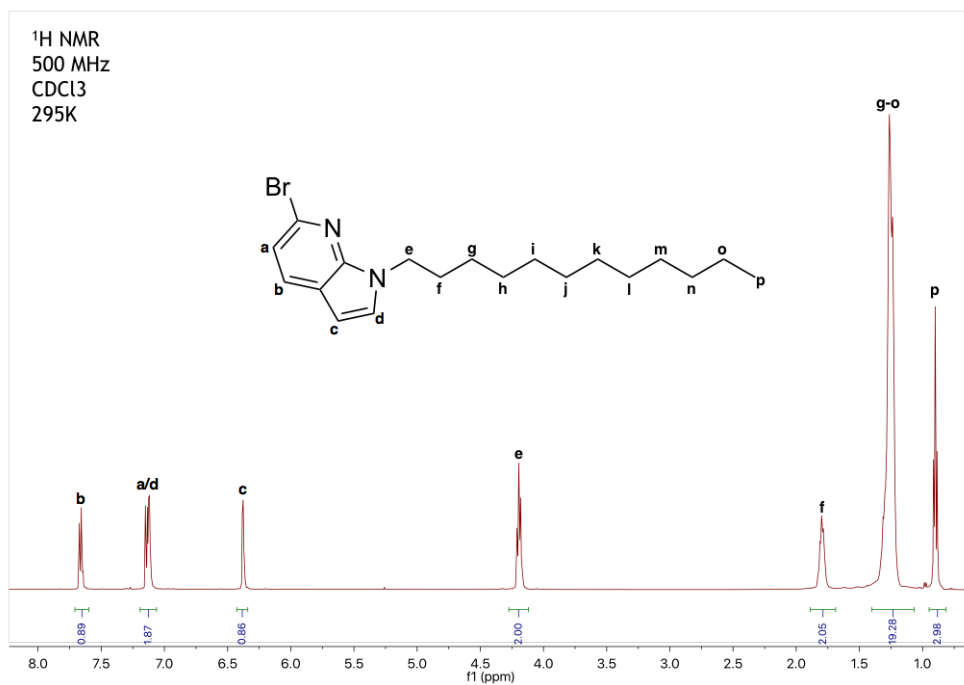
Figure 4.24. ^{1}H (500 MHz) and ^{13}C{^{1}H} (125 MHz) NMR of 6-bromo-1-dodecyl-1H-pyrrolo[2,3-b]pyridine in CDCl$_3$ at room temperature.
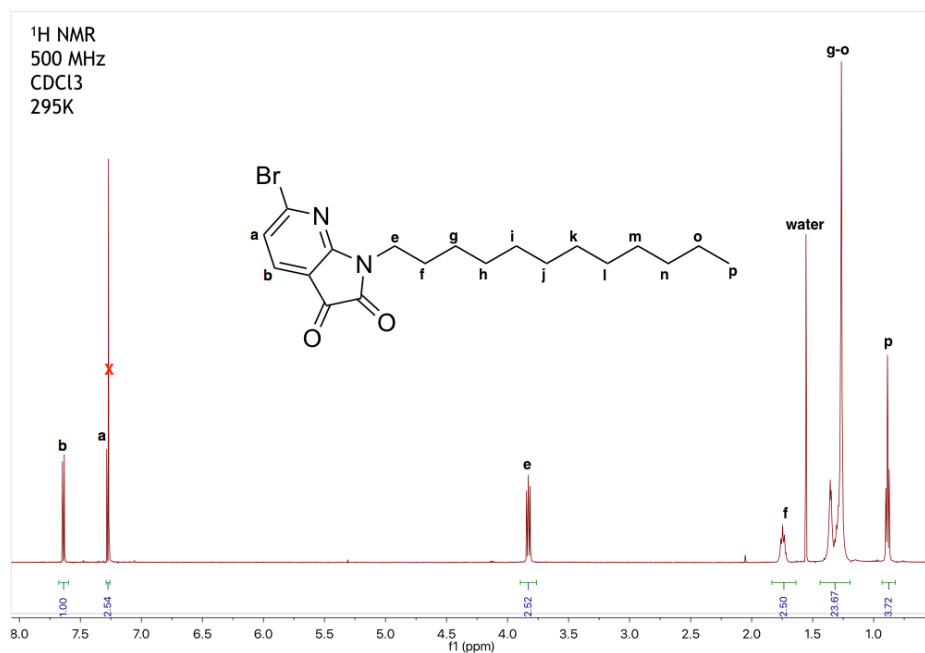
Figure 4.25. [1]H (500 MHz) of 6-bromo-1-dodecyl-1H-pyrrolo[2,3-b]pyridine-2,3-dione in CDCl₃ at room temperature.
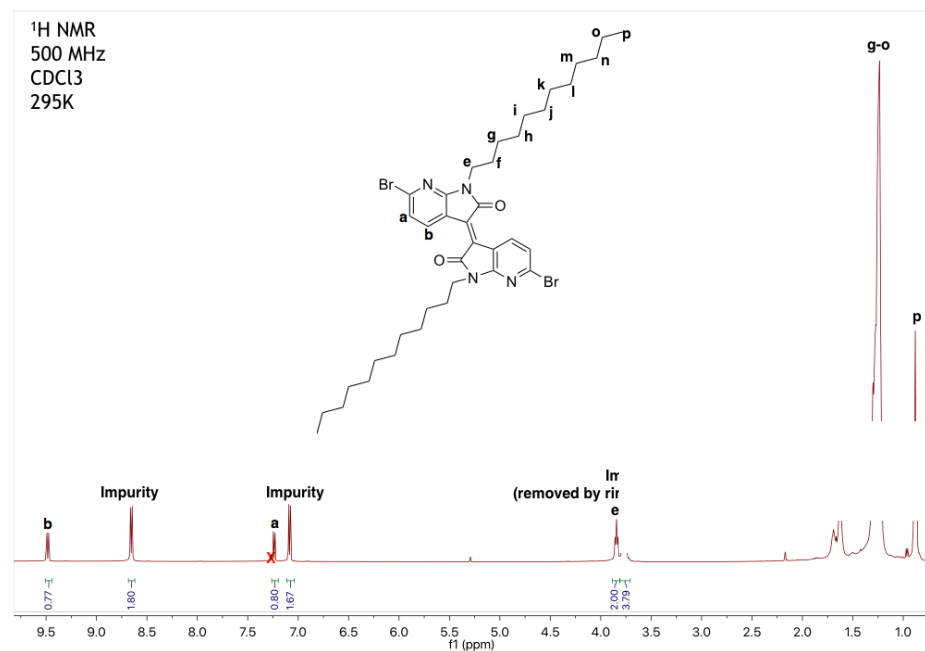
Figure 4.26. ^{1}H (500 MHz) NMR of N,N'-Bis(dodecyl)-6,6'-dibromo-7,7'-diazaisoindigo in CDCl₃ at room temperature.
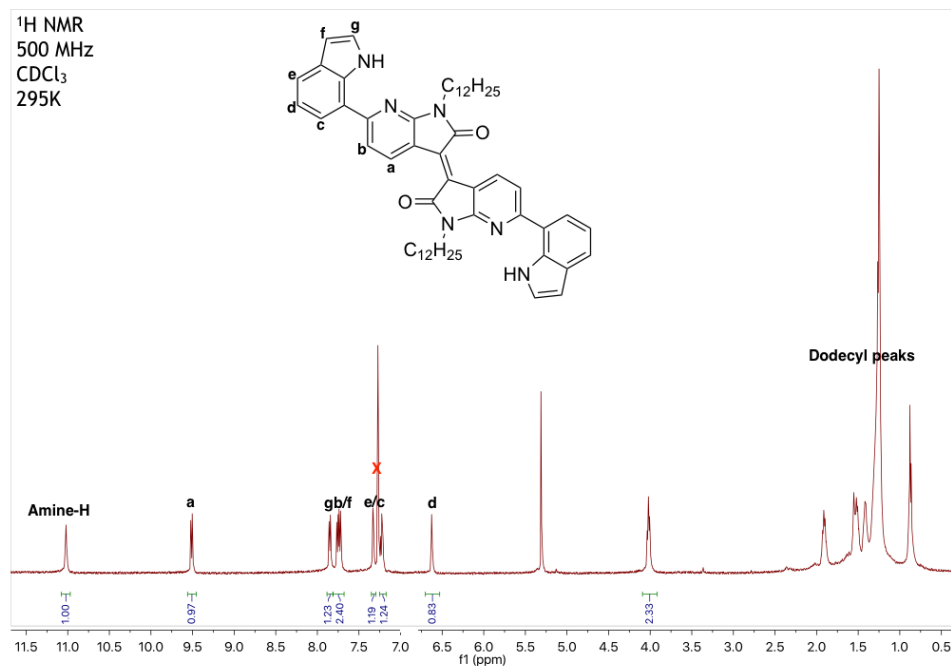
Figure 4.27. ^{1}H (500 MHz) NMR of C$_{12}$-*o*-AID in CDCl$_3$ at room temperature.
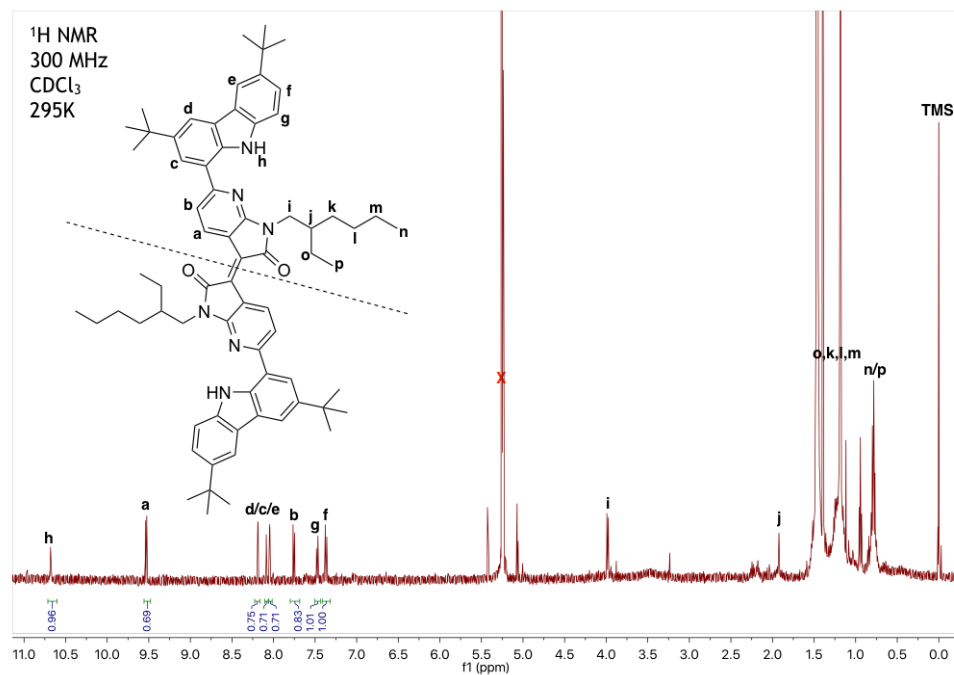
Figure 4.28. ^{1}H (500 MHz) NMR of EH-Carb-*o*-AID in CDCl$_3$ at room temperature.
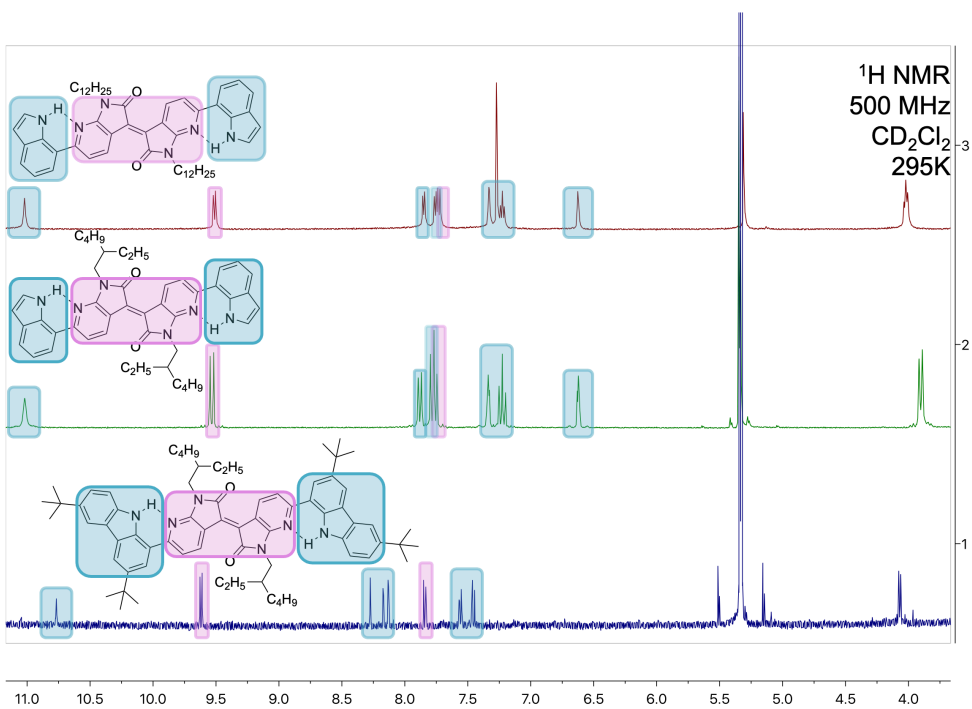
Figure 4.29. ^1H (500 MHz) NMR comparison of C$_{12}$-o-AID, EH-o-AID, and EH-Carb-o-AID at room temperature, respectively. Structures and peaks are marked with (pink) core-diazaisoindigo proton shifts and (blue) indole proton shifts.

CHAPTER V

TOWARD THE SYNTHESIS OF LADDER-TYPE POLYMERS FEATURING

INTRAMOLECULAR NONCOVALENT BONDS

5.1 Introduction

5.1.1 Hydrogen Bond Conformationally Controlled Polymers

Intramolecular hydrogen bonds are ubiquitous in biomacromolecules and prevalent in non-π-conjugated synthetic polymers. With the goal of imitating these large conformationally controlled structures, the aim is to develop π-conjugated polymers with ubiquitous hydrogen bonding across the conjugated backbone, leading to previously undiscovered properties. In the past decade, only a handful of H-bond conformationally locked π-conjugated polymers have been reported, most of which lacked reports of semiconducting capabilities.[51, 52, 178, 179] In the few examples that demonstrate promising semiconductor abilities, many contain rotationally uninhibited single-bonds because H-bonding did not occur across the entire backbone, resulting in pseudo-ladder-type structures.[41, 45, 47, 49] In the remaining examples based on benzodifurandione-based oligo(*p*-phenylene vinylene), conformational rigidity and coplanarity is also granted by the connecting carbon-carbon double bonds, complicating investigations into the H-bond effects.[39, 180-182] Because no examples of π-conjugated polymers have achieved these criteria, we aim to achieve the synthesis of π-conjugated polymers that (i) are entirely ladder-type polymers by global H-bond conformational locks, (ii) have H-bonding effects that can be easily elucidated using theoretical and experimental means, and (iii) demonstrate promising performances in semiconductor applications. On this front, the accumulated building blocks in this dissertation were expected to result in achieving this goal or discover further structure-property relationships to update molecular designs.

103

In addition to the **7DAIID** and **5DAIID** building blocks synthesized in the previous chapters, our group has also made use of a variety of other H-bond donor-/acceptor-equipped materials (**Scheme 5.1**). As used in the preceding B←N bridge containing work,[94] IDCZ-based donor-acceptor-type structures first exhibited promising semiconducting abilities after the improvement of solution processibility (detailed in **4.2.1**), leading to measurable electron mobilities in the magnitude of 10^{-4} cm^2 V^{-1} s^{-1}.
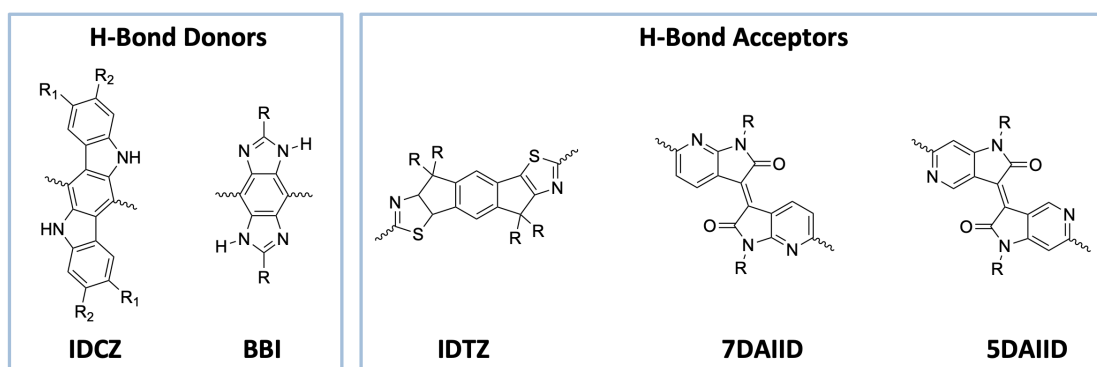
Scheme 5.1 Polymer building blocks: (left) H-Bond Donors and (right) H-Bond acceptors.

The indolocarbazole core was also expected to be an important building block for donor-acceptor polymers, even in the absence B←N-bridge installation, as a result of the already existent H-bond donor motif in a favorable geometric location for pairing with H-bond acceptor building blocks. Regarding these H-bond-acceptor building blocks, the recently developed *s*-indaceno[2,1-*d*:6,5-*d'*]bisthiazole (**IDTZ**) has exhibited especially notable ambipolar semiconductor performance when used as electron-rich building blocks in donor-acceptor polymers (ambipolar; $\mu_h = 0.87$ cm^2 V^{-1} s^{-1}; $\mu_e = 0.50$ cm^2 V^{-1} s^{-1}).[183] In collaboration with Dr. Maciej Barlog (Al-Hashimi Group; Texas A&M University at Qatar) the synthesis of IDTz was previously optimized during my summer internship (detailed in **5.4.2**), leading to efficient accumulation of this molecule. As a result, **IDCZ** and **IDTZ** have been used by Dr. Yirui Cao to extend the previous

IDCZ-based small molecules, demonstrating the synthesis of a 23-ring-fused molecule featuring four B←N coordinate bonds. The resulting compound was not only rigid and coplanar, but the presence of multiple B←N coordinate bonds was crucial in decreasing the LUMO energy levels (−3.82 eV), generating a novel strategy for imparting n-type characteristics on future organic electronics.[139]
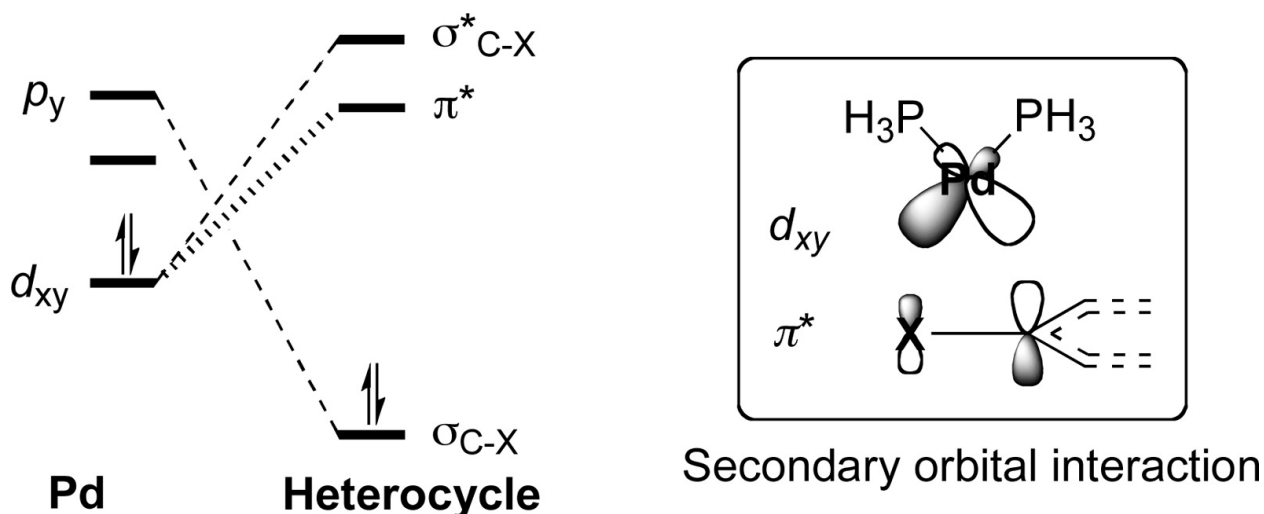
Figure 5.1. Major molecular orbital interactions of oxidative addition in Pd-catalyzed cross-coupling reactions. Adapted from *J. Am. Chem. Soc.* 2007, 129, 42, 12664–12665 with permission from the American Chemical Society.[184]

Furthermore, a persistent challenge faced in this work involved the HOMO-LUMO energy levels of the building blocks. In specific, palladium-catalyzed cross-coupling and coupling partner functionalization of multihalogenated heterocycles is heavily influenced by their frontier molecular orbital energies.[184] Explicitly, interaction between the heterocycle LUMO (π^*) and palladium catalyst HOMO demonstrates a correlation towards oxidative addition barriers. Moreover, stabilized p_y–$\sigma_{C\text{-}X}$ and d_{xy}–$\sigma^*_{C\text{-}X}$ interactions, as shown in **Figure 5.1**, must be present for oxidative additions. In light of this, many attempts at palladium-catalyzed cross-coupling were unsuccessful due to the unfavorable energy levels, i.e. decreased LUMO, of several building

blocks. Therefore, building blocks for cross-coupled must have suitable frontier molecular orbital levels in addition to the various criteria outlined in previous chapters.

	BBI	BBI-Boc2	Thiophene	Thiazole	Benzene	Pyrazine
LUMO (eV)	-0.57	-0.93	-0.42	-0.82	-0.22	-1.40
HOMO (eV)	-4.69	-4.99	-5.59	-6.01	-5.91	-5.93
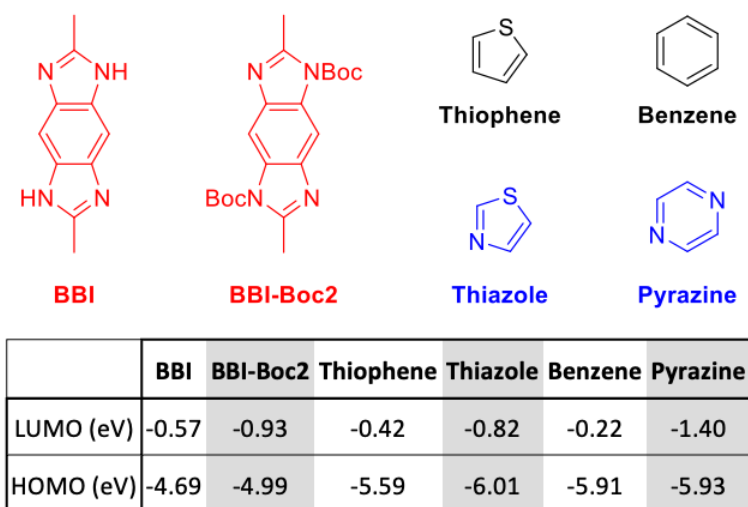
Figure 5.2. Frontier molecular orbital energies of BBI and BBI-Boc₂ in comparison to thiophene, benzene, thiazole, and pyrazine.

Regarding the aforementioned energy level requirement, Fang group member Octavio Miranda developed and optimized the synthesis for H-bond-donor benzobisimidazole (**BBI**), with consideration into the benchmarks outlined from previous H-bond donors. Based on DFT optimized structures of **BBI**, HOMO-LUMO energy levels were demonstrated to be similar to many other heteroarenes used for π-conjugated polymers. More importantly, thiophene, benzene, thiazole, and pyrazine have all demonstrated effective palladium-catalyzed cross-coupling reactions, indicating the advantages of BBI as an electron-rich cross-coupling partner (**Figure 5.2**).[185-187] Akin to the methods in Chapter II, preliminary DFT rotational scans were to verify the feasibility of the employment of **BBI** in high performing donor-acceptor π-conjugated materials. In cases of **BBI** coupled with H-bond acceptor-equipped pyridine, **IDTZ**, **5DAIID**, and **7DAID**, planarity index values ($\langle\cos^2\varphi\rangle$) were over 0.96 in all instances, indicating favorable H-bond strengths and geometries. With the collection of building blocks containing H-bonding motifs

(**Scheme 5.1**), the work in this chapter focuses on the feasibility of synthesizing hydrogen-bond-bridged polymers. Preliminary experiments demonstrate numerous synthetic hurdles, leading to clear polymeric design principles for perspective work.

5.1.2 Dynamic Bonds Beyond Hydrogen Bonds for Polymers

Electron-deficient molecules hold great promise as n-type semiconductors in organic electronics and non-fullerene electron acceptors in organic photovoltaics.[134, 188-192] B←N dative bonding as the noncovalent bridging has recently emerged as an promising strategy for tuning molecular orbital levels, transforming previously insulating compounds into semiconducting materials.[94, 139] Our group's B←N post-functionalization strategy represents an intriguing synthetic method for these emerging materials (**Figure 5.3**). Specifically, in pre-organized N–H···N hydrogen bond bridges in our present work, the substitution of the N–H covalent bond with a N–B covalent bond demonstrates the synthetic versatility of these pre-installed sites. This represents a powerful strategy for the tuning of electronic structures, optical properties, and chemical stabilities.[193-198]
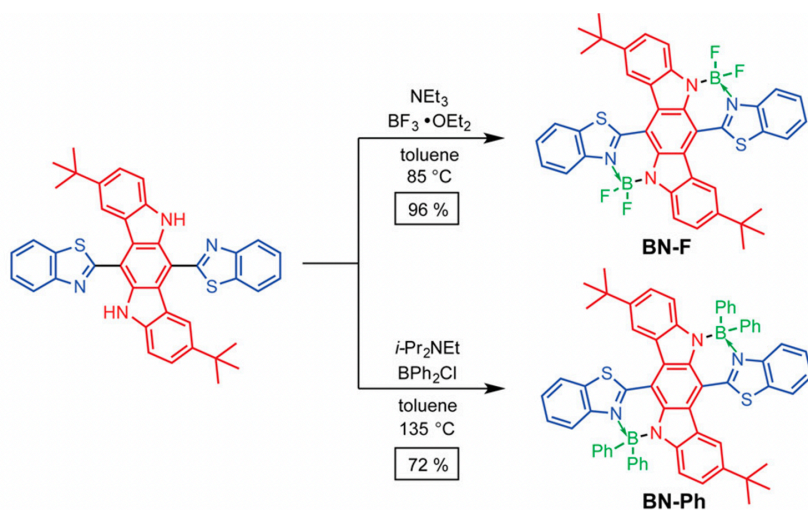
Figure 5.3. Synthesis of BN-Ph and BN-F through facile boron-installation strategy. Adapted from *J. Am. Chem. Soc.* 2018, 140, 51, 18173–18182 with permission from American Chemical Society.

In previous reports, decreases in LUMO energy levels were observed, while impacting HOMO energy levels to a lesser degree.[21, 139, 195] The resulting decreased bandgap promoted intermolecualr electron transfer[199] Furthermore, reported binding strengths of the B←N coordination are over three times that of H-bonding strengths. [200, 201] Therefore, this is expected to lead to enhanced rigidity and coplanarity even in comparison to the previous H-bond method.
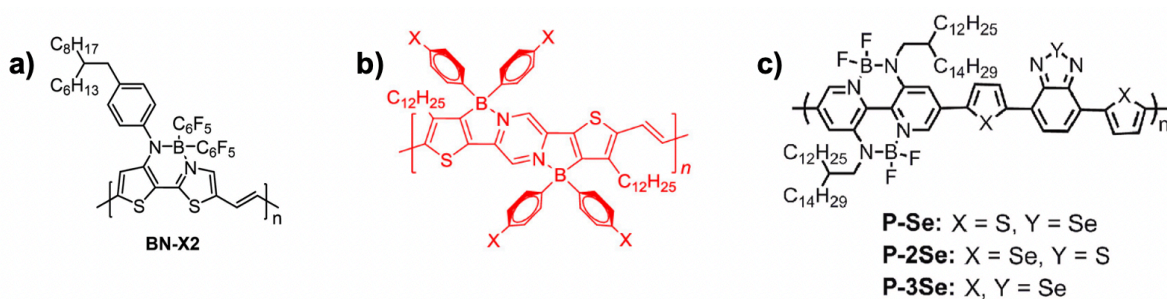
Figure 5.4. Examples of B←N bridging in π-conjugated pseudo-ladder polymers.[202-204]

As most of the reported B←N-bridged π-conjugated materials are small molecules, π-conjugated polymers exploiting these strategies are few and far between. Characteristic examples are shown in **Figure 5.4**, demonstrating the use of promising B←N coordination containing building blocks for polymer applications.[202-204] In fact, promising all-polymer solar cell performance has been demonstrated by these polymers, using them as the n-type semiconductors for efficient electron mobility (**Figure 5.4b,c**). Based on these results and similar to our goals for H-bonding, we aim to move beyond pseudo-ladder π-conjugated polymers to form fully ladder-type structures by incorporating B←N coordination bridges to conformationally lock the polymers.

5.2 Results and Discussion

5.2.1 Preliminary Attempts at H-Bond Polymer Synthesis

The starting materials outlined in **Figure 5.5** were all accumulated through optimized procedures or provided by group members for these polymerization investigations. Firstly, futile efforts were made to prepare **IDCZ** as a palladium-catalyzed coupling partner. In specific, Miyaura borylation was attempted by using palladium catalyst Pd(dppf)Cl$_2$ in the presence of bis(pinacolato)diboron as the borane reagent, and KOAc as the base in dioxane. Due to these results, it was suspected that **IDCZ** possessed unfavorable energy levels for Miyaura borylation or subsequent Suzuki cross-coupling reactions. In fact, the low frontier molecular orbital levels and electron deficiencies of **IDCZ**-based compounds are well documented.[205, 206] In this regard, palladium catalyst systems containing CyJohnPhos have recently demonstrated highly efficacious Miyaura borylation results for electron-poor substrates.[207] Consequently, CyJohnPhos was used as the catalyst ligand with Pd$_2$(dba)$_3$ as the palladium precatalyst, with pinacolborane (HBpin) as the borane reagent instead.
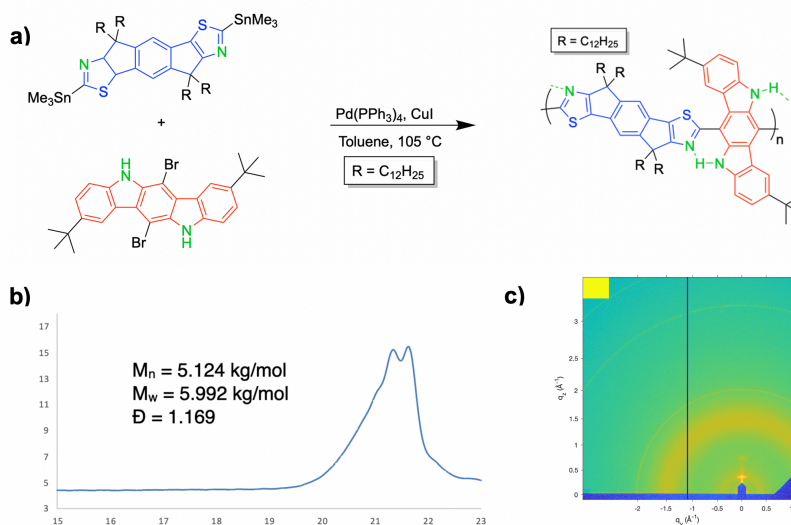
Figure 5.5. Copolymerization between IDCZ and IDTZ: (a) Synthetic scheme, (b) SEC trace and (c) GIWAXS diffraction pattern of oligomer thin-film.

Despite further attempts at optimization, the functionalization of **IDCZ** with boronic acid esters proved to be a major synthetic hurdle. In subsequent studies, the installation of Stille coupling motifs was also investigated through the stannylation of **IDCZ**. Similar to the Miyaura borylation, the palladium-catalyzed stannylation using hexamethylditin as the tin reagent and Pd(PPh$_3$)$_4$ as the catalyst was unsuccessful. Furthermore, lithiation-based stannylation using LDA or *n*BuLi were also unsuccessful. In fact, these methods were also tested on other building blocks from **Scheme 5.1**, namely, **7DAIID** and **5DAIID**, yielding little to no promise. These results are consistent with the hypothesis that this type of functionalization on electron-poor substrates remains a challenging synthetic hurdle.

Following these attempts, stannylated **IDTZ** was synthesized in collaboration with the Al-Hashimi Group, allowing subsequent attempts to copolymerize **IDTZ** with **IDCZ** through Stille coupling reactions. This was carried out using the optimized Stille coupling conditions of Pd(PPh$_3$)$_4$/CuI/toluene system as shown in **Figure 5.5a**. The Pd$_2$(dba)$_3$/P(*o*-tol)$_3$/toluene system also yielded successful cross-coupling. In the optimization process, different ratios of **IDCZ** and **IDTZ** were utilized to account for possible difficult to remove impurities in the building block materials. A 5% increase of **IDCZ** with respect to **IDTZ** demonstrating the most promising results. Further, the Stille polymerization was expected to result in higher molecular weight polymers than Suzuki polycondensation due to the known deboronation during Suzuki reactions.[208] Furthermore, the Suzuki-Miyaura polycondensations usually require basic conditions in a two-phase system, rapidly decreasing polymer solubility as molecular weight increases and leading to low molecular weights.[209] As the molecular weight of the repeating unit is roughly 1.31 kDa even after optimized Stille polymerization conditions **Figure 5.5b**, it was hypothesized that low frontier molecular

orbital energies of the dihalogenated **IDCZ** led to unfavorable oxidative addition during palladium-catalyzed reactions, similar to the previously discussed attempts at stannylation or boronic acid ester installation.

Several notable donor-acceptor-donor molecules were also analyzed at the [B3LYP/6-31g(d,p)] level of theory and notable optimized structures are shown in **Figure 5.6**. In comparison to non-H-bond-containing **IDCZ-IID-IDCZ**, with dihedral angles of 56°, intramolecular H-bonding demonstrates a dihedral angle minimization effect for **IDCZ-5DAIID-IDCZ** and **IDCZ-7DAIID-IDCZ**, with dihedral angles of 28° and 32° respectively (**Figure 5.6b-d)**. Despite this, all **IDCZ**-derived molecules, including **IDCZ-IDTZ-IDCZ** (**Figure 5.6a**), adopted twisted conformations with non-zero dihedral angles due to the steric hindrance of the benzylic C-H ring with the central ring systems. To corroborate this investigation, oligomers of **IDCZ-IDTZ** were analyzed by GIWAXS to determine the effects of intramolecular H-bonding on molecular conformation. A highly amorphous thin-film was demonstrated by the isotropic GIWAXS diffraction pattern in **Figure 5.5c**, which was indicative of poor oligomeric packing behavior. Consistent with the DFT results, poor packing was presumably due to the twisted conformation between **IDCZ** and **IDTZ** units exacerbated by steric interactions between the building blocks. From this building block system, numerous challenges in using **IDCZ** as a donor-acceptor π-conjugated molecular building block are as follows: (i) undesirably low frontier molecular orbital energies prevent the installation of active sites for palladium-catalyzed cross-coupling, and (ii) high steric hindrances caused by the benzylic C-H bulk which prevents the coplanarization of the polymeric backbone.
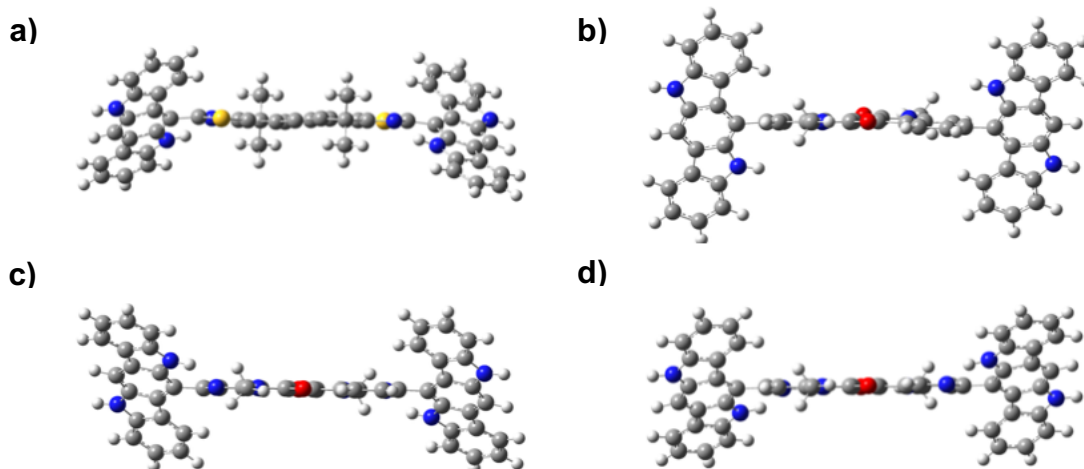
Figure 5.6 IDCZ-based donor-acceptor-donor small molecules calculated by DFT: Side views of (a) IDCZ-IDTZ-IDCZ, (b) IDCZ-IID-IDCZ, (c) IDCZ-5DAIID-IDCZ and (d) IDCZ-7DAIID-IDCZ.

As a solution to these problems, polymeric investigation was done in tandem with Fang group member Octavio Miranda (**Scheme 5.2**). First, as seen in **Figure 5.2**, **BBI** exhibited favorable frontier molecular orbital energies, like thiophene, for effective installation of palladium-catalyzed cross-coupling active sites. Secondly, less steric hindrance was expected for the resulting polymer backbones in cross-coupling, as evidenced by the $\langle \cos^2\varphi \rangle > 0.96$ values determined by DFT rotational scans, indicating extensive coplanar conformations. Regarding the aforementioned **IDCZ**, these properties were hypothesized to overcome the previous hurdles.
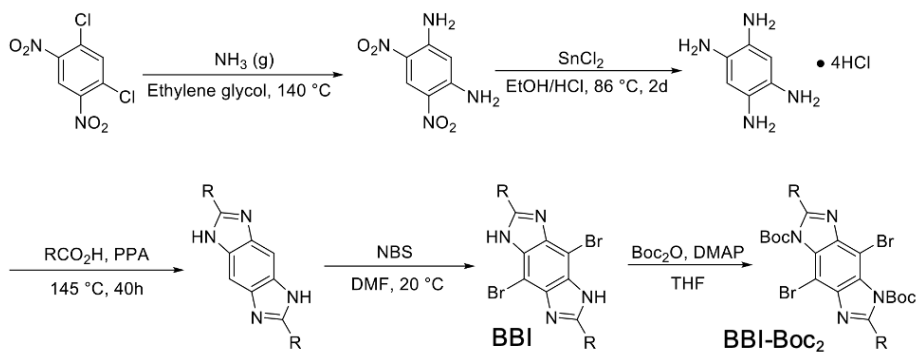
Scheme 5.2. Synthesis of BBI developed and optimized by Octavio Miranda.
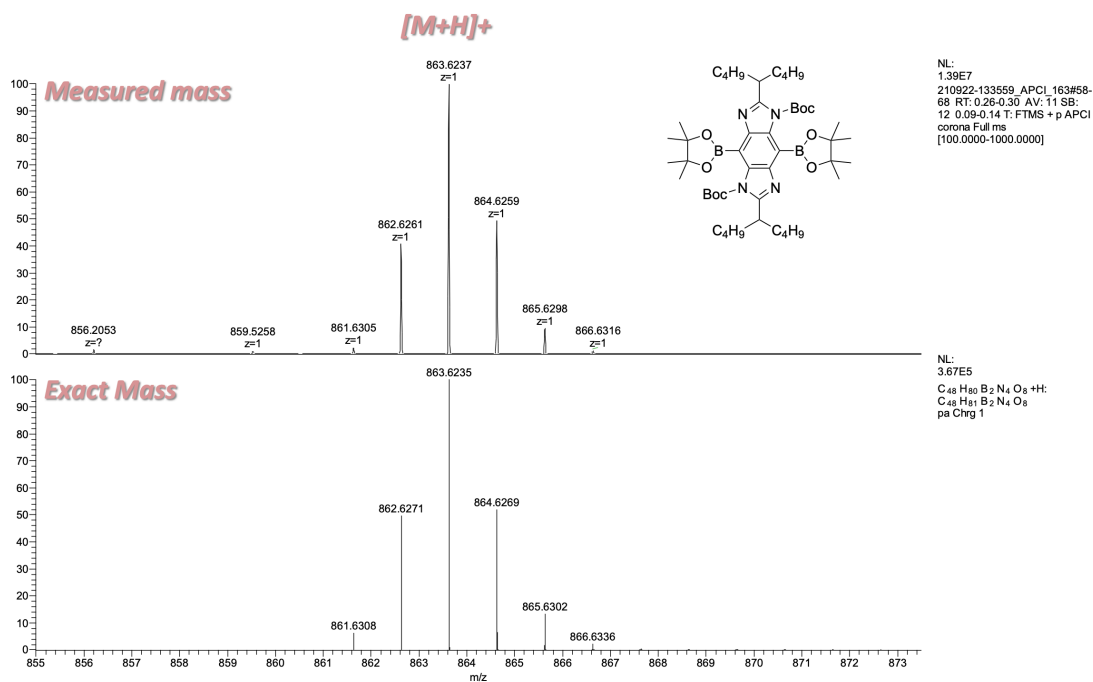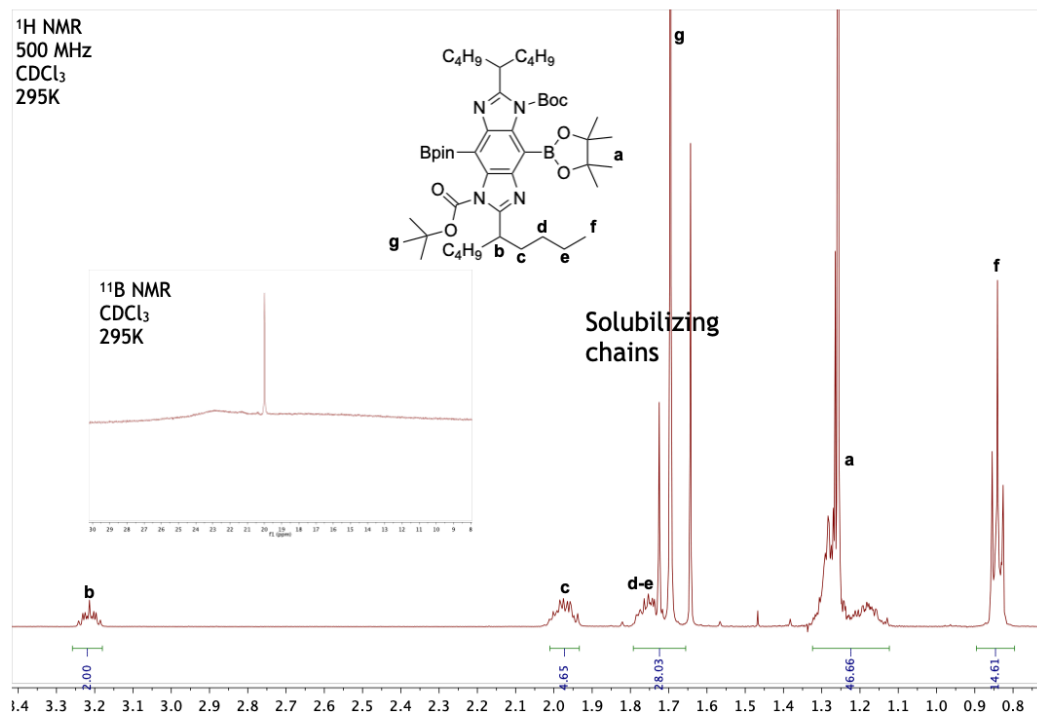
Figure 5.7. ^1H (500 MHz)/$^{11}B\{^1H\}$ (160 MHz) NMR (CDCl$_3$; RT) and APCI mass spectrum of **IN-BBI-Boc$_2$**.
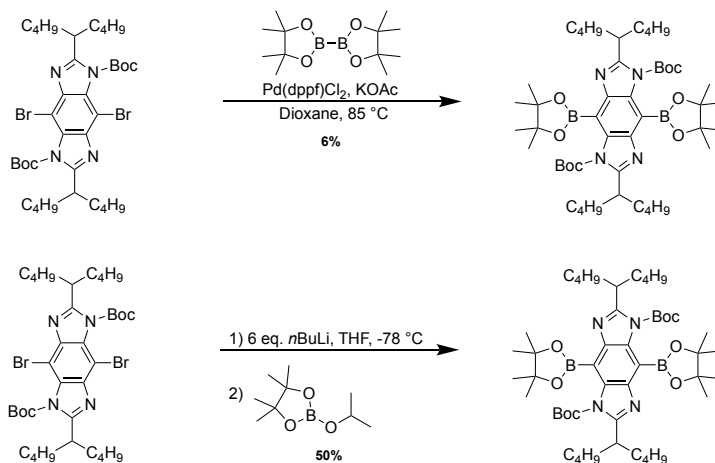
Scheme 5.3. Bpin installation of IN-BBI-Boc₂ to form IN-BBI-Boc₂-B₂pin₂.

With **BBI** starting material consisting of isononyl solubilizing chains **IN-BBI-Boc₂** provided by Octavio Miranda, success was first achieved on synthesizing **IN-BBI-Boc₂-(Bpin)₂** through the installation of boronic acid esters by two different methods (**Scheme 2.1**). Following the synthesis facilitated by Miyaura borylation, yields were unfavorably low. Out of various palladium-catalyzed reactions to either stannylate or borylate **IN-BBI-Boc₂**, the low temperature lithiation reaction offered the highest yield of 50%. During this reaction, it was determined that an excess of *n*-BuLi had to be added to ensure full conversion of starting material. Furthermore, trials on the non-Boc-protected **IN-BBI** were unsuccessful, likely due to the exposed N-H hydrogens, which disrupted the lithiation process.
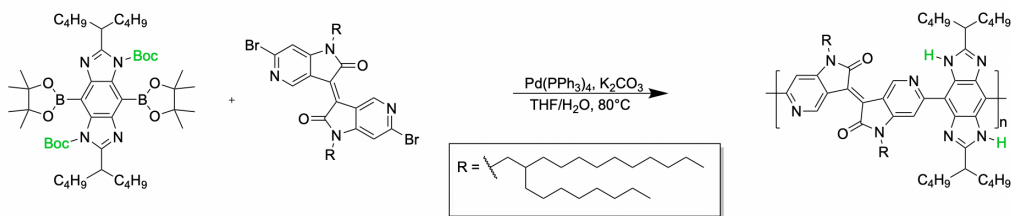
Scheme 5.4. Suzuki polymerization of IN-BBI-Boc₂ and 5DAIID.

The enhanced solubility of **IN-BBI-Boc₂** due to the solubilizing Boc groups and their H-bond masking was important for the eventual processing of the resulting polymer. Despite this, the Suzuki polymerization of **IN-BBI-Boc₂** yielded insoluble solids (**Scheme 5.4**). As evidenced in DFT calculations from Chapter II, the transition state activation energy of thermal Boc cleavage was theoretically stabilized by the neighboring pyridinyl unit due to intramolecular electrostatic interactions (**Figure 2.14**). This mechanism greatly accelerates the deprotection process, leading to a significantly lower thermal cleavage temperature of Boc (**Figure 2.15**). Therefore, the cause of the insoluble solids during Suzuki polymerization was expected to be due to the thermal cleavage of Boc groups, facilitated by the pyridinyl units of **5DAIID**. The unmasked H-bonding and absence of Boc solubilizing enhancement led to the insolubility of the polymer, further evidenced by the absence of starting materials in solution-state characterization data. To circumvent this emerging challenge, one method would be to install bulkier side chains to further enhance polymer solubility, either installed on the **BBI** or the **DAIID** backbones. Further, different reaction conditions that minimize Boc cleavage, either by avoiding harsh reagents, or through lower temperature Suzuki coupling conditions. For example, effective room-temperature Suzuki-Miyaura coupling reactions have been demonstrated in recent literature.[210-213]

5.2.2 Preliminary Results for B←N-bridging Ladder-Type Compounds

In moving towards stronger B←N dative bonds in place of H-bond interactions for π-conjugated molecules and polymers, the post-functionalization method outlined by our group's previous work was used (**Scheme 5.5**). Initial attempts were performed on the aforementioned small molecules of previous chapters in order to establish synthetic feasibility for lengthy

polymers. First, this post-functionalization method was attempted on **EH-*o*-AID** in which no reaction was observed. In order to screen possible synthetic hurdles, **EH-Carb-*o*-AID** was also used. Furthermore, triethylamine was replaced with stronger bases, 1,8-Diazabicyclo[5.4.0]undec-7-ene (DBU), lithium bis(trimethylsilyl)amide, and sodium bis(trimethylsilyl)amide. Additionally, the reaction mixture was heated to 120 °C in a pressure tube. Despite these efforts, no conversion was observed with ***o*-AID**-based structures.
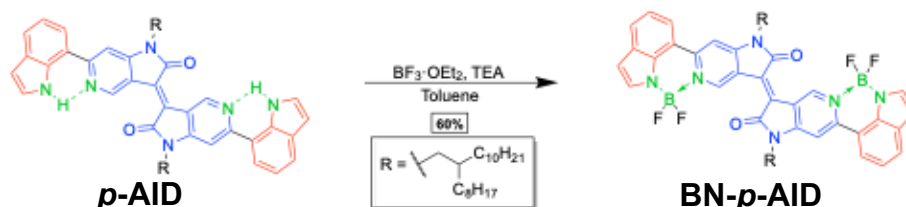
Scheme 5.5. B←N coordination bridge installation on *p*-AID.

In order to ensure the reaction conditions were facile, the reaction in **Scheme 5.6** was carried out with either triethylamine base or DBU. The resulting reaction gave evidence that the failure in installing the B←N-bridge on ***o*-AID** was unrelated to the reaction conditions. Moreover, these observations were corroborated by the substantial magnitude of over 500 equivalents of BF₃•Et₂O required to achieve saturated Lewis acid-base coordination with 7-diazaisinidigo-based compounds.[214]
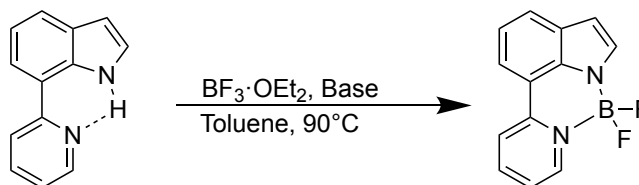
Scheme 5.6. Synthetic reaction for B←N-bridged control compound.

DFT optimizations on the theoretical product were carried out in order to investigate the causes behind this nonreactivity, as shown in **Figure 5.8b**. The DFT optimized structure

demonstrated a highly distorted backbone, attributed to the steric interactions between the large boron, its ligands, and the solubilizing chain, which were undesirably directed towards each other. To alleviate the steric strain, the B←N coordination distance increased, twisting the indole units around 20° out of the plane of the diazaisinidigo core. While the DFT optimized structure was calculated with methyl solubilizing group for the sake of computational simplicity, this effect was likely to increase with the larger octyldodecyl chain (**Figure 5.8a**), which was larger than even the literature reported 7-diazaisindigo analogue containing ethylhexyl chains, which requiring several hundreds of equivalents for Lewis acid-base coordination.[214] Therefore, access to H-bond-bridge substitution was determined to be impracticable for the installation of these B←N coordinative bridges.
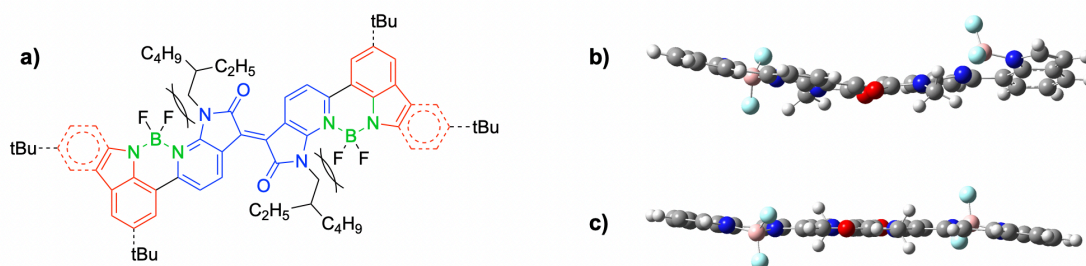
Figure 5.8. Steric of boron ligands and solubilizing chains of *o*-AID visualized by (a) side view of DFT optimized structure and (b) indicators on drawn structure.

In contrast to *o*-AID, steric strain was not present for the installation of the B←N coordinative bridges, as expected due to the aza-nitrogen of *p*-AID being located on the opposite side of the solubilizing chain. A slight distortion was observed in this structure, correlating to observations in previous work, demonstrating the propensity of the boron ligands in participating in a hyperconjugative interaction with the π-system.[94] This interaction favored axial ligands, which in turn slightly distorted the structure to achieve desirable conformations. In further DFT rotational energy scans, the hypothetically more rigid **BF₃-*p*-AID** demonstrated a 26.4 kcal/mol barrier as

compared to the 10.20 kcal/mol barrier of the hydrogen bonding *p*-AID (**Figure 5.9**). Despite this, the $\langle \cos^2\phi \rangle$ values did not differ significantly (0.967 vs 0.970, respectively). As a promising comparison to *p*-AID, the reaction as seen in **Scheme 5.5** was carried out. The resulting compound **BN-*p*-AID** was characterized, showing distinct ^{1}H peaks and signals in ^{11}B NMR as well as ^{19}F NMR (**Figure 5.17**).
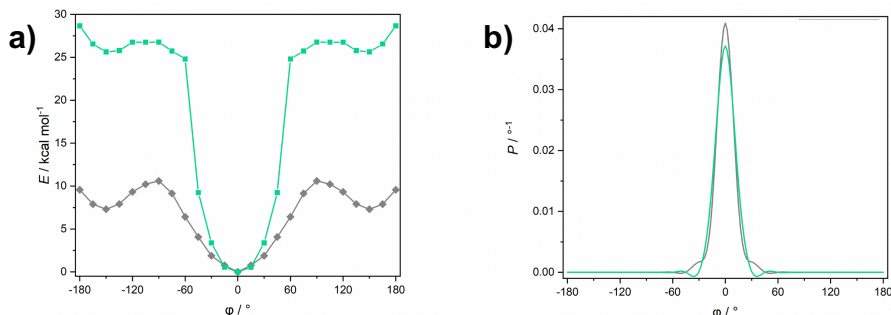
Figure 5.9. Rotational DFT scan of BF$_3$-*p*-AID (teal) in comparison to *p*-AID (gray) calculated at the [B3LYP/6-31g(d)] level of theory.

The optical spectroscopy revealed a redshifted absorbance for **BN-*p*-AID** as compared to *p*-AID, as expected by the introduction of these B←N coordinative bonds, leading to lower HOMO-LUMO bandgaps due to the reduction of LUMO levels.[21] Similarly, the experimental data showed less distinct packing peaks for **BN-*p*-AID**, although the absorbance peak was redshifted. The solid-state absorbance of the compound did not result in a significant difference in peak shape as compared to in solution-state **Figure 5.10**. Similarly, the GIWAXS diffraction patterns of the annealed thin-films were impacted by the B←N bridge in comparison to the H-bonded *p*-AID. While *p*-AID demonstrated very defined and ordered crystalline peaks (**Figure 4.8**), π-π stacking distances of **BN-*p*-AID** are entirely isotropic. Moreover, intense lamellar stacking peaks can be seen in the plane of the substrate, but also manifest as a series of faint equidistant peaks in the out-of-plane direction, indicating the possibility of multiphase crystallinity. Evidenced by the above-

mentioned DFT studies, the large boron moiety and its ligands could detrimentally impact the crystalline packing of the **BN-*p*-AID**. While molecular crystallinity remains important in terms of small molecules, polymers that demonstrate polycrystalline packing motifs are favored for semiconductor applications.[215, 216] Thus, these preliminary small molecule studies are important for the development of future B←N coordinative bond conformationally locked polymers, as discussed in the final chapter.
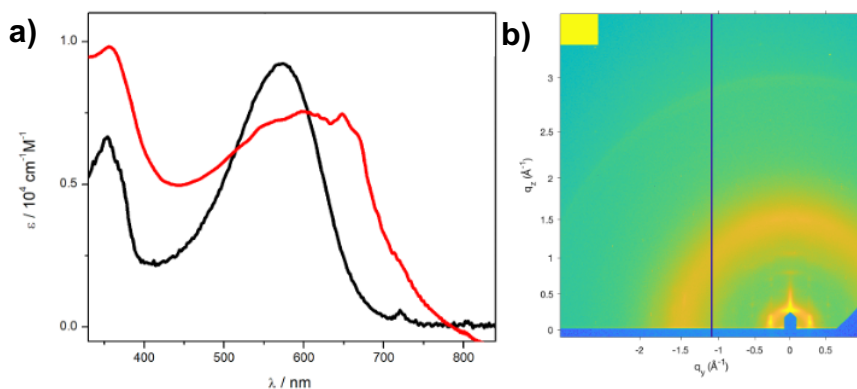
Figure 5.10. Optical and morphological results of BN-*p*-AID: (a) UV-Vis where thin-film is in red and solution-state (10^{-5} M in DCM) and (b) GIWAXS of annealed thin-film.

5.3 Conclusion

In summary, we herein designed a series of hydrogen-bond rigidified ladder-type polymers and established solutions to an assortment of crucial synthetic hurdles. For **IDCZ**, two notable issues were determined. First, undesirably low frontier molecular orbital energies were hypothesized to prevent the installation of active sites for palladium-catalyzed cross-coupling. Second, high steric hindrances caused by the benzylic C-H bulk prevented the coplanarization of the polymeric backbone and led to disordered packing in thin-film. As a solution to these issues, **BBI** was chosen as a donor-acceptor polymer building block, synthesized by group member Octavio Miranda. Its favorable FMO energy levels for cross coupling and absence of steric effects

when coupled to numerous H-bond acceptor materials made it a promising candidate for π-conjugated polymer synthesis. In coupling **BBI** to **5DAIID**, experimental data corroborated by theoretical simulations demonstrated the thermal lability of Boc groups due to the adjacent nucleophilic nitrogen. Design principles were established as solutions for these synthetic hurdles. First, frontier molecular orbital levels, specifically LUMO levels, must be tuned to allow for oxidative addition during palladium-catalyzed coupling. Second, solubility must be improved by either introducing excessively bulky solubilizing chains, or by screening benign reaction conditions that preserve Boc groups without leading to thermal cleavage. Therefore, favorable design strategies for the future synthesis of H-bond-bridged π-conjugated materials are laid out and can be incorporated with the previous design strategies from other chapters.

B←N dative bonds were shown to be sterically hindered during installation on *o*-**AID**, but demonstrated successful substitution of H-bond-bridging for *p*-**AID**, forming **BN-*p*-AID**. The resulting B←N coordination led to a high energy rotational barrier and slightly increased coplanarity index. The resulting red-shifted absorbance shows promising results for developing lower bandgap materials. Upon thin-film analysis through GIWAXS measurements, less ordered packing was observed for **BN-*p*-AID** in comparison to *p*-**AID**, corroborated by the slightly distorted structure and larger boron group as seen in the DFT calculations. While undesired for small molecule semiconducting materials, polycrystalline packing motifs are favored for polymer semiconductors, leading to more effective charge transport.[215, 216] Future perspectives and outlooks into the development of fused backbone π-conjugated poylmers featuring B←N coordination are outlined and discussed in the next chapter.

5.4 Experimental Section

5.4.1 General Methods and Materials

Starting materials and reagents were purchased from Sigma Aldrich, Acros Organics, Alfa Aesar, Oakwood, or Combi-Blocks and used as received. Anhydrous dichloromethane (CH_2Cl_2) was purchased from EMD Millipore and used without further purification. THF was dried and distilled under nitrogen from sodium using benzophenone as the indicator. Preparative gel permeation chromatography (GPC) was performed in chloroform solution at room temperature using Japan Analytical Industry recycling preparative HPLC (LC-92XXII NEXT SERIES). ^{1}H and ^{13}C NMR spectra were recorded on a Varian Inova 500 MHz spectrometer and variable temperature ^{1}H NMR spectra were recorded on a Varian VnmrS 500 MHz spectrometer. The NMR chemical shifts were reported in ppm relative to the signals corresponding to the residual non-deuterated solvents ($CDCl_3$: [1]H 7.26 ppm, [13]C 77.16 ppm; CD_3CN: [1]H 1.94 ppm) or the internal standard (tetramethylsilane: [1]H 0.00 ppm). Abbreviations for reported signal multiplicities are as follows: s, singlet; d, doublet; t, triplet; q, quartet; m, multiplet; br, broad. High resolution mass spectra were obtained via electrospray ionization (ESI) on an Applied Biosystems PE SCIEX QSTAR or matrix-assisted laser desorption/ionization (MALDI) on a Bruker microflex with a time-of-flight (TOF) analyzer. Column chromatography was carried out using Biotage® IsoleraTM Prime instrument with various size of SiO_2 Biotage ZIP® cartridge.

5.4.2 Synthesis

4,9-Dioctylidene-2,7-bis(triisopropylsilyl)-4,9-dihydro-sindaceno[2,1-d:6,5-d′]bis(thiazole) (IDTZ-1). Octyltriphenylphosphonium bromide (4.39 mg, 8.59 mmol) was dissolved in anhydrous THF (100 mL) at −78 °C. n-BuLi (8.59 mmol) was added dropwise. The mixture was stirred at

−78 °C for 1 h. To the cooled mixture at −78 °C, a solution of 2,7-bis(triisopropylsilyl)-s-indaceno-[2,1-d:6,5-d′]bis(thiazole)-4,9-dione (1.74 g, 2.86 mmol) in anhydrous THF (15 mL) was added dropwise over 30 min. After the addition, the mixture was stirred at −78 °C for 1 h and slowly warmed up to room temperature. The reaction mixture was further stirred at room temperature overnight. The reaction mixture was extracted with CH_2Cl_2 and washed with brine three times. The organic solution was dried over $MgSO_4$ and concentrated under reduced pressure. The residue was further purified through column chromatography (SiO_2, hexane/CH_2Cl_2 9:1) to give the product as a yellow solid. The product was identified as a mixture of three stereoisomers which were combined (69%) and used directly in the next step. ^{1}H NMR (400 MHz, CDCl$_3$) δ = 7.67 (s, 2H), 6.77 (t, J = 8.0 Hz, 2H), 3.20 (q, J = 7.6 Hz, 4H), 1.63 (quintet, J = 7.6 Hz, 4H), 1.48 (septet, J = 7.6 Hz, 6H), 1.40−1.25 (m, 20H), 1.20 (septet, J = 7.6 Hz, 36H), 0.87 (t, J = 6.8 Hz, 6H).

4,4,9,9-Tetraoctyl-2,7-bis(triisopropylsilyl)-4,9-dihydro-sindaceno[2,1-d:6,5-d′]bis(thiazole) (IDTZ-TIPS₂). To a suspension of $LiAlH_4$ in anhydrous THF (6 mL) at 0 °C, 1-bromooctane (2.29 g, 9.19 mmol) was added. A solution of **IDTZ-1** (366 mg, 0.45 mmol) was formed in anhydrous THF (26 mL) was added dropwise. The mixture was stirred at 0 °C for 1 h and subsequently at 50 °C for 8 h. The solvent was then removed under reduced pressure. The residue was dissolved in CH_2Cl_2 and washed with water twice and dried with $MgSO_4$. After removing the solvent under reduced pressure, the crude product was purified through column chromatography (SiO_2, hexane/CH_2Cl_2 9:1 to 7:1) to afford **S2** as a pale yellow solid (70%). ^{1}H NMR (400 MHz, CDCl$_3$) δ = 7.36 (s, 2H), 2.22 (m, 4H), 1.89 (m, 4H), 1.49 (septet, J = 7.6 Hz, 6H), 1.3−1.0 (m, 76H), 0.9−0.7 (m, 20H).

Deprotected IDTZ. A TBAF solution (2.2 mmol, 1.1 mL of a 2 M solution in THF) was added dropwise to a solution of compound **IDTZ-TIPS$_2$** (1 mmol) in anhydrous THF (20 mL) at 0 °C and stirred for 30 min. After quenching with water (100 mL), the product was extracted with chloroform (3 × 30 mL). The combined organic fractions were then dried over anhydrous MgSO$_4$, filtered, concentrated under reduced pressure, and redissolved in anhydrous chloroform (10 mL). Deprotected IDTZ was formed. The anhydrous chloroform solution of Deprotected IDTZ was added NBS (3 mmol) was added in one portion and the reaction mixture was stirred at ambient temperature in darkness until completion (typically 3–4 h). The reaction was then quenched with water (100 mL) and extracted with chloroform (3 × 30 mL). The combined organic fractions were dried over anhydrous MgSO$_4$, filtered, and concentrated under reduced pressure. After purification by flash chromatography with *n*-hexane/chloroform (0–5%) gradient, the desired products were obtained as a yellow solid. ^{1}H NMR (400 MHz, CDCl$_3$) δ = 7.28 (s, 2H), 2.15 (m, 4H), 1.88 (m, 4H), 1.20−1.07 (m, 40 H), 0.82−0.73 (m, 20H).

IDTZ-(SnMe₃)₂. To a stirring suspension of ladder monomer (90.1mg, 0.0957 mmol) in freshly prepared anhydrous THF (7ml) at -78 °C (acetone/dry ice) was added dropwise 107 µl of 2M LDA solution. The reaction mixture was stirred for further 30 mins and then placed in ice-water bath and stirred for 5-10 mins (during which the suspension becomes clear with some luminescence seen in solution indicating complete formation of dianion), again chilled to -78 °C and a solution of 1M trimethylstannyl chloride (383 µl, 3.83 mmol) was added. After stirring for further 15 mins the reaction mixture was bought to 0°C and quenched with distilled water. Reaction mixture was diluted with hexane and organic layer was separated, dried over anhyd. MgSO4 and concentrated to dryness to obtain Stannylated ladder as light-yellow microcrystals. ^{1}H NMR (500 MHz, CDCl$_3$):

7.33 (s, 3H), 2.49 (m, 4H), 1.88 (m, 4H), 1.76(s, 9H), 1.34 – 1.66 (m, 144H), 0.51 (t, J = 6.0, 2.2 Hz, 18H).

IN-BBI-Boc$_2$-(Bpin)$_2$. To a stirred solution of **IN-BBI-Boc$_2$** (50 mg, 0.07 mmol) in anhydrous THF (5 mL) cooled to -78 °C was added 6 eq. *n*-BuLi (0.49 mmol) dropwise. The reaction mixture was stirred for further 30 min at -78 °C and a solution of 2-isopropoxy-4,4,5,5-tetramethyl-1,3,2-dioxaborolane (52 mg, 0.28 mmol) was added. After stirring for 30 minutes further, the reaction mixture was brought to 0 °C and quenched with distilled water. The reaction mixture was diluted with DCM and the organic layer was extracted, dried over MgSO$_4$, concentrated, and purified by prep-GPC, yielding **IN-BBI-Boc$_2$-(Bpin)$_2$** as a white powder. ^{1}H NMR (500 MHz, CDCl$_3$): 3.24 (m, 2H), 1.99 (m, 4H), 1.75 (m, 24H), 1.25 (m, 46H), 0.84 (t, J = 6.0, 2.2 Hz, 34H). APCI-MS: m/z [M + H]$^+$ Calcd for C$_{48}$H$_{81}$B$_2$N$_4$O$_6$ 863.6235; Found 863.6237

7-(pyridin-2-yl)-1H-indole. The procedure was similar to that described above. ^{1}H NMR (500 MHz, CDCl$_3$): δ 11.42 (s, 1H), 8.75 (dd, J = 5.1, 1.9 Hz, 1H), 8.06 (d, J = 8.2 Hz, 1H), 7.85 – 7.78 (m, 3H), 7.41 (q, J = 2.9 Hz, 1H), 7.32 – 7.18 (m, 2H), 6.67 (p, J = 2.7 Hz, 1H).

1-(difluoroboraneyl)-7-(pyridin-2-yl)-1H-indole. To a pressure tube containing a solution of 7-(pyridin-2-yl)-1H-indole (16 mg, 0.08 mmol) in toluene (2 mL) was added 1,8-diazabicyclo[5.4.0]undec-7-ene (304 mg, 2.0 mmol) and BF$_3$OEt$_2$ (454 mg, 3.2 mmol) under nitrogen. The reaction mixture was heated to 90 °C overnight. After concentration of the reaction mixture the residue was rinsed with hexanes to afford 1-(difluoroboraneyl)-7-(pyridin-2-yl)-1H-indole (yield: 88%). ^{1}H NMR (500 MHz, CDCl$_3$): δ 8.92 (d, J = 6.1 Hz, 1H), 8.39 (d, J = 8.2 Hz,

1H), 8.18 (ddd, *J* = 8.5, 7.3, 1.6 Hz, 1H), 7.92 (dd, *J* = 7.7, 0.8 Hz, 1H), 7.87 (d, *J* = 7.6 Hz, 1H),

7.67 (d, *J* = 3.1 Hz, 1H), 7.59 (ddd, *J* = 7.3, 6.1, 1.3 Hz, 1H), 6.75 (d, *J* = 3.0 Hz, 1H). ^{19}F NMR

(500 MHz, CDCl$_3$): *δ* 133.40.

5.4.3 NMR Spectra
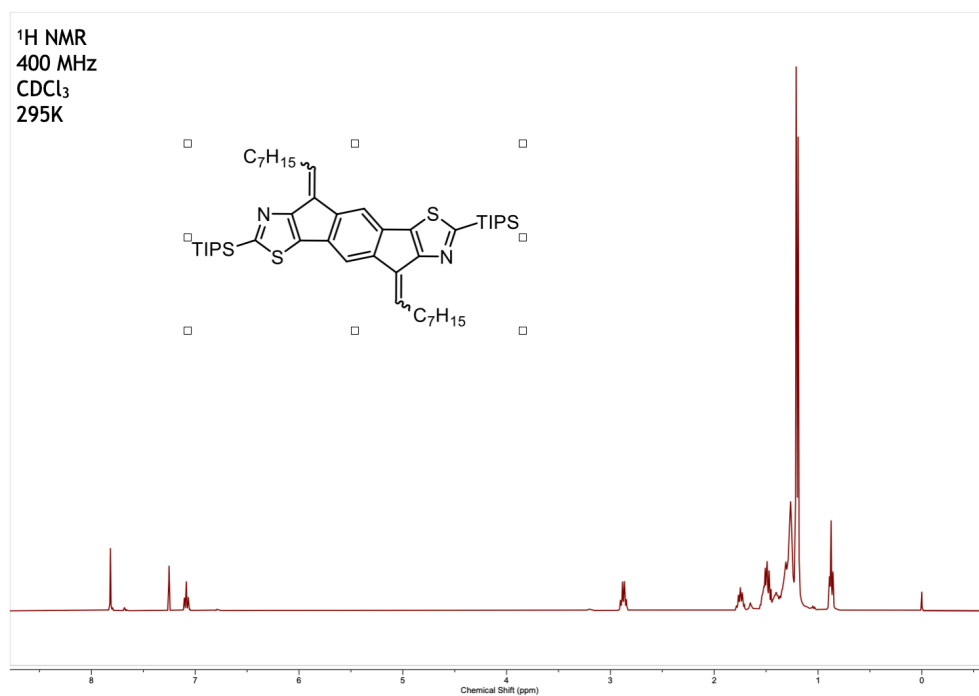
Figure 5.11. ^{1}H (400 MHz) NMR of IDTZ-1 in CDCl$_3$ at room temperature.
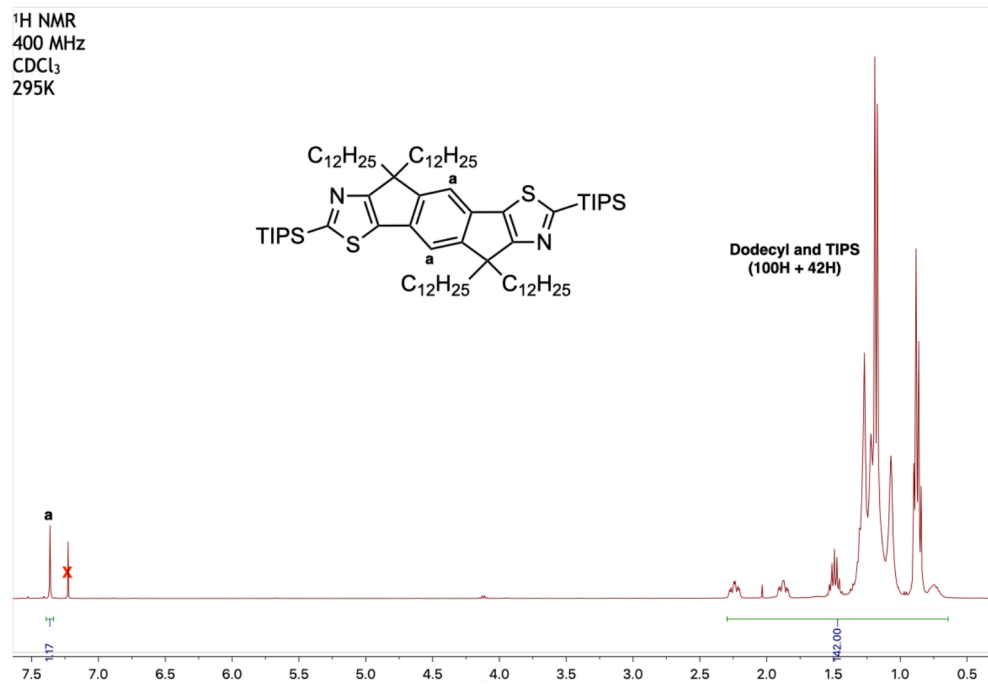
Figure 5.12. ¹H (400 MHz) NMR of deprotected IDTZ in CDCl₃ at room temperature.
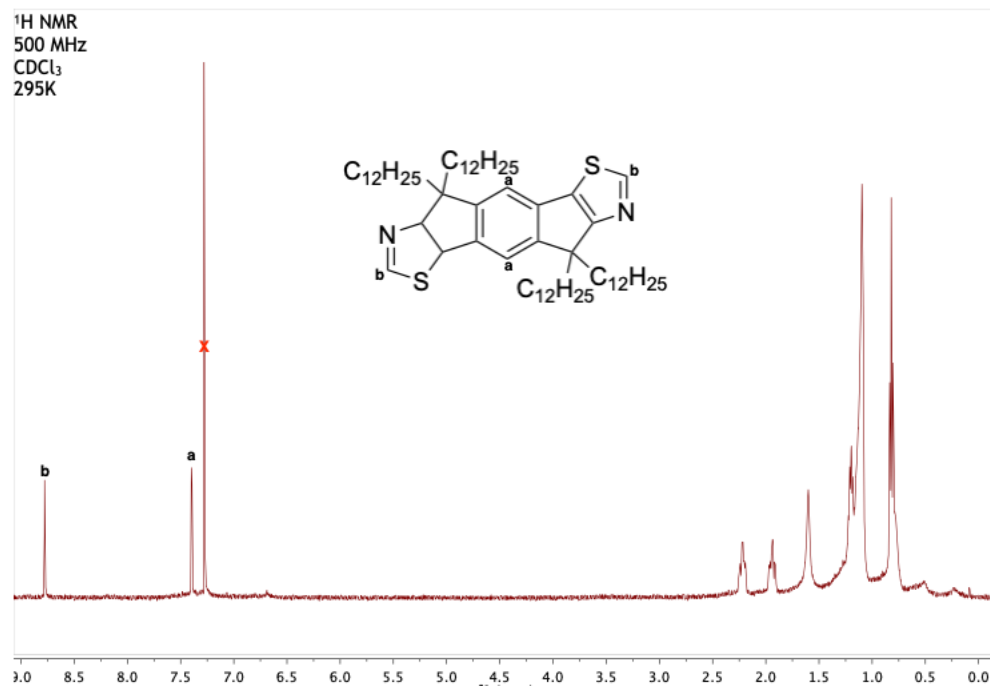
Figure 5.13. ¹H (500 MHz) NMR of deprotected IDTZ in CDCl₃ at room temperature.
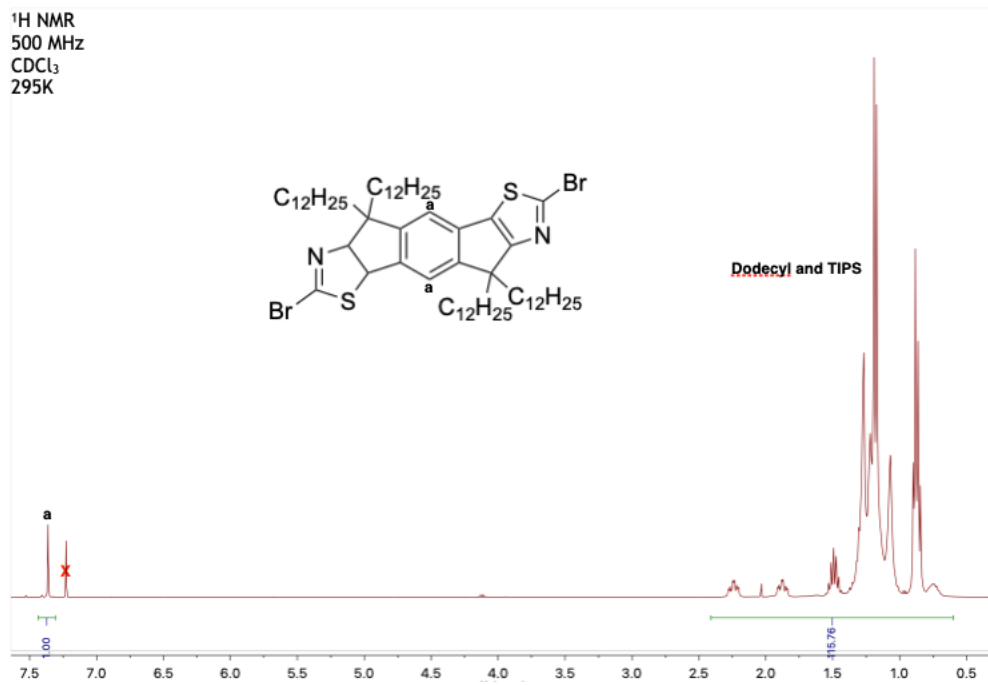
Figure 5.14. ¹H (500 MHz) NMR of IDTZ-Br₂ in CDCl₃ at room temperature.
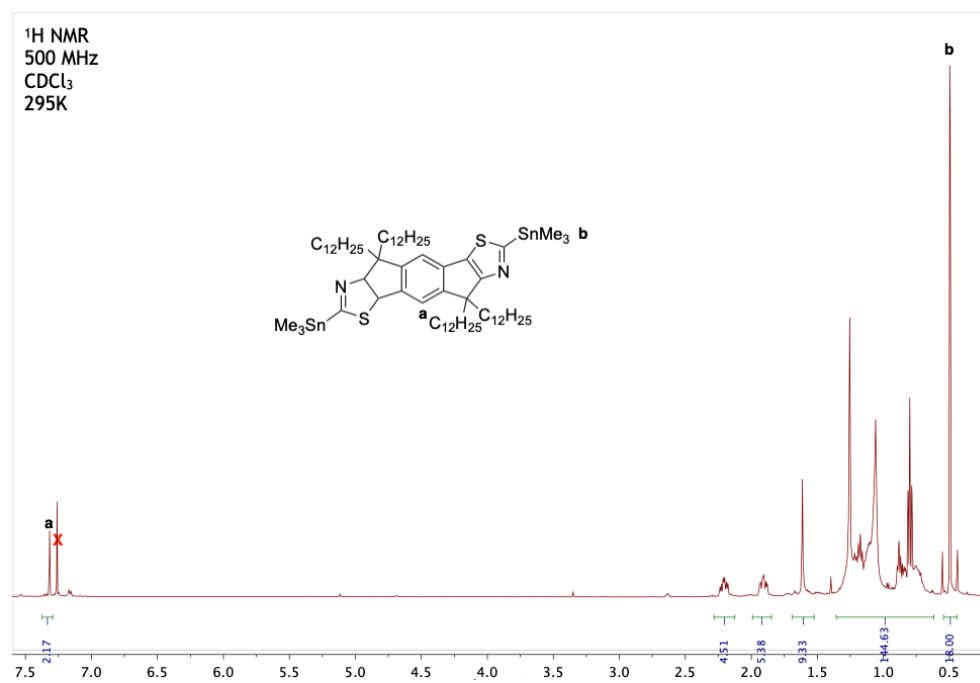
Figure 5.15. ¹H (500 MHz) NMR of IDTZ-(SnMe₃)₂ in CDCl₃ at room temperature.
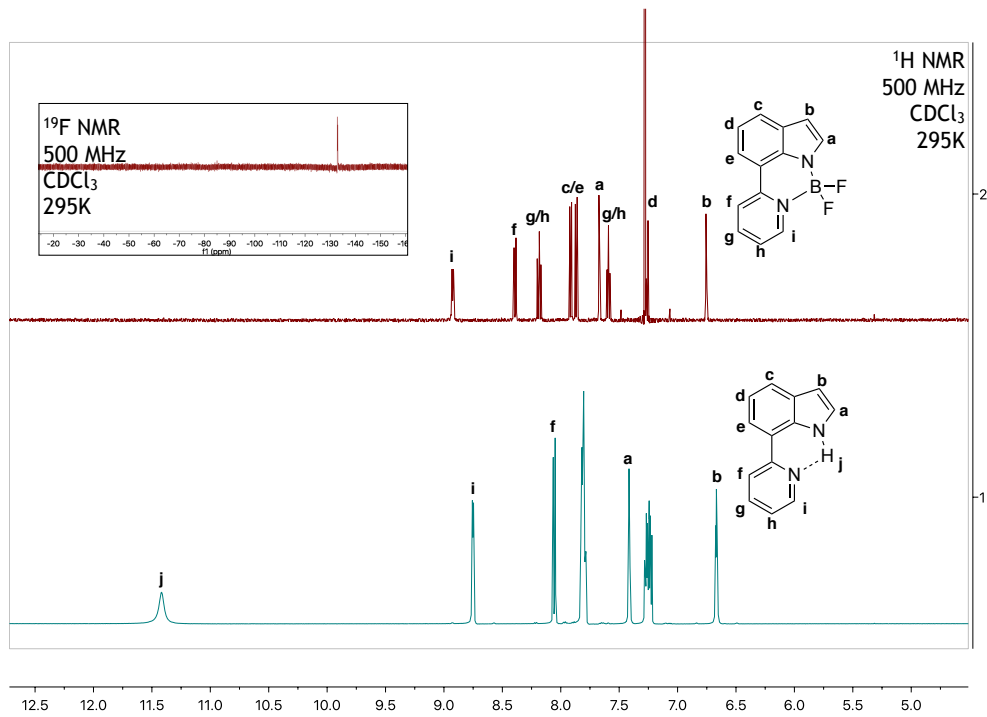
Figure 5.16. ^{1}H (500 MHz) and ^{19}F NMR (470 MHz) of B←N control in CDCl$_3$ at room temperature.
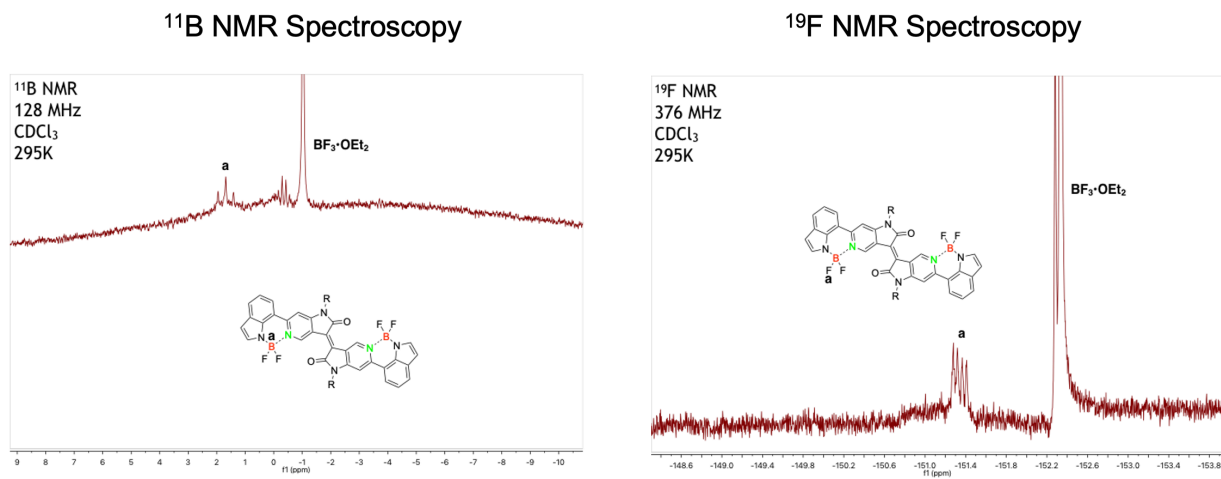
Figure 5.17 ^{11}B (128 MHz) and ^{19}F NMR (470 MHz) of BF$_3$-p-AID control in CDCl$_3$ at room temperature.
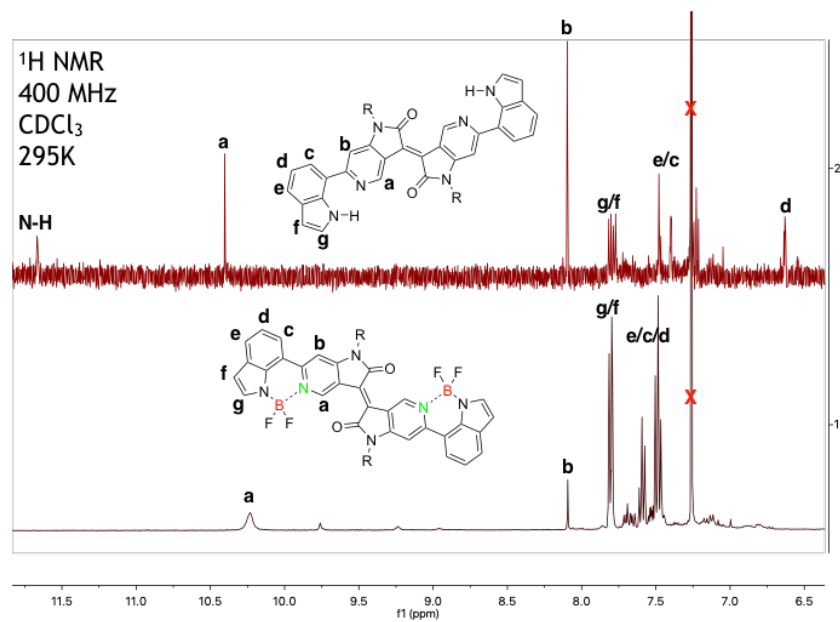
Figure 5.18. ^{1}H NMR (400 MHz) of BF$_3$-*p*-AID control in CDCl$_3$ at room temperature.

CHAPTER VI

CONCLUSIONS

6.1 Ladder-Type Conjugated Molecule Bridging by Hydrogen-Bonds

6.1.1 Summary

Demonstrated by our previous group members previously, hydrogen bonds prove themselves as extraordinary candidates for conformationally controlling the backbone conformation of conjugated molecules and macromolecules. By pre-organizing hydrogen-bond donating and accepting moieties on coupling building blocks (**Figure 1.4**), are group has shown success numerous times that conformational control can be achieved through these methods. In further work outlined in this dissertation, the strategy has not only been employed, but an effective workflow strategy was implemented, in which theoretical simulations, synthesis, morphological studies, and applications were all used to elucidate clear structure-property relationships of these π-conjugated molecules with intramolecular hydrogen bonds.

In the first project (Chapter II), we demonstrated the strength of computational density functional theory calculations as a means of screening molecular designs, corroborating experimental data, and mechanistically investigating unprecedented results. Particularly important methods were the investigations into the thermodynamics of torsional rotation for strategic structural comparisons, and also the correlation of simulated electrostatic potential maps to experimental investigations in intermolecular interactions. Reaching beyond the theoretical realm (Chapter III), we then integrated our pre-organized hydrogen bond strategy onto diazaisindigo building blocks and compared them to the non-hydrogen-bonding isoindigo counterpart. As a result of the robust intramolecular hydrogen bonds, thermally unyielding molecular conformations were achieved, elucidated not only by theoretical resources, but through thermal analysis and

variable temperature toughness experiments. Facile syntheses of these materials allowed for the systematic study from fundamental optical and electronic experiments to applications in organic electronics. In this context, issues of solubility, thin-film processibility, and other crucial supramolecular processing strategies for organic materials were developed through matching appropriate side-chain engineering with substrate surface treatments (Chapter IV). Once these conditions were optimized for the (diaza)isindigo materials, the robust H-bonds permitted thermal annealing treatments during thin-film processing and, consequently, led to effective organic field-effect transistor device fabrication. Furthermore, the measured organic field-effect transistor performances established clear correlations between rudimentary chemical properties, such as electrostatic polarization, and bulk organic electronic material engineering principles, such as thin-film processibility and intermolecular order. In summary, this work demonstrated a series of effective scientific methods through (i) density functional theory exploration of π-conjugated materials, (ii) installation of hydrogen bond conformational locks on these materials through pre-organized bridging moieties, (iii) effective supramolecular engineering for use in real-world applications, concluding in the eventual fabrication of functioning organic electronics.

6.2 Toward the Synthesis of Extended π-Conjugated Polymers with Rigidified Backbones.

In summary, a series of hydrogen-bond rigidified ladder-type polymers were designed and several synthetic challenges were encountered. Faced with these hurdles, solutions for future work were established. Initially, two notable issues were determined in which palladium-catalyzed cross-coupling was disfavored due to low frontier molecular orbital energies and high steric hindrances prevented the coplanarization of the polymeric backbone and led to disordered packing in thin-film. As a solution to these issues, **BBI** was proposed as a polymer building block, designed and synthesized by group member Octavio Miranda. In solution to the previous building blocks,

BBI exhibited favorable molecular orbital energy levels for cross coupling and lack of steric hindrance when coupled to various monomers. In coupling **BBI** to **5DAIID**, experimental data corroborated by theoretical simulations demonstrated the thermal lability of Boc groups due to the adjacent nucleophilic nitrogen. These results led to important design principles for synthesizing H-bond fused π-conjugated polymers. In addition to the strategies elucidated in previous chapters, frontier molecular orbital levels must be tuned for coupling reactions, and solubility must be improved for these particularly rigid structures, as accomplished through stable Boc protecting groups or installing bulkier side chains.

In addition, B←N dative bonds was also used as a strategy for bridging for ***p*-AID** and resulting in **BN-*p*-AID**. Although an increase was observed in rotational barrier, the coplanarity index was only slightly increased. The resulting red-shifted absorbance shows promising results for developing lower bandgap materials. Less ordered polycrystalline peaks were observed in the thin-film, which may lead to effective charge transport in polymeric materials.[215, 216] In the next section, we use these strategies in proposed future work for the eventual successful synthesis of fully H-bond rigidified π-conjugated polymers with enhanced semiconductor performance, and fully B←N coordination fused polymers.

6.3 Perspectives

As demonstrated by the results of diazaisindigo-based compounds for the development of H-bond-fused π-conjugated materials, we have begun a collaboration with Prof. Simon Rondeau-Gagné and his research group, in which pseudo-ladder polymers are the target. In this perspective work, pendant amine side chains will be installed onto thiophenes as H-bond donors, as demonstrated by the group's previous work.[47, 217] The resulting amide substituted thiophenes will

then be coupled to **7DAIID** and **5DAIID** and brominated, resulting in a π-extended building block

RG-1 featuring H-bonding conformational locks (**Scheme 6.1**).
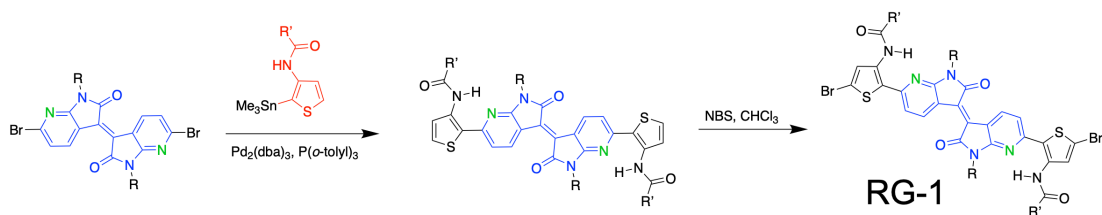
Scheme 6.1. Proposed synthesis of H-bond conformationally locked building block based on diazaisoindigo.

In the context of polymers, **RG-1** is expected to provide high performing semiconducting polymers as an electron poor building block. Two routes are proposed for the synthesis of such polymers. In Route 1, **RG-1** will be coupled with thiophene-flanked pyrazine with pendant amide side chains. This building block also features H-bond rigidification, and led to improved hole mobilities in the same magnitude of **p-AID** after polymerizing with diketopyrrolopyrrole.[47] The two high H-bond conformationally-locked building blocks are expected to synergistically enhance charge-transfer mobilities beyond what was reported for the individual building blocks. In Route 2, a systematic study of **RG-1** coupled to various traditional thiophene donors will be achieved (**Scheme 6.2b**), building up a larger library of semiconducting polymers based on diazaisindigo. As many of the state-of-the-art semiconducting polymers are analogues of polythiophene, this is expected to result in high performance semiconductors.[218, 219] This molecular design is supported by the performance of isoindigo and diazaisoindigo polymers containing thiophene, resulting in mobilities of up to 8 cm^2 V^{-1} s^{-1}.[108, 220, 221] Thus, the enhanced coplanarity of the resulting polymers containing **RG-1** is expected to improve the performance of past isoindigo and diazaisoindigo polymers by improving molecular packing orientation and extending π-conjugation.
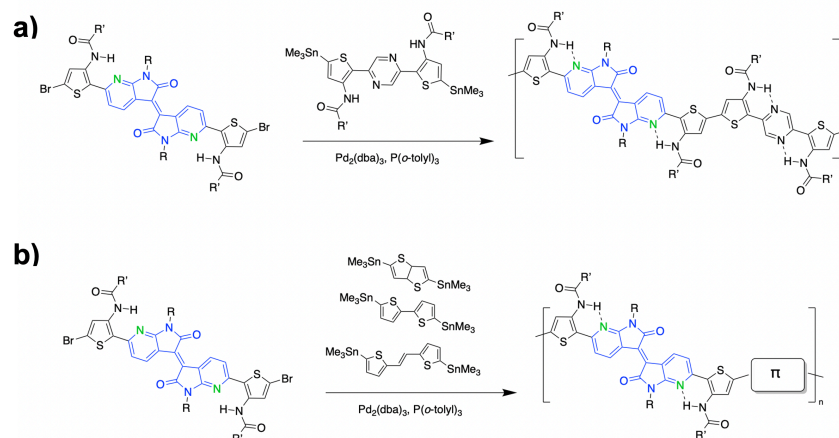
Scheme 6.2. Proposed synthesis of π-conjugated pseudo-ladder polymers based on RG-1.

In pushing the Chapter V work forward, Octavio Miranda has demonstrated the synthesis of **BBI-BDF-1 and BBI-BDF-2** through Suzuki cross-coupling (**Figure 6.1**). This has been achieved without thermal cleavage of Boc groups, thus yielding a polymer molecular weights of over 27 kg/mol. As these conditions have not yet been optimized, these results are promising in regard to the synthetic hurdles faced before. In specific, the proclivity of oxidation addition during the palladium-catalyzed coupling process was improved by using electron-rich **BDF** during the coupling process.
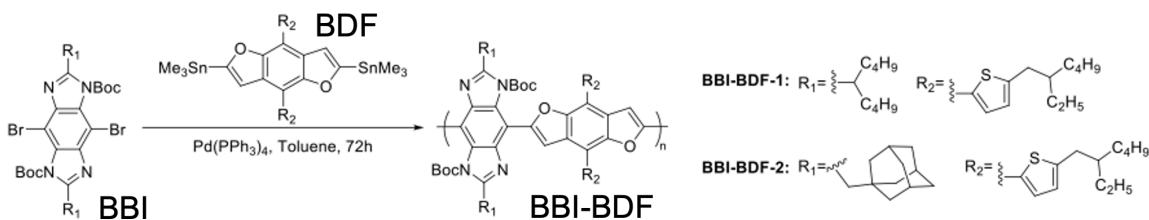
Figure 6.1 Polymerization of BBI with bisfuran compound to form polymer BBI-BDF in veseral different molecular weights.

More importantly, the organic solubility was maintained by two strategies, as mentioned in Chapter V. First, because oxygen was used as the H-bond acceptor in **BDF**, it was hypothesized that the less nucleophilic atom can lessen the effect towards the thermal cleavage of the Boc during Stille coupling. This hypothesis was substantiated by the intact Boc groups after polymerization, as preliminary evidenced by the further thermal annealing process (**Figure 6.2**), which could be unmasked to tune the optical band gap and further decrease solubility similar to previous work.[52] Second, the solubilizing group on **BBI** was also increased in bulkiness from **BBI-BDF-1** to **BBI-BDF-2**, using an adamantyl group in replacement of the isononyl group. Regarding the thermal Boc cleavage, a clear change in color can be seen between the thermally treated film and the as-cast film (**Figure 6.2**). Therefore, in this perspective work, Octavio Miranda's molecular design strategy is able to utilize the strategies outlined in Chapter V.
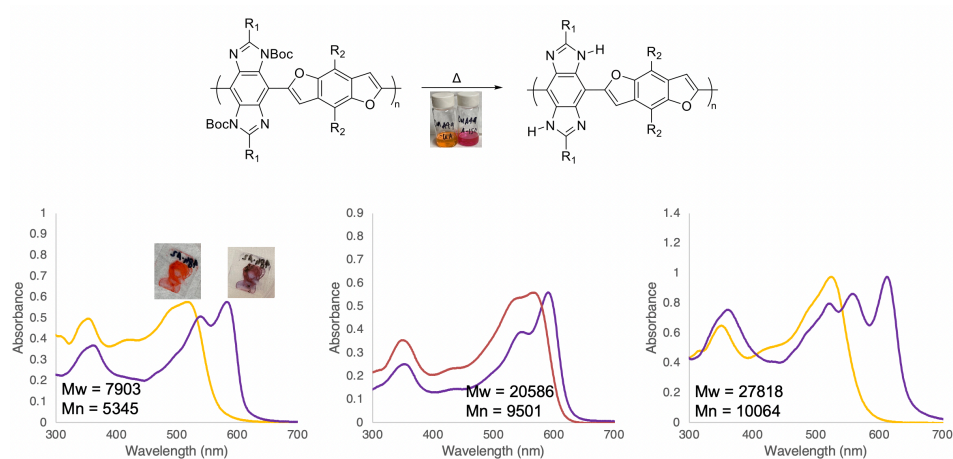
Figure 6.2. Thermally cleaved Boc groups as evidenced by UV-Vis spectroscopy.

In further using 5,5'-diazaisoindigo as a promising semiconductor material building block, the issues of electron-deficiency can be mitigated by using simple benzene-based building blocks with amide pendant groups, as used in very early examples of H-bond donating building blocks.[114,][179] In this respect, preliminary synthesis has been carried out, with further amide functionalization

with long bulky groups, as seen in **Figure 6.3**. In this design, Boc groups are not necessary in the solubility of the polymer due to the solubilizing moieties that are expected to be more thermally robust. The preliminary synthesis on this polymer has demonstrated oligomeric coupling up to 10 kg/mol, and remains promising for the future investigations. Furthermore, due to the nonfused nature of the H-bond donor, it is hypothesized that the H-bond dynamicity will be enhanced. As seen in previous work, H-bond dynamic H-bonds are potentially disrupted by H-bond competing solvents, such as DMSO.[51] This active control opens up the potential for controlling the solution processibility by altering the solubility with H-bond competitors. Furthermore, this allows the tuning of optical bandgaps in solution.
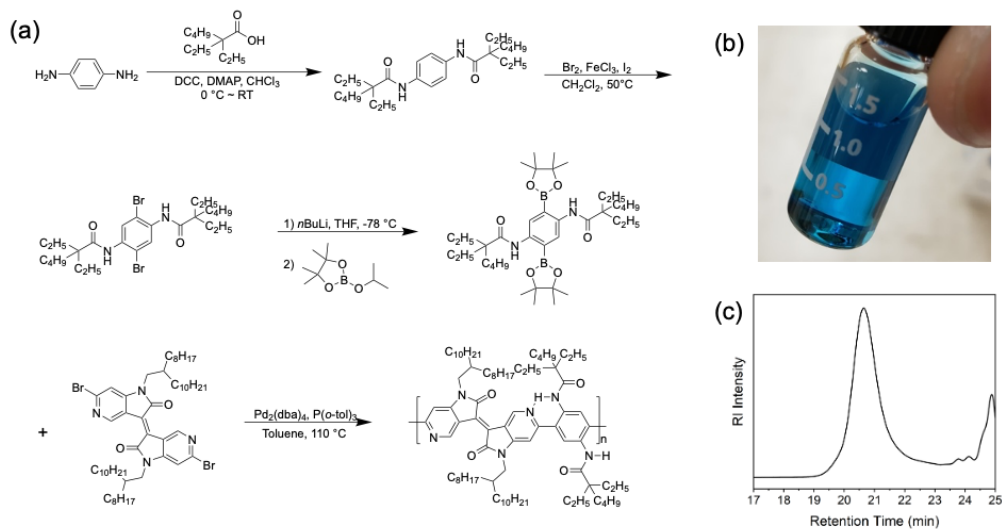
Figure 6.3. H-bond polymer of 5,5'-diazaisindigo and diamidobenzene coupling: (a) synthesis, (b) resulting solution-state color (in THF), and (c) SEC trace.

As these B←N-bridged materials have achieved semiconductor performance and have been utilized to great effect in all polymer solar cells,[202, 203] they represent a developing strategy in synthesizing high performing π-conjugated polymers for organic electronics. B←N bonding becomes feasible following the successful synthesis of the proposed H-bond π-conjugated

polymers. Equipped with the B←N-bridge installation strategy outlined in previous chapters (**Scheme 5.5**), H-bond bridges can be efficiently replaced with B←N bridges, leading to higher rigidity polymers as compared to their H-bond structures.
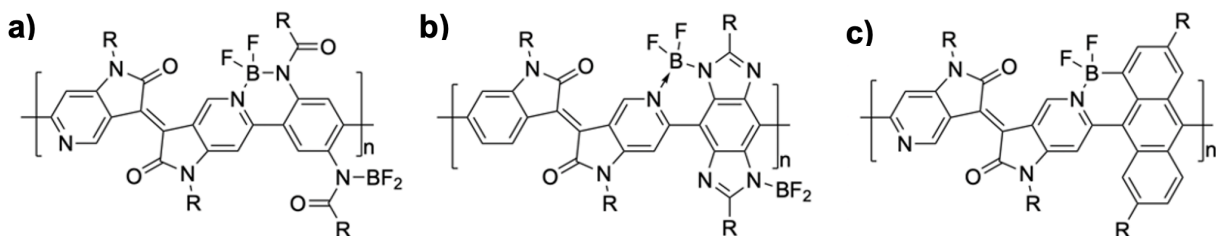
Scheme 6.3. Proposed polymers containing B–N coordination bond bridges.

As demonstrated in Chapter IV, previous attempts at B←N-bridged compounds did not demonstrate high charge-carrier mobilities. As an electron mobility of 1.60 cm^{-1} V^{-1} s^{-1} has been achieved in the reported quadruply B←N-fused dibenzo-azaacene with low solubility, this approach can be improved upon by addressing several areas $\partial$of concern. Other high-performing state-of-the-art building blocks can be tested using this B←N-fusion strategy. For example, the H-bonding polymers outlined in the previous chapters are already geometrically primed for B←N-bridge installation, as seen in **Scheme 6.3**. As isoindigo is already a well-established electron deficient conjugated building block for electronic organic materials,[106] the B←N-bridge is predicted to further lower LUMO levels and reduce bandgap energies, resulting in improved n-type semiconductors. Furthermore, anthracene has also demonstrated promising enhancement of π-π-stacking abilities in π-conjugated polymers.[222, 223] Thus, the diazaisoindigo-anthracene based polymer is proposed in **Scheme 6.3b** for its effective building blocks as well as geometrically favorable B←N-bridge installation.

REFERENCES

(1) Shirakawa, H.; Louis, E. J.; MacDiarmid, A. G.; Chiang, C. K.; Heeger, A. J. Synthesis of electrically conducting organic polymers: halogen derivatives of polyacetylene, (CH). *J. Chem. Soc., Chem. Commun.* **1977**, (16), 578-580, 10.1039/C39770000578.

(2) Zheng, Z.; Wang, J.; Bi, P.; Ren, J.; Wang, Y.; Yang, Y.; Liu, X.; Zhang, S.; Hou, J. Tandem Organic Solar Cell with 20.2% Efficiency. *Joule* **2022**, *6* (1), 171-184.

(3) Chen, Y.; Zhang, D.; Zhang, Y.; Zeng, X.; Huang, T.; Liu, Z.; Li, G.; Duan, L. Approaching Nearly 40% External Quantum Efficiency in Organic Light Emitting Diodes Utilizing a Green Thermally Activated Delayed Fluorescence Emitter with an Extended Linear Donor–Acceptor–Donor Structure. *Adv. Mater.* **2021**, *33* (44), 2103293.

(4) Zeng, W.; Lai, H.-Y.; Lee, W.-K.; Jiao, M.; Shiu, Y.-J.; Zhong, C.; Gong, S.; Zhou, T.; Xie, G.; Sarma, M.; et al. Achieving Nearly 30% External Quantum Efficiency for Orange–Red Organic Light Emitting Diodes by Employing Thermally Activated Delayed Fluorescence Emitters Composed of 1,8-Naphthalimide-Acridine Hybrids. *Adv. Mater.* **2018**, *30* (5), 1704961.

(5) Chu, M.; Fan, J.-X.; Yang, S.; Liu, D.; Ng, C. F.; Dong, H.; Ren, A.-M.; Miao, Q. Halogenated Tetraazapentacenes with Electron Mobility as High as 27.8 cm2 V−1 s−1 in Solution-Processed n-Channel Organic Thin-Film Transistors. *Adv. Mater.* **2018**, *30* (38), 1803467.

(6) Forrest, S. R. *Organic Electronics: Foundations to Applications*; Oxford University Press, 2020.

(7) Zheng, B.; Huo, L. Recent advances of dithienobenzodithiophene-based organic semiconductors for organic electronics. *Science China Chemistry* **2021**, *64* (3), 358-384.

(8) Gu, Y.; Zhang, T.; Chen, H.; Wang, F.; Pu, Y.; Gao, C.; Li, S. Mini Review on Flexible and Wearable Electronics for Monitoring Human Health Information. *Nanoscale Research Letters* **2019**, *14* (1), 263.

(9) Butt, M. A.; Kazanskiy, N. L.; Khonina, S. N. Revolution in Flexible Wearable Electronics for Temperature and Pressure Monitoring—A Review. *Electronics* **2022**, *11* (5), 716.

(10) Giannini, S.; Blumberger, J. Charge Transport in Organic Semiconductors: The Perspective from Nonadiabatic Molecular Dynamics. *Acc. Chem. Res.* **2022**, *55* (6), 819-830.

(11) Tsumura, A.; Koezuka, H.; Ando, T. Macromolecular electronic device: Field-effect transistor with a polythiophene thin film. *Appl. Phys. Lett.* **1986**, *49* (18), 1210-1212.

(12) Yuan, Y.; Giri, G.; Ayzner, A. L.; Zoombelt, A. P.; Mannsfeld, S. C. B.; Chen, J.; Nordlund, D.; Toney, M. F.; Huang, J.; Bao, Z. Ultra-high mobility transparent organic thin film transistors grown by an off-centre spin-coating method. *Nat. Commun.* **2014**, *5* (1), 3005.

(13) Luo, C.; Kyaw, A. K. K.; Perez, L. A.; Patel, S.; Wang, M.; Grimm, B.; Bazan, G. C.; Kramer, E. J.; Heeger, A. J. General Strategy for Self-Assembly of Highly Oriented Nanocrystalline Semiconducting Polymers with High Mobility. *Nano Lett.* **2014**, *14* (5), 2764-2771.

(14) Kim, M.; Ryu, S. U.; Park, S. A.; Choi, K.; Kim, T.; Chung, D.; Park, T. Donor–Acceptor-Conjugated Polymer for High-Performance Organic Field-Effect Transistors: A Progress Report. *Adv. Funct. Mater.* **2020**, *30* (20), 1904545.

(15) Kim, M.; Ryu, S. U.; Park, S. A.; Choi, K.; Kim, T.; Chung, D.; Park, T. Organic Field-Effect Transistors: Donor–Acceptor-Conjugated Polymer for High-Performance Organic Field-Effect Transistors: A Progress Report (Adv. Funct. Mater. 20/2020). *Adv. Funct. Mater.* **2020**, *30* (20), 2070130.

(16) Lüssem, B.; Riede, M.; Leo, K. Doping of organic semiconductors. *physica status solidi (a)* **2013**, *210* (1), 9-43.

(17) Sirringhaus, H. 25th Anniversary Article: Organic Field-Effect Transistors: The Path Beyond Amorphous Silicon. *Advanced Materials* **2014**, *26* (9), 1319-1335.

(18) Huang, H.; Yang, L.; Facchetti, A.; Marks, T. J. Organic and Polymeric Semiconductors Enhanced by Noncovalent Conformational Locks. *Chemical Reviews* **2017**, *117* (15), 10291-10318.

(19) Grozema, F. C.; van Duijnen, P. T.; Berlin, Y. A.; Ratner, M. A.; Siebbeles, L. D. A. Intramolecular Charge Transport along Isolated Chains of Conjugated Polymers: Effect of Torsional Disorder and Polymerization Defects. *The Journal of Physical Chemistry B* **2002**, *106* (32), 7791-7795.

(20) Yu, Z.-D.; Lu, Y.; Wang, J.-Y.; Pei, J. Conformation Control of Conjugated Polymers. *Chem. Eur. J.* **2020**, *26* (69), 16194-16205.

(21) Zhu, C.; Guo, Z.-H.; Mu, A. U.; Liu, Y.; Wheeler, S. E.; Fang, L. Low Band Gap Coplanar Conjugated Molecules Featuring Dynamic Intramolecular Lewis Acid–Base Coordination. *J. Org. Chem.* **2016**, *81* (10), 4347-4352.

(22) Brédas, J.-L.; Beljonne, D.; Coropceanu, V.; Cornil, J. Charge-Transfer and Energy-Transfer Processes in π-Conjugated Oligomers and Polymers: A Molecular Picture. *Chem. Rev.* **2004**, *104* (11), 4971-5004.

(23) Briseno, A. L.; Mannsfeld, S. C. B.; Shamberger, P. J.; Ohuchi, F. S.; Bao, Z.; Jenekhe, S. A.; Xia, Y. Self-Assembly, Molecular Packing, and Electron Transport in n-Type Polymer Semiconductor Nanobelts. *Chemistry of Materials* **2008**, *20* (14), 4712-4719.

(24) Liu, Y.; Liu, Y.; Zhan, X. High-Mobility Conjugated Polymers Based on Fused-Thiophene Building Blocks. *Macromolecular Chemistry and Physics* **2011**, *212* (5), 428-443.

(25) Yang, J.; Zhao, Z.; Wang, S.; Guo, Y.; Liu, Y. Insight into High-Performance Conjugated Polymers for Organic Field-Effect Transistors. *Chem* **2018**, *4* (12), 2748-2785.

(26) Sun, Y.; Guo, Y.; Liu, Y. Design and synthesis of high performance π-conjugated materials through antiaromaticity and quinoid strategy for organic field-effect transistors. *Materials Science and Engineering: R: Reports* **2019**, *136*, 13-26.

(27) Lee, J.; Kalin, A. J.; Yuan, T.; Al-Hashimi, M.; Fang, L. Fully conjugated ladder polymers. *Chemical Science* **2017**, *8* (4), 2503-2521, 10.1039/C7SC00154A.

(28) Sun, H.; Liu, B.; Koh, C. W.; Zhang, Y.; Chen, J.; Wang, Y.; Chen, P.; Tu, B.; Su, M.; Wang, H.; et al. Imide-Functionalized Heteroarene-Based n-Type Terpolymers Incorporating Intramolecular Noncovalent Sulfur···Oxygen Interactions for Additive-Free All-Polymer Solar Cells. *Advanced Functional Materials* **2019**, *29* (42), 1903970.

(29) Li, S.; Zhao, W.; Zhang, J.; Liu, X.; Zheng, Z.; He, C.; Xu, B.; Wei, Z.; Hou, J. Influence of Covalent and Noncovalent Backbone Rigidification Strategies on the Aggregation Structures of a Wide-Band-Gap Polymer for Photovoltaic Cells. *Chemistry of Materials* **2020**, *32* (5), 1993-2003.

(30) Sinclair, G. S.; Claridge, R. C. M.; Kukor, A. J.; Hopkins, W. S.; Schipper, D. J. N-Oxide S–O chalcogen bonding in conjugated materials. *Chem Sci* **2021**, *12* (6), 2304-2312, 10.1039/D0SC06583H.

(31) Tang, C.; Ma, X.; Wang, J.-Y.; Zhang, X.; Liao, R.; Ma, Y.; Wang, P.; Wang, P.; Wang, T.; Zhang, F.; et al. High-Performance Ladder-Type Heteroheptacene-Based Nonfullerene Acceptors Enabled by Asymmetric Cores with Enhanced Noncovalent Intramolecular Interactions. *Angewandte Chemie International Edition* **2021**, *60* (35), 19314-19323.

(32) Wang, C.-H.; Gao, Z.-C.; Sun, W.; Guo, X.; Zhang, F.-B. P···O noncovalent conformational locks for constructing highly planar Bis(diphenylphosphanyl) Bi(benzofurano). *Dyes and Pigments* **2021**, *184*, 108820.

(33) Zhang, X.; Li, C.; Qin, L.; Chen, H.; Yu, J.; Wei, Y.; Liu, X.; Zhang, J.; Wei, Z.; Gao, F.; et al. Side-Chain Engineering for Enhancing the Molecular Rigidity and Photovoltaic Performance of Noncovalently Fused-Ring Electron Acceptors. *Angewandte Chemie International Edition* **2021**, *60* (32), 17720-17725.

(34) Zhang, X.; Qin, L.; Yu, J.; Li, Y.; Wei, Y.; Liu, X.; Lu, X.; Gao, F.; Huang, H. High-Performance Noncovalently Fused-Ring Electron Acceptors for Organic Solar Cells Enabled by Noncovalent Intramolecular Interactions and End-Group Engineering. *Angewandte Chemie International Edition* **2021**, *60* (22), 12475-12481.

(35) Black, H. T.; Perepichka, D. F. Crystal Engineering of Dual Channel p/n Organic Semiconductors by Complementary Hydrogen Bonding. *Angewandte Chemie International Edition* **2014**, *53* (8), 2138-2142.

(36) Dhar, J.; Karothu, D. P.; Patil, S. Herringbone to cofacial solid state packing via H-bonding in diketopyrrolopyrrole (DPP) based molecular crystals: influence on charge transport. *Chemical Communications* **2015**, *51* (1), 97-100, 10.1039/C4CC06063F.

(37) Dai, Y.-Z.; Ai, N.; Lu, Y.; Zheng, Y.-Q.; Dou, J.-H.; Shi, K.; Lei, T.; Wang, J.-Y.; Pei, J. Embedding electron-deficient nitrogen atoms in polymer backbone towards high performance n-type polymer field-effect transistors. *Chemical Science* **2016**, *7* (9), 5753-5757, 10.1039/C6SC01380E.

(38) Chen, Z.; Li, H.; Tao, Y.; Chen, L.; Chen, C.; Jiang, H.; Xu, S.; Zhou, X.; Chen, R.; Huang, W. Tuning Intramolecular Conformation and Packing Mode of Host Materials through Noncovalent Interactions for High-Efficiency Blue Electrophosphorescence. *ACS Omega* **2019**, *4* (5), 9129-9134.

(39) Lu, Y.; Yu, Z.-D.; Zhang, R.-Z.; Yao, Z.-F.; You, H.-Y.; Jiang, L.; Un, H.-I.; Dong, B.-W.; Xiong, M.; Wang, J.-Y.; et al. Rigid Coplanar Polymers for Stable n-Type Polymer Thermoelectrics. *Angewandte Chemie International Edition* **2019**, *58* (33), 11390-11394.

(40) Wang, D.; Qiao, X.; Ouyang, G.; Wu, H.; Li, H. Fluorine-substituted quinoidal thiophene with a F–H hydrogen bond locked conformation for high-performance n-channel organic transistors. *Chemical Communications* **2019**, *55* (44), 6253-6256, 10.1039/C9CC02872B.

(41) Wang, Y.; Hasegawa, T.; Matsumoto, H.; Michinobu, T. Significant Improvement of Unipolar n-Type Transistor Performances by Manipulating the Coplanar Backbone Conformation of Electron-Deficient Polymers via Hydrogen Bonding. *Journal of the American Chemical Society* **2019**, *141* (8), 3566-3575.

(42) Liu, Z.-F.; Chen, X.; Mou, Z. F.; Jin, W. J. Stimuli-responsive luminescent bithiophene-dicarbaldehyde molecular rotors by hydrogen bonding. *Journal of Materials Chemistry C* **2020**, *8* (45), 16100-16106, 10.1039/D0TC03651J.

(43) Maeda, T.; Liess, A.; Kudzus, A.; Krause, A.-M.; Stolte, M.; Amitani, H.; Yagi, S.; Fujiwara, H.; Würthner, F. Hydrogen bond-rigidified planar squaraine dye and its electronic and organic semiconductor properties. *Chemical Communications* **2020**, *56* (68), 9890-9893, 10.1039/D0CC04306K.

(44) Zhang, H.; Li, R.; Deng, Z.; Cui, S.; Wang, Y.; Zheng, M.; Yang, W. π-Conjugated oligomers based on aminobenzodifuranone and diketopyrrolopyrrole. *Dyes and Pigments* **2020**, *181*, 108552.

(45) Liu, B.; Li, J.; Zeng, W.; Yang, W.; Yan, H.; Li, D.-c.; Zhou, Y.; Gao, X.; Zhang, Q. High-Performance Organic Semiconducting Polymers by a Resonance-Assisted Hydrogen Bonding Approach. *Chemistry of Materials* **2021**, *33* (2), 580-588.

(46) Morisue, M.; Kawanishi, M.; Ueno, I.; Nakamura, T.; Nabeshima, T.; Imamura, K.; Nozaki, K. Evidence of C–F···H–C Attractive Interaction: Enforced Coplanarity of a Tetrafluorophenylene-Ethynylene-Linked Porphyrin Dimer. *The Journal of Physical Chemistry B* **2021**, *125* (32), 9286-9295.

(47) Ocheje, M. U.; Goodman, R. B.; Lu, K.-T.; Wang, Y.; Galuska, L. A.; Soullard, L.; Cao, Z.; Zhang, S.; Yadiki, M.; Gu, X.; et al. Precise Control of Noncovalent Interactions in Semiconducting Polymers for High-Performance Organic Field-Effect Transistors. *Chemistry of Materials* **2021**, DOI: 10.1021/acs.chemmater.1021c02426.

(48) Özen, B.; Fadaei Tirani, F.; Schenk, K.; Lin, K.-H.; Scopelliti, R.; Corminboeuf, C.; Frauenrath, H. Structure–Property Relationships in Bithiophenes with Hydrogen-Bonded Substituents. *Chemistry – A European Journal* **2021**, *27* (10), 3348-3360.

(49) Wang, Q.; Böckmann, S.; Günther, F.; Streiter, M.; Zerson, M.; Scaccabarozzi, A. D.; Tan, W. L.; Komber, H.; Deibel, C.; Magerle, R.; et al. Hydrogen Bonds Control Single-Chain Conformation, Crystallinity, and Electron Transport in Isoelectronic Diketopyrrolopyrrole Copolymers. *Chemistry of Materials* **2021**, *33* (7), 2635-2645.

(50) Zhu, C.; Luo, Q.; Shen, Y.; Lv, C.; Zhao, S.; Lv, X.; Cao, F.; Wang, K.; Song, Q.; Zhang, C.; et al. Red to Near-Infrared Mechanochromism from Metal-free Polycrystals: Noncovalent Conformational Locks Facilitating Wide-Range Redshift. *Angewandte Chemie International Edition* **2021**, *60* (15), 8510-8514.

(51) Zhu, C.; Mu, A. U.; Lin, Y.-H.; Guo, Z.-H.; Yuan, T.; Wheeler, S. E.; Fang, L. Molecular Coplanarity and Self-Assembly Promoted by Intramolecular Hydrogen Bonds. *Org. Lett.* **2016**, *18* (24), 6332-6335.

(52) Zhu, C.; Mu, A. U.; Wang, C.; Ji, X.; Fang, L. Synthesis and Solution Processing of a Rigid Polymer Enabled by Active Manipulation of Intramolecular Hydrogen Bonds. *ACS Macro Letters* **2018**, *7* (7), 801-806.

(53) Burrows, J. A. Pauling, Linus. The nature of the chemical bond and the structure of molecules aid crystals. Ithaca: The Cornell University Press, 1939. 430 p. $4.50. *Science Education* **1941**, *25* (2), 120-120.

(54) Luzar, A.; Chandler, D. Hydrogen-bond kinetics in liquid water. *Nature* **1996**, *379* (6560), 55-57.

(55) Watson, J. D.; Crick, F. H. C. Molecular Structure of Nucleic Acids: A Structure for Deoxyribose Nucleic Acid. *Nature* **1953**, *171*, 737.

(56) Hubbard, R. E.; Kamran Haider, M. Hydrogen Bonds in Proteins: Role and Strength. In *eLS*.

(57) Desiraju, G. R. A Bond by Any Other Name. *Angew. Chem. Int. Ed.* **2011**, *50* (1), 52-59.

(58) Pimentel, G. C.; McClellan, A. L.; MacClellan, A. L. *The hydrogen bond*; WH freeman, 1960.

(59) Steiner, T.; Saenger, W. Role of CH. cntdot.. cntdot.. cntdot. O hydrogen bonds in the coordination of water molecules. Analysis of neutron diffraction data. *Journal of the American Chemical Society* **1993**, *115* (11), 4540-4547.

(60) Jeffrey, G. A.; Saenger, W. *Hydrogen bonding in biological structures*; Springer Science & Business Media, 2012.

(61) Arunan, E.; Desiraju, G. R.; Klein, R. A.; Sadlej, J.; Scheiner, S.; Alkorta, I.; Clary, D. C.; Crabtree, R. H.; Dannenberg, J. J.; Hobza, P. Defining the hydrogen bond: An account (IUPAC Technical Report). *Pure Appl. Chem.* **2011**, *83* (8), 1619-1636.

(62) Puranik, P. G.; Kumar, V. The charge transfer theory of the hydrogen bond. *Proceedings of the Indian Academy of Sciences - Section A* **1963**, *58* (6), 327-335.

(63) Herbert, J. M.; Carter-Fenk, K. Electrostatics, Charge Transfer, and the Nature of the Halide–Water Hydrogen Bond. *The Journal of Physical Chemistry A* **2021**, *125* (5), 1243-1256.

(64) Gellman, S. H.; Dado, G. P.; Liang, G. B.; Adams, B. R. Conformation-directing effects of a single intramolecular amide-amide hydrogen bond: variable-temperature NMR and IR studies on a homologous diamide series. *Journal of the American Chemical Society* **1991**, *113* (4), 1164-1173.

(65) Morozov, A. V.; Kortemme, T.; Tsemekhman, K.; Baker, D. Close agreement between the orientation dependence of hydrogen bonds observed in protein structures and quantum mechanical calculations. *Proceedings of the National Academy of Sciences of the United States of America* **2004**, *101* (18), 6946-6951.

(66) Kroon, J.; Kanters, J. A. Non-linearity of hydrogen bonds in molecular crystals. *Nature* **1974**, *248* (5450), 667-669.

(67) Fargher, H. A.; Sherbow, T. J.; Haley, M. M.; Johnson, D. W.; Pluth, M. D. C–H···S hydrogen bonding interactions. *Chem. Soc. Rev.* **2022**, *51* (4), 1454-1469, 10.1039/D1CS00838B.

(68) Liu, F.; Zhang, J. Z. H.; Mei, Y. The origin of the cooperativity in the streptavidin-biotin system: A computational investigation through molecular dynamics simulations. *Scientific Reports* **2016**, *6* (1), 27190.

(69) Herschlag, D.; Pinney, M. M. Hydrogen Bonds: Simple after All? *Biochemistry* **2018**, *57* (24), 3338-3352.

(70) Martínez-Cifuentes, M.; Cardona, W.; Saitz, C.; Weiss-López, B.; Araya-Maturana, R. A Study about Regioisomeric Hydroquinones with Multiple Intramolecular Hydrogen Bonding. *Molecules* **2017**, *22* (4), 593.

(71) George, P.; Bock, C. W.; Trachtman, M. An AB initio study of intramolecular hydrogen-bonding interactions in four-, five- and six-membered ring systems. *J. Mol. Struct.* **1983**, *92*, 109-139.

(72) Bilton, C.; Allen, F. H.; Shields, G. P.; Howard, J. A. K. Intramolecular hydrogen bonds: common motifs, probabilities of formation and implications for supramolecular organization. *Acta Crystallographica Section B* **2000**, *56* (5), 849-856.

(73) Kohn, W.; Sham, L. J. Self-Consistent Equations Including Exchange and Correlation Effects. *Physical Review* **1965**, *140* (4A), A1133-A1138.

(74) Møller, C.; Plesset, M. S. Note on an Approximation Treatment for Many-Electron Systems. *Physical Review* **1934**, *46* (7), 618-622.

(75) Han, R.; Luber, S. Fast Estimation of Møller–Plesset Correlation Energies Based on Atomic Contributions. *The Journal of Physical Chemistry Letters* **2021**, *12* (22), 5324-5331.

(76) McGibbon, R. T.; Taube, A. G.; Donchev, A. G.; Siva, K.; Hernández, F.; Hargus, C.; Law, K.-H.; Klepeis, J. L.; Shaw, D. E. Improving the accuracy of Møller-Plesset perturbation theory with neural networks. *The Journal of Chemical Physics* **2017**, *147* (16), 161725.

(77) Wiberg, K. B. Ab Initio Molecular Orbital Theory by W. J. Hehre, L. Radom, P. v. R. Schleyer, and J. A. Pople, John Wiley, New York, 548pp. Price: $79.95 (1986). *J. Comput. Chem.* **1986**, *7* (3), 379-379.

(78) El-Azhary, A. A.; Suter, H. U. Comparison between Optimized Geometries and Vibrational Frequencies Calculated by the DFT Methods. *The Journal of Physical Chemistry* **1996**, *100* (37), 15056-15063.

(79) Tirado-Rives, J.; Jorgensen, W. L. Performance of B3LYP Density Functional Methods for a Large Set of Organic Molecules. *Journal of Chemical Theory and Computation* **2008**, *4* (2), 297-306.

(80) Stewart, J. J. P. Optimization of parameters for semiempirical methods V: Modification of NDDO approximations and application to 70 elements. *J. Mol. Model.* **2007**, *13* (12), 1173-1213.

(81) Brandenburg, J. G.; Grimme, S. Dispersion Corrected Hartree–Fock and Density Functional Theory for Organic Crystal Structure Prediction. In *Prediction and Calculation of Crystal*

Structures: Methods and Applications, Atahan-Evrenk, S., Aspuru-Guzik, A. Eds.; Springer International Publishing, 2014; pp 1-23.

(82) Körzdörfer, T.; Brédas, J.-L. Organic Electronic Materials: Recent Advances in the DFT Description of the Ground and Excited States Using Tuned Range-Separated Hybrid Functionals. *Acc. Chem. Res.* **2014**, *47* (11), 3284-3291.

(83) Becke, A. Density-functional thermochemistry. III. The role of exact exchange (1993) J. *Chem. Phys 98*, 5648.

(84) Ditchfield, R.; Hehre, W. J.; Pople, J. A. Self-Consistent Molecular-Orbital Methods. IX. An Extended Gaussian-Type Basis for Molecular-Orbital Studies of Organic Molecules. *The Journal of Chemical Physics* **1971**, *54* (2), 724-728.

(85) Stephens, P. J.; Devlin, F. J.; Chabalowski, C. F.; Frisch, M. J. Ab Initio Calculation of Vibrational Absorption and Circular Dichroism Spectra Using Density Functional Force Fields. *The Journal of Physical Chemistry* **1994**, *98* (45), 11623-11627.

(86) Riley, K. E.; Op't Holt, B. T.; Merz, K. M. Critical Assessment of the Performance of Density Functional Methods for Several Atomic and Molecular Properties. *Journal of Chemical Theory and Computation* **2007**, *3* (2), 407-433.

(87) Rao, L.; Ke, H.; Fu, G.; Xu, X.; Yan, Y. Performance of Several Density Functional Theory Methods on Describing Hydrogen-Bond Interactions. *Journal of Chemical Theory and Computation* **2009**, *5* (1), 86-96.

(88) Xu, X.; Zhang, Q.; Muller, R. P.; III, W. A. G. An extended hybrid density functional (X3LYP) with improved descriptions of nonbond interactions and thermodynamic properties of molecular systems. *The Journal of Chemical Physics* **2005**, *122* (1), 014105.

(89) Kafafi, S. A. Novel Density Functional Methodology for the Computation of Accurate Electronic and Thermodynamic Properties of Molecular Systems and Improved Long-Range Behavior. *The Journal of Physical Chemistry A* **1998**, *102* (50), 10404-10413.

(90) Wong, B. M.; Cordaro, J. G. Electronic Properties of Vinylene-Linked Heterocyclic Conducting Polymers: Predictive Design and Rational Guidance from DFT Calculations. *The Journal of Physical Chemistry C* **2011**, *115* (37), 18333-18341.

(91) Song, P.; Ma, F. Tunable Electronic Structures and Optical Properties of Fluorenone-Based Molecular Materials by Heteroatoms. *The Journal of Physical Chemistry A* **2010**, *114* (5), 2230-2234.

(92) Yin, J.; Chaitanya, K.; Ju, X.-H. Theoretical study of the fluorination effect on charge transport properties in fused thiophene derivatives. *RSC Advances* **2015**, *5* (80), 65192-65202, 10.1039/C5RA06418J.

(93) Bourass, M.; El Alamy, A.; Bouachrine, M. Structural and photophysical studies of triphenylamine-based nonlinear optical dyes: effects of π-linker moieties on the D-π-A structure. *Comptes Rendus Chimie* **2019**, *22* (5), 373-385.

(94) Zhu, C.; Ji, X.; You, D.; Chen, T. L.; Mu, A. U.; Barker, K. P.; Klivansky, L. M.; Liu, Y.; Fang, L. Extraordinary Redox Activities in Ladder-Type Conjugated Molecules Enabled by B ← N Coordination-Promoted Delocalization and Hyperconjugation. *Journal of the American Chemical Society* **2018**, *140* (51), 18173-18182.

(95) Jacquemin, D.; Adamo, C. Bond Length Alternation of Conjugated Oligomers: Wave Function and DFT Benchmarks. *Journal of Chemical Theory and Computation* **2011**, *7* (2), 369-376.

(96) Bois, J.; Körzdörfer, T. How Bond Length Alternation and Thermal Disorder Affect the Optical Excitation Energies of π-Conjugated Chains: A Combined Density Functional Theory and Molecular Dynamics Study. *Journal of Chemical Theory and Computation* **2016**, *12* (4), 1872-1882.

(97) Körzdörfer, T.; Parrish, R. M.; Sears, J. S.; Sherrill, C. D.; Brédas, J.-L. On the relationship between bond-length alternation and many-electron self-interaction error. *The Journal of Chemical Physics* **2012**, *137* (12), 124305.

(98) Che, Y.; Perepichka, D. F. Quantifying Planarity in the Design of Organic Electronic Materials. *Angew. Chem. Int. Ed.* **2021**, *60* (3), 1364-1373.

(99) Comí, M.; Ocheje, M. U.; Attar, S.; Mu, A. U.; Philips, B. K.; Kalin, A. J.; Kakosimos, K. E.; Fang, L.; Rondeau-Gagné, S.; Al-Hashimi, M. Synthesis and Photocyclization of Conjugated Diselenophene Pyrrole-2,5-dione Based Monomers for Optoelectronics. *Macromolecules* **2021**, *54* (2), 665-672.

(100) Ogoshi, T.; Kanai, S.; Fujinami, S.; Yamagishi, T.-a.; Nakamoto, Y. para-Bridged Symmetrical Pillar[5]arenes: Their Lewis Acid Catalyzed Synthesis and Host–Guest Property. *Journal of the American Chemical Society* **2008**, *130* (15), 5022-5023.

(101) Cao, D.; Kou, Y.; Liang, J.; Chen, Z.; Wang, L.; Meier, H. A Facile and Efficient Preparation of Pillararenes and a Pillarquinone. *Angewandte Chemie International Edition* **2009**, *48* (51), 9721-9723.

(102) Hu, X.-B.; Chen, Z.; Chen, L.; Zhang, L.; Hou, J.-L.; Li, Z.-T. Pillar[n]arenes (n = 8–10) with two cavities: synthesis, structures and complexing properties. *Chem. Commun.* **2012**, *48* (89), 10999-11001, 10.1039/C2CC36027F.

(103) Wang, K.; Tan, L.-L.; Chen, D.-X.; Song, N.; Xi, G.; Zhang, S. X.-A.; Li, C.; Yang, Y.-W. One-pot synthesis of pillar[n]arenes catalyzed by a minimum amount of TfOH and a solution-phase mechanistic study. *Organic & Biomolecular Chemistry* **2012**, *10* (47), 9405-9409, 10.1039/C2OB26635K.

(104) Wu, J.-R.; Mu, A. U.; Li, B.; Wang, C.-Y.; Fang, L.; Yang, Y.-W. Desymmetrized Leaning Pillar[6]arene. *Angew. Chem. Int. Ed.* **2018**, *57* (31), 9853-9858.

(105) Zhang, D.; Heeney, M. Organic Donor–Acceptor Systems. *Asian Journal of Organic Chemistry* **2020**, *9* (9), 1251-1251, https://doi.org/10.1002/ajoc.202000465.

(106) Stalder, R.; Mei, J.; Graham, K. R.; Estrada, L. A.; Reynolds, J. R. Isoindigo, a Versatile Electron-Deficient Unit For High-Performance Organic Electronics. *Chem. Mater.* **2014**, *26* (1), 664-678.

(107) Randell, N. M.; Kelly, T. L. Recent Advances in Isoindigo-Inspired Organic Semiconductors. *The Chemical Record* **2019**, *19* (6), 973-988.

(108) Huang, J.; Mao, Z.; Chen, Z.; Gao, D.; Wei, C.; Zhang, W.; Yu, G. Diazaisoindigo-Based Polymers with High-Performance Charge-Transport Properties: From Computational Screening to Experimental Characterization. *Chem. Mater.* **2016**, *28* (7), 2209-2218.

(109) Lu, Y.; Liu, Y.; Dai, Y.-Z.; Yang, C.-Y.; Un, H.-I.; Liu, S.-W.; Shi, K.; Wang, J.-Y.; Pei, J. 5,5′-Diazaisoindigo: an Electron-Deficient Building Block for Donor–Acceptor Conjugated Polymers. *Chemistry – An Asian Journal* **2017**, *12* (3), 302-307.

(110) Kojj -Prodj , B.; Mom anov, K. The Nature of Hydrogen Bond : New Iinsights Into Old Theories. *Acta Chimica Slovenica* **2008**, *55*, 692-708.

(111) Gorelik, M. V.; Gladysheva, T. K.; Shapet'ko, N. N.; Zaitsev, B. E.; Kurkovskaya, L. N.; Trankvil'nitskaya, N. A.; Mikhailova, T. A. Intramolecular hydrogen bonding with the participation of the nitrogen atom of five- and six-membered heterocycles. *Chemistry of Heterocyclic Compounds* **1971**, *7* (2), 220-225.

(112) Li, J.-L.; Chai, Y.-F.; Wang, W. V.; Shi, Z.-F.; Xu, Z.-G.; Zhang, H.-L. Pyrazine-fused isoindigo: a new building block for polymer solar cells with high open circuit voltage. *Chemical Communications* **2017**, *53* (43), 5882-5885, 10.1039/C7CC01973D.

(113) Vijayan, S. M.; Sparks, N.; Roy, J. K.; Smith, C.; Tate, C.; Hammer, N. I.; Leszczynski, J.; Watkins, D. L. Evaluating Donor Effects in Isoindigo-Based Small Molecular Fluorophores. *The Journal of Physical Chemistry A* **2020**, *124* (51), 10777-10786.

(114) Bondi, A. van der Waals Volumes and Radii. *The Journal of Physical Chemistry* **1964**, *68* (3), 441-451.

(115) Bastida, A.; Zúñiga, J.; Requena, A.; Miguel, B.; Cerezo, J. On the Role of Entropy in the Stabilization of α-Helices. *Journal of Chemical Information and Modeling* **2020**, *60* (12), 6523-6531.

(116) Exarchou, V.; Troganis, A.; Gerothanassis, I. P.; Tsimidou, M.; Boskou, D. Do strong intramolecular hydrogen bonds persist in aqueous solution? Variable temperature gradient 1H, 1H–13C GE-HSQC and GE-HMBC NMR studies of flavonols and flavones in organic and aqueous mixtures. *Tetrahedron* **2002**, *58* (37), 7423-7429.

(117) Lin, P.-P.; Qin, G.-Y.; Zhang, N.-X.; Fan, J.-X.; Hao, X.-L.; Zou, L.-Y.; Ren, A.-M. The roles of heteroatoms and substituents on the molecular packing motif from herringbone to π-stacking: A theoretical study on electronic structures and intermolecular interaction of pentacene derivatives. *Organic Electronics* **2020**, *78*, 105606.

(118) Zou, Y.; Ji, X.; Cai, J.; Yuan, T.; Stanton, D. J.; Lin, Y.-H.; Naraghi, M.; Fang, L. Synthesis and Solution Processing of a Hydrogen-Bonded Ladder Polymer. *Chem* **2017**, *2* (1), 139-152.

(119) Guo, Z.-H.; Ai, N.; McBroom, C. R.; Yuan, T. Y.; Lin, Y. H.; Roders, M.; Zhu, C. Z.; Ayzner, A. L.; Pei, J.; Fang, L. A side-chain engineering approach to solvent-resistant semiconducting polymer thin films. *Polymer Chemistry* **2016**, *7* (3), 648-655.

149

(120) Zhang, H.; Tung, W.-Y.; Li, X.; Jin, H.; Deng, R.; Chen, Y.-M.; Mao, Y.; Zhu, Y. Conjugated polymer with dynamic and thermoreversible hydrogen bonding on the backbone. *Polymer* **2020**, *203*, 122787.

(121) Yang, K.; He, T.; Chen, X.; Cheng, S. Z. D.; Zhu, Y. Patternable Conjugated Polymers with Latent Hydrogen-Bonding on the Main Chain. *Macromolecules* **2014**, *47* (24), 8479-8486.

(122) *Gaussian 16 Rev. C.01*; Wallingford, CT, 2016. (accessed.

(123) Samiullah, M.; Moghe, D.; Scherf, U.; Guha, S. Diffusion length of triplet excitons in organic semiconductors. *Physical Review B* **2010**, *82* (20), 205211.

(124) Zhu, C.; Fang, L. Locking the Coplanar Conformation of π-Conjugated Molecules and Macromolecules Using Dynamic Noncovalent Bonds. *Macromol. Rapid Commun.* **2018**, *39* (2), 1700241.

(125) Mullin, W. J.; Sharber, S. A.; Thomas III, S. W. Optimizing the self-assembly of conjugated polymers and small molecules through structurally programmed non-covalent control. *Journal of Polymer Science* **2021**, *59* (15), 1643-1663.

(126) Ocheje, M. U.; Goodman, R. B.; Lu, K.-T.; Wang, Y.; Galuska, L. A.; Soullard, L.; Cao, Z.; Zhang, S.; Yadiki, M.; Gu, X.; et al. Precise Control of Noncovalent Interactions in Semiconducting Polymers for High-Performance Organic Field-Effect Transistors. *Chemistry of Materials* **2021**.

(127) Mei, J.; Graham, K. R.; Stalder, R.; Reynolds, J. R. Synthesis of Isoindigo-Based Oligothiophenes for Molecular Bulk Heterojunction Solar Cells. *Org. Lett.* **2010**, *12* (4), 660-663.

(128) Zhou, R.; Zhang, K.; Chen, Y.; Meng, Q.; Liu, Y.; Li, R.; He, Z. P(NMe2)3-mediated reductive [1+4] annulation of isatins with enones: a facile synthesis of spirooxindole-dihydrofurans. *Chemical Communications* **2015**, *51* (78), 14663-14666, 10.1039/C5CC03676C.

(129) Wang, S. R.; Radosevich, A. T. P(NMe2)3-Mediated Umpolung Alkylation and Nonylidic Olefination of α-Keto Esters. *Organic Letters* **2015**, *17* (15), 3810-3813.

(130) Dhanishta, P.; Sai Siva kumar, P.; Mishra, S. K.; Suryaprakash, N. Intramolecular hydrogen bond directed stable conformations of benzoyl phenyl oxalamides: unambiguous evidence from extensive NMR studies and DFT-based computations. *RSC Advances* **2018**, *8* (20), 11230-11240, 10.1039/C8RA00357B.

(131) Scheiner, S. Assessment of the Presence and Strength of H-Bonds by Means of Corrected NMR. *Molecules* **2016**, *21* (11), 1426.

(132) Cagardová, D.; Lukeš, V. Molecular orbital analysis of selected organic p-type and n-type conducting small molecules. *Acta Chimica Slovaca* **2017**, *10* (1), 6-16.

(133) Filo, J.; Putala, M. Semiconducting Organic Molecular Materials. *Journal of Electrical Engineering* **2011**, *61* (5), 314-320.

(134) Quinn, J. T. E.; Zhu, J.; Li, X.; Wang, J.; Li, Y. Recent progress in the development of n-type organic semiconductors for organic field effect transistors. *Journal of Materials Chemistry C* **2017**, *5* (34), 8654-8681, 10.1039/C7TC01680H.

(135) de Miguel, G.; Camacho, L.; García-Frutos, E. M. 7,7′-Diazaisoindigo: a novel building block for organic electronics. *Journal of Materials Chemistry C* **2016**, *4* (6), 1208-1214, 10.1039/C5TC03464G.

(136) Elsawy, W.; Lee, C.-L.; Cho, S.; Oh, S.-H.; Moon, S.-H.; Elbarbary, A.; Lee, J.-S. Isoindigo-based small molecules for high-performance solution-processed organic photovoltaic devices: the electron donating effect of the donor group on photo-physical properties and device performance. *Physical Chemistry Chemical Physics* **2013**, *15* (36), 15193-15203, 10.1039/C3CP52151F.

(137) Guo, Z.-H.; Ai, N.; McBroom, C. R.; Yuan, T.; Lin, Y.-H.; Roders, M.; Zhu, C.; Ayzner, A. L.; Pei, J.; Fang, L. A side-chain engineering approach to solvent-resistant semiconducting polymer thin films. *Polymer Chemistry* **2016**, *7* (3), 648-655, 10.1039/C5PY01669J.

(138) Zhu, C.; Kalin, A. J.; Fang, L. Covalent and Noncovalent Approaches to Rigid Coplanar π-Conjugated Molecules and Macromolecules. *Acc. Chem. Res.* **2019**, *52* (4), 1089-1100.

(139) Cao, Y.; Zhu, C.; Barłóg, M.; Barker, K. P.; Ji, X.; Kalin, A. J.; Al-Hashimi, M.; Fang, L. Electron-Deficient Polycyclic π-System Fused with Multiple B←N Coordinate Bonds. *J. Org. Chem.* **2021**, *86* (3), 2100-2106.

(140) Ando, S.; Murakami, R.; Nishida, J.-i.; Tada, H.; Inoue, Y.; Tokito, S.; Yamashita, Y. n-Type Organic Field-Effect Transistors with Very High Electron Mobility Based on Thiazole Oligomers with Trifluoromethylphenyl Groups. *Journal of the American Chemical Society* **2005**, *127* (43), 14996-14997.

(141) Yan, H.; Chen, Z.; Zheng, Y.; Newman, C.; Quinn, J. R.; Dötz, F.; Kastler, M.; Facchetti, A. A high-mobility electron-transporting polymer for printed transistors. *Nature* **2009**, *457* (7230), 679-686.

(142) Dou, C.; Ding, Z.; Zhang, Z.; Xie, Z.; Liu, J.; Wang, L. Developing Conjugated Polymers with High Electron Affinity by Replacing a C C Unit with a B←N Unit. *Angew. Chem. Int. Ed.* **2015**, *54* (12), 3648-3652.

(143) Keum, C.-M.; Bae, J.-H.; Kim, M.-H.; Choi, W.; Lee, S.-D. Solution-processed low leakage organic field-effect transistors with self-pattern registration based on patterned dielectric barrier. *Org. Electron.* **2012**, *13* (5), 778-783.

(144) Martínez Hardigree, J. F.; Dawidczyk, T. J.; Ireland, R. M.; Johns, G. L.; Jung, B.-J.; Nyman, M.; Österbacka, R.; Marković, N.; Katz, H. E. Reducing Leakage Currents in n-Channel Organic Field-Effect Transistors Using Molecular Dipole Monolayers on Nanoscale Oxides. *ACS Applied Materials & Interfaces* **2013**, *5* (15), 7025-7032.

(145) Cao, Y. FUSED-RING HETEROCYCLIC AROMATIC COMPOUNDS. Ph.D., Texas A&M University, College Station, TX, 77843, 2022.

(146) Chen, H.; Hu, Z.; Wang, H.; Liu, L.; Chao, P.; Qu, J.; Chen, W.; Liu, A.; He, F. A Chlorinated π-Conjugated Polymer Donor for Efficient Organic Solar Cells. *Joule* **2018**, *2* (8), 1623-1634.

(147) Zhou, Z.; Wu, Q.; Wang, S.; Huang, Y.-T.; Guo, H.; Feng, S.-P.; Chan, P. K. L. Field-Effect Transistors Based on 2D Organic Semiconductors Developed by a Hybrid Deposition Method. *Advanced Science* **2019**, *6* (19), 1900775.

(148) Liman, C. D.; Choi, S.; Breiby, D. W.; Cochran, J. E.; Toney, M. F.; Kramer, E. J.; Chabinyc, M. L. Two-Dimensional GIWAXS Reveals a Transient Crystal Phase in Solution-Processed Thermally Converted Tetrabenzoporphyrin. *The Journal of Physical Chemistry B* **2013**, *117* (46), 14557-14567.

(149) Ryno, S. M.; Risko, C.; Brédas, J.-L. Impact of Molecular Orientation and Packing Density on Electronic Polarization in the Bulk and at Surfaces of Organic Semiconductors. *ACS Applied Materials & Interfaces* **2016**, *8* (22), 14053-14062.

(150) Renaud, G.; Lazzari, R.; Leroy, F. Probing surface and interface morphology with Grazing Incidence Small Angle X-Ray Scattering. *Surf. Sci. Rep.* **2009**, *64* (8), 255-380.

(151) Hexemer, A.; Muller-Buschbaum, P. Advanced grazing-incidence techniques for modern soft-matter materials analysis. *IUCrJ* **2015**, *2* (1), 106-125.

(152) Gomez, M.; Nogales, A.; García-Gutiérrez, M. C.; Ezquerra, T. *Applications of Synchrotron Light to Scattering and Diffraction in Materials and Life Sciences by Marian Gomez, Aurora Nogales, Mari Cruz Garcia-Gutierrez, T.A. Ezquerra. Lecture Notes in Physics, Vol. 776. Berlin: Springer, 2009*; 2009.

(153) Richter, L. J.; DeLongchamp, D. M.; Amassian, A. Morphology Development in Solution-Processed Functional Organic Blend Films: An In Situ Viewpoint. *Chemical Reviews* **2017**, *117* (9), 6332-6366.

(154) Wang, W.-C.; Chen, S.-Y.; Yang, Y.-W.; Hsu, C.-S.; Tajima, K. Face-on reorientation of π-conjugated polymers in thin films by surface-segregated monolayers. *Journal of Materials Chemistry A* **2020**, *8* (13), 6268-6275, 10.1039/D0TA00030B.

(155) Mahmood, A.; Wang, J.-L. A Review of Grazing Incidence Small- and Wide-Angle X-Ray Scattering Techniques for Exploring the Film Morphology of Organic Solar Cells. *Solar RRL* **2020**, *4* (10), 2000337.

(156) Thuau, D.; Begley, K.; Dilmurat, R.; Ablat, A.; Wantz, G.; Ayela, C.; Abbas, M. Exploring the Critical Thickness of Organic Semiconductor Layer for Enhanced Piezoresistive Sensitivity in Field-Effect Transistor Sensors. *Materials* **2020**, *13* (7), 1583.

(157) Li, S.; Guérin, D.; Lmimouni, K. Improving performance of OFET by tuning occurrence of charge transport based on pentacene interaction with SAM functionalized contacts. *Microelectron. Eng.* **2018**, *195*, 62-67.

(158) Ren, H.; Ouyang, M.; Wang, J.; Zhang, L.; Fu, Y. Direct self-assembled monolayers treatment on the polar polymer dielectric towards ultra-flexible organic field-effect transistors. *Mater. Lett.* **2022**, *324*, 132495.

(159) Yamashita, Y. Organic semiconductors for organic field-effect transistors. *Science and Technology of Advanced Materials* **2009**, *10* (2), 024313.

(160) Inoue, S.; Nikaido, K.; Higashino, T.; Arai, S.; Tanaka, M.; Kumai, R.; Tsuzuki, S.; Horiuchi, S.; Sugiyama, H.; Segawa, Y.; et al. Emerging Disordered Layered-Herringbone Phase in Organic Semiconductors Unveiled by Electron Crystallography. *Chem. Mater.* **2022**, *34* (1), 72-83.

(161) Friedel, B.; McNeill, C. R.; Greenham, N. C. Influence of Alkyl Side-Chain Length on the Performance of Poly(3-alkylthiophene)/Polyfluorene All-Polymer Solar Cells. *Chem. Mater.* **2010**, *22* (11), 3389-3398.

(162) Zhou, Y.; Zhang, W.; Yu, G. Recent structural evolution of lactam- and imide-functionalized polymers applied in organic field-effect transistors and organic solar cells. *Chem. Sci.* **2021**, *12* (20), 6844-6878, 10.1039/D1SC01711J.

(163) Chen, F.; Jiang, Y.; Sui, Y.; Zhang, J.; Tian, H.; Han, Y.; Deng, Y.; Hu, W.; Geng, Y. Donor–Acceptor Conjugated Polymers Based on Bisisoindigo: Energy Level Modulation toward Unipolar n-Type Semiconductors. *Macromolecules* **2018**, *51* (21), 8652-8661.

(164) Chen, X.; Zhang, Z.; Ding, Z.; Liu, J.; Wang, L. Diketopyrrolopyrrole-based Conjugated Polymers Bearing Branched Oligo(Ethylene Glycol) Side Chains for Photovoltaic Devices. *Angew. Chem. Int. Ed.* **2016**, *55* (35), 10376-10380.

(165) Kim, G.; Kang, S.-J.; Dutta, G. K.; Han, Y.-K.; Shin, T. J.; Noh, Y.-Y.; Yang, C. A Thienoisoindigo-Naphthalene Polymer with Ultrahigh Mobility of 14.4 cm2/V·s That Substantially Exceeds Benchmark Values for Amorphous Silicon Semiconductors. *Journal of the American Chemical Society* **2014**, *136* (26), 9477-9483.

(166) Yang, J.; Zhao, Z.; Geng, H.; Cheng, C.; Chen, J.; Sun, Y.; Shi, L.; Yi, Y.; Shuai, Z.; Guo, Y.; et al. Isoindigo-Based Polymers with Small Effective Masses for High-Mobility Ambipolar Field-Effect Transistors. *Adv. Mater.* **2017**, *29* (36), 1702115.

(167) Li, H.; Mei, J.; Ayzner, A. L.; Toney, M. F.; Tok, J. B. H.; Bao, Z. A simple droplet pinning method for polymer film deposition for measuring charge transport in a thin film transistor. *Org. Electron.* **2012**, *13* (11), 2450-2460.

(168) Ma, Z.; Geng, H.; Wang, D.; Shuai, Z. Influence of alkyl side-chain length on the carrier mobility in organic semiconductors: herringbone vs. pi–pi stacking. *Journal of Materials Chemistry C* **2016**, *4* (20), 4546-4555, 10.1039/C6TC00755D.

(169) Shaker, M.; Park, B.; Lee, S.; Lee, K. Face-on oriented thermolabile Boc-isoindigo/thiophenes small molecules: From synthesis to OFET performance. *Dyes and Pigments* **2020**, *172*, 107784.

(170) Patil, H.; Chang, J.; Gupta, A.; Bilic, A.; Wu, J.; Sonar, P.; Bhosale, S. V. Isoindigo-Based Small Molecules with Varied Donor Components for Solution-Processable Organic Field Effect Transistor Devices. *Molecules (Basel, Switzerland)* **2015**, *20* (9), 17362-17377.

(171) Xu, S.; Ai, N.; Zheng, J.; Zhao, N.; Lan, Z.; Wen, L.; Wang, X.; Pei, J.; Wan, X. Extended isoindigo core: synthesis and applications as solution-processable n-OFET materials in ambient conditions. *RSC Advances* **2015**, *5* (11), 8340-8344, 10.1039/C4RA14072A.

(172) Hasegawa, T.; Ashizawa, M.; Matsumoto, H. Design and structure–property relationship of benzothienoisoindigo in organic field effect transistors. *RSC Advances* **2015**, *5* (75), 61035-61043, 10.1039/C5RA07660A.

(173) Wu, T.; Yu, C.; Guo, Y.; Liu, H.; Yu, G.; Fang, Y.; Liu, Y. Synthesis, Structures, and Properties of Thieno[3,2-b]thiophene and Dithiophene Bridged Isoindigo Derivatives and Their Organic Field-effect Transistors Performance. *The Journal of Physical Chemistry C* **2012**, *116* (43), 22655-22662.

(174) Sun, M.; Sun, Y.; Chen, R.; Hu, Y.; Zhang, G. Small molecule semiconductors based on hemi-isoindigo and diketopyrrolopyrrole for solution-processed organic field-effect transistors. *Synthetic Metals* **2021**, *278*, 116833.

(175) Zhang, G.; Chen, R.; Sun, Y.; Kang, B.; Sun, M.; Lu, H.; Qiu, L.; Cho, K.; Ding, Y. Improved charge transport in fused-ring bridged hemi-isoindigo-based small molecules by incorporating a thiophene unit for solution-processed organic field-effect transistors. *Journal of Materials Chemistry C* **2020**, *8* (4), 1398-1404, 10.1039/C9TC05374C.

(176) Jiang, Z.; Li, X.; Strzalka, J.; Sprung, M.; Sun, T.; Sandy, A. R.; Narayanan, S.; Lee, D. R.; Wang, J. The dedicated high-resolution grazing-incidence X-ray scattering beamline 8-ID-E at the Advanced Photon Source. *Journal of Synchrotron Radiation* **2012**, *19* (4), 627-636.

(177) Jiang, Z. GIXSGUI: a MATLAB toolbox for grazing-incidence X-ray scattering data visualization and reduction, and indexing of buried three-dimensional periodic nanostructured films. *Journal of Applied Crystallography* **2015**, *48* (3), 917-926.

(178) Moroni, M.; Le Moigne, J.; Luzzati, S. Rigid rod conjugated polymers for nonlinear optics: 1. Characterization and linear optical properties of poly(aryleneethynylene) derivatives. *Macromolecules* **1994**, *27* (2), 562-571.

(179) Hu, W.; Yan, Q.; Zhao, D. Oligo(p-phenylene-ethynylene)s with Backbone Conformation Controlled by Competitive Intramolecular Hydrogen Bonds. *Chem. Eur. J.* **2011**, *17* (25), 7087-7094.

(180) Lei, T.; Xia, X.; Wang, J.-Y.; Liu, C.-J.; Pei, J. "Conformation Locked" Strong Electron-Deficient Poly(p-Phenylene Vinylene) Derivatives for Ambient-Stable n-Type Field-Effect

Transistors: Synthesis, Properties, and Effects of Fluorine Substitution Position. *Journal of the American Chemical Society* **2014**, *136* (5), 2135-2141.

(181) Dou, J.-H.; Zheng, Y.-Q.; Yao, Z.-F.; Yu, Z.-A.; Lei, T.; Shen, X.; Luo, X.-Y.; Sun, J.; Zhang, S.-D.; Ding, Y.-F.; et al. Fine-Tuning of Crystal Packing and Charge Transport Properties of BDOPV Derivatives through Fluorine Substitution. *Journal of the American Chemical Society* **2015**, *137* (50), 15947-15956.

(182) Chen, X.-X.; Li, J.-T.; Fang, Y.-H.; Deng, X.-Y.; Wang, X.-Q.; Liu, G.; Wang, Y.; Gu, X.; Jiang, S.-D.; Lei, T. High-mobility semiconducting polymers with different spin ground states. *Nat. Commun.* **2022**, *13* (1), 2258.

(183) Barłóg, M.; Zhang, X.; Kulai, I.; Yang, D. S.; Sredojevic, D. N.; Sil, A.; Ji, X.; Salih, K. S. M.; Bazzi, H. S.; Bronstein, H.; et al. Indacenodithiazole-Ladder-Type Bridged Di(thiophene)-Difluoro-Benzothiadiazole-Conjugated Copolymers as Ambipolar Organic Field-Effect Transistors. *Chem. Mater.* **2019**, *31* (22), 9488-9496.

(184) Legault, C. Y.; Garcia, Y.; Merlic, C. A.; Houk, K. N. Origin of Regioselectivity in Palladium-Catalyzed Cross-Coupling Reactions of Polyhalogenated Heterocycles. *Journal of the American Chemical Society* **2007**, *129* (42), 12664-12665.

(185) Song, J.; Wei, F.; Sun, W.; Cao, X.; Liu, C.; Xie, L.; Huang, W. Highly efficient C–C cross-coupling for installing thiophene rings into π-conjugated systems. *Organic Chemistry Frontiers* **2014**, *1* (7), 817-820, 10.1039/C4QO00167B.

(186) Fleckenstein, C. A.; Plenio, H. Efficient Suzuki−Miyaura Coupling of (Hetero)aryl Chlorides with Thiophene- and Furanboronic Acids in Aqueous n-Butanol. *J. Org. Chem.* **2008**, *73* (8), 3236-3244.

(187) Shen, G.; Yang, B.; Huang, X.; Hou, Y.; Gao, H.; Cui, J.; Cui, C.; Zhang, T. Copper- and Palladium-Catalyzed Cross-Coupling Reactions for the Synthesis of N-Fused Benzo[4,5]imidazo[2,1-b]thiazole Derivatives via Substituted trans-1,2-Diiodoalkenes, 1H-Benzo[d]imidazole-2-thiols, and Halobenzenes. *J. Org. Chem.* **2017**, *82* (7), 3798-3805.

(188) Nielsen, C. B.; Holliday, S.; Chen, H.-Y.; Cryer, S. J.; McCulloch, I. Non-Fullerene Electron Acceptors for Use in Organic Solar Cells. *Accounts of Chemical Research* **2015**, *48* (11), 2803-2812.

(189) Yan, C.; Barlow, S.; Wang, Z.; Yan, H.; Jen, A. K. Y.; Marder, S. R.; Zhan, X. Non-fullerene acceptors for organic solar cells. *Nature Reviews Materials* **2018**, *3* (3), 18003.

(190) Shan, B.; Miao, Q. Molecular design of n-type organic semiconductors for high-performance thin film transistors. *Tetrahedron Letters* **2017**, *58* (20), 1903-1911.

(191) Naibi Lakshminarayana, A.; Ong, A.; Chi, C. Modification of acenes for n-channel OFET materials. *Journal of Materials Chemistry C* **2018**, *6* (14), 3551-3563, 10.1039/C8TC00146D.

(192) Dou, J.-H.; Yu, Z.-A.; Zhang, J.; Zheng, Y.-Q.; Yao, Z.-F.; Tu, Z.; Wang, X.; Huang, S.; Liu, C.; Sun, J.; et al. Organic Semiconducting Alloys with Tunable Energy Levels. *Journal of the American Chemical Society* **2019**, *141* (16), 6561-6568.

(193) Liu, K.; Lalancette, R. A.; Jäkle, F. Tuning the Structure and Electronic Properties of B–N Fused Dipyridylanthracene and Implications on the Self-Sensitized Reactivity with Singlet Oxygen. *Journal of the American Chemical Society* **2019**, *141* (18), 7453-7462.

(194) Vanga, M.; Lalancette, R. A.; Jäkle, F. Controlling the Optoelectronic Properties of Pyrene by Regioselective Lewis Base-Directed Electrophilic Aromatic Borylation. *Chem. Eur. J.* **2019**, *25* (43), 10133-10140.

(195) Crossley, D. L.; Cade, I. A.; Clark, E. R.; Escande, A.; Humphries, M. J.; King, S. M.; Vitorica-Yrezabal, I.; Ingleson, M. J.; Turner, M. L. Enhancing electron affinity and tuning band gap in donor-acceptor organic semiconductors by benzothiadiazole directed C-H borylation. *Chem Sci* **2015**, *6* (9), 5144-5151.

(196) Min, Y.; Dou, C.; Liu, D.; Dong, H.; Liu, J. Quadruply B←N-Fused Dibenzo-azaacene with High Electron Affinity and High Electron Mobility. *Journal of the American Chemical Society* **2019**, *141* (42), 17015-17021.

(197) Fischer, G. M.; Daltrozzo, E.; Zumbusch, A. Selective NIR chromophores: Bis(Pyrrolopyrrole) Cyanines. *Angew. Chem. Int. Ed.* **2011**, *50* (6), 1406-1409.

(198) Shimogawa, H.; Murata, Y.; Wakamiya, A. NIR-Absorbing Dye Based on BF2-Bridged Azafulvene Dimer as a Strong Electron-Accepting Unit. *Org. Lett.* **2018**, *20* (17), 5135-5138.

(199) Grandl, M.; Rudolf, B.; Sun, Y.; Bechtel, D. F.; Pierik, A. J.; Pammer, F. Intramolecular N→B Coordination as a Stabilizing Scaffold for π-Conjugated Radical Anions with Tunable Redox Potentials. *Organometallics* **2017**, *36* (14), 2527-2535.

(200) Grandl, M.; Kaese, T.; Krautsieder, A.; Sun, Y.; Pammer, F. Hydroboration as an Efficient Tool for the Preparation of Electronically and Structurally Diverse N→B-Heterocycles. *Chem. Eur. J.* **2016**, *22* (40), 14373-14382.

(201) Rodrigues Silva, D.; de Azevedo Santos, L.; Freitas, M. P.; Guerra, C. F.; Hamlin, T. A. Nature and Strength of Lewis Acid/Base Interaction in Boron and Nitrogen Trihalides. *Chemistry – An Asian Journal* **2020**, *15* (23), 4043-4054.

(202) Xiang, Y.; Meng, H.; Yao, Q.; Chang, Y.; Yu, H.; Guo, L.; Xue, Q.; Zhan, C.; Huang, J.; Chen, G. B ← N Bridged Polymer Acceptors with 900 nm Absorption Edges Enabling High-Performance All-Polymer Solar Cells. *Macromolecules* **2020**, *53* (21), 9529-9538.

(203) Yu, Y.; Zhang, L.; Liu, J.; Wang, L. Incorporating Se atoms to organoboron polymer electron acceptors to tune opto-electronic properties. *Polymer* **2022**, *242*, 124547.

(204) Shao, X.; Wang, J.; Marder, T. B.; Xie, Z.; Liu, J.; Wang, L. N–B ← N Bridged Bithiophene: A Building Block with Reduced Band Gap to Design n-Type Conjugated Polymers. *Macromolecules* **2021**, *54* (14), 6718-6725.

(205) Wu, Y.; Li, Y.; Gardner, S.; Ong, B. S. Indolo[3,2-b]carbazole-Based Thin-Film Transistors with High Mobility and Stability. *Journal of the American Chemical Society* **2005**, *127* (2), 614-618.

(206) Boudreault, P.-L. T.; Wakim, S.; Tang, M. L.; Tao, Y.; Bao, Z.; Leclerc, M. New indolo[3,2-b]carbazole derivatives for field-effect transistor applications. *J. Mater. Chem.* **2009**, *19* (19), 2921-2928, 10.1039/B900271E.

(207) Bulfield, D.; Huber, S. M. Synthesis of Polyflourinated Biphenyls; Pushing the Boundaries of Suzuki–Miyaura Cross Coupling with Electron-Poor Substrates. *J. Org. Chem.* **2017**, *82* (24), 13188-13203.

(208) Kettle, J.; Horie, M.; Majewski, L. A.; Saunders, B. R.; Tuladhar, S.; Nelson, J.; Turner, M. L. Optimisation of PCPDTBT solar cells using polymer synthesis with Suzuki coupling. *Sol. Energy Mater. Sol. Cells* **2011**, *95* (8), 2186-2193.

(209) Carsten, B.; He, F.; Son, H. J.; Xu, T.; Yu, L. Stille Polycondensation for Synthesis of Functional Materials. *Chem. Rev.* **2011**, *111* (3), 1493-1528.

(210) Jeon, Y.-K.; Lee, J.-Y.; Kim, S.-E.; Kim, W.-S. Highly Selective Room-Temperature Suzuki–Miyaura Coupling of Bromo-2-sulfonyloxypyridines for Unsymmetrical Diarylpyridines. *J. Org. Chem.* **2020**, *85* (11), 7399-7412.

(211) Li, S.; Lin, Y.; Cao, J.; Zhang, S. Guanidine/Pd(OAc)2-Catalyzed Room Temperature Suzuki Cross-Coupling Reaction in Aqueous Media under Aerobic Conditions. *J. Org. Chem.* **2007**, *72* (11), 4067-4072.

(212) Yang, J.; Liu, S.; Zheng, J.-F.; Zhou, J. Room-Temperature Suzuki–Miyaura Coupling of Heteroaryl Chlorides and Tosylates. *Eur. J. Org. Chem.* **2012**, *2012* (31), 6248-6259.

(213) Jawale, D. V.; Gravel, E.; Boudet, C.; Shah, N.; Geertsen, V.; Li, H.; Namboothiri, I. N. N.; Doris, E. Room temperature Suzuki coupling of aryl iodides, bromides, and chlorides using a heterogeneous carbon nanotube-palladium nanohybrid catalyst. *Catalysis Science & Technology* **2015**, *5* (4), 2388-2392, 10.1039/C4CY01680G.

(214) Randell, N. M.; Fransishyn, K. M.; Kelly, T. L. Lewis Acid–Base Chemistry of 7-Azaisoindigo-Based Organic Semiconductors. *ACS Applied Materials & Interfaces* **2017**, *9* (29), 24788-24796.

(215) Salleo, A.; Chabinyc, M. L.; Yang, M. S.; Street, R. A. Polymer thin-film transistors with chemically modified dielectric interfaces. *Appl. Phys. Lett.* **2002**, *81* (23), 4383-4385.

(216) Street, R. A.; Northrup, J. E.; Salleo, A. Transport in polycrystalline polymer thin-film transistors. *Physical Review B* **2005**, *71* (16), 165202.

(217) Ocheje, M. U.; Selivanova, M.; Zhang, S.; Van Nguyen, T. H.; Charron, B. P.; Chuang, C.-H.; Cheng, Y.-H.; Billet, B.; Noori, S.; Chiu, Y.-C.; et al. Influence of amide-containing side chains on the mechanical properties of diketopyrrolopyrrole-based polymers. *Polym. Chem.* **2018**, *9* (46), 5531-5542, 10.1039/C8PY01207E.

(218) McCulloch, I.; Heeney, M.; Chabinyc, M. L.; DeLongchamp, D.; Kline, R. J.; Cölle, M.; Duffy, W.; Fischer, D.; Gundlach, D.; Hamadani, B.; et al. Semiconducting Thienothiophene Copolymers: Design, Synthesis, Morphology, and Performance in Thin-Film Organic Transistors. *Adv. Mater.* **2009**, *21* (10-11), 1091-1109.

(219) Larik, F. A.; Faisal, M.; Saeed, A.; Abbas, Q.; Kazi, M. A.; Abbas, N.; Thebo, A. A.; Khan, D. M.; Channar, P. A. Thiophene-based molecular and polymeric semiconductors for organic field effect transistors and organic thin film transistors. *Journal of Materials Science: Materials in Electronics* **2018**, *29* (21), 17975-18010.

(220) Deng, P.; Zhang, Q. Recent developments on isoindigo-based conjugated polymers. *Polym. Chem.* **2014**, *5* (10), 3298-3305, 10.1039/C3PY01598J.

(221) Wu, H.-C.; Hung, C.-C.; Hong, C.-W.; Sun, H.-S.; Wang, J.-T.; Yamashita, G.; Higashihara, T.; Chen, W.-C. Isoindigo-Based Semiconducting Polymers Using Carbosilane Side Chains for High Performance Stretchable Field-Effect Transistors. *Macromolecules* **2016**, *49* (22), 8540-8548.

(222) Egbe, D. A. M.; Türk, S.; Rathgeber, S.; Kühnlenz, F.; Jadhav, R.; Wild, A.; Birckner, E.; Adam, G.; Pivrikas, A.; Cimrova, V.; et al. Anthracene Based Conjugated Polymers: Correlation between π−π-Stacking Ability, Photophysical Properties, Charge Carrier Mobility, and Photovoltaic Performance. *Macromolecules* **2010**, *43* (3), 1261-1269.

(223) Jung, J. W.; Liu, F.; Russell, T. P.; Jo, W. H. Anthracene-Based Medium Bandgap Conjugated Polymers for High Performance Polymer Solar Cells Exceeding 8% PCE Without Additive and Annealing Process. *Advanced Energy Materials* **2015**, *5* (11), 1500065.